

# First-principles investigation of fluoride doping in bulk and on surfaces of aluminium (oxo)hydroxides

INAUGURAL-DISSERTATION

to obtain the academic degree  
DOCTOR RERUM NATURALIUM (DR. RER. NAT.)

submitted to  
THE DEPARTMENT OF BIOLOGY, CHEMISTRY, AND PHARMACY  
OF FREIE UNIVERSITÄT BERLIN

by  
JOHANNES HORST BUDAU  
from BERLIN

2018



This work was prepared under supervision of  
PROF. DR. BEATE PAULUS (FREIE UNIVERSITÄT BERLIN)

in the time frame of  
DECEMBER 2014 TO MAY 2018

at the  
DEPARTMENT OF BIOLOGY, CHEMISTRY, AND PHARMACY  
PHYSICAL AND THEORETICAL CHEMISTRY

1<sup>st</sup> Reviewer

PROF. DR. BEATE PAULUS

2<sup>nd</sup> Reviewer

PROF. DR. ERHARD KEMNITZ

Date of Defence

19th July 2018



Für meinen Großvater

Horst Albert Hermann Heimann



## Danksagung

An dieser Stelle möchte ich meinen besonderen Dank an die Menschen richten, die mich die gesamte Zeit direkt oder indirekt bei der Erstellung dieser Arbeit unterstützt haben.

Beginnen möchte ich dabei mit meiner Betreuerin Prof. Dr. Beate Paulus. Sie gab mir nicht nur ein interessantes Thema zur Bearbeitung, sondern war auch mit Rat und Tat für mich da. Des Weiteren eröffneten sich mit ihrer Hilfe viele Gelegenheiten der Zusammenarbeit mit anderen Gruppen, wodurch einige neue Aspekte und Ansätze zu Tage gefördert wurden. Ebenso bin ich sehr dankbar für die verschiedenen Möglichkeiten mein Wissen in Sommerschulen, auf Symposien und auf Konferenzen zu erweitern. Besonders froh bin ich über die Möglichkeit gewesen, dass ich durch sie über die Jahre einige Praktika mitbetreuen durfte und so Einblicke, wenn auch kleine, in die Lehrtätigkeit erhielt.

Nicht weniger Dank möchte ich an meinen zweiten Betreuer Prof. Dr. Erhard Kemnitz richten, welcher meine theoretische Arbeit mit seinem Wissen über experimentelle Möglichkeiten und Ergebnisse stets beflügeln konnte und mich gleichzeitig vor Wasser und Sonne warnte.

Ebenfalls gilt mein Dank Priv.-Doz. Dr. Dirk Andrae und Priv.-Doz. Dr. Gudrun Scholz, welche mir bei offenen Fragen und Problemen mit Diskussionen und Anregungen eine große Hilfe waren.

Einen weiteren großen Teil meines Dankes möchte ich, in alphabetischer Reihenfolge und „Ladies First“, an meine gewonnenen Freunde Jingjing, Christian, Gunter, Lukas, Marcel und Vincent richten. Sie sorgten nicht nur für eine stets sehr angenehme und

heitere Arbeitsatmosphäre, sondern standen mir auch immer mit Rat und Tat zur Seite und sorgten so dafür, dass ich nicht nur gut voran kam mit meinen Aufgaben, sondern dies auch mit Freude und Spaß tun konnte. An dieser Stelle möchte ich mich auch bei den Studenten Dennis Meinhold und Riddhish Pandharkar bedanken, die ich bei ihren Forschungspraktika bzw. Masterarbeiten unterstützen durfte. Auch bei diesen Gelegenheiten konnten neue Eindrücke und Ansätze entdeckt werden, die mir neue Standpunkte offenbarten.

Für eine freundliche Atmosphäre während der Bearbeitung dieser Arbeit ist der gesamten Arbeitsgruppe Paulus und den Arbeitsgruppen von Dr. Jean-Christophe Tremblay und J.-Prof. Dr. Bettina Keller zu danken.

Der Alltag als Doktorand bringt natürlich auch einige bürokratische und technische Akte mit sich, welche nicht immer nur Frohsinn und Begeisterung bei einem Auslösen. Dennoch sind diese unvermeidbar für einen regelkonformen, flüssigen und reibungslosen Ablauf. Daher möchte ich an dieser Stelle den Menschen danken, welche für einen ebensolchen Ablauf während meiner Arbeit sorgten: Julija Djordjevic und Xenia Krüger für ihre Hilfe bei bürokratischen Fragen und Dr. Loris Bennett, Dr. Holger Naundorf, Dr. Boris Proppe, Robert Schüttler und Dr. Christian Tuma für ihre Hilfe bei technischen Problemen und Fragen.

Ich bin ebenso sehr dankbar sowohl Teil des Sonderforschungsbereichs 1109: „Molekulare Einblicke in Metalloxid-Wasser-Systeme: Strukturelle Evolution, Grenzflächen und Auflösung“, als auch Teil des Graduiertenkollegs 1582: „Fluor als Schlüsselement“ zu sein. Beide Institutionen ermöglichten mir einen breiteren Einblick in die wissenschaftliche Arbeit, eine Erweiterung meines wissenschaftlichen Horizonts und eine einfache Möglichkeit der Zusammenarbeit in einem gemeinsamen Themenbereich.

Damit diese Arbeit überhaupt erst zustande kommen konnte, waren natürlich zahlreiche Berechnungen von Nöten, die eine Menge Ressourcen benötigten. Aus diesem Grund, möchte ich ebenfalls meinen Dank an die Mitarbeiter der Rechenzentren des HLRN, „Norddeutscher Verbund für Hoch- und Höchstleistungsrechnen“ und der ZE-



DAT, „High-Performance Computing“, entrichten.

Last but not least möchte ich meiner Familie danken, darunter besonders meinem Bruder Jacob, für ihre Unterstützung und Aufmunterungen in schweren Situationen und natürlich auch für ihren Beitrag in Diskussionen und an Formulierungen. Ganz besonders hervorheben möchte ich auch meine Verlobte Nithiya, für ihren unermüdlichen und selbstlosen Beistand während meiner gesamten bisherigen akademischen Laufbahn, ohne die ich unter keinen Umständen so weit gekommen wäre.

*„Leider lässt sich eine wahrhafte Dankbarkeit  
mit Worten nicht ausdrücken.“*

Johann Wolfgang von Goethe

Dennoch möchte ich es gerne versuchen:

**VIELEN HERZLICHEN DANK EUCH ALLEN!!!**



# Abstract

As some of the most abundant minerals on earth, aluminium hydroxides, oxohydroxides and oxides are used in a variety of applications ranging from catalysis to ion adsorption from water and usage in cement and anti-corrosive coatings and even in anti-cancer treatments. In all these applications, their performance highly depends on interactions with water. Therefore, different fields of application can be broached by tackling the complex processes involved in the assembly or dissolution of macroscopic structures via nanostructures in water while simultaneously influencing those processes by incorporating defects.

Within this work, nanostructures are modelled with a bulk-like core and a flat surface-like shell. Periodic density functional theory is used to investigate different aluminium hydroxides and oxohydroxides as core materials and  $\alpha$ -aluminium oxide surfaces as shell representatives. The bulk calculations with fluoride ions as dopants not only show their influence on the stability of the concerned systems, but also that the aluminium hydroxides thermodynamically favour the uptake of fluoride ions, which makes them more suitable candidates for fluoride removal from water in comparison to the aluminium oxohydroxides. Doping the  $\alpha$ -aluminium oxide surfaces with various amounts of fluoride shows in general no reconstruction of the surface. This in turn highlights their robustness during the fluorination. The adsorption strength of water on these surfaces decreases with an increasing amount of surface fluoride ions. Although the hydrogen bonds to terminal fluoride ions are stronger than to terminal hydroxide groups, this verifies the water repellent effect of fluoride ions even in ionic compounds. Based on this observation, it is assumed that fluorinated aluminium ox-

ides are less likely to dissolve and that the corresponding fluorinated nanostructures are more likely to assemble themselves into macroscopic structures.

Due to the comparably high amount of water molecules per surface area, the water molecules are able to form different structural motifs. The obtained different arrangements of water molecules are compared to known structure motifs in various ice phases. In many cases, the adsorbed water structure motifs resemble ones found in ice-**I<sub>h</sub>** or ice-**I<sub>c</sub>**, which leads to a potential application of certain modified surfaces to grow specifically ice-**I<sub>c</sub>** on them.

For a better and easier collaboration of theory and experiments, NMR shifts as well as OH stretch wavenumbers are calculated and result in a good accordance of both fields. Thus, the findings can also be used to verify, assign, and mutually check the findings of experimental studies and draw conclusions about the structure at hand.

## Kurzzusammenfassung

Als einige der am häufigsten vorkommenden Mineralien werden Aluminiumhydroxide, -oxohydroxide und -oxide in vielen Gebieten verwendet. Diese reichen von Krebsbehandlungskomponenten und der Anwendung in der Katalyse bis hin zur Nutzung in Zementen und Korrosionsschutzüberzügen. Ihre Leistung hängt dabei stets stark von ihren Wechselwirkungen mit Wasser ab. Aus diesem Grund können bei der Untersuchung der komplexen Prozesse während des Aufbaus bzw. der Auflösung von makroskopischen Strukturen aus bzw. in Nanostrukturen in Wasser unterschiedliche Anwendungsgebiete behandelt werden. Bei gleichzeitigem Einwirken auf diese Prozesse mittels Defekten, wird die Zahl der möglichen Anwendungen weiter erhöht.

In dieser Arbeit werden Nanostrukturen mit einem festkörperähnlichen Kern und einer flachen oberflächenähnlichen Hülle modelliert. Zur Analyse der unterschiedlichen Aluminiumhydroxide und -oxohydroxide als Kern bzw.  $\alpha$ -Aluminiumoxidoberflächen als Hülle wird die periodische Dichtefunktionaltheorie verwendet. Die Festkörperrechnungen mit Fluoriddotierung belegen nicht nur deren Einfluss auf die Stabilität der betrachteten Systeme, sondern auch, dass die Aluminiumhydroxide die Aufnahme von Fluoridionen thermodynamisch bevorzugen. Dementsprechend zeigen sie gegenüber den Aluminiumoxohydroxiden eine bessere Fluoridaufnahme aus Wasser. Die Dotierung der unterschiedlichen  $\alpha$ -Aluminiumoxidoberflächen mit variierenden Mengen an Fluoridionen zeigt in nahezu allen Fällen keine Rekonstruktion der Oberfläche und unterstreicht damit ihre Robustheit während der Fluorierung. Bei der Adsorption von Wasser auf diesen Oberflächen zeigt sich eine abnehmende Stärke mit steigendem Fluoridgehalt. Dies bestätigt den wasserabweisenden Effekt von Fluoridionen selbst in

ionischen Verbindungen, obwohl Wasserstoffbrückenbindungen zu terminalen Fluoridionen stärker sind als zu terminalen Hydroxidgruppen. Infolge dieser Beobachtungen kann angenommen werden, dass fluorierte Aluminiumoxide auflösungsresistenter sind und dementsprechend fluorierte Nanostrukturen den Aufbau makroskopischer Strukturen bevorzugen.

Auf Grund der relativ hohen Menge an Wassermolekülen pro Fläche, ist es diesen möglich variierende Struktur motive auszubilden. Die erhaltenen verschiedenen Anordnungen der Wassermoleküle werden mit bekannten Struktur motiven von Wasser in unterschiedlichen Eisphasen verglichen. In vielen Fällen zeigen die Wasserstrukturen auf der Oberfläche Motive, wie sie in Eis- $\mathbf{I}_h$  bzw. Eis- $\mathbf{I}_c$  zu finden sind. Daher könnten die zugehörigen modifizierten Oberflächen potentiell zum Züchten von Eis- $\mathbf{I}_c$  verwendet werden.

Um eine bessere Zusammenarbeit von Theorie und Experiment zu gewährleisten, wurden sowohl NMR-Verschiebungen als auch OH-Streckschwingungen untersucht. Diese zeigten eine gute Übereinstimmung der Ergebnisse aus beiden Gebieten. Daher können die erhaltenen Ergebnisse auch zur Bestätigung, Zuordnung und gegenseitigem Überprüfen von künftigen experimentellen Resultaten und für Rückschlüsse auf die untersuchte Struktur verwendet werden.

# Contents

<b>1</b>	<b>Introduction</b>	<b>1</b>
<b>2</b>	<b>Theory and Computational Approach</b>	<b>7</b>
2.1	Theoretical Background	7
2.1.1	The Hartree-Fock Approach	9
2.1.2	The Density Functional Theory	12
2.1.3	Dispersion Correction	14
2.1.4	Theory for Solid State Systems	17
2.1.5	Statistical Thermodynamics	24
2.1.6	Normal Mode and Phonon Wavenumbers	27
2.1.7	Nuclear Magnetic Resonance Shifts	28
2.2	Computational Approaches	33
2.2.1	Slab Model	33
2.2.2	Surface Energies	36
2.2.3	Wulff Plots	37
2.2.4	Surface Scans	37
2.2.5	Analysis of Ice Structures	39
2.3	Computational Details	41
<b>3</b>	<b>Structure-Stability-Relation Parameters</b>	<b>43</b>
3.1	Distortion of Cation Coordination Spheres	43
3.2	Symmetry after Relaxation	45
3.3	Charge Centre Deviation	46
3.4	Homogeneity of the Fluoride Arrangement	47
3.5	Hydrogen Bonding	49
3.6	Slice/Layer Distances	50
3.7	Slice Stoichiometry	53
<b>4</b>	<b>Results</b>	<b>55</b>
4.1	Aluminium (oxo)hydroxides	55
4.1.1	Fluorinated Aluminium (oxo)hydroxide Structures	59
4.1.2	Fluoride Depending NMR Shifts in Aluminium (oxo)hydroxides	68
4.2	$\alpha$ -Aluminium Oxide Surfaces	83
4.2.1	Hydration of $\alpha$ -Aluminium Oxide Surfaces	87

4.2.2	Fluorination of Hydrated $\alpha$ -Aluminium Oxide Surfaces . . . . .	92
4.2.3	NMR Shifts of $\alpha$ -Aluminium Oxide Surfaces . . . . .	103
4.3	Water Adsorption on Modified $\alpha$ -Aluminium Oxide Surfaces . . . . .	108
4.3.1	The (0001) Surface . . . . .	108
4.3.2	The (1 $\bar{1}$ 02) Surface . . . . .	126
4.3.3	The (11 $\bar{2}$ 3) Surface . . . . .	150
4.3.4	Summary of the Water Adsorption . . . . .	177
4.4	Structure Motifs of Water . . . . .	180
4.4.1	Ice Phases . . . . .	180
4.4.2	Comparison of Water's Structure Motifs . . . . .	194
<b>5</b>	<b>Summary</b>	<b>215</b>
	<b>Bibliography</b>	<b>223</b>
	<b>Appendix</b>	<b>243</b>
A.1	Molecules . . . . .	243
A.2	Bulk . . . . .	244
A.3	Surfaces . . . . .	260
A.4	Ice . . . . .	271
A.5	Adsorbed Water . . . . .	282



## List of Figures

1.1	Examples of aluminium hydroxides and oxohydroxides . . . . .	4
1.2	Structure of $\alpha$ -Al <sub>2</sub> O <sub>3</sub> . . . . .	4
3.1	Bulk parameters - slice distance parameter; example . . . . .	50
3.2	Bulk parameters - diaspore “slice” explanation . . . . .	51
3.3	Bulk parameters - slice stoichiometry parameter; example . . . . .	53
4.1	Aluminium (oxo)hydroxides - UC representations . . . . .	56
4.2	Aluminium (oxo)hydroxides - reaction energies . . . . .	61
4.3	Aluminium (oxo)hydroxides - structure motif examples . . . . .	62
4.4	Aluminium (oxo)hydroxides - structure-stability relation; examples . . . . .	66
4.5	Aluminium (oxo)hydroxides - doyleite weighting check . . . . .	67
4.6	Aluminium (oxo)hydroxides - <sup>27</sup> Al NMR of gibbsite . . . . .	69
4.7	Aluminium (oxo)hydroxides - <sup>19</sup> F NMR of gibbsite . . . . .	71
4.8	Aluminium (oxo)hydroxides - <sup>27</sup> Al NMR of bayerite . . . . .	73
4.9	Aluminium (oxo)hydroxides - <sup>19</sup> F NMR of bayerite . . . . .	74
4.10	Aluminium (oxo)hydroxides - <sup>27</sup> Al NMR of diaspore . . . . .	75
4.11	Aluminium (oxo)hydroxides - <sup>19</sup> F NMR of diaspore . . . . .	77
4.12	Aluminium (oxo)hydroxides - <sup>27</sup> Al NMR of boehmite . . . . .	78
4.13	Aluminium (oxo)hydroxides - <sup>19</sup> F NMR of boehmite . . . . .	80
4.14	Aluminium oxide surfaces - Wulff plots of previous results . . . . .	83
4.15	Aluminium oxide surfaces - termination study . . . . .	84
4.16	Aluminium oxide surfaces - Wulff plot . . . . .	85
4.17	Aluminium oxide surfaces - plain surface structures . . . . .	86
4.18	Aluminium oxide surfaces - hydrated (0001) surface . . . . .	87
4.19	Aluminium oxide surfaces - hydrated (1 $\bar{1}$ 02) surface . . . . .	88
4.20	Aluminium oxide surfaces - hydrated (11 $\bar{2}$ 3) surface . . . . .	89
4.21	Aluminium oxide surfaces - fluorinated (0001) surfaces . . . . .	92
4.22	Aluminium oxide surfaces - fluorinated (1 $\bar{1}$ 02) surfaces . . . . .	94
4.23	Aluminium oxide surfaces - fluorinated (11 $\bar{2}$ 3) surfaces . . . . .	97
4.24	Aluminium oxide surfaces - <sup>27</sup> Al NMR; CN dependence . . . . .	103
4.25	Aluminium oxide surfaces - <sup>27</sup> Al NMR; F <sup>-</sup> and distortion effects . . . . .	104
4.26	Aluminium oxide surfaces - <sup>19</sup> F NMR; CN and F <sup>-</sup> effects . . . . .	106
4.27	Water adsorption - 1 H <sub>2</sub> O on hydrated (0001) UC . . . . .	109
4.28	Water adsorption - 2 H <sub>2</sub> O on hydrated (0001) SC . . . . .	110

4.29	Water adsorption - 2 H <sub>2</sub> O on hydrated (0001) UC . . . . .	111
4.30	Water adsorption - 3 H <sub>2</sub> O on hydrated (0001) UC . . . . .	112
4.31	Water adsorption - 1 H <sub>2</sub> O on singly fluorinated (0001) UC . . . . .	113
4.32	Water adsorption - 2 H <sub>2</sub> O on singly fluorinated (0001) SC . . . . .	114
4.33	Water adsorption - 2 H <sub>2</sub> O on singly fluorinated (0001) UC . . . . .	116
4.34	Water adsorption - 3 H <sub>2</sub> O on singly fluorinated (0001) UC . . . . .	117
4.35	Water adsorption - 1 H <sub>2</sub> O on doubly fluorinated (0001) UC . . . . .	118
4.36	Water adsorption - 2 H <sub>2</sub> O on doubly fluorinated (0001) SC . . . . .	119
4.37	Water adsorption - 2 H <sub>2</sub> O on doubly fluorinated (0001) UC . . . . .	120
4.38	Water adsorption - 3 H <sub>2</sub> O on doubly fluorinated (0001) UC . . . . .	121
4.39	Water adsorption - 1 H <sub>2</sub> O on triply fluorinated (0001) UC . . . . .	122
4.40	Water adsorption - 2 H <sub>2</sub> O on triply fluorinated (0001) UC . . . . .	123
4.41	Water adsorption - 3 H <sub>2</sub> O on triply fluorinated (0001) UC . . . . .	124
4.42	Water adsorption - 1 H <sub>2</sub> O on hydrated (1 $\bar{1}$ 02) UC . . . . .	127
4.43	Water adsorption - 2 H <sub>2</sub> O on hydrated (1 $\bar{1}$ 02) SC . . . . .	128
4.44	Water adsorption - 2 H <sub>2</sub> O on hydrated (1 $\bar{1}$ 02) UC . . . . .	129
4.45	Water adsorption - 3 H <sub>2</sub> O on hydrated (1 $\bar{1}$ 02) UC . . . . .	130
4.46	Water adsorption - 1 H <sub>2</sub> O on singly fluorinated (1 $\bar{1}$ 02) UC . . . . .	131
4.47	Water adsorption - 2 H <sub>2</sub> O on singly fluorinated (1 $\bar{1}$ 02) SC . . . . .	132
4.48	Water adsorption - 2 H <sub>2</sub> O on singly fluorinated (1 $\bar{1}$ 02) UC . . . . .	133
4.49	Water adsorption - 3 H <sub>2</sub> O on singly fluorinated (1 $\bar{1}$ 02) UC . . . . .	134
4.50	Water adsorption - 1 H <sub>2</sub> O on doubly fluorinated (1 $\bar{1}$ 02) UC . . . . .	135
4.51	Water adsorption - 2 H <sub>2</sub> O on doubly fluorinated (1 $\bar{1}$ 02) SC . . . . .	136
4.52	Water adsorption - 2 H <sub>2</sub> O on doubly fluorinated (1 $\bar{1}$ 02) UC . . . . .	137
4.53	Water adsorption - 3 H <sub>2</sub> O on doubly fluorinated (1 $\bar{1}$ 02) UC . . . . .	138
4.54	Water adsorption - 1 H <sub>2</sub> O on triply fluorinated (1 $\bar{1}$ 02) UC . . . . .	139
4.55	Water adsorption - 2 H <sub>2</sub> O on triply fluorinated (1 $\bar{1}$ 02) SC . . . . .	140
4.56	Water adsorption - 2 H <sub>2</sub> O on triply fluorinated (1 $\bar{1}$ 02) UC . . . . .	141
4.57	Water adsorption - 3 H <sub>2</sub> O on triply fluorinated (1 $\bar{1}$ 02) UC . . . . .	142
4.58	Water adsorption - 1 H <sub>2</sub> O on fourfold fluorinated (1 $\bar{1}$ 02) UC . . . . .	143
4.59	Water adsorption - 2 H <sub>2</sub> O on fourfold fluorinated (1 $\bar{1}$ 02) SC . . . . .	144
4.60	Water adsorption - 2 H <sub>2</sub> O on fourfold fluorinated (1 $\bar{1}$ 02) UC . . . . .	145
4.61	Water adsorption - 3 H <sub>2</sub> O on fourfold fluorinated (1 $\bar{1}$ 02) UC . . . . .	146
4.62	Water adsorption - 1 H <sub>2</sub> O on hydrated (11 $\bar{2}$ 3) UC . . . . .	151
4.63	Water adsorption - 2 H <sub>2</sub> O on hydrated (11 $\bar{2}$ 3) UC . . . . .	152
4.64	Water adsorption - 3 H <sub>2</sub> O on hydrated (11 $\bar{2}$ 3) UC . . . . .	152
4.65	Water adsorption - 1 H <sub>2</sub> O on singly fluorinated (11 $\bar{2}$ 3) UC . . . . .	153
4.66	Water adsorption - 2 H <sub>2</sub> O on singly fluorinated (11 $\bar{2}$ 3) UC . . . . .	155
4.67	Water adsorption - 3 H <sub>2</sub> O on singly fluorinated (11 $\bar{2}$ 3) UC . . . . .	156
4.68	Water adsorption - 1 H <sub>2</sub> O on doubly fluorinated (11 $\bar{2}$ 3) UC . . . . .	157
4.69	Water adsorption - 2 H <sub>2</sub> O on doubly fluorinated (11 $\bar{2}$ 3) UC . . . . .	158
4.70	Water adsorption - 3 H <sub>2</sub> O on doubly fluorinated (11 $\bar{2}$ 3) UC . . . . .	159
4.71	Water adsorption - 1 H <sub>2</sub> O on triply fluorinated (11 $\bar{2}$ 3) UC . . . . .	160
4.72	Water adsorption - 2 H <sub>2</sub> O on triply fluorinated (11 $\bar{2}$ 3) UC . . . . .	161
4.73	Water adsorption - 3 H <sub>2</sub> O on triply fluorinated (11 $\bar{2}$ 3) UC . . . . .	161

4.74	Water adsorption - 1 H <sub>2</sub> O on fourfold fluorinated (11 $\bar{2}$ 3) UC . . . . .	163
4.75	Water adsorption - 2 H <sub>2</sub> O on fourfold fluorinated (11 $\bar{2}$ 3) UC . . . . .	164
4.76	Water adsorption - 3 H <sub>2</sub> O on fourfold fluorinated (11 $\bar{2}$ 3) UC . . . . .	164
4.77	Water adsorption - 1 H <sub>2</sub> O on fivefold fluorinated (11 $\bar{2}$ 3) UC . . . . .	165
4.78	Water adsorption - 2 H <sub>2</sub> O on fivefold fluorinated (11 $\bar{2}$ 3) UC . . . . .	166
4.79	Water adsorption - 3 H <sub>2</sub> O on fivefold fluorinated (11 $\bar{2}$ 3) UC . . . . .	167
4.80	Water adsorption - 1 H <sub>2</sub> O on sixfold fluorinated (11 $\bar{2}$ 3) UC . . . . .	168
4.81	Water adsorption - 2 H <sub>2</sub> O on sixfold fluorinated (11 $\bar{2}$ 3) UC . . . . .	170
4.82	Water adsorption - 3 H <sub>2</sub> O on sixfold fluorinated (11 $\bar{2}$ 3) UC . . . . .	171
4.83	Water adsorption - 1 H <sub>2</sub> O on sevenfold fluorinated (11 $\bar{2}$ 3) UC . . . . .	172
4.84	Water adsorption - 2 H <sub>2</sub> O on sevenfold fluorinated (11 $\bar{2}$ 3) UC . . . . .	173
4.85	Water adsorption - 3 H <sub>2</sub> O on sevenfold fluorinated (11 $\bar{2}$ 3) UC . . . . .	174
4.86	Ice structures - ice- <b>I<sub>h</sub></b> macroscopic structure . . . . .	181
4.87	Ice structures - ice- <b>I<sub>c</sub></b> macroscopic structure and substructure . . . . .	182
4.88	Ice structures - ice- <b>II</b> macroscopic structure . . . . .	182
4.89	Ice structures - ice- <b>II</b> O <sub>6</sub> -ring connection . . . . .	183
4.90	Ice structures - ice- <b>III</b> larger structure motif (1) . . . . .	184
4.91	Ice structures - ice- <b>III</b> larger structure motif (2) . . . . .	184
4.92	Ice structures - ice- <b>IV</b> macroscopic structures . . . . .	185
4.93	Ice structures - ice- <b>IV</b> substructure . . . . .	185
4.94	Ice structures - ice- <b>V</b> macroscopic structure and substructure (1) . . . . .	186
4.95	Ice structures - ice- <b>V</b> macroscopic structure and substructure (2) . . . . .	187
4.96	Ice structures - ice- <b>VI</b> macroscopic structure and substructure . . . . .	188
4.97	Ice structures - ice- <b>VI</b> substructure . . . . .	189
4.98	Ice structures - ice- <b>VII</b> macroscopic structure . . . . .	190
4.99	Ice structures - ice- <b>XII</b> macroscopic structure and substructure . . . . .	190
4.100	Ice structures - ice- <b>XVI</b> macroscopic structure . . . . .	191
4.101	Ice structures - ice- <b>XVI</b> substructures . . . . .	192
4.102	Ice structures - ice- <b>XVII</b> substructures . . . . .	193
4.103	Ice structures - ice- <b>XVII</b> macroscopic structure and substructure . . . . .	194
4.104	Water structure motifs - hydrated (0001) . . . . .	195
4.105	Water structure motifs - singly and triply fluorinated (0001) . . . . .	197
4.106	Water structure motifs - doubly fluorinated (0001) . . . . .	198
4.107	Water structure motifs - hydrated (1 $\bar{1}$ 02) (1) . . . . .	199
4.108	Water structure motifs - hydrated (1 $\bar{1}$ 02) (2) . . . . .	201
4.109	Water structure motifs - singly and doubly fluorinated (1 $\bar{1}$ 02) . . . . .	202
4.110	Water structure motifs - hydrated (11 $\bar{2}$ 3) . . . . .	203
4.111	Water structure motifs - singly fluorinated (11 $\bar{2}$ 3) . . . . .	205
4.112	Water structure motifs - doubly fluorinated (11 $\bar{2}$ 3) (1) . . . . .	206
4.113	Water structure motifs - doubly fluorinated (11 $\bar{2}$ 3) (2) . . . . .	207
4.114	Water structure motifs - triply fluorinated (11 $\bar{2}$ 3) . . . . .	208
4.115	Water structure motifs - fourfold fluorinated (11 $\bar{2}$ 3) . . . . .	210
4.116	Water structure motifs - fivefold fluorinated (11 $\bar{2}$ 3) . . . . .	211
4.117	Water structure motifs - sixfold fluorinated (11 $\bar{2}$ 3) . . . . .	213

A.1	$E_{\text{rea}}$ and $D(i)$ for the first four fluorination degrees of gibbsite. . . .	245
A.2	$E_{\text{rea}}$ and $D(i)$ for the last four fluorination degrees of gibbsite. . . .	246
A.3	$E_{\text{rea}}$ and $D(i)$ for the first four fluorination degrees of bayerite. . . .	247
A.4	$E_{\text{rea}}$ and $D(i)$ for the last four fluorination degrees of bayerite. . . .	248
A.5	$E_{\text{rea}}$ and $D(i)$ for the first four fluorination degrees of diaspore. . . .	249
A.6	$E_{\text{rea}}$ and $D(i)$ for the last four fluorination degrees of diaspore. . . .	250
A.7	$E_{\text{rea}}$ and $D(i)$ for the first four fluorination degrees of boehmite. . . .	251
A.8	$E_{\text{rea}}$ and $D(i)$ for the last four fluorination degrees of boehmite. . . .	252
A.9	AES of the first water molecule on (0001) surfaces . . . . .	260
A.10	AES of the second water molecule on (0001) SC-surfaces . . . . .	261
A.11	AES of the second water molecule on (0001) surfaces . . . . .	262
A.12	AES of the third water molecule on (0001) surfaces . . . . .	263
A.13	AES of the first water molecule on ( $1\bar{1}02$ ) surfaces . . . . .	264
A.14	AES of the second water molecule on ( $1\bar{1}02$ ) SC-surfaces . . . . .	265
A.15	AES of the second water molecule on ( $1\bar{1}02$ ) surfaces . . . . .	266
A.16	AES of the third water molecule on ( $1\bar{1}02$ ) surfaces . . . . .	267
A.17	AES of the first water molecule on ( $11\bar{2}3$ ) surfaces . . . . .	268
A.18	AES of the second water molecule on ( $11\bar{2}3$ ) surfaces . . . . .	269
A.19	AES of the third water molecule on ( $11\bar{2}3$ ) surfaces . . . . .	270
A.20	Water structure motifs in ice- <b>II</b> - $O_8$ -rings . . . . .	271
A.21	Water structure motifs in ice- <b>II</b> - $O_{10}$ -rings . . . . .	271
A.22	Water structure motifs in ice- <b>II</b> - $O_{12}$ -rings . . . . .	272
A.23	Water structure motifs in ice- <b>III</b> - $O_n$ -rings . . . . .	272
A.24	Water structure motifs in ice- <b>IV</b> - $O_8$ -rings . . . . .	272
A.25	Water structure motifs in ice- <b>IV</b> - $O_{10}$ -rings . . . . .	273
A.26	Water structure motifs in ice- <b>IV</b> - $O_{12}$ -rings . . . . .	274
A.27	Water structure motifs in ice- <b>V</b> - $O_n$ -rings . . . . .	275
A.28	Water structure motifs in ice- <b>V</b> - $O_{10}$ -rings . . . . .	275
A.29	Water structure motifs in ice- <b>V</b> - $O_{11}$ -rings . . . . .	276
A.30	Water structure motifs in ice- <b>V</b> - $O_{12}$ -rings (1) . . . . .	276
A.31	Water structure motifs in ice- <b>V</b> - $O_{12}$ -rings (2) . . . . .	277
A.32	Water structure motifs in ice- <b>VI</b> - $O_n$ -rings . . . . .	278
A.33	Water structure motifs in ice- <b>XII</b> - $O_n$ -rings (1) . . . . .	279
A.34	Water structure motifs in ice- <b>XII</b> - $O_n$ -rings (2) . . . . .	280
A.35	Water structure motifs in ice- <b>XVI</b> - $O_n$ -rings . . . . .	281
A.36	Water structure motifs on a hydrated (0001) surface . . . . .	282
A.37	Water structure motifs on a singly fluorinated (0001) surface . . . .	283
A.38	Water structure motifs on a doubly fluorinated (0001) surface . . . .	283
A.39	Water structure motifs on a triply fluorinated (0001) surface . . . .	284
A.40	Water structure motifs on a hydrated ( $1\bar{1}02$ ) surface . . . . .	285
A.41	Water structure motifs on a singly fluorinated ( $1\bar{1}02$ ) surface . . . .	286
A.42	Water structure motifs on a doubly fluorinated ( $1\bar{1}02$ ) surface . . . .	287
A.43	Water structure motifs on a triply fluorinated ( $1\bar{1}02$ ) surface . . . .	288
A.44	Water structure motifs on a fourfold fluorinated ( $1\bar{1}02$ ) surface . . . .	288
A.45	Water structure motifs on a hydrated ( $11\bar{2}3$ ) surface . . . . .	289

A.46	Water structure motifs on a singly fluorinated $(11\bar{2}3)$ surface . . . .	290
A.47	Water structure motifs on a doubly fluorinated $(11\bar{2}3)$ surface . . . .	291
A.48	Water structure motifs on a triply fluorinated $(11\bar{2}3)$ surface . . . .	292
A.49	Water structure motifs on a fourfold fluorinated $(11\bar{2}3)$ surface . . . .	292
A.50	Water structure motifs on a fivefold fluorinated $(11\bar{2}3)$ surface . . . .	293
A.51	Water structure motifs on a sixfold fluorinated $(11\bar{2}3)$ surface . . . .	293
A.52	Water structure motifs on a sevenfold fluorinated $(11\bar{2}3)$ surface . . . .	294



## List of Tables

2.1	Surface model and energies - examined slabs . . . . .	35
3.1	Bulk parameters - distortion parameter; shape criteria . . . . .	44
4.1	Aluminium (oxo)hydroxides - lattice constant comparison . . . . .	57
4.2	Aluminium (oxo)hydroxides - thermodynamic stability comparison . .	58
4.3	Aluminium (oxo)hydroxides - $^{27}\text{Al}$ NMR shift comparison . . . . .	58
4.4	Aluminium (oxo)hydroxides - fit coefficients/weightings . . . . .	65
4.5	Aluminium oxide surfaces - surface energy comparison . . . . .	85
4.6	Aluminium oxide surfaces - $\Gamma$ phonon wavenumbers of hydrated surfaces	90
4.7	Aluminium oxide surfaces - (0001) fluorination energies . . . . .	93
4.8	Aluminium oxide surfaces - ( $1\bar{1}02$ ) fluorination energies . . . . .	96
4.9	Aluminium oxide surfaces - ( $11\bar{2}3$ ) fluorination energies . . . . .	98
4.10	Aluminium oxide surfaces - $\Gamma$ phonon wavenumbers of fluorinated surfaces	100
4.11	Water adsorption - summary of modified (0001) surfaces . . . . .	125
4.12	Water adsorption - summary of modified ( $1\bar{1}02$ ) surfaces . . . . .	148
4.13	Water adsorption - summary of modified ( $11\bar{2}3$ ) surfaces . . . . .	175
A.1	K-point grids for the considered molecule structures . . . . .	243
A.2	K-point grids for the considered bulk structures . . . . .	244
A.3	Values and parameters for fluorinated gibbsite structures. . . . .	253
A.3	Values and parameters for fluorinated gibbsite structures. . . . .	254
A.4	Values and parameters for fluorinated doyleite structures. . . . .	255
A.5	Values and parameters for fluorinated bayerite structures. . . . .	256
A.5	Values and parameters for fluorinated bayerite structures. . . . .	257
A.6	Values and parameters for fluorinated diaspore structures. . . . .	258
A.7	Values and parameters for fluorinated boehmite structures. . . . .	259
A.8	K-point grids for the considered surface structures . . . . .	260





## Abbreviations and Glossary

- AO** atomic orbitals
- CN** coordination number — number of counterions around a central ion
- CS** coordination sphere — arrangement of counterions around a central ion
- D3-BJ** dispersion correction by Grimme and co-workers (third version) with Becke-Johnson damping
- DFT** density functional theory
- GGA** generalised gradient approximation of the exchange-correlation energy
- GIPAW** gauge-including PAW — extension of the PAW approach by including the gauge origin while preserving the translational invariance
- HF** method developed by Hartree and Fock
- ice rules** in ice every oxygen has four hydrogen bonds; two donating and two accepting
- MD** molecular dynamics
- MO** molecular orbitals
- NMR** nuclear magnetic resonance
- PAW** projector augmented wave approach — to efficiently describe core regions using plane waves
- PBE** GGA functional developed by Perdew, Burke and Ernzerhof
- SC** supercell — cell structure which describes the same crystal as the unit cell but with a larger volume, i.e. a combination of  $n$  unit cells
- TEM** transmission electron microscopy
- UC** unit cell — smallest group of atoms resembling the crystal/surface, which can form the entire lattice by repetition in three/two dimensions
- VASP** Vienna *ab-initio* Simulation Package
- vdW** van-der-Waals interactions — comparably weak long range interactions between particles



# Chapter 1

## Introduction

Some of the most abundant minerals on earth are aluminium oxides [1] and their hydrates: aluminium oxohydroxides and aluminium hydroxides [2], which are known under mineralogical names like corundum, gibbsite and boehmite, for example. Unsurprisingly, there is a huge range of those materials' application, such as: anti-cancer treatment components [3–6], in fireproof or flame retardant materials [7–12], as part in different ceramics [13–15], or as substrate or actual catalyst in different reactions [16–19], to name only a few.

For the aluminium hydroxides another field of application arises due to their sliced structures, where each slice is formed by ionically bound aluminium ions and hydroxide groups while the slices are interconnected only via hydrogen bonds. This structural layout can be used to catch different ions [20, 21] because their quite weak inter-slice connection can be intercalated by those ions. For example the aluminium hydroxide gibbsite, pre-intercalated with lithium ions, can adsorb phosphate ions [20], for example, to clean drinking-water. Since their sliced structure is not unique for metal hydroxides, one can even build structures with alternating slices of aluminium and other species, for example, zinc which then is capable of adsorbing chromate ions [22].

Focussing on a very special ion to catch, numerous publications reported the usage of aluminium hydroxides [23], aluminium hydroxide based [24–26], and even the also

sliced aluminium oxohydroxide boehmite [27] to clean waste water by adsorbing fluoride ions. Although, fluoride is considered to be beneficiary for caries prevention in low concentrations, high concentrations of it, especially in drinking water, can lead to toxic effects in a variety of different soft tissues and even reverse the positive effects on teeth [28–39]. Thus, the amount of fluoride ions in drinking water needs to be controlled and high concentrations of it need to be avoided. As a consequence, the removal of fluoride ions becomes more and more important, and by association, compounds which do so need to be studied more closely to understand and possibly even improve their fluoride uptake.

But fluoride ions are not only important regarding health issues. Considering the application of aluminium oxides, oxohydroxides, and hydroxides in the field of catalysis, the addition of fluoride ions into the structure can change their catalytic behaviour drastically [40]. In order to synthesise these compounds, various techniques can be used [41–46], where the most promising method seems to be the sol-gel approach [47–52] because of its comparable ease of use, high versatility, high purity, and its low energy demands. The Lewis and Brønsted acidic sites of such fluorinated compounds were studied and addressed, for example, by Kemnitz and co-workers [53–61]. Therefore, fluorinated aluminium oxides, oxohydroxides, and hydroxides become more and more important in a variety of catalysed reactions.

Other very important usages of this substance class, and for me the most interesting ones, are firstly, their utilisation in different cements [62] and secondly, their application to hinder or even prevent corrosion as a protective coating [63–65]. In both cases the interaction of water with the considered material is of utmost importance to understand the processes involved in the material's dissolution, particularly, on the atomic level. For the use in cements, a reduction of the aluminium material's corrosion could lead to more durable concrete bridges, for example, which could reduce costs for maintaining them and other related infrastructure. Regarding the usage in anti-corrosive coatings, a deeper understanding of the involved processes might lead

---

to even better and more stable coatings. Fluorine might play an important role here as well to decrease the material's interactions with water molecules since fluorine is well known to influence those interactions quite drastically for carbon based materials like teflon [66] or polyvinylidene fluoride [67–69], for example. Thus, the assumption is justified that it might be able to influence the aluminium oxides, oxohydroxides, and hydroxides in the same way as well.

Trying to tackle the very complex processes of  $\alpha$ -Al<sub>2</sub>O<sub>3</sub>'s, also known as corundum [70], formation via assembly of nanostructures and the reversion of this process during dissolution, this theoretical work will focus on a possibility to describe such nanostructures and how their stability can be influenced. Since only few compositions of such nanostructures are fully known, they are modelled here by having a bulk-like core and a flat surface-like shell. To influence the stability of these structures and their interactions with water molecules, fluoride ions will be introduced into the considered structures via substitution of existing hydroxide groups.

Those studies will be conducted by using first-principles quantum chemical approaches on the atomic scale to investigate the binding conditions within the examined crystalline structures and their surfaces. In order to calculate the interacting electronic system underlying these structures, the independent particle picture will be used. Although two possible approaches are possible in this regard, Hartree-Fock (HF) [71–73] and the density functional theory (DFT) [74, 75]. Since DFT includes electron correlations implicitly while HF only has exchange terms, DFT will be used. In addition, it can easier applied to periodic systems if non-local functionals are used. Further use of dispersion correction methods [76–79] will compensate for DFT's only partly description of van-der-Waals (vdW) interactions and hydrogen bonding.

Firstly, examining the bulk-like core of the nanostructure, five different aluminium hydroxides and oxohydroxides will be studied (see figure 1.1): the aluminium hydroxides gibbsite [80], doyleite [81], bayerite [82] as well as the aluminium oxohydroxides diaspore [83] and boehmite [84]. These crystalline systems will be fluorinated with

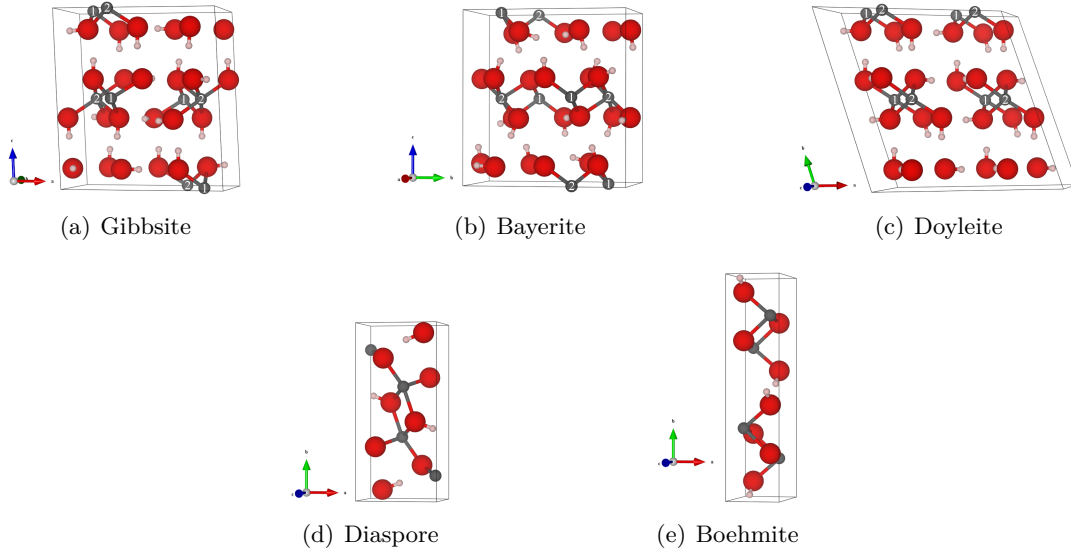


**Figure 1.1:** Structure depictions of the three aluminium hydroxides (top row) and two aluminium oxohydroxides (bottom row); white numbers for symmetrically inequivalent aluminium ions in (a), (b) and (c) - gray = aluminium, red = oxygen, and white = hydrogen.

different amounts and different arrangements of fluoride ions within their structure, to study the effect those two “adjusting wheels” on the systems’ stability. By calculation the reaction energies for the substitution reaction of hydroxide groups with fluoride ions, this will also handily give insights into the thermodynamics of these crystalline systems with added fluoride ions and, by association, give insight into their potential usage to control the amount of fluoride ions in drinking water.

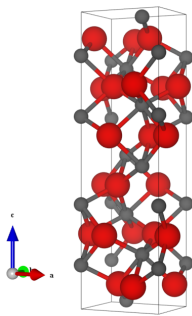


**Figure 1.2:** Structure depiction of  $\alpha\text{-Al}_2\text{O}_3$  - gray = aluminium and red = oxygen.

Focussing on the shell of the nano-structures, different surface cuts of  $\alpha\text{-Al}_2\text{O}_3$  will be studied regarding their most stable termination and their hydration. This part will be based and compared with numerous previous work regarding the hydrated surfaces of  $\alpha\text{-Al}_2\text{O}_3$  [85–105]. Afterwards, the formed hydroxide groups will be substituted once

---

more with fluoride ion. The amount of added fluoride ions will vary from unfluorinated up to a fully fluorinated surfaces, where all surface hydroxide groups are substituted. Once again, the influence of the fluoride ions' addition on the stability of such surfaces will be examined. Subsequently, the adsorption of water molecules on these differently modified surfaces will be studied by progressively adding one to three water molecules on each surface unit cell. The resulting adsorption positions and their corresponding adsorption energies can give more insight how they actually bind to the surface and how this can be influenced by the addition of fluoride ions. These studies not only give first insights into the interaction of non- and fluorinated aluminium hydroxide and oxohydroxide nanostructures, but also potentially reveal how  $\alpha$ -Al<sub>2</sub>O<sub>3</sub> surfaces can be modified to be more water resistant.

Due to the high water coverage on the comparably small unit cells, it might be also possible to identify reasonable water structure motifs on the modified surfaces. Therefore, these structure motifs might be similar to already known water structure motifs as found in different ice phases. This might even open up possibility to grow a specific ice phase on certain modified surfaces as another potential application. Thus, the 18 different ice phases [106–130] will be investigated and analysed to find their structure motifs and compare them with the structure motifs of adsorbed water.

To enable the comparison of this completely theoretical work with experimental findings, nuclear magnetic resonance (NMR) chemical shifts of <sup>27</sup>Al and <sup>19</sup>F will be calculated for numerous selected bulk phase structures and all modified surfaces. This potentially results in reasonable trends of the differently fluorinated aluminium centres and fluoride ions themselves. Furthermore, to enable a second possibility for comparison between theory and experiments, OH stretch wave numbers will be calculated for the differently modified surfaces of  $\alpha$ -Al<sub>2</sub>O<sub>3</sub>. Both approaches might help future investigations to assign and distinguish the experimentally found NMR chemical shifts and OH stretch wave numbers more easily and might help experimentalists to draw their conclusions about the structure or structure motifs at hand.

Recapitulating, different aluminium hydroxides and oxohydroxides and various  $\alpha$ -aluminium oxide surfaces will be fluorinated with different amounts to study the dopant's influence on the substrates stability and interaction with water molecules. Thus, the very complex processes during assembly and dissolution of solid state systems via nanostructures will be modelled and studied to provide a first insight. Modelling the nanostructures' cores with bulk like aluminium hydroxides and oxohydroxides doped with fluoride ions, information about the stability of these systems and how to influence it will be obtained. Due to adsorbing different amounts of water molecules on the varying fluorinated  $\alpha$ -aluminium oxide surfaces, the nanostructures' interactions with a watery environment are going to be portrayed. This also enables the investigation of different water molecule arrangements that form on the surface with already known structure motifs in various ice phases. Therefore, this study will potentially open up another application of those systems by facilitating the growing of a specific ice phase. Strengthen the collaboration of theory and experiment in tackling complex processes, calculation of [NMR](#) shifts and OH stretch wavenumbers will be used to enable an easier comparison and mutually checking of their results.



## Chapter 2

# Theory and Computational Approach

### 2.1 Theoretical Background

In order to clarify the equations and to simplify their expressions, only closed shell/spin paired formulations with atomic units will be shown and discussed if not otherwise stated.

In 1926, Erwin Schrödinger explained in three articles [131–133] how a so-called wave function  $\Phi$  defines a quantum state that is derived via the partial differential equation:

$$\hat{H}\Phi = i\frac{\partial\Phi}{\partial t}, \quad (2.1)$$

where  $\hat{H}$  represents the system's Hamiltonian. For explicitly time-independent Hamiltonians, the time-dependent part can be separated, which results in the time-independent Schrödinger equation:

$$\hat{H}\Psi = E\Psi. \quad (2.2)$$

where  $\hat{H}$  corresponds to the Hamiltonian, which describes the particles in the system,  $\Psi$  is now the stationary wave function, and  $E$  is the energy of the considered system. Solving this equation is difficult for systems with more than two interacting particles.  $\hat{H}$  is formulated as:

$$\hat{H} = \hat{T}_n + \hat{T}_e + \hat{V}_{nn} + \hat{V}_{ne} + \hat{V}_{ee}, \quad (2.3)$$

where  $\hat{T}_n$  is the kinetic energy operator of the nuclei,  $\hat{T}_e$  the kinetic energy operator of the electrons,  $\hat{V}_{nn}$  the potential energy operator between nuclei,  $\hat{V}_{ne}$  the potential energy operator between nuclei and electrons, and  $\hat{V}_{ee}$  the potential energy operator between electrons.

The complexity of the interacting particles causes the still challenging solution of the Schrödinger equation. Different approximations were made simplifying it and allowing the solution of it. The most prominent is the Born-Oppenheimer-Approximation [134]. It considers the nuclei to be clamped with respect to the much faster moving electrons in the system. Due to this, the expectation value of  $\hat{T}_n$  becomes zero and of  $\hat{V}_{nn}$  a constant value. This makes the electronic Hamiltonian  $\hat{H}_{el}$  solely parametrically depending on the nuclei. Thus, the three remaining terms of  $\hat{H}_{el}$  can be written as:

$$\hat{H}_{el} = -\frac{1}{2} \sum_i^N \nabla_i^2 - \sum_i^N \sum_A^M \frac{Z_A}{r_{iA}} + \sum_{i>j}^N \frac{1}{r_{ij}}, \quad (2.4)$$

where the first term corresponds to  $\hat{T}_e$ , the second to  $\hat{V}_{ne}$ , and the third to  $\hat{V}_{ee}$  while  $Z_A$  represents the charge of the considered nucleus  $A$  and  $r_{iA}/r_{ij}$  the distance between two particles in a system with  $N$  electrons and  $M$  nuclei. Despite the previously mentioned approximations, the Schrödinger equation is still not exactly solvable due to the complexity of the electron electron interactions, and therefore, further approximations have to be made.

### 2.1.1 The Hartree-Fock Approach

Based on the work of Hartree [71, 72], Fock [73] extended and improved the method to approximate the solution of the Schrödinger equation for a manybody system. Requiring an antisymmetric product ansatz to approximate the wave function that obeys the Pauli principle, Slater [135] described the wave function  $\Psi$  with a determinant of the following form:

$$\Psi(\mathbf{x}_1, \mathbf{x}_2, \dots, \mathbf{x}_N) = \frac{1}{\sqrt{N!}} \begin{vmatrix} \chi_1(\mathbf{x}_1) & \chi_2(\mathbf{x}_1) & \cdots & \chi_N(\mathbf{x}_1) \\ \chi_1(\mathbf{x}_2) & \chi_2(\mathbf{x}_2) & \cdots & \chi_N(\mathbf{x}_2) \\ \vdots & \vdots & \ddots & \vdots \\ \chi_1(\mathbf{x}_N) & \chi_2(\mathbf{x}_N) & \cdots & \chi_N(\mathbf{x}_N) \end{vmatrix}, \quad (2.5)$$

where  $N$  denotes the number of orthonormal spin orbitals  $\chi_a(\mathbf{x}_i)$  as well as the number of electrons in the system. The spin orbitals  $\chi_a(\mathbf{x}_i)$  are products of the spatial one-electron functions  $\psi_a(\mathbf{r}_i)$  and the spin function  $\gamma_a(\omega_i)$  while  $\mathbf{x}_i$  represents both, the spatial coordinate  $\mathbf{r}_i$  and the spin coordinate  $\omega_i$ . Simplifying  $\widehat{V}_{ee}$  in equation (2.4) by approximating the electron electron interactions via treating them independently from each other and describing their interaction with an effective potential,  $\widehat{V}_{ee}$  becomes  $\widehat{v}_{\text{eff}}$ . To get the ground state energy of the system within this so called mean-field method and the corresponding ground state electronic wave function, the following  $N$  Hartree-Fock equations need to be solved for each electron:

$$\widehat{F}(\mathbf{x}_i) |\chi_a(\mathbf{x}_i)\rangle = \epsilon_a |\chi_a(\mathbf{x}_i)\rangle, \quad (2.6)$$

where  $\epsilon_a$  represents the energy of the corresponding spin orbital  $\chi_a(\mathbf{x}_i)$ .  $\widehat{F}(\mathbf{x}_i)$  denotes the Fock operator and is effectively an one-electron Hamiltonian:

$$\widehat{F}(\mathbf{x}_i) = -\frac{1}{2} \nabla_i^2 - \sum_A \frac{Z_A}{r_{iA}} + \widehat{v}_{\text{eff}}^{\text{HF}}, \quad (2.7)$$

with the effective potential operator  $\widehat{v}_{\text{eff}}^{\text{HF}}$ , which is composed of the Coulomb operator  $\widehat{J}_b$  and the exchange operator  $\widehat{K}_b$ :

$$\widehat{v}_{\text{eff}}^{\text{HF}} = \sum_b^N \widehat{J}_b - \widehat{K}_b \quad \text{with} \quad (2.8)$$

$$\widehat{J}_b \chi_a(\mathbf{x}_i) = \left( \int (\chi_b(\mathbf{x}_j))^\dagger \frac{1}{r_{ij}} \chi_b(\mathbf{x}_j) \, d\mathbf{x}_j \right) \chi_a(\mathbf{x}_i) \quad \text{and} \quad (2.9)$$

$$\widehat{K}_b \chi_a(\mathbf{x}_i) = \left( \int (\chi_b(\mathbf{x}_j))^\dagger \frac{1}{r_{ij}} \chi_a(\mathbf{x}_j) \, d\mathbf{x}_j \right) \chi_b(\mathbf{x}_i). \quad (2.10)$$

The exact energy of the considered system is the lower limit of the used Hamiltonian  $\widehat{H}_{\text{el}}^{\text{HF}}$ 's expectation value with a trial wave function  $\widetilde{\Psi}$  composed of the initially guessed spin orbitals  $\chi_a(\mathbf{x}_i)$ , which is called the variational principle:

$$E_{\text{el}} \leq \frac{\langle \widetilde{\Psi} | \widehat{H}_{\text{el}}^{\text{HF}} | \widetilde{\Psi} \rangle}{\langle \widetilde{\Psi} | \widetilde{\Psi} \rangle}, \quad (2.11)$$

The Hartree-Fock equations of [equation \(2.6\)](#) can now be solved iteratively within the so-called self-consistent-field approach. Using an initial set of spin orbitals  $\chi_a(\mathbf{x}_i)$  with their corresponding orbital energies  $\epsilon_a$  the related Slater determinant [equation \(2.5\)](#) can be build up. Solving the Hartree-Fock equations [equation \(2.6\)](#) with this initial guess of the spin orbitals  $\chi_a(\mathbf{x}_i)$ , the results are used as starting points for a next cycle. Repetition of this procedure, until a given convergence criterion is accomplished, finally results in optimised  $\chi_a(\mathbf{x}_i)$  and  $\epsilon_a$ .

While the spin functions  $\gamma_a(\omega_i)$  can be expressed quite easily, different approaches are used to get reasonable representations of the spatial one-electron functions  $\psi_a(\mathbf{r}_i)$  of  $\chi_a(\mathbf{x}_i)$ . For molecules, the spatial one-electron functions  $\psi_a(\mathbf{r}_i)$  are referred to as molecular orbitals (MO)s. In case of atoms other than the hydrogen atom, the spatial one-electron functions  $\psi_a(\mathbf{r}_i)$  can not be analytically solved, but due to their spherical symmetry, the angular part can be described by spherical harmonics. Together with

the radial function, usually of the form suggested by Slater [136], the resulting Slater type orbitals are obtained. For molecules, the spatial one-electron functions  $\psi_a(\mathbf{r}_i)$  are referred to as **MOs**.

In general, these spatial molecular functions  $\psi_a(\mathbf{r}_i)$  are approximated as linear combinations of given one-electron spatial functions  $\phi_a(\mathbf{r}_i)$ , so-called basis sets:

$$\psi_a(\mathbf{r}_i) = \sum_k^n c_{ak} \phi_k(\mathbf{r}_i). \quad (2.12)$$

If the basis functions are atom-centred, these  $n$  one-electron spatial functions represent the entirety of the atomic orbitals (AO)s of each atom in the molecule. Using a basis set expansion, the Hartree-Fock equations become a specific matrix eigenvalue equation, the Roothaan-Hall equation [137, 138], for the expansion coefficients:

$$\mathbf{FC} = \varepsilon \mathbf{SC}. \quad (2.13)$$

In this matrix equation  $\mathbf{C}$  represents a  $n \times n$  matrix with the expansion coefficients  $c_{ak}$ ,  $\varepsilon$  is a diagonal matrix containing the corresponding orbital energies  $\epsilon_a$ , while  $\mathbf{F}$  and  $\mathbf{S}$  represent the Fock matrix and the overlap matrix, respectively. The elements of both these matrices are defined as:

$$F_{kl} = \langle \phi_k | \hat{F}(\mathbf{r}_i) | \phi_l \rangle, \quad (2.14)$$

$$S_{kl} = \langle \phi_k | \phi_l \rangle. \quad (2.15)$$

Solving equation (2.13) yields the corresponding **MOs**, where only the energetically lowest lying  $N/2$  are occupied and contribute to the energy of the system.

### 2.1.2 The Density Functional Theory

A different approach to solve the Schrödinger equation (equation (2.2)) is the DFT. While the HF method optimises the wave function, DFT utilises the two theorems of Hohenberg and Kohn [74] to bypass this. The electron density  $\rho$  of a system is obtained by integrating over all electrons' coordinates except one:

$$\rho(\mathbf{r}_1) = N \int \dots \int \Psi^*(\mathbf{r}_2, \dots, \mathbf{r}_N) \Psi(\mathbf{r}_2, \dots, \mathbf{r}_N) d\mathbf{r}_2 \dots d\mathbf{r}_N. \quad (2.16)$$

This electron's coordinates can be seen as reference point. Following the first theorem, the ground state energy of this system becomes a functional of its electron density:

$$E_{\text{el}}[\rho] = T_{\text{e}}[\rho] + V_{\text{ne}}[\rho] + V_{\text{ee}}[\rho]. \quad (2.17)$$

The second theorem states that the energy resulting from a trial density  $\rho_{\text{trial}}$  is always higher than the actual ground state energy. This enables the use of the variational principle for the density.  $V_{\text{ne}}[\rho]$ , representing the potential energy between nuclei and electrons, is system-dependent and can be calculated analytically. The remaining two terms are system-independent and can be combined to the Hohenberg-Kohn functional  $F_{\text{HK}}[\rho]$ .

Although the exact expression of it is not known, Kohn and Sham [75] proposed to map the Hohenberg-Kohn functional of the interacting system onto a fictional non-interacting system with the same density than the interacting one. This non-interacting system's so-called Kohn-Sham orbitals  $\psi_a^{\text{KS}}(\mathbf{r}_i)$  build up a corresponding Slater determinant that describes the system completely. Part of this approximation is the separation of  $T_{\text{e}}[\rho]$  and  $V_{\text{ee}}[\rho]$  in two parts each. While the kinetic term is split into a non-interacting part  $T_{\text{e,ni}}[\rho]$  and an interacting part  $T_{\text{e,i}}[\rho]$  part, the potential term is split into a classical, i.e. Coulomb interaction  $V_{\text{ee,c}}[\rho]$ , and a non-classical  $V_{\text{ee,nc}}[\rho]$  part:

$$T_e[\rho] = T_{e,ni}[\rho] + T_{e,i}[\rho], \quad (2.18)$$

$$V_{ee}[\rho] = V_{ee,c}[\rho] + V_{ee,nc}[\rho]. \quad (2.19)$$

Combining the two second terms on each right hand side of [equation \(2.18\)](#) and [equation \(2.19\)](#) the so-called exchange-correlation functional  $E_{XC}[\rho]$  is obtained:

$$E_{XC}[\rho] = T_{e,i}[\rho] + V_{ee,nc}[\rho]. \quad (2.20)$$

Since both parts of this functional are not exactly known, different approximations were made to approach the correct description. The first to mention is the method of the local density approximation (LDA), which assumes the local functional of the homogeneous electron gas:

$$E_{XC}^{\text{LDA}}[\rho] = \int f[\rho] \, d^3r. \quad (2.21)$$

Within this approximation, the exchange part of the exchange-correlation functional is solved analytically for a homogeneous electron gas [[135](#), [139](#)]. The correlation part is only analytically solvable at the high- and low-density limit [[140](#), [141](#)]. For values between these limits a number of points were very accurately calculated by a quantum Monte Carlo method [[142](#)] and were then used to interpolate between the two density limits.

Since the approximation of a homogeneous electron gas is a crude approximation, one can improve this approach by also taking the derivative of the density at each point into account. This will result in the so-called generalised gradient approximation (GGA):

$$E_{XC}^{\text{GGA}}[\rho] = \int f[\rho, \nabla\rho] \, d^3r. \quad (2.22)$$

Over the last years, several approaches within the **GGA** were proposed, such as the PW91 [140] functional and the PBE [143–145] functional, which was used in this thesis. By adding the second and even higher order derivatives to the **GGA**, the so-called meta-**GGA** functionals like TPSS [146] can be formulated.

Other strategies to improve the **GGA**s are the hybrid or double hybrid functionals, which mix exchange and correlation approaches of different resources. The mixing parameters can be adjusted to the considered system and can therefore be kind of empirical. While the hybrid functionals partially add exact exchange to their expressions, the double hybrid functionals add doubly perturbed correlations to their formalisms as well. The most popular functionals for both variants are the hybrid functional B3-LYP [135, 147–150] and the double hybrid functional B2-PLYP [151].

### 2.1.3 Dispersion Correction

Although **DFT** using **GGA** and meta-**GGA** functionals performs very well in general, especially for covalently bound or metallic systems, it is lacking a description to include long range effects like **vdW** interactions. But particularly for larger systems, these comparably small interactions can add up to significant values, and by association, sophisticated methods are needed for their accurate description.

The most prominent examples of such methods are the dispersion corrections introduced by Tkatchenko and Scheffler [152] and Grimme and co-workers [76–79], respectively. Since the latter is used within this work, its formalisms [78] will be looked at in this section.

This dispersion correction introduces an additive energy term  $E^{\text{D3}}$  to the obtained energy from Kohn-Sham-**DFT**  $E^{\text{KS-DFT}}$  to yield the corrected energy of the system  $E^{\text{DFT-D3}}$ :

$$E^{\text{DFT-D3}} = E^{\text{KS-DFT}} + E^{\text{D3}}, \quad (2.23)$$



where  $E^{\text{D3}}$  consists of a two body term  $E_{(2)}^{\text{D3}}$  and a three body term  $E_{(3)}^{\text{D3}}$ :

$$E^{\text{D3}} = E_{(2)}^{\text{D3}} + E_{(3)}^{\text{D3}}. \quad (2.24)$$

Since the inclusion of  $E_{(3)}^{\text{D3}}$  turned out to worsen the results during their test calculations due to an overestimation of the three-body effects [78], this term was dropped in many computational programs. Thus,  $E_{(2)}^{\text{D3}}$  is the only term to be considered and is given by:

$$E_{(2)}^{\text{D3}} = - \sum_{B>A}^M \sum_{n=6,8,\dots} s_n \frac{C_n^{AB}}{r_{AB}^n} f_{d,n}(r_{AB}), \quad (2.25)$$

where  $s_n$  are scaling factors,  $C_n^{AB}$  the averaged dispersion coefficient of  $n$ th order,  $r_{AB}$  stands for the distance between the two nuclei  $A$  and  $B$ , and  $f_{d,n}(r_{AB})$  is a damping function to restrict the range of dispersion correction. While  $s_6$  equals unity, the other scaling factors for higher  $C_n^{AB}$  are functional dependent and were adjusted to fulfil the correct asymptotic behaviour.

Regarding  $C_n^{AB}$ , they are calculated *ab initio* by time-dependent DFT and using recursion relations for higher multipole terms. For  $C_6^{AB}$  the Casimir-Polder equation [153] is the origin and results in:

$$C_6^{AB} = \frac{3}{\pi} \int_0^\infty \alpha^A(i\omega) \alpha^B(i\omega) d\omega, \quad (2.26)$$

where  $\alpha^A(i\omega)$  represents the averaged dipole polarisability at imaginary frequency  $\omega$  for the nucleus  $A$ . In order to include  $C_n^{AB}$ 's dependency on the coordination number (CN) of the considered nucleus  $A$ ,  $\alpha(i\omega)$  is no longer considered for nuclei but rather for their hydrides  $A_m\text{H}_n$  and  $B_k\text{H}_l$  while neglecting the hydrogen contribution  $\alpha^{\text{H}_2}(i\omega)$ . This omission of the hydrogen contributions results in a cross product within equation (2.26) and the normalisation via  $1/m$  and  $1/k$ , respectively. For the higher order  $C_8^{AB}$  a recursion relation is used:

$$C_8^{AB} = 3C_6^{AB} \sqrt{Q^A Q^B}, \quad (2.27)$$

with:

$$Q^A = s_Q \sqrt{Z^A} \frac{\langle r^4 \rangle^A}{\langle r^2 \rangle^A}, \quad (2.28)$$

where  $\langle r^4 \rangle^A$  and  $\langle r^2 \rangle^A$  are the geometrically averaged atomic densities' multipole-type expectation values. In their tests Grimme and co-workers showed that higher order dispersion coefficients ( $n \geq 10$ ) led to unstable results while dropping them did not change the results significantly, so [equation \(2.25\)](#)'s sum over  $n$  can be rewritten to the simple addition of two terms.

Going to the damping function  $f_{d,n}(r_{AB})$ , two very prominent variations should be mentioned. While the first one is the so-called “zero damping” method, which was proposed by Chai and Head-Gordon [[154](#)], the second one, which is used in this work, is a damping function proposed by Becke and Johnson [[79](#), [155](#)] and has the form:

$$f_{d,n}(r_{AB}) = \frac{r_{AB}^n}{r_{AB}^n + (p_1 R_{0AB} + p_2)^n}, \quad (2.29)$$

where  $p_1$  and  $p_2$  are adjustable parameters and  $R_{0AB}$  is the square root of  $C_8^{AB}/C_6^{AB}$ . This damping function introduces an additional empirical parameter, compared to the first one, but provides a better description for short and medium range distances.

Condensing all mentioned approaches back into [equation \(2.23\)](#), the formulation used within this work becomes:

$$E^{\text{DFT-D3}} = E^{\text{KS-DFT}} - \sum_{B>A}^M \frac{C_6^{AB}}{r_{AB}^6 + (p_1 R_{0AB} + p_2)^6} + \frac{s_8 C_8^{AB}}{r_{AB}^8 + (p_1 R_{0AB} + p_2)^8} \quad (2.30)$$

and now includes long range interactions between nuclei in the considered systems.

### 2.1.4 Theory for Solid State Systems [156]

Up to this point, only molecules can be described and reasonably calculated with the given formulations. Although real solid state systems are basically huge molecules, their vast amount of atoms compared to molecules makes it nearly impossible to calculate them the same way. Thus, solid state systems are approximated to “ideal crystalline systems” which are infinitely extended systems that feature a particular translational periodicity. This means that the crystalline system provides a comparably small set of atoms, within a certain space that can reproduce the whole system by translational repetition of itself. The mentioned space containing this particular set of atoms is called a unit cell (UC) while multiples of it are called supercell (SC)s. There are different types of UCs: (i) the *conventional UC*, representing a repetitive arrangement of atoms that can not be further partitioned (different conventional UCs are possible for the same crystal system, but higher point group symmetry of the UC is favoured), (ii) the *primitive UC*, which is the smallest possible UC containing the smallest possible amount of atoms to resemble the crystal structure, and (iii) the *Wigner-Seitz cell* showing a primitive cell around such a group of atoms. Each UC is described by three non-coplanar so-called lattice constants  $a$ ,  $b$ , and  $c$  as well as their generated angles or by their vector representations  $\mathbf{a}_1$ ,  $\mathbf{a}_2$ , and  $\mathbf{a}_3$ , respectively. The translation vector  $\mathbf{T}$  is then given by:

$$\mathbf{T} = m_1\mathbf{a}_1 + m_2\mathbf{a}_2 + m_3\mathbf{a}_3, \quad (2.31)$$

where  $m_k \in \mathbb{Z}$  while also representing the SC coefficients.

Due to the periodicity resulting from the translations, the effective potential  $\hat{v}_{\text{eff}}$  acting on electrons becomes periodic as well and provides a corresponding periodic function  $V(\mathbf{r}_i)$ :

$$V(\mathbf{r}_i) = V(\mathbf{T} + \mathbf{r}_i). \quad (2.32)$$

$V(\mathbf{r}_i)$  is invariant to translation and can be simplified by rewriting it as a Fourier series:

$$V(\mathbf{r}_i) = \sum_n V_n e^{i\mathbf{G}_n \cdot \mathbf{r}_i}, \quad (2.33)$$

where  $V_n$  represents the Fourier coefficients and  $\mathbf{G}_n$  are vectors in the Fourier space. Due to the needed invariance in [equation \(2.32\)](#), the vectors  $\mathbf{G}_n$  are required to fulfil this invariance as well.

At this point the reciprocal lattice comes into play, where the axis vectors of the reciprocal space are constructed via:

$$\mathbf{b}_1 = 2\pi \frac{\mathbf{a}_2 \times \mathbf{a}_3}{\mathbf{a}_1 \cdot \mathbf{a}_2 \times \mathbf{a}_3}, \quad (2.34)$$

$$\mathbf{b}_2 = 2\pi \frac{\mathbf{a}_3 \times \mathbf{a}_1}{\mathbf{a}_1 \cdot \mathbf{a}_2 \times \mathbf{a}_3}, \quad (2.35)$$

$$\mathbf{b}_3 = 2\pi \frac{\mathbf{a}_1 \times \mathbf{a}_2}{\mathbf{a}_1 \cdot \mathbf{a}_2 \times \mathbf{a}_3}. \quad (2.36)$$

Since each reciprocal lattice vector  $\mathbf{b}_k$  is orthogonal to two lattice vectors  $\mathbf{a}_l$ , their scalar product is:

$$\mathbf{b}_k \cdot \mathbf{a}_l = 2\pi \delta_{kl}, \quad (2.37)$$

where  $\delta_{kl}$  is the Kronecker delta. With this set of reciprocal lattice vectors, translational points  $\mathbf{K}$  in the reciprocal lattice are given by:

$$\mathbf{K} = n_1 \mathbf{b}_1 + n_2 \mathbf{b}_2 + n_3 \mathbf{b}_3 \quad (2.38)$$

with  $n_k \in \mathbb{Z}$  while  $n_1$ ,  $n_2$  and  $n_3$  are also known as  $h$ ,  $k$ , and  $l$ , the so-called Miller indices, which are used to name surface cuts ( $hkl$ ) where the corresponding  $\mathbf{K}$  is the

surface normal. Stating that  $\mathbf{G}_n$  equals  $\mathbf{K}$  and with [equation \(2.37\)](#), the translational invariance of  $V(\mathbf{r}_i)$  is ensured and becomes:

$$V(\mathbf{r}_i) = \sum_{\mathbf{K}} V_{\mathbf{K}} e^{i\mathbf{K}\cdot\mathbf{r}_i}. \quad (2.39)$$

Thus, even mathematically complex expressions of  $\hat{v}_{\text{eff}}$  in real space can be expressed by sums of comparably simple periodic functions in reciprocal space.

Considering the single electron Hamiltonian being composed of the electron's kinetic energy and the periodic effective potential  $V(\mathbf{r}_i)$ , [equation \(2.2\)](#) becomes:

$$\left(-\frac{1}{2}\nabla^2 + V(\mathbf{r}_i)\right) \psi_a(\mathbf{r}_i) = \left(-\frac{1}{2}\nabla^2 + \sum_{\mathbf{K}} V_{\mathbf{K}} e^{i\mathbf{K}\cdot\mathbf{r}_i}\right) \psi_a(\mathbf{r}_i) = \epsilon_a \psi_a(\mathbf{r}_i), \quad (2.40)$$

where  $\psi_a(\mathbf{r}_i)$  represents the electron's wave function,  $\sum_{\mathbf{K}} V_{\mathbf{K}} e^{i\mathbf{K}\cdot\mathbf{r}_i}$  the Fourier series of  $V(\mathbf{r}_i)$ , and  $\epsilon_a$  the electron's energy in  $\psi_a(\mathbf{r}_i)$ .

According to Bloch's theorem [[157](#)], the solution of [equation \(2.2\)](#) for periodic systems have to have a special form:

$$\psi_a(\mathbf{k}, \mathbf{r}_i) = u(\mathbf{r}_i) e^{i\mathbf{k}\cdot\mathbf{r}_i}, \quad (2.41)$$

where  $\mathbf{k}$  represents the continuous wave vector in reciprocal space,  $u(\mathbf{r}_i)$  a periodic function providing the same periodicity as the solid state system, and  $e^{i\mathbf{k}\cdot\mathbf{r}_i}$  a plane wave. As before for  $V(\mathbf{r}_i)$ ,  $u(\mathbf{r}_i)$  can also be expressed via a Fourier series:

$$\psi_a(\mathbf{k}, \mathbf{r}_i) = \left(\sum_{\mathbf{K}} u_{\mathbf{K}} e^{i\mathbf{K}\cdot\mathbf{r}_i}\right) e^{i\mathbf{k}\cdot\mathbf{r}_i}. \quad (2.42)$$

By putting the plane wave  $e^{i\mathbf{k}\cdot\mathbf{r}_i}$  into the sum's bracket, the result has the form of a linear combination of plane waves, which therefore serve as basis functions.

Inserting equation (2.42) in equation (2.40) and considering all electrons of the system, an analogue to equation (2.13) is obtained, where every matrix is now dependent on  $\mathbf{k}$ :

$$\mathbf{F}(\mathbf{k})\mathbf{U}(\mathbf{k}) = \varepsilon(\mathbf{k})\mathbf{S}(\mathbf{k})\mathbf{U}(\mathbf{k}). \quad (2.43)$$

Thus, equation (2.43) needs to be solved for each  $\mathbf{k}$ . Due to periodicity of the system in real and reciprocal space, not every possible  $\mathbf{k}$  needs to be evaluated, only the ones in the UC in reciprocal space. This UC is also known as the first Brillouin zone, whose central point is denoted as  $\Gamma$  point while the zone's real space analogue is the Wigner-Seitz cell. Thus, the reciprocal space needs "only" be evaluated within this first Brillouin zone, but since  $\mathbf{k}$  is continuous, integration is needed. Fortunately, the integration can be approximated quite well with the summation of equidistantly (along  $\mathbf{b}_i$ ) arranged distinct values of  $\mathbf{k}$  within the first Brillouin zone. The most convenient method to generate such a  $\mathbf{k}$ -mesh is provided by Monkhorst and Pack [158] and is used within this work. It uses three adjustable integer  $Q_1, Q_2$ , and  $Q_3$  that determine the number of special  $\mathbf{k}$ -mesh grid-points along the corresponding reciprocal lattice vector  $\mathbf{b}_k$ . This results in  $Q_1 \cdot Q_2 \cdot Q_3$  single  $\mathbf{k}$  of:

$$\mathbf{k} = \mathbf{b}_1 \frac{q_1 + 0.5}{Q_1} + \mathbf{b}_2 \frac{q_2 + 0.5}{Q_2} + \mathbf{b}_3 \frac{q_3 + 0.5}{Q_3}, \quad (2.44)$$

where  $q_k \in \mathbb{Z}$  while  $0 \leq q_k < Q_k$ .

Besides occurring quite naturally as the basis set for periodic calculations, plane waves provide a number of advantages compared to atomic centred basis sets as in HF or DFT. Firstly, only a single value, the energy cut-off, is needed to control the basis set size by taking only plane waves into account whose kinetic energy is below the specified value. Secondly, basis set superposition errors are simply bypassed due to their independence of atomic positions, which simplifies the calculation of adsorption energies, for example. Unfortunately, they lack a convincing description of core

electrons due to the rapid oscillations of these electrons' wave functions. Thus, higher amounts of plane waves are needed to improve the description of this region, which drastically increases the computational costs. This shortcoming can be circumvented by using pseudo-potentials that describe the core electrons potential via an effective potential [159–162]. An even better approach to improve the use of plane waves was introduced by Blöchl, namely the projector augmented wave (PAW) approach [163], which is used within this work and is based on the works of Slater [164], Marcus [165] and Andersen [166].

First of all, the PAW approach maps the one-electron wave functions  $\psi_a(\mathbf{r}_i)$  onto pseudo-one-electron wave functions  $\tilde{\psi}_a(\mathbf{r}_i)$  via the transformation  $\mathcal{T}^{-1}$ , so that the inverse transform becomes:

$$\psi_a(\mathbf{r}_i) = \mathcal{T}\tilde{\psi}_a(\mathbf{r}_i). \quad (2.45)$$

Thus, the desired quantities can be obtained as the expectation value of the corresponding operator after inverse transform of  $\tilde{\psi}_a(\mathbf{r}_i)$  or as the expectation value of a related pseudo-operator  $\tilde{\hat{O}}$ :

$$\tilde{\hat{O}} = \mathcal{T}^\dagger \hat{O} \mathcal{T}. \quad (2.46)$$

Secondly, it defines a considerably small region around the core of an atom, the augmentation region  $\Omega_A$ . In the context of pseudo-potentials this region is also known as core region. Since the rapid oscillations only occur within  $\Omega_A$  while outside of it  $\tilde{\psi}_a(\mathbf{r}_i)$  coincides with  $\psi_a(\mathbf{r}_i)$ , the inverse transformation is only required inside  $\Omega_A$ . Additionally, considering the inverse transformation per atom  $A$  and its position  $\mathbf{R}$ ,  $\mathcal{T}$  can be written as the sum of each local, atom centred contribution  $\mathcal{T}_A$ :

$$\mathcal{T} = 1 + \sum_A \mathcal{T}_A. \quad (2.47)$$

Requiring a set of initial pseudo-functions  $|\tilde{\phi}_{A\kappa}\rangle$ , also called pseudo-partial waves that are orthogonal to the core states and form a complete set,  $\mathcal{T}_A$  can be defined within  $\Omega_A$  with the help of partial waves  $|\phi_{A\kappa}\rangle$  derived from radial integration of isolated atom's Schrödinger equation:

$$|\phi_{A\kappa}\rangle = (1 + \mathcal{T}_A) |\tilde{\phi}_{A\kappa}\rangle, \quad (2.48)$$

where the index  $\kappa$  combined index of the angular momentum quantum numbers and an index distinguishing plane waves with the same angular momentum.

Since  $\psi_a(\mathbf{r}_i)$  and  $\tilde{\psi}_a(\mathbf{r}_i)$  can both be represented by the linear combination of their respective sets of partial waves and pseudo-partial waves,  $\psi_a(\mathbf{r}_i)$  can be written as:

$$\psi_a(\mathbf{r}_i) = \tilde{\psi}_a(\mathbf{r}_i) - \sum_{A\kappa} |\tilde{\phi}_{A\kappa}\rangle c_{A\kappa} + \sum_{A\kappa} |\phi_{A\kappa}\rangle c_{A\kappa}, \quad (2.49)$$

where the coefficients  $c_{A\kappa}$  are the same for both linear combinations due to [equation \(2.45\)](#), [equation \(2.47\)](#), and [equation \(2.48\)](#). Since  $\mathcal{T}$  is a linear transformation bringing  $\tilde{\psi}_a(\mathbf{r}_i)$  to  $\psi_a(\mathbf{r}_i)$ ,  $c_\kappa$  can be written as:

$$c_\kappa = \langle \tilde{p}_\kappa | \tilde{\psi}_a \rangle, \quad (2.50)$$

with  $\langle \tilde{p}_\kappa |$  being a corresponding smooth so-called projector function. Assuming that there is no overlap between  $\Omega_A$ , two statements can be made:

$$\sum_{\kappa} |\tilde{\phi}_{A\kappa}\rangle \langle \tilde{p}_{A\kappa}| = 1 \quad \text{and} \quad (2.51)$$

$$\langle \tilde{p}_{A\kappa} | \tilde{\phi}_{A\ell} \rangle = \delta_{\kappa\ell}, \quad (2.52)$$



Exploiting [equation \(2.49\)](#) and [equation \(2.50\)](#),  $\psi_a(\mathbf{r}_i)$  becomes:

$$\psi_a(\mathbf{r}_i) = \tilde{\psi}_a(\mathbf{r}_i) + \sum_{A\kappa} (|\phi_{A\kappa}\rangle - |\phi_{A\kappa}\rangle) \langle \tilde{p}_{A\kappa} | \tilde{\psi}_a \rangle \quad (2.53)$$

and the transformation:

$$\mathcal{T} = 1 + \sum_{A\kappa} (|\phi_{A\kappa}\rangle - |\phi_{A\kappa}\rangle) \langle \tilde{p}_{A\kappa} |. \quad (2.54)$$

With this transformation, the rapidly oscillating region of the one electron wave function  $\psi_a(\mathbf{r}_i)$  near the nuclei  $A$  can now be expressed via an one-electron pseudo-wave function  $\tilde{\psi}_a(\mathbf{r}_i)$  within the corresponding augmentation region  $\Omega_A$ . The pseudo-operator for a desired quantity is expressed via:

$$\tilde{\hat{O}} = \hat{O} + \sum_{A\kappa\iota} |\tilde{p}_{A\kappa}\rangle \left( \langle \phi_{A\kappa} | \hat{O} | \phi_{A\iota} \rangle - \langle \tilde{\phi}_{A\kappa} | \hat{O} | \tilde{\phi}_{A\iota} \rangle \right) \langle \tilde{p}_{A\iota} |. \quad (2.55)$$

With these formulations solid state systems can finally be well described and reasonably calculated using a plane wave basis set. Unfortunately, another challenge arises from the use of plane waves as basis set, their dependency on a three dimensional periodicity. While this is of course no problem for the calculation of bulk materials, the calculation of surfaces and the adsorption of molecules on them requires the usage of a sufficiently thick vacuum layer above and/or beneath the atomic layers representing the surface. This ensures the three dimensional periodicity while preventing surface surface interactions and is called the ‘‘slab model’’. Since the thickness of the added vacuum has a strong impact on the computational demands of the calculation, it needs to be thoroughly tested and evaluated to find a vacuum layer as thick as necessary and as thin as possible.

Finally, due to the use of comparably small UCs and the periodicity of the solid state systems, the additive term for the dispersion correction (second term of [equation \(2.30\)](#)’s right hand side) needs to be adjusted to this computational set-up, as it

is done in the Vienna *ab-initio* Simulation Package (VASP), and becomes:

$$E^{\text{D3}} = - \sum_{B \geq A}^M \sum_{\mathbf{T}} \frac{C_6^{AB}}{r_{AB,\mathbf{T}}^6 + (p_1 R_{0AB} + p_2)^6} + \frac{s_8 C_8^{AB}}{r_{AB,\mathbf{T}}^8 + (p_1 R_{0AB} + p_2)^8}. \quad (2.56)$$

The summation over the translational vector  $\mathbf{T}$  accounts for the dispersion interaction beyond the UC boundaries while the summation over  $A$  and  $B$  is solely more strongly restricted ( $B > A$ ) for  $\mathbf{T} = 0$ .

### 2.1.5 Statistical Thermodynamics [167]

For realistic systems, their energy and, by association, reaction energies of them are described by the Gibbs free (reaction) energy, which is composed of an enthalpic part  $H$  and an entropic part  $TS$ , where  $T$  is the temperature. In order to simplify the following expressions, the electronic part  $E$  is separated from  $H$ , while  $H$  only represents the remaining part from now on:

$$G(T, p) = E + H - TS. \quad (2.57)$$

Until now the calculated energies only provide the bare  $E$  of  $G$ , or in other words,  $T$ , the pressure  $p$ , and the zero point energy of the system are neglected so far. In order to provide more realistic reaction energy values, namely  $G$ , by including these missing quantities, the partition function  $q(V, T)$  is needed.  $S$  and  $H$  both can be expressed using  $q(V, T)$  by:

$$H(V, T) = \mathcal{M}k_{\text{B}}T^2 \left( \frac{\partial \ln(q(V, T))}{\partial T} \right)_V, \quad (2.58)$$

$$S(V, T) = \mathcal{M}k_{\text{B}} + \mathcal{M}k_{\text{B}} \ln \left( \frac{q(V, T)}{\mathcal{M}} \right) + \mathcal{M}k_{\text{B}}T \left( \frac{\partial \ln(q(V, T))}{\partial T} \right)_V, \quad (2.59)$$

where  $\mathcal{M}$  represents the number of molecules/systems and  $k_B$  the Boltzmann constant. Setting  $\mathcal{M}$  to one since the contribution per molecule/system is desired, placing  $k_B$  outside the brackets, and using  $q(V, T) = q_{\text{ele}}(T) \cdot q_{\text{trans}}(V, T) \cdot q_{\text{rot}}(T) \cdot q_{\text{vib}}(T)$  while omitting their dependencies, [equation \(2.59\)](#) and [equation \(2.58\)](#) become:

$$H(V, T) = k_B T^2 \left( \frac{\partial \ln(q_e q_t q_r q_v)}{\partial T} \right)_V, \quad (2.60)$$

$$S(V, T) = k_B \left( \ln(q_e q_t q_r q_v e) + T \left( \frac{\partial \ln(q_e q_t q_r q_v)}{\partial T} \right)_V \right), \quad (2.61)$$

where the indices ele, trans, rot, and vib stand for electronic, translational, rotational, and vibrational.

Utilising logarithm laws,  $\ln(q_e q_t q_r q_v)$  can be written as  $\ln(q_e) + \ln(q_t) + \ln(q_r) + \ln(q_v)$ , and by association,  $S(V, T)$  and  $H(V, T)$  can be expressed by the sum of the four parts. Assuming the electronic excited states to be inaccessible due to a comparably large energy difference to the ground state and setting the ground state energy to zero, the electronic part of the partition function vanishes. Besides, the other three parts of the partition function are, within a harmonic approximation, expressed by:

$$q_t(T, V) = \left( \frac{2\pi m k_B T}{h^2} \right)^{3/2} V, \quad (2.62)$$

$$q_r(T) = \frac{\sqrt{\pi I_X I_Y I_Z}}{\varsigma} \left( \frac{8\pi^2 k_B T}{h^2} \right)^{3/2}, \quad (2.63)$$

$$q_v(T) = \prod_k \frac{e^{(-hc\tilde{\nu}_k/2k_B T)}}{1 - e^{(-hc\tilde{\nu}_k/k_B T)}}, \quad (2.64)$$

where  $m$  represents the mass of the considered molecule,  $h$  stands for the Planck constant,  $I_L$  is the moment of inertia for a rotation around the L axis,  $\varsigma$  acts as a tabulated index of symmetry, and  $\tilde{\nu}_k$  represents the wavenumber of the considered

normal mode (for molecules) or phonon (for solid state systems).

Concerning the enthalpy and substituting [equation \(2.62\)](#), [equation \(2.63\)](#), and [equation \(2.64\)](#) in [equation \(2.60\)](#) gives:

$$H_{\text{trans}}(T) = \frac{5}{2}k_{\text{B}}T, \quad (2.65)$$

$$H_{\text{rot}}(T) = \frac{3}{2}k_{\text{B}}T, \quad (2.66)$$

$$H_{\text{vib}}(T) = \sum_k hc\tilde{\nu}_k \left( \frac{1}{2} + \frac{1}{e^{(hc\tilde{\nu}_k/k_{\text{B}}T)} - 1} \right), \quad (2.67)$$

where  $H_{\text{trans}}(T)$  additionally includes a thermal correction term of  $k_{\text{B}}T$ . With these three contributions of the enthalpic part,  $H(T)$  becomes:

$$H(T) = H_{\text{trans}}(T) + H_{\text{rot}}(T) + H_{\text{vib}}(T). \quad (2.68)$$

Concerning the entropy, substituting [equation \(2.62\)](#), [equation \(2.63\)](#), and [equation \(2.64\)](#) in [equation \(2.61\)](#) and assuming that the molecules behave like an ideal gas, results in:

$$S_{\text{trans}}(T, p) = k_{\text{B}} \left( \ln \left( \left( \frac{2\pi mk_{\text{B}}T}{h^2} \right)^{3/2} \frac{k_{\text{B}}T}{p} \right) + \frac{5}{2} \right), \quad (2.69)$$

$$S_{\text{rot}}(T) = k_{\text{B}} \left( \ln \left( \frac{\sqrt{\pi I_X I_Y I_Z}}{\sigma} \left( \frac{8\pi^2 k_{\text{B}}T}{h^2} \right)^{3/2} \right) + \frac{3}{2} \right), \quad (2.70)$$

$$S_{\text{vib}}(T) = k_{\text{B}} \left( \sum_k \ln \left( 1 - e^{-(hc\tilde{\nu}_k/k_{\text{B}}T)} \right) + \frac{hc\tilde{\nu}_k}{k_{\text{B}}T} \cdot \frac{1}{e^{(hc\tilde{\nu}_k/k_{\text{B}}T)} - 1} \right), \quad (2.71)$$

where the term  $5/2$  in [equation \(2.69\)](#) is the result of the additional  $e$  in [equation \(2.61\)](#). Analogous to [equation \(2.68\)](#),  $S(T, p)$  is plainly the sum of its contributions in [equation \(2.69\)](#), [equation \(2.70\)](#), and [equation \(2.71\)](#).

Finally,  $G(T, p)$  can be calculated for varying temperatures and pressures and, by association, gives rise to more realistic reaction energies. Therefore, statements on the considered reactions and their likelihood get more weight and can be compared to experiments more easily than the electronic reaction energies.

### 2.1.6 Normal Mode and Phonon Wavenumbers [156]

As stated in subsection 2.1.5 [Statistical Thermodynamics](#), the calculation of normal mode and phonon wave numbers  $\tilde{\nu}_k$  is essential for obtaining more realistic reaction energies. Additionally, they are a great tool for comparison with experimental data by comparing them to infrared and Raman spectroscopy measurements, for example, to draw conclusions about the structure of the experimentally investigated system or about the used theoretical structure model vice versa.

The calculation of normal modes and phonons requires the calculation of the Hessian matrix, which is given by:

$$\mathbf{H} = \begin{bmatrix} \frac{\partial^2 E(\mathcal{R})}{\partial x_1^2} & \frac{\partial^2 E(\mathcal{R})}{\partial x_1 \partial x_2} & \dots & \frac{\partial^2 E(\mathcal{R})}{\partial x_1 \partial x_{\mathcal{N}}} \\ \frac{\partial^2 E(\mathcal{R})}{\partial x_2 \partial x_1} & \frac{\partial^2 E(\mathcal{R})}{\partial x_2^2} & \dots & \frac{\partial^2 E(\mathcal{R})}{\partial x_2 \partial x_{\mathcal{N}}} \\ \vdots & \vdots & \ddots & \vdots \\ \frac{\partial^2 E(\mathcal{R})}{\partial x_{\mathcal{N}} \partial x_1} & \frac{\partial^2 E(\mathcal{R})}{\partial x_{\mathcal{N}} \partial x_2} & \dots & \frac{\partial^2 E(\mathcal{R})}{\partial x_{\mathcal{N}}^2} \end{bmatrix}. \quad (2.72)$$

where  $E(\mathcal{R})$  represents the energy of the system dependent on the position of all nuclei in the system, whose coordinates are given by  $\mathcal{R}$ ,  $x_l$  stands for one of those coordinates, and  $\mathcal{N}$  is the number of them. Assuming a harmonic potential, the decoupled matrix entries can also be calculated using the forces resulting from small displacements of each atom in each Cartesian coordinate, which is computationally cheaper, while the used harmonic approximation performs quite well in most cases. Evaluation of the eigenvalue equation for the mass weighted  $\mathbf{H}$  results in the normal modes and phonons represented by the eigenvectors while their respective eigenvalues

give the force constant  $\lambda_k$ . From this force constant, the corresponding wavenumber  $\tilde{\nu}_k$  can be calculated using the speed of light  $c$  via:

$$\tilde{\nu}_k = \frac{\sqrt{\lambda_k}}{2\pi c}. \quad (2.73)$$

While there are  $3\mathcal{M}-6(5)$  vibrational degrees of freedom for molecules (linear molecules), there are  $3\mathcal{M}$  vibrational degrees of freedom for solid state systems that are divided in subgroups: longitudinal acoustical, transverse acoustical, longitudinal optical, and transverse optical phonons. Since the acoustical phonons provide wavenumbers of zero at the centre of first Brillouin zone, the  $\Gamma$  point, only optical phonons are evaluated at this point. For other values of  $\mathbf{k}$  all subgroups of the solid state system's vibrations need to be analysed. Taking all  $\mathbf{k}$  dependent phonons wavenumbers into account, which would result in a phonon dispersion relation diagram, requires an integration over  $\mathbf{k}$  or at least a summation over the defined  $\mathbf{k}$ -mesh (analogous to [equation \(2.43\)](#)). Due to the comparably small impact of this dispersion on the thermodynamic quantities and the actual frequencies, at least for the optical phonons, while requiring a disproportionate higher amount of computation time and resources, only phonons at the  $\Gamma$  point are calculated and taken into account within this work.

### 2.1.7 Nuclear Magnetic Resonance Shifts

Besides the calculation of infrared and Raman wavenumbers for comparison with experimental data, the evaluation of [NMR](#) shifts provides a second and very useful tool to mutually compare experimental and theoretical studies. Therefore, this work also covers the calculation of [NMR](#) shifts for the nuclei  $^{27}\text{Al}$  and  $^{19}\text{F}$  in the different bulk and surface structures.

The chemical shift or [NMR](#) shift  $\delta_A$  is simply the difference of the considered nucleus' and a reference nucleus' magnetic shieldings  $\sigma_A$  and  $\sigma_{\text{ref}}$  or, to be more precise,

the traces of their shielding tensors:

$$\delta_A = \sigma_{\text{ref,tr}} - \sigma_{A,\text{tr}}, \quad (2.74)$$

for a single electron  $i$  with:

$$\sigma_{A,\text{tr}}(\mathbf{r}_i) = \frac{1}{3} \text{tr}(\sigma_A(\mathbf{r}_i)) = \frac{1}{3} \text{tr} \begin{pmatrix} \sigma_{A,11}(\mathbf{r}_i) & \sigma_{A,12}(\mathbf{r}_i) & \sigma_{A,13}(\mathbf{r}_i) \\ \sigma_{A,21}(\mathbf{r}_i) & \sigma_{A,22}(\mathbf{r}_i) & \sigma_{A,23}(\mathbf{r}_i) \\ \sigma_{A,31}(\mathbf{r}_i) & \sigma_{A,32}(\mathbf{r}_i) & \sigma_{A,33}(\mathbf{r}_i) \end{pmatrix}, \quad (2.75)$$

where  $\sigma_A(\mathbf{r}_i)$  can be obtained component wise via:

$$\sigma_{A,kl}(\mathbf{r}_i) = \frac{\partial B_{A,k}^{\text{in}}(\mathbf{r}_i)}{\partial B_l^{\text{ex}}}. \quad (2.76)$$

Here  $B_l^{\text{ex}}$  are the components of an applied external magnetic field  $\mathbf{B}^{\text{ex}}$ , and  $B_{A,k}^{\text{in}}(\mathbf{r}_i)$  represent the components of the corresponding induced magnetic field  $\mathbf{B}_A^{\text{in}}(\mathbf{r}_i)$  in nucleus  $A$ , which itself is the partial derivative of the energy  $E$  with respect to the considered nucleus' magnetic moment. Thus, following the method proposed by Mauri and co-workers [168, 169],  $\mathbf{B}_A^{\text{in}}$  needs to be evaluated. This is done via:

$$\mathbf{B}_A^{\text{in}}(\mathbf{r}_i) = \frac{1}{c} \int \mathbf{j}^{(1)}(\mathbf{r}') \times \frac{\mathbf{r}_i - \mathbf{r}'}{|\mathbf{r}_i - \mathbf{r}'|^3} d\mathbf{r}', \quad (2.77)$$

where  $\mathbf{j}^{(1)}(\mathbf{r}')$  represents the first order-induced current at the position  $\mathbf{r}'$  and  $c$  is the speed of light. To evaluate  $\mathbf{j}^{(1)}(\mathbf{r}')$  while utilising the PAW approach, firstly, the electric current operator  $\hat{\mathbf{J}}(\mathbf{r}')$  and the single electron Hamiltonian  $\hat{h}_{\text{el}}(\mathbf{r}_i)$  (in accordance to equation (2.4)) need to be transformed to their pseudo counterparts  $\tilde{\mathbf{J}}(\mathbf{r}')$  and  $\tilde{h}_{\text{el}}(\mathbf{r}_i)$ . Unfortunately, by applying an external magnetic field, the PAW approach no longer preserves the translational invariance of  $\psi_a(\mathbf{r}_i)$ , but instead, an additional phase factor  $e^{(i/2c)\mathbf{r}_i \cdot \mathbf{T} \times \mathbf{B}^{\text{ex}}}$  arises. Thus, the expression for transformation, equation (2.55), needs to be adjusted accordingly to again preserve the translational

invariance, and with  $\Theta = e^{(i/2c)\mathbf{r}_i \cdot \mathbf{R}_A \times \mathbf{B}^{\text{ex}}}$  it becomes:

$$\tilde{\hat{O}} = \hat{O} + \sum_{A\kappa\ell} e^\Theta |\tilde{p}_{A\kappa}\rangle \left( \langle \phi_{A\kappa} | e^{-\Theta} \hat{O} e^\Theta | \phi_{A\ell} \rangle - \langle \tilde{\phi}_{A\kappa} | e^{-\Theta} \hat{O} e^\Theta | \tilde{\phi}_{A\ell} \rangle \right) \langle \tilde{p}_{A\ell} | e^{-\Theta}. \quad (2.78)$$

The inclusion of this phase factor extends the PAW approach to the gauge-including projector augmented wave (GIPAW) approach. Now it is possible to safely transform  $\hat{\mathbf{J}}(\mathbf{r}')$ :

$$\hat{\mathbf{J}}(\mathbf{r}') = \frac{\mathbf{p} |\mathbf{r}'\rangle \langle \mathbf{r}'| + |\mathbf{r}'\rangle \langle \mathbf{r}'| \mathbf{p}}{2} - \frac{\mathbf{B}^{\text{ex}} \times \mathbf{r}'}{2c} |\mathbf{r}'\rangle \langle \mathbf{r}'| \quad (2.79)$$

and  $\hat{h}_{\text{el}}(\mathbf{r}_i)$ , which becomes:

$$\hat{h}_{\text{el}}(\mathbf{r}_i) = \frac{1}{2} \mathbf{p}^2 + V(\mathbf{r}_i) + \frac{1}{2c} \mathbf{p} \times \mathbf{r}_i \cdot \mathbf{B}^{\text{ex}} + \frac{1}{8c^2} (\mathbf{B}^{\text{ex}} \times \mathbf{r}_i)^2 \quad (2.80)$$

in the presence of an external field, via equation (2.78) to their two pseudo counterparts:

$$\begin{aligned} \tilde{\hat{h}}_{\text{el}}(\mathbf{r}_i) = \frac{1}{2} \mathbf{p}^2 + V^{\text{loc}}(\mathbf{r}_i) + \sum_A e^\Theta V_A^{\text{nl}} e^{-\Theta} + \frac{1}{2c} \mathbf{p} \times \mathbf{r}_i \cdot \mathbf{B}^{\text{ex}} + \\ \frac{1}{8c^2} (\mathbf{B}^{\text{ex}} \times \mathbf{r}_i)^2 \quad \text{and} \end{aligned} \quad (2.81)$$

$$\begin{aligned} \tilde{\hat{\mathbf{J}}}(\mathbf{r}') = \frac{\mathbf{p} |\mathbf{r}'\rangle \langle \mathbf{r}'| + |\mathbf{r}'\rangle \langle \mathbf{r}'| \mathbf{p}}{2} - \frac{\mathbf{B}^{\text{ex}} \times \mathbf{r}'}{2c} |\mathbf{r}'\rangle \langle \mathbf{r}'| + \\ \sum_A e^\Theta \left[ \Delta \hat{\mathbf{J}}_A^{\text{p}}(\mathbf{r}') + \Delta \hat{\mathbf{J}}_A^{\text{d}}(\mathbf{r}') \right] e^{-\Theta} \quad \text{with} \end{aligned} \quad (2.82)$$



$$\Delta\hat{\mathbf{J}}_A^{\text{p}}(\mathbf{r}') = \sum_{\kappa\ell} |\tilde{p}_{A\kappa}\rangle \left( \left\langle \phi_{A\kappa} \left| \frac{\mathbf{p}|\mathbf{r}'\rangle \langle \mathbf{r}'| + |\mathbf{r}'\rangle \langle \mathbf{r}'|\mathbf{p}}{2} \right| \phi_{A\ell} \right\rangle - \left\langle \tilde{\phi}_{A\kappa} \left| \frac{\mathbf{p}|\mathbf{r}'\rangle \langle \mathbf{r}'| + |\mathbf{r}'\rangle \langle \mathbf{r}'|\mathbf{p}}{2} \right| \tilde{\phi}_{A\ell} \right\rangle \right) \langle \tilde{p}_{A\ell}| \quad \text{and} \quad (2.83)$$

$$\Delta\hat{\mathbf{J}}_A^{\text{d}}(\mathbf{r}') = -\frac{\mathbf{B}^{\text{ex}} \times (\mathbf{r}' - \mathbf{R}_A)}{2c} \sum_{\kappa\ell} |\tilde{p}_{A\kappa}\rangle \left( \langle \phi_{A\kappa}|\mathbf{r}'\rangle \langle \mathbf{r}'|\phi_{A\ell}\rangle - \langle \tilde{\phi}_{A\kappa}|\mathbf{r}'\rangle \langle \mathbf{r}'|\tilde{\phi}_{A\ell}\rangle \right) \langle \tilde{p}_{A\ell}|. \quad (2.84)$$

In equations [equation \(2.79\)](#) to [equation \(2.84\)](#)  $\mathbf{p}$  represents the momentum operator,  $V^{\text{loc}}(\mathbf{r}_i)$  stands for the local part of the potential, and  $V_A^{\text{nl}}$  for the nonlocal part, accordingly. While  $\Delta\hat{\mathbf{J}}_A^{\text{p}}(\mathbf{r}')$  is called the paramagnetic augmentation region,  $\Delta\hat{\mathbf{J}}_A^{\text{d}}(\mathbf{r}')$  is called the diamagnetic augmentation region.

Furthermore, the two operators need to be expanded in powers of  $\mathbf{B}^{\text{ex}}$  ( $\tilde{\mathcal{O}} = \tilde{\mathcal{O}}^{(0)} + \tilde{\mathcal{O}}^{(1)} + \mathcal{O}((\mathbf{B}^{\text{ex}})^2)$ ) resulting in:

$$\tilde{h}_{\text{el}}^{(0)}(\mathbf{r}_i) = \frac{1}{2}\mathbf{p}^2 + V^{\text{loc}}(\mathbf{r}_i) + \sum_A V_A^{\text{nl}}, \quad (2.85)$$

$$\tilde{h}_{\text{el}}^{(1)}(\mathbf{r}_i) = \frac{1}{2c} \left( \mathbf{p} \times \mathbf{r}_i + \sum_A \mathbf{R}_A \times \left( \frac{1}{i} [\mathbf{r}_i, V_A^{\text{nl}}] \right) \right) \cdot \mathbf{B}^{\text{ex}}, \quad (2.86)$$

$$\tilde{\mathbf{J}}^{(0)}(\mathbf{r}') = \frac{\mathbf{p}|\mathbf{r}'\rangle \langle \mathbf{r}'| + |\mathbf{r}'\rangle \langle \mathbf{r}'|\mathbf{p}}{2} + \sum_A \Delta\hat{\mathbf{J}}_A^{\text{p}}(\mathbf{r}'), \quad \text{and} \quad (2.87)$$

$$\tilde{\mathbf{J}}^{(1)}(\mathbf{r}') = -\frac{\mathbf{B}^{\text{ex}} \times \mathbf{r}'}{2c} |\mathbf{r}'\rangle \langle \mathbf{r}'| + \sum_A \left( \Delta\hat{\mathbf{J}}_A^{\text{d}}(\mathbf{r}') + \frac{1}{2ci} [(\mathbf{B}^{\text{ex}} \times \mathbf{R}_A \cdot \mathbf{r}') \Delta\hat{\mathbf{J}}_A^{\text{p}}(\mathbf{r}')] \right) \quad (2.88)$$

where square brackets indicate commutators. Thus, [equation \(2.85\)](#) to [equation \(2.88\)](#) now enable the evaluation of  $\mathbf{j}^{(1)}(\mathbf{r}')$  via:

$$\mathbf{j}^{(1)}(\mathbf{r}') = 2 \sum_{\mu} \left( \left\langle \tilde{\psi}_{\mu}^{(1)} \left| \tilde{\mathbf{J}}^{(0)}(\mathbf{r}') \right| \tilde{\psi}_{\mu}^{(0)} \right\rangle + \left\langle \tilde{\psi}_{\mu}^{(0)} \left| \tilde{\mathbf{J}}^{(0)}(\mathbf{r}') \right| \tilde{\psi}_{\mu}^{(1)} \right\rangle + \left\langle \tilde{\psi}_{\mu}^{(0)} \left| \tilde{\mathbf{J}}^{(1)}(\mathbf{r}') \right| \tilde{\psi}_{\mu}^{(0)} \right\rangle \right), \text{ where} \quad (2.89)$$

$$\tilde{\psi}_{\mu}^{(1)} = \hat{\mathcal{G}}(\epsilon_{\mu}) \tilde{h}_{\text{el}}^{(1)}(\mathbf{r}_i) |\tilde{\psi}_{\mu}^{(0)}\rangle \quad (2.90)$$

is the linear variation of  $\tilde{\psi}_{\mu}^{(0)}$  of the occupied orbital  $\mu$  projected in the empty subspace using the Green-function  $\hat{\mathcal{G}}(\epsilon_{\mu})$  running over all empty orbitals.

Reordering of [equation \(2.89\)](#)'s right hand side terms allows the differentiation between and summation of a bare current term  $\mathbf{j}_{\text{bare}}^{(1)}(\mathbf{r}')$ , a paramagnetic correction term  $\mathbf{j}_{\Delta\text{p}}^{(1)}(\mathbf{r}')$ , and a diamagnetic correction term  $\mathbf{j}_{\Delta\text{d}}^{(1)}(\mathbf{r}')$ . At this point, the foundation is laid to calculate a nucleus' magnetic shielding, at least for finite, comparably small systems like molecules. But for the evaluation in solid state systems and the explicit inclusion of translational invariance via the usage of Bloch functions, further adaptations are necessary. Since the complexity and size of the resulting adapted equations would be beyond the scope of this theory section, the interested reader is referred to the work of Pickard and Mauri [[168](#)].

The inclusion of Bloch functions also forces the inclusion of and/or adaption to  $\mathbf{k}$ -dependent quantities and includes the Green-function  $\hat{\mathcal{G}}(\epsilon_{\mu})$ , the nonlocal potential  $V_A^{\text{nl}}$ , the projector functions  $|\tilde{p}_{A\kappa}\rangle$ , and the first part of the current operator  $\tilde{\mathbf{J}}(\mathbf{r}')$  in [equation \(2.82\)](#). Taking these adaptations and the translational invariance into account allows the expression of the three first-order current contributions  $\mathbf{j}_{\text{bare}}^{(1)}(\mathbf{r}')$ ,  $\mathbf{j}_{\Delta\text{p}}^{(1)}(\mathbf{r}')$ , and  $\mathbf{j}_{\Delta\text{d}}^{(1)}(\mathbf{r}')$  for periodic systems. With them, the calculation of  $\mathbf{B}_A^{\text{in}}(\mathbf{r}_i)$  (see [equation \(2.77\)](#)) can be done and the subsequent evaluation of  $\sigma_{A,kl}(\mathbf{r}_i)$  via [equation \(2.76\)](#) leads to the desired magnetic shielding of the considered nucleus.

## 2.2 Computational Approaches

This section will give insights into the used approaches within this work by explaining in more detail which assumptions are made, which formulas are used, which models are applied, etc. Thus, it is easier to follow the approaches in this work and to classify and compare the obtained results with respect to their origin.

### 2.2.1 Slab Model

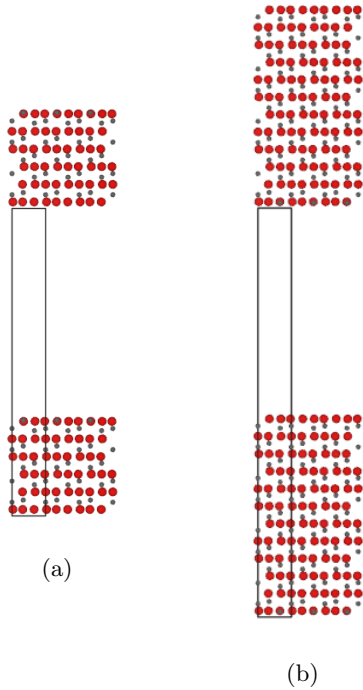


**Figure 2.1:** Optimised slab models for the aluminium terminated (0001) surface cut with 25.5 Å vacuum and varying atomic region thicknesses; (a) 18 atomic layers and (b) 36 atomic layers; gray = aluminium and red = oxygen (VASP-DFT, PBE/PAW, 600.0 eV energy cut-off, D3-BJ).

In order to study the different surface cuts of  $\alpha$ -Al<sub>2</sub>O<sub>3</sub>, the experimentally determined UC of corundum ( $a = 4.76$  Å,  $c = 13.00$  Å, six formula units, and R $\bar{3}$ C space group) is used. To resemble a certain cut and, by association, a certain surface of  $\alpha$ -Al<sub>2</sub>O<sub>3</sub>, the slab model is used. This model uses a sufficiently thick atomic region, where the middle part represents the bulk structure and the top and the bottom parts resemble the surface. Since the two surfaces should only interact with the bulk-like middle part, a vacuum has to be included in the UC.

Otherwise, the periodicity of the calculation would, for example, result in an interaction of the topside surface with the bottomside surface of the above UC. For

each constructed termination, there are two important convergence criteria: the thickness of the vacuum and the thickness of the atomic region.

The different slabs of this crystalline system are generated using the program XCrySDen [170, 171] by selecting the cut, the termination, and the number of layers within the atomic region. Therefore, various atomic region thicknesses (see figure 2.1) for each different termination are generated, and different vacuum thicknesses are added for each structure, resulting in a large variety of slab model UCs. Regarding the slab thickness, the calculations reveal a vacuum of 15 Å to be sufficient to neglect the topside-bottomside interaction. Nonetheless, due to the intention of adsorbing water molecules on the surface and applying the D3-BJ method with a reasonable correction radius of 20 Å, the vacuum thickness is set to 25.5 Å. Regarding the atomic region, two additional properties are important: the symmetry (should provide an inversion centre or a mirror plane) and the stoichiometry (if  $n \in \mathbb{N}$  formula units are present). Focussing on fulfilling the symmetry criterion, the atomic region can provide non-stoichiometric amounts of aluminium and oxygen atoms. Careful testing with combinations of the atomic region thickness and termination, provides the results seen in table 2.1.

**Table 2.1:** Listing of all calculated slabs for different cuts, terminations, and atomic region thicknesses.

Cut	Termination	$n$ $\text{Al}_2\text{O}_3$	# Atomic Layers		
		$n \in \mathbb{N}$	1	2	3
(0001)	Al 1 two other <sup>a</sup>	yes	18	36	54
( $1\bar{1}02$ )	O 1 four other <sup>a</sup>	yes	15	30	45
(11 $\bar{2}3$ )	Al/O 1	yes	18	36	65
	O 1	no	22	40	58
	Al 1	no	26	44	62
	Al 2	yes	42	84	126
	O 2	no	22	40	58
	Al/O 2	no	26	44	62
(11 $\bar{2}0$ )	O 1 five other <sup>a</sup>	yes	20	40	60
(10 $\bar{1}0$ )	O 1	no	20	38	56
	O 2	yes	18	36	54
	Al 1	no	16	34	52
(10 $\bar{1}1$ )	O 1	yes	30	60	90
	Al 1	no	28	58	88
	O 2	no	26	56	86
	Al 2	no	24	54	84
	O 3	no	32	62	92
(22 $\bar{4}3$ )	Al 1	yes	56	112	168
	O 1	no	46	102	158
	Al 2	no	52	108	164
	O 2	no	50	106	162
	O 3	yes	56	112	168
	Al 3	no	46	102	158
	O 4	no	52	108	164
	Al 4	no	50	106	162

<sup>a</sup> due to previous termination investigations of Kurita *et al.* [88], which were conducted with great care, the termination study was not repeated for this surface in this work

### 2.2.2 Surface Energies

To evaluate which of those slabs is sufficiently thick and which termination is the most favourable for the crystalline system, the calculation of the surface energy is needed. In principle, this is done by calculation of the total energy of the slab, subtracting the energy of one bulk-like unit multiplied by its number of occurrence in the slab, and division of this result with the surface area. For  $\alpha$ -Al<sub>2</sub>O<sub>3</sub> a single point calculation (VASP-DFT, PBE/PAW, 600.0 eV energy cut-off, D3-BJ) yields an energy of -232.16 eV per UC, resulting in an energy of -38.69 eV for a bulk-like unit (formula unit). Thus the formulated equation described above would become:

$$E_{\text{surf}} = \frac{1}{2A} (E_{\text{surf}} - n \cdot (-38.396 \text{ eV})). \quad (2.91)$$

Unfortunately, equation (2.91) is only applicable if the slab is stoichiometric but in most presented cases it is not. Thus, equation (2.91) needs to be adjusted. To do so, the energy of  $n$  bulk-like units is set to the sum of all atoms' chemical potentials  $\mu_i$ :

$$E_{\text{surf}} = \frac{1}{2A} \left( E_{\text{surf}} - \sum_i N_i \mu_i \right). \quad (2.92)$$

The challenge of this approach is the correctness of the used chemical potentials  $\mu_i$ , because in principle they are unknown. Nonetheless, there are two boundaries for them, one where the chemical potential of aluminium resembles metallic aluminium, denoted as the aluminium-rich boundary, and one where the chemical potential of oxygen resembles gaseous oxygen, denoted as the oxygen-rich boundary. Therefore, metallic aluminium and gaseous oxygen are calculated at the same computational level to obtain the respective chemical potentials ( $\mu_{\text{Al,Al-rich}} = 4.08 \text{ eV}$  and  $\mu_{\text{O,O-rich}} = 4.40 \text{ eV}$ ). The respectively missing chemical potentials ( $\mu_{\text{O}}$  for an aluminium-rich environment and vice versa) are calculated using  $E_{\text{bulkunit}}$ :

$$E_{\text{bulkunit}} = 2 \cdot \mu_{\text{Al}} + 3 \cdot \mu_{\text{O}}. \quad (2.93)$$

Thus, the resulting four chemical potentials can be used to calculate the surface energies of the plain surfaces at the two different boundaries. Considering the aluminium-rich environment, the sufficient thickness of the atomic region for the different terminations and cuts is in most cases already reached with smallest one. Solely the Al/O 1 termination of  $(11\bar{2}3)$  and the majority of  $(22\bar{4}3)$ 's terminations require the second thickest atomic region to provide converged surface energies, which convergence criteria is set to  $0.01 \text{ eV}/\text{\AA}^2$ .

### 2.2.3 Wulff Plots

A Wulff plot, Wulff construction or Wulff shape represents the equilibrium shape of a crystal. It results from the endeavour of the crystal to minimise its surface Gibbs free energy [172]. By neglecting the temperature and pressure and only considering the electronic energy of the crystal, the result of the following formula needs to be minimised,

$$\Delta E = \sum_i E_{\text{surf},i} A_i, \quad (2.94)$$

where  $A_i$  represents the provided area of the considered surface cut  $i$ . It was hypothesised by Wulff [173] and proven by, for example, Laue [174] that the distance of a certain cut to the crystal's centre is proportional to its  $E_{\text{surf}}$ . Thus starting from a central point, the Wulff plot can be constructed by drawing planes of all surface cuts and their symmetry equivalents at distances equal to constant multiples of their respective surface energies. Finally, the smallest encasing of these planes represents the equilibrium shape of the crystal and, by association, the Wulff plot itself.

### 2.2.4 Surface Scans

To probe the adsorption of water on the different surfaces and, simultaneously, obtaining an adsorption energy surface of it, a reasonable automation is desirable. Thus, two aspects has to probed beforehand: the orientation of the adsorbing water molecule

and its initial distance to the surface. While testing the former, it is revealed that due to the high adaptability of the hydrogen atoms the initial orientation of the adsorbing water molecules plays a very minor role but depends in some cases on the surface sites. Therefore, a fixed orientation can be used, which is only changed if it is needed. Regarding the initial distance of the water molecule to the surface, testing shows that 2.7 Å is a reasonable distance to let the water molecule really advance to the surface without being already too close and preventing the adaptation of the hydrogen atoms. To automate this initial distance to the surface on a rough shape, the initial height of the adsorbing water molecule is determined by the height of surface atoms within a lateral radius of 2.0 Å. On each investigated surface a eleven times eleven grid is laid with equidistant steps along the lateral **UC** vectors *a* and *b*, respectively. Due to periodicity, this resulted 100 grid points per surface. For each grid point a structure optimisation is performed. In order to reduce the computational effort for this large amount of calculations, the atomic regions of the used slabs are cut and the remaining fraction is partially fixed to still resemble the underlying bulk material. Therefore, slabs with a thicker atomic and, by association, a thicker bulk-like region are taken into account. Considering the shifts of the atoms in different atomic layers after the relaxation, those thicker slabs are cut at positions where the resulting new slab has enough atomic layers that have not notably moved, so they still resemble the underlying bulk material reasonably well and can be fixed. During structure optimisations of each grid point, the lateral position of the water's oxygen atom is fixed. After each calculation, the adsorption energy is computed:

$$E_{\text{ads}} = E_{\text{slab}+\text{H}_2\text{O}} - E_{\text{slab}} - E_{\text{H}_2\text{O}}. \quad (2.95)$$

To effectively visualize the corresponding adsorption energy surfaces, the results for a **UC** are used to build a virtual  $2 \times 2 \times 1$  **SC**. Thus, the **UC** crossings do not interrupt the depiction, and by association, the interpretation becomes easier.



### 2.2.5 Analysis of Ice Structures

The search for structure motifs in the different ice phases is done via the following scheme. At first the structure of the corresponding phase is examined for larger structure motifs like helices, chains of rings, penetrated rings or simply “eye-catching” structural abnormalities or peculiarities. This is done by hand and careful screening of the structure. Once this is done, the second step focuses on locating rings, which are formed within the structural network of the considered ice phase. This is done computer-assisted by applying a similar approach as the one used by Herrero *et al.* [175] who also investigated the different possible ring sizes in ice phases. Both, Herrero’s and the approach used for this work, require each oxygen atom of the water molecule to be fourfold coordinated. Thus, each water molecule has to donate two hydrogen bonds and accept two hydrogen bonds at the same time. Those restrictions are also known as the ice rules. The difference of both approaches is that for this work not only the size of the found rings is important, but also the actual structure. Furthermore, in this work the found structure motifs will be compared to the networks formed by the adsorbed water molecules on the  $\alpha$ -aluminium oxide surfaces. Hence, some restrictions have to be changed. Since the amount of adsorbed water will be very small compared to an actual ice phase, bridging of larger rings is unlikely to occur. For Herrero’s investigation the prevention of finding rings, which can be cut short by such bridges, was an important issue, but in this work it is not. On the other hand, without this restriction the amount of possible ring shapes and sizes increases dramatically. Thus, this work does not neglect this restriction but simplifies it. While the original restriction searched for all possible sizes of short cuts, only short cuts via a single water molecule are considered here. Therefore, the approach of this work and Herrero’s provide the same results for ring sizes until seven, while for higher ring sizes the former reveals more possible ring structures.

The third step includes the comparison of all found ring structures with each other, in order to eliminate redundancies. This is first done computer-assisted and in a refined round by hand. While the first round purges multiples as well as mirrored ring structures, the second round is necessary to prevent very slight distortions to result in double occurrences.

For the visualisation of the different structure motifs of the ice phases, the larger structure motifs are shown independently and/or within a larger representation of their respective ice phase. Considering the different ring structures, however, their visualisation requires conventions for their depiction. Thus, the following rules will be tried to follow:

- maximise the amount of water molecules in the transverse plane of the depiction
- minimise crossing of bonds
- try to make all bonds visible
  - ⇒ prevent them from being hidden by oxygen atoms
- tilt traverse plane reasonably
  - ⇒ enough to comply with rules, while remaining a clear traverse plane
- disregard all rules if there is a more clear way to depict the ring structure

## 2.3 Computational Details

The calculations of the periodic total energies utilise the framework of Kohn-Sham DFT [74, 75]. Ion-electron interactions are treated by the PAW approach [163, 176] as implemented in the VASP [177–181]. Non-classical electron-electron interactions are treated by applying the GGA with the PBE [143–145] functional. The influence of dispersion corrections is studied by utilising the D3-BJ-method [76–79]. Brillouin zones are sampled with suitable k-point grids (see table A.1, table A.2 and table A.8) based on the Monkhorst-Pack scheme [158]. Optimisations are done by applying the residual minimisation method with direct inversion in the iterative subspace (RMM-DIIS) [182, 183] together with the tetrahedron method with Blöchl corrections [184]. Sufficient accuracy of 1 meV for the total energy is obtained with an energy cut-off of 500.0 eV for bulk calculations and 600.0 eV for surface calculations. The convergence criteria are set to  $10^{-5}$  eV for the electronic self-consistent field procedure, while the ionic relaxation is stopped when acting forces on ions decrease below 0.01 eV/Å. For the more detailed investigations of the structures, like calculation of  $\Gamma$ -point phonon frequencies and calculation of NMR shielding constants, the thresholds for the structure optimisations are adjusted to an energy cut-off of 600.0 eV for bulk structures, an electronic convergence criteria of  $10^{-7}$  eV, and an ionic convergence criteria of 0.001 eV/Å. For the calculation of the  $\Gamma$ -point phonon frequencies the method of Methfessel-Paxton [185] with a smearing parameter of 0.05 eV is used. The calculations of the NMR shielding constants are performed with an electronic convergence criteria of  $10^{-10}$  eV and by using the linear response method [168, 169, 186, 187]. Shieldings are referenced to  $[\text{Al}(\text{OH}_2)_6]^{3+}$  and  $\text{CCl}_3\text{F}$ , respectively, which are calculated at the same computational level in a 30 Å cubic UC, to obtain the chemical shifts  $\delta$ .

Bulk structures are relaxed by a step by step coarse to fine optimisation of the lattice constants while the internal coordinates are optimised for each set of lattice constants.

This procedure minimises the energy by ionic relaxations during consecutive and individual variation of the lattice constants. E.g., the lattice constants  $b$  and  $c$  are kept constant while the value of  $a$  is varied within a given range around its starting value. The value resulting in the lowest energy is taken and kept constant together with  $c$  to check different values of  $b$  and so on. This procedure is repeated while the ranges become finer and finer until the values for the three lattice constants do not change any more. For the surface structure optimisations the cell shape and the cell volume are fixed while ions are allowed to relax. Structure depictions and Wulff plots are obtained by using VESTA [188].

## Chapter 3

### Structure-Stability-Relation Parameters

In order to quantify the structure at hand, different parameters were introduced to describe certain structure characteristics in corresponding values. Some of those parameters' descriptions were already presented in an earlier work based on a research internship in the group of Prof. Dr. Beate Paulus [189]. For simplicity and a better understanding, those definitions are presented here as well and are marked accordingly.

#### 3.1 Distortion of Cation Coordination Spheres [189]

The distortion parameter describes the mean percentage deviation of the first aluminium coordination sphere (CS)s from their corresponding ideally shaped ones for a given structure, with its related fluoride arrangement. In other words, it shows how strongly a tetrahedron is distorted in comparison to a perfect tetrahedron, for example.

At first, the **CN** of a given aluminium cation is determined by the number of fluoride and oxide/hydroxide ions within a radius of  $2.4 \text{ \AA}$  ( $\approx \frac{5}{4} \cdot d(\text{Al-O})$  in  $\text{Al}_2\text{O}_3$  ( $\approx 1.9 \text{ \AA}$ ) and  $\approx \frac{4}{3} \cdot d(\text{Al-F})$  in  $\text{AlF}_3$  ( $\approx 1.8 \text{ \AA}$ )). Afterwards, the shape of the **CS** has to be determined because of the most probable **CNs** (four, five, and six) provide two prominent representatives each. They can be distinguished utilising the angles present in the given **CS**. The used selection criteria are shown in [table 3.1](#), which was taken from the supporting information of the previous work [189].

**Table 3.1:** Selection criteria for choosing the best fitting ideal CS for the considered aluminium CS based on the combination of ideal angles' appearances present.

CN	CS	Ideal Angles $\alpha_{\text{nominal}}(A)$					Criteria
		90°	109.47°	120°	135°	180°	
4	tetrahedral	-	6	-	-	-	$6 \cdot (90^\circ < \alpha < 130^\circ)$
	sq. planar	4	-	-	-	2	$2 \cdot (150^\circ < \alpha)$
5	trig. bi-pyramidal	6	-	3	-	1	$1 \cdot (150^\circ < \alpha)$
	sq. pyramidal	8	-	-	-	2	$2 \cdot (150^\circ < \alpha)$
6	octahedral	12	-	-	-	3	$3 \cdot (150^\circ < \alpha)$
	trig. prismatic	9	-	-	6	-	$6 \cdot (115^\circ < \alpha < 155^\circ)$

During the determination of the CS, the nominal values for the occurring angles  $\alpha_{\text{nominal}}(A)$  are set as well. In order to get the nominal value for the distance  $d_{\text{nominal}}(A)$  between the cation  $A$  and the anions  $a$ , the average distance of the anions to the central cation  $A$  is calculated:

$$d_{\text{nominal}}(A) = \frac{1}{n_a} \sum_a d_{Aa}. \quad (3.1)$$

Subsequently, the percentage distortion  $dist(A)$  of the considered cation  $A$  is calculated by averaging the percentage deviations of the angles  $\alpha_{aAb}$  and distances  $d_{Aa}$  within the given CS of  $A$ :

$$dist(A) = \frac{1}{n_\alpha + n_d} \left( \sum_a \sum_b \left| \frac{\alpha_{aAb}}{\alpha_{\text{nominal}}} - 1 \right| + \sum_a \left| \frac{d_{Aa}}{d_{\text{nominal}}} - 1 \right| \right), \quad (3.2)$$

where  $n_\alpha$  and  $n_d$  denote the amount of angles and distances in the given CS of  $A$ .

Afterwards, the obtained results for each CS present in the given structure  $i$  are averaged over all occurring aluminium ions' CSs to get a single value describing the distortion in the considered structure  $dist(i)$ :

$$dist(i) = \frac{1}{n_A} \sum_A dist(A). \quad (3.3)$$

To allow the comparison of different parameters and take the possibility of a pre-existing distortion into account as well, the  $dist(i)$  values are normalised to the range of all results for the corresponding crystalline system:

$$D_{\text{dist}}(i) = \frac{dist(i) - dist_{\text{MIN}}}{dist_{\text{MAX}} - dist_{\text{MIN}}}, \quad (3.4)$$

where  $D_{\text{dist}}(i)$  finally represents the normalised parameter describing the distortion of cation CSs within a given structure  $i$  of the corresponding crystalline system with its related fluoride arrangement.

### 3.2 Symmetry after Relaxation [189]

The symmetry of a crystalline system is a crucial property in describing it and is also intuitively linked to the stability of such systems since a higher symmetry indicates a higher long range order. Since the fluorination of the different crystalline systems often results in a decrease of the symmetry of those systems, the quantification of such a symmetry loss is essential to relate the newly formed structure and its fluoride arrangement to its stability.

In order to do so, the remaining symmetry elements of the corresponding crystalline system after fluorination and relaxation of the given structure  $i$  are evaluated. Afterwards, the amount of remaining symmetry elements  $sym(i)$  is divided by the amount of symmetry elements before the fluorination  $sym_{\text{MAX}}$  to get the percentage amount of symmetry still present after the substitution and relaxation:

$$D_{\text{sym}}(i) = \frac{sym(i)}{sym_{\text{MAX}}}, \quad (3.5)$$

which directly gives the comparable parameter  $D_{\text{sym}}(i)$  that describes the remaining symmetry in a given structure  $i$  of the corresponding crystalline system with its related fluoride arrangement.

### 3.3 Charge Centre Deviation [189]

This parameter describes the average charge distribution within the CSs of a given structure and its related fluoride arrangement. More precisely, the amount of displacement of the negative charge centre  $\vec{r}_{\text{neg}}$  of the CS towards its positive charge centre  $\vec{r}_A$  is evaluated. While the position of the latter is simply given by the position of the aluminium ion  $A$ , the former has to be calculated. This is done in analogy to the evaluation of the centre of mass, where the formal charges  $q_a$  for fluoride(1-), oxide(2-), and hydroxide ions(1-) are used to replace the masses:

$$\vec{r}_{\text{neg}}(A) = \frac{\sum_a q_a \cdot \vec{r}_{a,A}}{\sum_a q_a}. \quad (3.6)$$

Subsequently, the distance of both charge centres  $char(A)$  is calculated:

$$char(A) = |\vec{r}_A - \vec{r}_{\text{neg}}| \quad (3.7)$$

and averaged over all CSs of a given structure  $i$ :

$$char(i) = \frac{1}{n_A} \sum_A char(A). \quad (3.8)$$

Again, this parameter provides the possibility of a pre-existing deviation of the two charge centres of each CS. To consider this eventuality and in order to make this parameter comparable with other parameters, it is normalised to the range of all obtained  $char(i)$  for the corresponding crystalline system:

$$D_{\text{char}}(i) = \frac{char(i) - char_{\text{MIN}}}{char_{\text{MAX}} - char_{\text{MIN}}}, \quad (3.9)$$

where  $D_{\text{char}}(i)$  now stands for the normalised description of the average charge distribution of all CSs of a given structure  $i$  of the corresponding crystalline system with its related fluoride arrangement.



### 3.4 Homogeneity of the Fluoride Arrangement [189]

To tackle the importance of a homogeneously distributed fluoride arrangement, this parameter takes into account the stoichiometry and the formation of clusters and planes, containing only fluoride ions, for a predetermined region within a given structure and its related fluoride arrangement. The mentioned regions are centred around a selected fluoride ion  $A$ . There are three of them for each fluoride ion  $A$  to represent three different ranges  $\mathbf{s}$ . This opens up the possibility to analyse the effect of distance on this parameter. The first considered region ( $\mathbf{s} = 1$ ) is a sphere with the radius  $3.6 \text{ \AA}$  ( $2 \cdot d(\text{Al-F})$ ), the second ( $\mathbf{s} = 2$ ) covers the spheric shell with the radius ranging from  $3.6 \text{ \AA}$  to  $5.4 \text{ \AA}$ , and the third one ( $\mathbf{s} = 3$ ) describes the next spheric shell from  $5.4 \text{ \AA}$  to  $7.2 \text{ \AA}$ . Thus, this parameter is split in three single parameters, which are calculated in the same way, but represent three different regions  $\mathbf{s}$ .

Firstly, the stoichiometry within the considered region should be as close as possible to the stoichiometry of the corresponding structure  $i$ . Therefore, the preferably small difference of the percentage fluoride amount in both, the region and the structure, is calculated (please note that this is a slight adjustment of the formula given in the supporting information of the previous work [189]):

$$\text{stois}(A) = \frac{n_{\text{F}}}{n_{\text{F}} + n_{\text{O}}} - \frac{n_{\text{F},\mathbf{s}}}{n_{\text{F},\mathbf{s}} + n_{\text{O},\mathbf{s}}} . \quad (3.10)$$

Secondly, the possible formation of fluoride clusters is evaluated by calculating the preferably high average distance  $\bar{r}_a(A)$  of all fluoride ions  $a_{\text{F}}$  surrounding the considered fluoride ion  $A$  in the looked at region  $\mathbf{s}$ :

$$\bar{r}_a(A) = \frac{1}{n_{a_{\text{F}}}} \sum_{a_{\text{F}}} d_{Aa_{\text{F}}} . \quad (3.11)$$

The evaluation of possible fluoride planes within the structure is done by calculation the root mean square deviation of the three space coordinates  $x, y$ , and  $z$  of all fluoride

ions  $a_F$  surrounding the considered fluoride ion  $A$  in the looked at region  $\mathbf{s}$ . This is shown exemplarily for the x coordinate here:

$$RMSDs_{\mathbf{s}_x}(A) = \sqrt{\frac{1}{n_{a_F}} \sum_{a_F} (x_{a_F})^2}, \quad (3.12)$$

which results in higher values, if no fluoride plane is present perpendicular to that space coordinate.

Combining the stoichiometry, the possible clustering, and possible formation of planes of fluoride ions results in the description of the parameter  $homs(A)$  for the homogeneity of the fluoride distribution around a given fluoride ion  $A$  in a looked at region  $\mathbf{s}$ :

$$homs(A) = \frac{stois(A)}{RMSDs_{\mathbf{s}_x}(A) \cdot RMSDs_{\mathbf{s}_y}(A) \cdot RMSDs_{\mathbf{s}_z}(A) \cdot \bar{r}_a(A)}. \quad (3.13)$$

Now those  $homs(A)$  values are averaged over all fluoride ions  $A$  of a given structure  $i$  to be condensed in a single value  $homs(A)$  per region  $\mathbf{s}$ :

$$homs(i) = \frac{1}{n_A} \sum_A homs(A). \quad (3.14)$$

For the comparison with other parameters, the resulting three parameters, representing three different regions  $\mathbf{s}$ , are normalised to the maximal occurring value of their respective region's  $homs(i)$  for the corresponding crystalline system:

$$D_{homs}(i) = \frac{homs(i)}{homs_{MAX}}, \quad (3.15)$$

where  $D_{homs}(i)$  now represents the normalised description of the fluoride distribution's homogeneity for a given structure  $i$  of the corresponding crystalline system with its related fluoride arrangement in the considered region  $\mathbf{s}$ .

### 3.5 Hydrogen Bonding

This parameter or, to be more precise, this set of parameters quantify the amount and strength of hydrogen bonds for a given structure and its related fluoride arrangement. To do so, two different aspects are considered. Firstly, the anion to which the hydrogen binds and secondly the length of this hydrogen bond, which correlates with the strength of the corresponding hydrogen bond. Therefore, there are four parameters resulting from these considerations. The first segmentation of the four parameters takes the different anionic species into account while the second one provides two different ranges of hydrogen bond lengths to provide a separation into stronger and weaker hydrogen bonds. The two mentioned regions are set to bond lengths of 1.15 Å to 2.00 Å for stronger hydrogen bonds and 2.00 Å to 3.00 Å for weaker hydrogen bonds.

To quantify the hydrogen bonding in the fluorinated systems, each anion  $a$  is considered independently concerning two different aspects at the same time. One is the amount of possible hydrogen bonds  $n_{\text{H},a}$  connected to the considered anion  $a$  while the other is the distance of such a bond  $d_{\text{H},a}$ . Assuming that  $n_{\text{H},a}$  should favour higher amounts and  $d_{\text{H},a}$  should favour smaller values, the influence of hydrogen bonding  $hbs(a)$  to this anion  $a$  in the considered region  $\mathbf{s}$  is calculated by:

$$hbs(a) = \frac{n_{\text{H},a}}{\sum_{\text{H}} d_{\text{H},a}}. \quad (3.16)$$

To get the corresponding  $hbs(i)$  of a given anion species  $a$  for a given structure  $i$  and the considered region  $\mathbf{s}$ , those single values are added up and weighted with its SC coefficients  $ma$ ,  $mb$ , and  $mc$ :

$$hbs_{\mathbf{s}_a}(i) = \frac{4}{m_1 \cdot m_2 \cdot m_3} \cdot \sum_a hbs(a), \quad (3.17)$$

where  $hbs(i)$  now represents the hydrogen bonding of a given structure  $i$  in its largest considered SC of the corresponding crystalline system.

To make sure the four parameters are comparable with the other ones, they are normalized to the range of the  $hbs(i)$  values of the corresponding crystalline system:

$$D_{hbs_a}(i) = \frac{hbs_a(i) - hbs_{a,MIN}}{hbs_{a,MAX} - hbs_{a,MIN}}, \quad (3.18)$$

where  $D_{hbs_a}(i)$  describes the hydrogen bonding to the considered anionic species  $a$  for a given structure  $i$  in its largest SC representation of the corresponding crystalline system with its related fluoride distribution in the considered region  $s$ .

### 3.6 Slice/Layer Distances

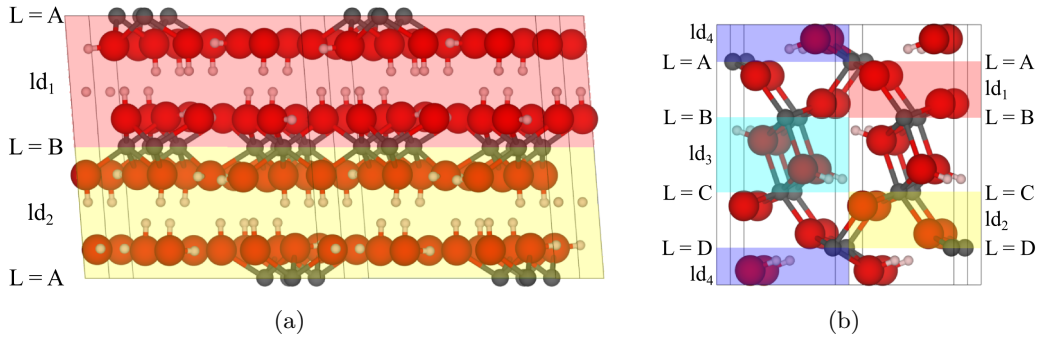


**Figure 3.1:** Depictions of the considered linked layer distances; (a) aluminium hydroxide representative gibbsite with the aluminium layers ( $L$ ) and the linked distances of red and yellow and (b) aluminium oxhydroxide representative diaspore with the aluminium layers ( $L$ ) and the linked distances of blue and light blue (oxide slice distance) and red and yellow (hydroxide slice distance) - gray = aluminium, red = oxygen, and white = hydrogen.

Taking the sliced structure of the considered crystalline systems into account, this parameter or, more specifically, those two parameters quantify the homogeneity of the distribution of those slices within the corresponding structure and its related fluoride distribution. In other words, they quantify the deviation of two distances describing the space between two slices of the same nature. To explain this in more detail, figure 3.1 shows the aluminium hydroxide gibbsite (figure 3.1(a)) and the aluminium oxhydroxide diaspore (figure 3.1(b)) to visualize the slice distances and their connections.

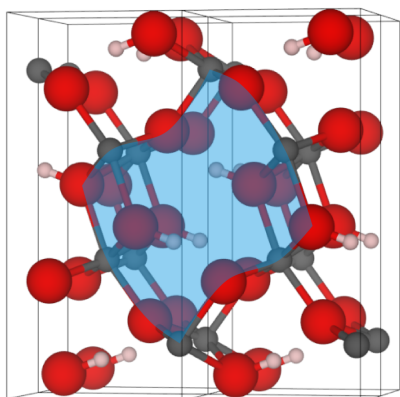


**Figure 3.2:** Illustration of the “wafting rectangular” shaped building blocks (light blue) in diaspore - gray = aluminium, red = oxygen, and white = hydrogen.

As it was already seen from [figure 1.1](#) and in [figure 3.1](#) as well, diaspore is the only considered crystalline system which lacks a clear sliced structure. Nonetheless, its region of hydrogen bonding is as important for the stability of this crystalline system as it is for the other ones.

Diaspore is made from “wafting rectangular” shaped building blocks, as seen in [figure 3.2](#). Within those blocks, the hydrogen bonds are essential to keep the

concave shape of the longer edges of this “rectangle”. Since those building blocks are heavily influenced by the hydrogen bonding, the regions on top and at the bottom of those hydroxide regions are, by analogy with the other crystalline systems, considered as slices as well.

Now, only one more definition has to be made which is important for the aluminium oxohydroxides. It concerns the two regions of differently charged anions. In boehmite and diaspore distinct regions are present which only contain oxide or hydroxide/fluoride ions. Therefore, those regions are also defined as slices, because both are influenced differently by the fluorination degrees. While the hydroxide slices are influenced directly, the oxide slices are only influenced indirectly via the resulting structural change of the aluminium CSs.

Taking those considerations into account, the definition of the different slice distances in [figure 3.1](#) can be tracked easily. The slices are represented by their corresponding aluminium layers. For the aluminium oxohydroxides, represented by diaspore ([figure 3.1\(b\)](#)), there are two sets of those linked distances. The first links the two distances of one oxide slice to the other (blue and light blue), coincidentally, the second does so as well by considering the hydroxide slices (red and yellow). In

case of the aluminium hydroxides, represented by gibbsite (figure 3.1(a)), simply the distance (red) of slice **A** to slice **B** is linked to the slice distance (yellow) of **B** to , due to periodicity, **A** again.

To quantify the homogeneity of the slice distribution within the related structure, firstly, the height  $\bar{h}_{\mathbf{L}}$  of the slices is defined. This is done via the averaged height  $z_A$  of the aluminium layer **L**'s ions, where the slices are centred at (aluminium hydroxides) or by the averaged heights  $z_A$  of the aluminium ions defining the top and the bottom aluminium layers **L** of the slices (aluminium oxohydroxides), respectively:

$$\bar{h}_{\mathbf{L}} = \frac{1}{n_{\mathbf{Al},\mathbf{L}}} \sum_A z_{A,\mathbf{L}}, \quad (3.19)$$

where **L** represents the aluminium layers **A**, **B**, **C** and **D**, respectively.

Those heights are then used to calculate the considered values  $ld_{1/2}$  for the hydroxide slice distances and  $ld_{3/4}$  for the oxide slice distances. Subsequently, those distances serve to calculate the slice distance parameters  $lds(i)$  for the considered links **s** (**s** = 1 for oxide slice distances; **s** = 2 for hydroxide slice distances) and a given structure *i*:

$$lds(i) = \left( 1 + \frac{\Delta ld}{ld_{k/1}} \right) \cdot \frac{ld_k + ld_l}{2}, \quad (3.20)$$

where the denominator within the brackets is always the larger one of both distances, to ensure a consistent evaluation of this parameter.

Thus, equation (3.20) combines the need of similar distance values, e.g. a small percentage deviation between the linked distances, and rates the actual value of this distance as well. Under perfect conditions, the percentage close to zero while the actual distances should be reasonable small to increase the slice to slice interactions.

Since the comparability of those possibly two parameters to the other ones is very important for their correct weighting, the  $lds(i)$  are normalised to the range of them for the corresponding crystalline system to also take the need of certain minimum distances into account:

$$D_{lds}(i) = \frac{lds(i) - lds_{MIN}}{lds_{MAX} - lds_{MIN}}, \quad (3.21)$$

where  $D_{lds}(i)$  now describes the homogeneity of the slices' distribution of a certain species  $s$  (oxides/hydroxides) within a given structure  $i$  of the corresponding crystalline system with its related fluoride arrangement.

### 3.7 Slice Stoichiometry

A second parameter concerning the sliced structure quantifies the possibility of different stoichiometries regarding the slices and their connection regions for a given structure and its related fluoride arrangement. Therefore, two different regional aspects  $s$  are defined. One comprises the region of hydrogen bonding  $r_{1/2}$  for  $s = 1$  while the other one contains the actual slices  $R_{1/2}$  for  $s = 2$ . As it can be seen in figure 3.3, the different regional aspects occur twice per crystalline system. Thus, the regions describing the same aspect are linked to each other. For a comparably homogeneous structure the two regions should be as similar as possible to each other, and therefore, the stoichiometric deviation of the two linked regions should be very small.

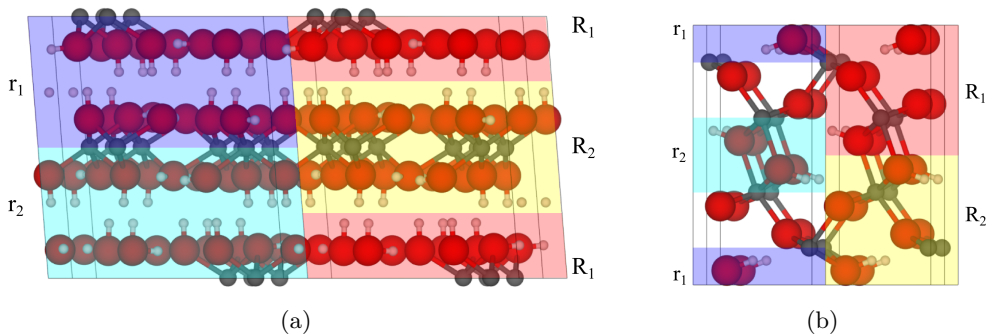


**Figure 3.3:** Depictions of the considered linked slice stoichiometries; (a) aluminium hydroxide representative gibbsite with the linked regions blue-light blue (hydrogen bonding region) and red-yellow (slice region) and (b) aluminium oxhydroxide representative diaspore with the linked regions blue-light blue (hydrogen bonding region) and red-yellow (slice region) - gray = aluminium, red = oxygen, and white = hydrogen.

Hence, the numbers  $n_{a,\mathbf{s}}$  of the anions  $a$  concerning a given regional aspect  $\mathbf{s}$  are used to evaluate the deviation of the related linked regions' percentage stoichiometry (here  $\mathbf{r}_1$  and  $\mathbf{r}_2 \Rightarrow \mathbf{s} = \mathbf{1}$  as an example) for the considered structure  $i$ :

$$reg\mathbf{1}(i) = \left| \frac{n_{\mathbf{F},\mathbf{r}_1}}{n_{\mathbf{F},\mathbf{r}_1} + n_{\mathbf{OH},\mathbf{r}_1}} - \frac{n_{\mathbf{F},\mathbf{r}_2}}{n_{\mathbf{F},\mathbf{r}_2} + n_{\mathbf{OH},\mathbf{r}_2}} \right|. \quad (3.22)$$

To be comparable with the other parameters, these two parameters are normalized as well to the maximum of the obtained values of  $reg\mathbf{s}(i)$  of the considered underlying crystalline system:

$$D_{reg\mathbf{s}}(i) = \frac{reg\mathbf{s}(i)}{reg\mathbf{s}_{MAX}}, \quad (3.23)$$

where  $D_{reg\mathbf{s}}(i)$  finally describes the deviation of the percentage stoichiometry of a considered regional aspect  $\mathbf{s}$  for the considered structure  $i$  of the corresponding crystalline system with its related fluoride arrangement.



# Chapter 4

## Results

### 4.1 Aluminium (oxo)hydroxides

This section focuses on the bulk structures of several aluminium hydroxides and aluminium oxohydroxides (see [figure 4.1](#)) and how the inclusion of fluoride doping affects them. As examples for the former gibbsite [80], bayerite [82], and doyleite [81] are taken while diaspore [83] and boehmite [84] will represent the latter. Despite resembling different atom compositions, the aluminium hydroxides and boehmite share a notable property; all of them provide sliced structures. Those slices consist of ionically bound, edge-sharing, and octahedrally coordinated aluminium centres, which are then connected via hydrogen bonding to the next slice. Although diaspore does not provide such a sliced structure, its structure features markable motifs containing hydrogen bonds as well. They seem to play a major role in the rigidity of the edge- and corner-sharing as well as octahedrally coordinated aluminium centres's interconnections (see [figure 3.2](#) section 3.6 [Slice/Layer Distances](#)).

The first analysis focuses on the correctness and reliability of the [D3-BJ](#)-method for its use in the solid state calculations. Therefore, the previously mentioned aluminium (oxo)hydroxides with and without dispersion correction are studied and their resulting lattice constants are compared with experimental data as well as their thermodynamic stability with earlier theoretical and experimental results, which can be seen in [table 4.1](#) and [table 4.2](#).

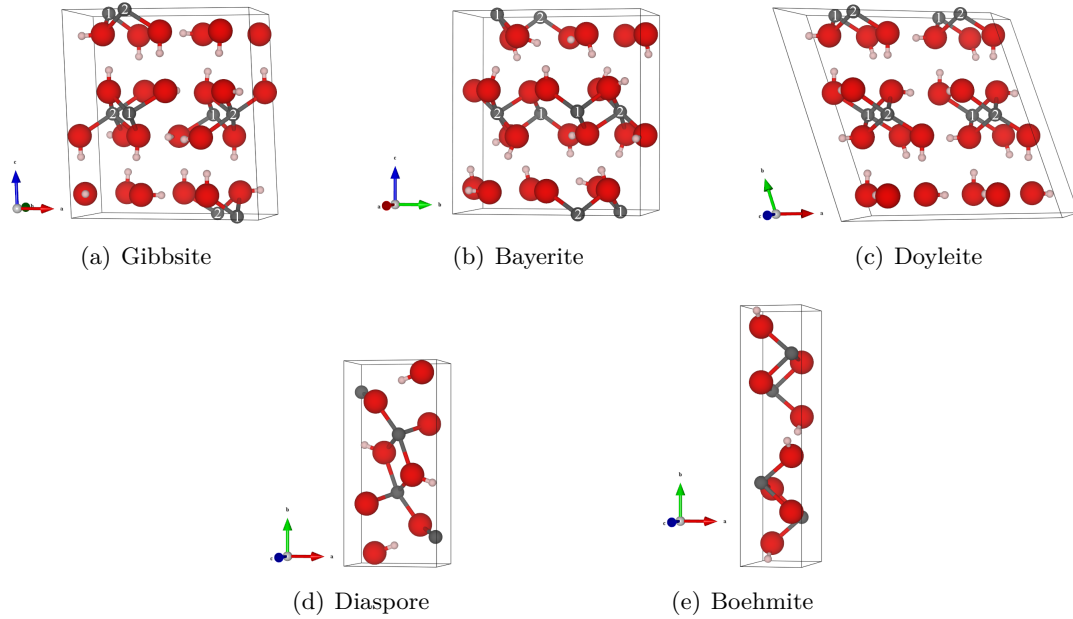


**Figure 4.1:** UC representations of the optimised structures for the three considered aluminium hydroxides (top row) and the two studied aluminium oxhydroxides (bottom row); white numbers for equivalent aluminium ions — if needed - gray = aluminium, red = oxygen, and white = hydrogen (VASP-DFT, PBE/PAW, 600.0 eV energy cut-off, D3-BJ).

By taking a look at the first table, it can be seen that calculations without dispersion correction result in a slightly better agreement with experimental data. Those calculations provide longer as well as shorter lattice vectors compared to experiment while they seem to prefer longer ones. Computations utilising D3-BJ yield in smaller lattice constants due to the fact that they tend to overestimate the binding energy in solids [190–192]. This is especially true in the cases of the aluminium hydroxides and boehmite since their sliced structures heavily rely on the hydrogen bonding between those slices. That is why for these crystalline systems the underestimation of the lattice constants is highest for the lattice vector in whose direction the slices stack (see table 4.1).

Comparing the ground state energies, thus the thermodynamic stability, of the considered five crystalline structures (see table 4.2), it can be seen that calculations with D3-BJ not only provide consistent stability rankings with experimental data found by

**Table 4.1:** Comparison of lattice constants after the optimisation procedure with experimentally obtained lattice constants and the corresponding average error (VASP-DFT, PBE/PAW, 600.0 eV energy cut-off(, D3-BJ)).

Structure		Cell Constants			Error		
		a [Å]	b [Å]	c [Å]	a [%]	b [%]	c [%]
Gibbsite [80]	exp.	8.684	5.078	9.736			
	w/ D3	8.650	5.038	9.527	-0.4	-0.8	-2.1 <sup>a</sup>
	w/o D3	8.810	5.100	9.700	1.5	0.4	-0.4
Bayerite [82]	exp.	5.096	8.729	9.489			
	w/ D3	5.039	8.673	9.241	-1.1	-0.6	-2.6 <sup>a</sup>
	w/o	5.110	8.800	9.560	0.3	0.8	0.8
Doyleite [81]	exp.	5.000	5.168	4.983			
	w/ D3	5.083	5.105	4.880	1.7	-1.2	-2.1 <sup>a</sup>
	w/o D3	5.170	5.200	4.970	3.5	0.6	-0.3
Diaspore [83]	exp.	4.401	9.421	2.845			
	w/ D3	4.378	9.430	2.849	-0.5	0.1	0.2
	w/o D3	4.430	9.500	2.870	0.7	0.8	0.9
Boehmite [84]	exp.	2.880	12.205	3.761			
	w/ D3	2.871	11.913	3.717	-0.3	-2.4 <sup>a</sup>	-1.2
	w/o D3	2.890	12.170	3.740	0.4	-0.3	-0.6

<sup>a</sup> lattice vector in whose direction the slices stack

Hemingway and *et al.* [193], but it also provides very well agreeing relative energies per formula unit. Regarding the calculations without D3-BJ, they also provide relative energies per formula unit in the correct range but can not resemble the correct ranking for the aluminium oxohydroxides. Both findings coincides with previously done theoretical calculations [194, 195].

Although not perfect in terms of lattice constants, D3-BJ is essential for getting the relative stability of the aluminium oxohydroxides and aluminium hydroxides right. Additionally, the worse agreement with experimental data regarding the lattice constants is still acceptable. Including vdW interaction is a conceptually more advanced method than bare DFT. Therefore it is used in further calculations, although, the lattice constants are somewhat too small. Taking everything into account, D3-BJ is the go to choice while keeping in mind the slight overestimation of hydrogen bonding.

**Table 4.2:** Comparison of the thermodynamic stability per formula unit obtained in this work, with and without dispersion correction, with previously obtained stability of experimental results (VASP-DFT, PBE/PAW, 600.0 eV energy cut-off(, D3-BJ)).

Stability	this work w/ D3		this work w/o D3		Experiment [193]	
	$E_{\text{rel}}$ [eV]		$E_{\text{rel}}$ [eV]		$H_{\text{rel}}$ [eV]	
1.	0.00	Gibbsite	0.00	Gibbsite	0.00	Gibbsite
2.	0.02	Doyleite	0.04	Doyleite	0.04	Doyleite
3.	0.05	Bayerite	0.06	Bayerite	0.05	Bayerite
1.	0.00	Diaspore	0.00	Boehmite	0.00	Diaspore
2.	0.04	Boehmite	0.02	Diaspore	0.04	Boehmite

**Table 4.3:** Comparison of the calculated NMR  $^{27}\text{Al}$  shifts (all cations are octahedrally coordinated) to previously obtained results - (1) and (2) denote symmetrically inequivalent aluminium centres.

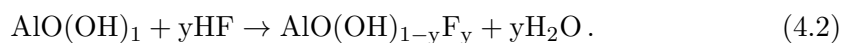
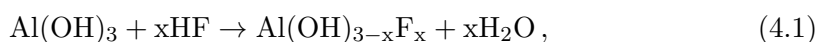
Crystalline System	This Work		Experimental $\delta$ [ppm]		
	[ppm]	Isobe [196]	Damodaran [197]	Slade [198–200]	
Gibbsite(1)	21.5	9.5	17.2	6.0	6.9
Gibbsite(2)	19.3	6.5	11.6		
Bayerite(1)	22.4	11.5	13.1	8.3	8.8
Bayerite(2)	22.6	10.0	9.1		
Diaspore	20.8				
Boehmite	17.6	9.5	12.6	3.4	6.7

Focusing on the validation of the calculated  $^{27}\text{Al}$  NMR shifts (referenced against  $[\text{Al}(\text{OH}_2)_6]^{3+}$ ), the obtained results are compared to experimentally [196–201] and theoretically [202, 203] obtained NMR shifts. This comparison can be seen in table 4.3 while there is also a work which provides values of 7-9 ppm for all crystal structures [201]. Single values for diaspore of 8.2 ppm [204] and for boehmite of 9.0 ppm [205] can also be found in the literature. The experimental results differ significantly from each other due to different frequencies (resonance detection) from 78.2 MHz to 165.4 MHz, spin frequencies (probe spinning) ranging from 4 kHz to 35 kHz, and magnetic flux densities from 7.1 T to 14.1 T. The varying experimental set-ups make a comparison or even a validation of the theoretically calculated shifts quite difficult even if only

the NMR shift differences are compared. Comparing the results of this work with the previously obtained theoretical NMR shifts [202, 203], the agreement for gibbsite is exceptionally good ( $\delta(\text{Al}(1)) - \delta(\text{Al}(2)) = \Delta\delta = 2.2$  ppm compared to 2.2 ppm in this work) while for boehmite the results ( $\Delta\delta = -0.9$  ppm compared to -1.7 ppm in this work; against gibbsite(2)) are quantitatively off but qualitatively correct. In agreement with the most recent experiments [196, 197], gibbsite provides a slightly smaller NMR shift for the second aluminium site than for the first aluminium site (see figure 4.1(a) while for bayerite the two NMR shifts for the different aluminium sites are nearly equal, as it was shown in the experiment of Isobe and *et al.* [196] as well. Due to the lack of consistency in experimental results, we rely on the quality of the theoretical data and being aware of that the absolute shifts might be off but qualitatively correct. Thus, trends within the aluminium crystals should be possible to identify and reproducible.

#### 4.1.1 Fluorinated Aluminium (oxo)hydroxide Structures

The fluorination of the different crystalline systems is done by exchanging hydroxide groups with fluoride ions following one of those two reaction formulas:



Since those two exchanged ions are isoelectronic and provide the same charge per coordination site, the structural adaptation is comparably small and reconstruction is unlikely. This provides a good possibility for comparison and analysis of structures with differently amounts of fluoride ions.

The fluoride amounts  $x$  and  $y$  are varied to resemble different fluorination degrees and to systematically increase them from  $x, y = 0$  to  $x = 0.25$  ( $x = 0.5$  for doyleite

only) and  $y = 0.5$ . Thus, the exchanged fluoride ions still resemble defects within the crystalline structure while the computational costs remain at convenient values. For each crystalline system eight fluorination degrees and SCs up to  $2 \times 1 \times 2$  (for the hydroxides) and  $2 \times 2 \times 1$  (for the oxohydroxides) are investigated. Within each of those fluorination degrees, different arrangements of the fluoride ions are chosen to resemble various structure motifs. Those considerations lead to 47 gibbsite, 62 bayerite, 6 doyleite, 38 diaspore and 34 boehmite structures with their related fluoride arrangements. Please note that those structures solely represent a selection of the huge amount of possibilities to arrange various amount of fluoride ions differently within those systems. The small amount of doyleite structures results from its use as a test case later on.

#### 4.1.1.1 Fluoride Depending Stability

To compare the stability of the different fluorination degrees per crystalline system and the crystalline systems with each other, [equation \(4.1\)](#) and [equation \(4.2\)](#) are used to calculate the electronic part of the reaction energy. Throughout this section, (reaction) energy always refers solely to its electronic part. Those energies are then taken as measures of the corresponding fluoride arrangement's stability. To visualize the reaction energies of all 187 structures, they are condensed in [figure 4.2](#). It shows the average of the maximum and minimum reaction energy of each fluorination degree with the corresponding maximum spread due to different fluoride arrangements represented by the error bars. This spread increases with the fluorination degree, showing the stronger influence of the selected fluoride arrangements in higher fluorination degrees. Furthermore, it can be seen that the reaction energy for the aluminium hydroxides is energetically favoured and decreases with increasing fluorination degree, while for the oxohydroxides it is energetically disfavoured and increases.

Both trends seem to be quite linear and illustrate that the fluorination of the oxohydroxides is thermodynamically unfavourable while it is quite likely to occur for

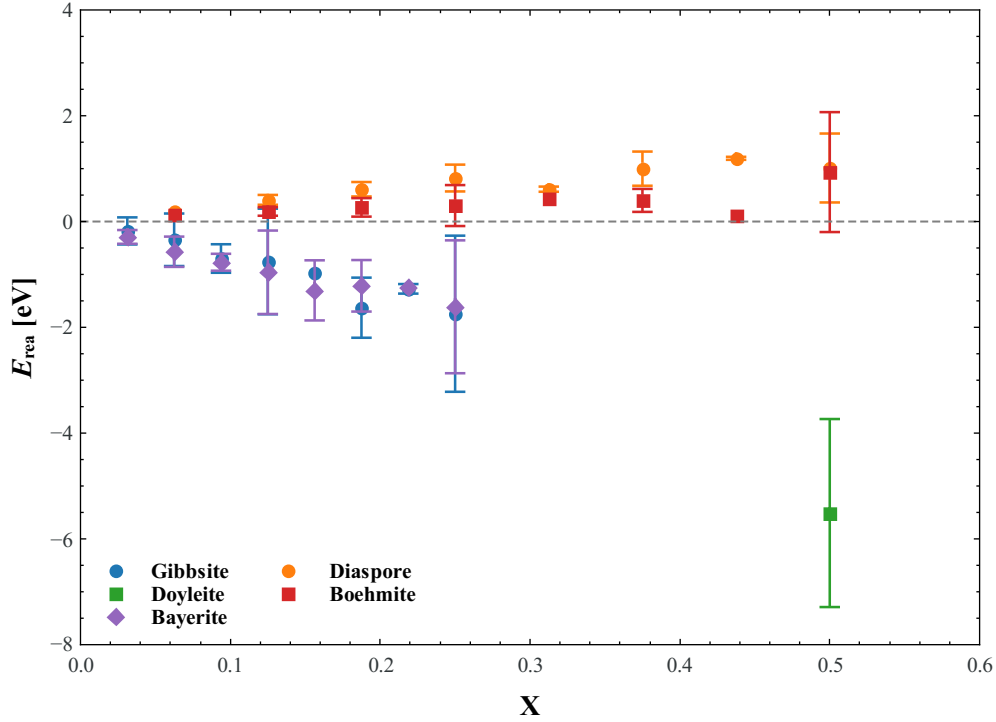


**Figure 4.2:** Reaction energies  $E_{\text{rea}}$  for the five considered crystalline systems gibbsite, bayerite, and doyleite as well as diaspore and boehmite - data points represent the average of the maximum and minimum reaction energy in dependency on the fluoride content  $\mathbf{X}$ , error bars represent the range of reaction energies of the corresponding fluoride content  $\mathbf{X}$  (VASP-DFT, PBE/PAW, 600.0 eV energy cut-off, D3-BJ).

the hydroxides. Since bayerite and boehmite are both used as adsorbent for fluoride ions to clean water [23–27], these results become very interesting for further investigations and considerations within this field of application. The results show that the hydroxides are more likely to take up more fluoride ions than their oxohydroxide counterparts, which makes the hydroxide systems more attractive in that regard.

Since figure 4.2 provides very different and quite large spreads of the reaction energies per fluorination degree, a closer look should be taken. Considering the crystalline system boehmite, four different fluoride arrangements (see figure 4.3) are chosen to highlight how the different arrangements can influence the stability of the corresponding structure.

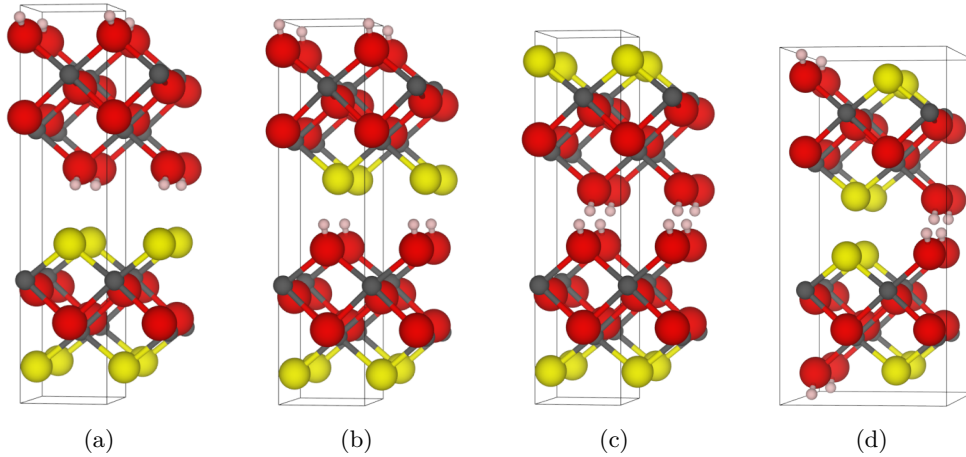


**Figure 4.3:** Four different, optimised fluoride arrangements of boehmite with the composition  $\text{AlO}(\text{OH})_{0.5}\text{F}_{0.5}$  - gray = aluminium, red = oxygen, yellow = fluorine, and white = hydrogen (VASP-DFT, PBE/PAW, 600.0 eV energy cut-off, D3-BJ).

Starting with [figure 4.3\(a\)](#), which resembles a less-stable structure within the given fluorination degree, it can be seen that an entire slice is fluorinated, which also results in two fluoride layers within the structure. This yields in hydrogen bonding solely to fluoride ions as well. By variation of the fluoride arrangement to the one shown in [figure 4.3\(b\)](#), both slices now have the same stoichiometry and the fluoride ions are farther away from each other. At the same time, there are still two fluoride layers present and hydrogen bonding is still solely possible to fluoride ions as well. This simple change results in an increased stability of 1.39 eV per  $2 \times 2 \times 1$  supercell. Changing again the position of an entire fluoride layer, the new arrangement in [figure 4.3\(c\)](#) now provides very close fluoride ions, but at the same time, only hydrogen bonds to oxygen ions are present. The slice stoichiometry remains the same. Thus, the system is even further stabilised by 0.64 eV. Going to [figure 4.3\(d\)](#), the fluoride layers are separated and the fluoride ions are arranged in a more distributed manner, while keeping the other previously mentioned structure motifs intact. Therefore, the stability of the system increases again by 0.24 eV and reaches the maximum of this fluorination degree for boehmite with a total difference of 2.27 eV compared to [figure 4.3\(a\)](#).



Looking at other crystalline systems and fluoride arrangements, similar observations are made. Nonetheless, the energy differences are sometimes very small. Thus, it is also possible that those differences are smaller than  $kT \approx 0.026$  eV ( $T = 25^\circ\text{C}$ ), which, in experiments, might result in multiple arrangements per fluorinated crystalline system.

#### 4.1.1.2 Structure-Stability-Relation

To efficiently investigate all fluoride arrangements in all fluorination degrees for all crystalline systems, different parameters are used to quantify the given structures with their corresponding structure motifs. The defined parameters (see chapter 3 [Structure-Stability-Relation Parameters](#) for a detailed description) include short-range characteristics, like the distortion of the aluminium CS and the deviation of the positive and negative charge centres in those CSs. How the fluorides are distributed within the cell and the amount of remaining symmetry elements after fluorination and relaxation are examples for included long-range characteristics.

To start the investigation of all considered crystalline systems, the mentioned parameters are assembled as a linear combination to result in a single parameter  $D(i)$  which represents the selected structure itself:

$$\begin{aligned}
 D(i) = & C_1 \cdot D_{\text{dist}}(i) + C_2 \cdot D_{\text{sym}}(i) + C_3 \cdot D_{\text{char}}(i) + C_4 \cdot D_{\text{hom1}}(i) \\
 & + C_5 \cdot D_{\text{hom2}}(i) + C_6 \cdot D_{\text{hom3}}(i) + C_7 \cdot D_{\text{hb1O}}(i) + C_8 \cdot D_{\text{hb2O}}(i) \\
 & + C_9 \cdot D_{\text{hb1F}}(i) + C_{10} \cdot D_{\text{hb2F}}(i) + C_{11} \cdot D_{\text{ld1}}(i) + C_{12} \cdot D_{\text{ld2}}(i) \\
 & + C_{13} \cdot D_{\text{reg1}}(i) + C_{14} \cdot D_{\text{reg2}}(i), \tag{4.3}
 \end{aligned}$$

where  $C_j$  represents the linear coefficients, which resemble the weighting of the different parameters.

To obtain the correct weightings, the structure parameter  $D(i)$  is correlated to the reaction energy  $E_{\text{rea}}(i)$  by plotting both values against the corresponding structure for a given crystalline system. Unfortunately, doing so reveals certain steps in the reaction energy, which simply result from the difference in the atomic contribution to this energy by the different atomic species for the different fluorination degrees. These steps can not be reproduced by the structure parameter, unless a step-function is added to it. Thus, the different step heights need to be known, which is not possible with this small sample size of possible fluoride arrangements per fluorination degree per crystalline system. Therefore, the focus is set to each fluorination degree individually. Within a given fluorination degree the changes in energy are only linked to the fluoride arrangement. Unfortunately, there are too less structures per fluorination degree to do a reasonable fitting. Furthermore, a computer driven fitting would aim for equal values of  $D(i)$  and  $E_{\text{rea}}(i)$ , this would result in weightings which are not chemically reasonable or in a random absolute shift. To overcome the mentioned challenges and chemically unreasonable results, the fitting procedure is done user-directed and with great care while only the two line shapes of the structure parameter  $D(i)$  and the reaction energy  $E_{\text{rea}}(i)$  have to be similar, not the actual values. To do so, all fluorination degrees of all crystalline systems, except for doyleite, are viewed at the same time. Since the slices of the various crystalline systems influence them differently, their corresponding parameters are optimised only for one crystalline system at the same time but still together with the other parameters. The weightings  $C_j$  are therefore adjusted step by step, starting from the results of AIOF [189], until a reasonably good similarity of the two line shapes of  $D(i)$  and  $E_{\text{rea}}(i)$  in dependence on the fluoride arrangement per fluorination degree is found.

The advantage of this unusual user-directed fitting procedure is the avoidance of step functions, the simultaneous fitting of all fluorination degrees and all crystalline systems, the avoidance of absolute shifts and, most importantly, the prevention of chemically unreasonable results. For example, it is possible to allow a slightly worse

**Table 4.4:** Obtained weightings  $C_j$  for the considered structures gibbsite, bayerite, diaspore and boehmite.

Parameter	Crystalline System				
	Gibbsite	Bayerite	Diaspore	Boehmite	AlOF [189]
$D_{\text{dist}}(i)$		0.950			0.961
$D_{\text{sym}}(i)$		0.800			0.866
$D_{\text{char}}(i)$		0.350			0.359
$D_{\text{hom1}}(i)$		0.400			0.378
$D_{\text{hom2}}(i)$		0.120			0.110
$D_{\text{hom3}}(i)$		0.050			0.026
$D_{\text{hb1O}}(i)$		0.500			
$D_{\text{hb2O}}(i)$		0.125			
$D_{\text{hb1F}}(i)$		0.200			
$D_{\text{hb1F}}(i)$		0.050			
$D_{\text{ld1}}(i)$		0.300			
$D_{\text{ld2}}(i)$	–	–		0.300	
$D_{\text{reg1}}(i)$		0.350	0.700	0.000	
$D_{\text{reg2}}(i)$		0.350	0.000	0.700	

accordance of the line shapes but ensuring that stronger hydrogen bonds ( $D_{\text{hb1a}}(i)$ ) have a higher weighting than weaker ones ( $D_{\text{hb2a}}(i)$ ).

The results of this fitting procedure can be seen in [table 4.4](#) and some selected graphical representations in [figure 4.4](#). The remaining comparisons of the reaction energy  $E_{\text{rea}}(i)$  with the structure parameter  $D(i)$  can be found in section A.2 [Bulk](#) from [figure A.1](#) to [figure A.8](#). As it is shown in [figure 4.4](#), the weightings from [table 4.4](#) provide a quite good agreement of the two line shapes. This shows that the used approach and the used parameters for describing the structure are very promising and can be used for different crystalline systems. The weightings in [table 4.4](#) also reveal that the distortion ( $D_{\text{dist}}(i)$ ), the symmetry of the whole cell ( $D_{\text{sym}}(i)$ ), and the slice stoichiometries ( $D_{\text{regs}}(i)$ ) play very important roles for the stability of the systems. Furthermore, the charge centre deviation ( $D_{\text{char}}(i)$ ), the short-ranged hydrogen bonding to oxide/hydroxide ions ( $D_{\text{hb1O}}(i)$ ), the short-ranged homogeneity of the cell ( $D_{\text{hom1}}(i)$ ), and the layer distances ( $D_{\text{lds}}(i)$ ) still influence the stability

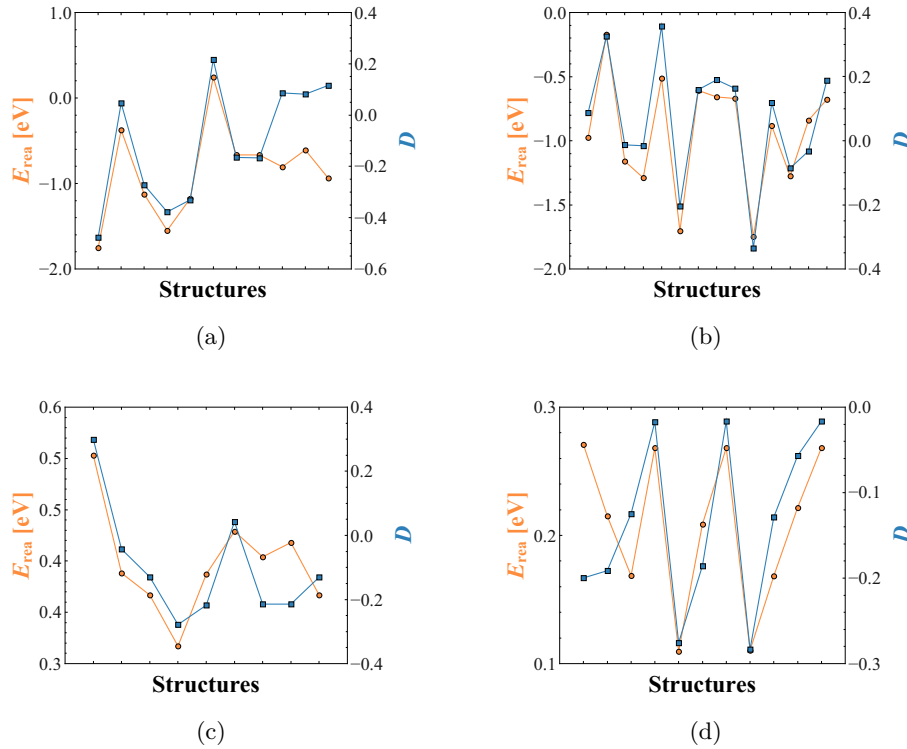


**Figure 4.4:** Graphical representation of the reaction energy  $E_{\text{rea}}(i)$  and the structure parameter  $D(i)$  for a specific fluorination degree - (a) gibbsite with  $\text{Al}(\text{OH})_{2.875}\text{F}_{0.125}$ , (b) bayerite with  $\text{Al}(\text{OH})_{2.875}\text{F}_{0.125}$ , (c) diaspore with  $\text{AlO}(\text{OH})_{0.875}\text{F}_{0.125}$ , and (d) boehmite  $\text{AlO}(\text{OH})_{0.875}\text{F}_{0.125}$ .

while the remaining parameter play only minor roles. Taking a closer look at [table 4.4](#) and the weightings for the slice stoichiometries ( $D_{\text{regs}}(i)$ ), it can be seen that those weightings differ significantly between the different crystalline systems. This shows that for the aluminium hydroxides gibbsite and bayerite in both regions a balanced distribution of the fluoride ions is important for the stability of the system. Whereas for diaspore the region of hydroxide bonding is much more important, since this is the site which defines the shape of the “wafting rectangular” building blocks (see [figure 3.2](#)). Two different stoichiometries in the two linked regions would otherwise result in two different building blocks which then do not match any longer and have to adjust themselves. Thus, the system would need to forfeit a portion of its stability. In the case of boehmite, however, the stoichiometry deviation of the slices is a very

important one. This emphasises the importance of evenly spread slices and that this region, due to its rigidly bound oxide ions, is more important for this crystalline system than for the other sliced structures of the aluminium hydroxides.

In addition to the quite good agreement of the two line shapes, the weightings also handily prove experimental findings concerning the strength of hydrogen bonds to different hydrogen acceptors. Especially for dimers and small molecules, the hydrogen bonding with fluorine as the hydrogen acceptor is much stronger than the one where oxygen is the hydrogen acceptor [206]. For solid states, however, inverse observations can be made [207–209], so that hydrogen bonding to oxide ions is now more favourable than to fluoride ions. Due to the higher CN of the fluoride ions, their ability to accept hydrogen bonds decreases. This ranking of the hydrogen bonding strengths in solid state is very well reproduced by the obtained weightings of  $D_{\text{hb1O}}(i)$  (0.500) and  $D_{\text{hb1F}}(i)$  (0.200).

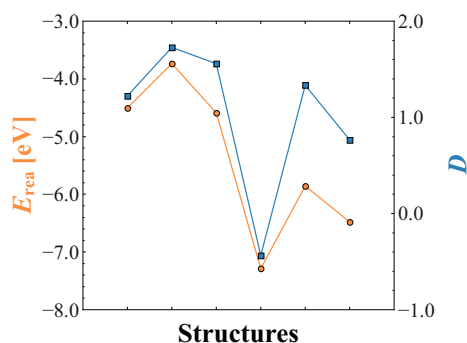


**Figure 4.5:** Graphical representation of the reaction energy  $E_{\text{rea}}(i)$  and the structure parameter  $D(i)$  for doyleite with the composition  $\text{Al}(\text{OH})_{2.5}\text{F}_{0.5}$ .

In order to further check and verify the found weightings, the third aluminium hydroxide, doyleite, comes into play. To ensure that those weightings and the parameter descriptions as well do not only apply to the considered fluorination degrees, the stoichiometry of the fluorinated doyleite is set to  $\text{Al}(\text{OH})_{2.5}\text{F}_{0.5}$ . Since all three aluminium hydroxides provide similar structures, where only the slices are shifted against each other

differently, the slice stoichiometry weightings from gibbsite and bayerite are taken.

Six different fluoride arrangements within this crystalline system are considered and investigated. As figure 4.5 shows that even for a higher fluorination degree as in the fitting range, and a less symmetrical UC, the structure parameter’s line shape is

in good agreement with the one of the reaction energy. This confirms the obtained weightings and shows the transferability of them and the parameters for similar crystalline systems.

Taking the results of the doyleite check and [table 4.4](#) into account, the weightings and the parameter descriptions perform very well and quite reliable for aluminium oxide/hydroxide/fluoride compounds. Especially the obtained weightings can provide very helpful information to improve the process of building models for nanostructures or smaller clusters with different compositions of the previously mentioned ions. Using the gained knowledge from the weightings, possible structures can be less try and error and the educational guess for them can be improved.

#### 4.1.2 Fluoride Depending NMR Shifts in Aluminium (oxo)hydroxides

Although, fluoride arrangements are difficult to measure directly, some methods are more useful than other to tackle this challenge, one of them is solid state [NMR](#). It is a very good and standard tool to classify materials and local structures and, by association, can give a good insight in the averaged atomic environment of the analysed species. With additional knowledge of certain well tested atomic environments, the averaged signals can be separated, so even more information can be extracted from the measured results. At this point, theory can step in and provide better segregated results of local atomic environments to enable such a signal breakdown. Therefore, it is very important to be comparable with experimental results in order to verify and improve the results mutually. Thus, the  $^{27}\text{Al}$  and  $^{19}\text{F}$  [NMR](#) shifts for 63 selected structures of all crystalline structures are calculated. For the calculations of those [NMR](#) shifts, the shieldings of the aluminium ions in the structure are referenced to the  $^{27}\text{Al}$  shielding in a  $[\text{Al}(\text{OH}_2)_6]^{3+}$  complex while the shieldings of fluoride ions in the structure are referenced to the  $^{19}\text{F}$  shielding in  $\text{CCl}_3\text{F}$ . In order to investigate and explain the influence of fluoride ions and their arrangement within the structure on the

obtained  $^{27}\text{Al}$  NMR shifts, the  $\text{dist}(A)$  (see section 3.1 [Distortion of Cation Coordination Spheres](#)), because of its strong influence on the stability of the system (see [table 4.4](#)), and the corresponding number of fluoride ions in the aluminium CSs are taken into account. While the latter's influence was already experimentally evaluated by Kemnitz and co-workers [[53](#), [54](#), [210](#), [211](#)] as well as Fischer *et al.* [[212](#)], the influence of the CN was theoretically studied by Copéret and *et al.* [[213](#)]. They revealed the influence of orbital interactions between occupied and unoccupied orbitals on the paramagnetic part of the  $^{27}\text{Al}$  NMR shifts. For solid state systems the orbitals are replaced with bands, which is why this effect will be called “band interaction effect” throughout this work. Since the strength of this effect correlates with the band gap (HOMO-LUMO gap for molecules), the respective values for the studied unfluorinated crystalline systems are as follows: gibbsite: 5.79 eV, bayerite: 5.93 eV, diaspore: 6.75 eV, and boehmite: 6.10 eV.

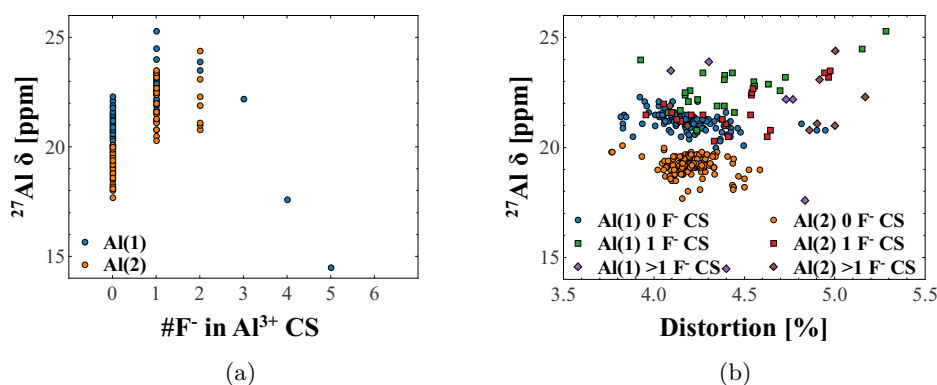


**Figure 4.6:**  $^{27}\text{Al}$  NMR shifts of selected fluorinated structures of the aluminium hydroxide gibbsite - (a) in dependence on the CS stoichiometry and (b) in dependence on the distortion of the corresponding CS (VASP-DFT, PBE/PAW, 600.0 eV energy cut-off, D3-BJ).

Starting with the  $^{27}\text{Al}$  NMR shifts for gibbsite (see [figure 4.6](#)), it can be seen from [figure 4.6\(a\)](#) that the  $^{27}\text{Al}$  NMR shifts first increase with the amount of fluoride ions in the corresponding CS while they decrease for two and more fluoride ions, which results in a negative parabolic shape. This reveals a decrease in the shielding at

the aluminium centre by going from zero to one fluoride ion in the corresponding aluminium CS while it shows an increase of the shielding with a further increasing amount of fluoride ions in the CS. Taking a closer look at the different contributions (see equation (2.89)) to the shifts, it can be seen that the major contribution comes from the paramagnetic part not only in absolute values but also in differences for the different aluminium centres. In addition to its dependency on the electronic density, the paramagnetic contribution depends also on the possibility of occupied and unoccupied bands to interact with each other [213]. Focusing on the effect of the electron density: the more electron density is located at the considered aluminium centre, the stronger the shielding and the smaller the chemical shift. The second effect, which can be much stronger than the first one, mainly results in larger deshielding and, by association, in larger shifts if the interaction gets stronger. Both effects can be in opposition to each other depending on the actual interaction of the occupied and unoccupied bands. Since the trend shown in figure 4.6(a) provides a parabolic shape in dependence on the amount of fluoride in the aluminium CSs, it seems that the addition of fluoride ions weakens the band interaction effect not linearly but of higher order, while the electron density effect is strengthened linearly. Comparing this trend with the experimentally found trend [54], which shows a negative linear dependence of the  $^{27}\text{Al}$  NMR shifts with increasing amount of fluoride in their respective CSs, a clear difference for small fluoride amounts can be seen. This might be attributed to the sliced structure of gibbsite, which cuts a large amount possible interactions from the considered aluminium CS with the surrounding ones, and by association, the local effects increase. Besides, for each fluorination degree, if there is enough data, the  $^{27}\text{Al}$  NMR shifts are spread very heavily within  $\approx 5$  ppm. Those deviations within the same fluorination degree can be explained by looking at figure 4.6(b). It reveals a quite good linear dependence of the  $^{27}\text{Al}$  NMR shifts on the distortion of the aluminium CSs. For aluminium centres without fluoride ions, the  $^{27}\text{Al}$  NMR shifts decrease with increasing distortion, while they increase with the distortion if fluoride ions are



present in the corresponding aluminium CS. This shows that distorted CSs enhance the electron withdrawing nature of fluoride ions while they weaken it of the hydroxide ions. Thus, the distortion of the aluminium CSs seems to provide more favourable intra-slice hydrogen bonds which then result in a weaker electron withdrawing effect of the hydroxide ions and, by association, in smaller  $^{27}\text{Al}$  NMR shifts. At the same time, the increasing distortion decreases the strength of the *para*-effect which describes the competition of two opposing ligands for the electron density from the central ion and thus, enhances the electron withdrawing effect of the ligands. Therefore, an increasing distortion enhances the electron withdrawing effect of the ligands. Since both effects are opposite to each other and the first one is much smaller for the fluoride ions, they together explain the varying dependency on the distortion of the  $^{27}\text{Al}$  NMR shifts.

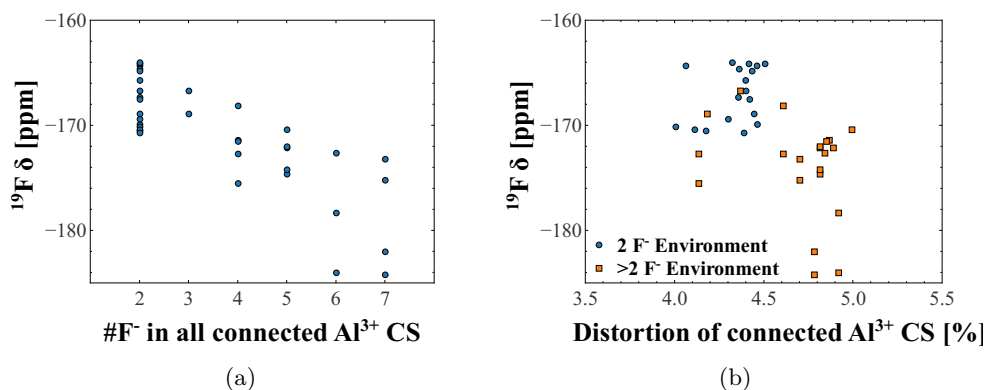


**Figure 4.7:**  $^{19}\text{F}$  NMR shifts of selected fluorinated structures of the aluminium hydroxide gibbsite - (a) in dependence on the combined CS stoichiometry of the connected aluminium centres and (b) in dependence on the average distortion of the corresponding aluminium CSs (VASP-DFT, PBE/PAW, 600.0 eV energy cut-off, D3-BJ).

Going from the  $^{27}\text{Al}$  to the  $^{19}\text{F}$  NMR shifts (see figure 4.7), first of all the term “#F<sup>-</sup> in all connected Al<sup>3+</sup> CS” needs to be clarified. If a fluoride ion is bound to two aluminium centres, it would be the sum of the amount of fluoride ions in each aluminium CS. In the aluminium hydroxides each anion is connected to two cations. Therefore, for those crystalline systems always two CSs are considered. Since it is the sum over the regarded aluminium centres, the selected fluoride ion is counted as

often as it is connected to aluminium centres, in this case two. That is why this graph starts at “2”.

Taking a closer look at [figure 4.7\(a\)](#), a quite good linear trend can be identified with an increasing number of fluoride ions. It states that the more fluoride is present in the connected aluminium centres, the more the  $^{19}\text{F}$  NMR shift is decreasing, which sets up a range of  $\approx 20$  ppm. The same trend was also experimentally observed by Kemnitz and co-workers [211] for crystalline  $\text{AlF}_x(\text{OH})_{3-x}\cdot\text{H}_2\text{O}$  samples in the pyrochlor structure. This can again be explained with the help of the band interaction effect, which results in a deshielding of the fluoride ions. But with an increasing amount of surrounding fluoride ions, this effect gets weaker, and by association, the  $^{19}\text{F}$  nuclei become more shielded. The electron density effect for the fluoride ions is very small since only their second CS changes and not their first one, as it was the case for the aluminium centres. Since the number of fluoride ions in the diagram depends on two aluminium centres, the band interaction effect is still in its low decreasing region, and by association, there is no clear parabolic trend observable. Again, it can be seen that the shifts of the same fluorination degree show a quite large range. In order to analyse the origin of this range, the shifts are again grouped and plotted against the averaged distortion of the connected aluminium CSs (see [figure 4.7\(b\)](#)). Unfortunately, this time there are no clear trends in dependence on the distortion of the aluminium centres. Besides, it can be stated that for two fluorides (one fluoride on two aluminium centres) there seems to be two different groups: one around  $-163$  ppm and the other one around  $-170$  ppm. For higher amounts of fluoride neither such grouping nor any trend can be identified. Therefore, the occurring range of the  $^{19}\text{F}$  NMR shifts do not correlate mainly with the distortion but also on, for example, the structural distribution of the fluoride ions in the connected aluminium centres (*para* or *ortho*; *facial* or *meridional*; etc.). Thus, the  $^{19}\text{F}$  NMR shift would be different if there is a facial assembly of the fluoride ions, an meridional assembly, or of course any combination of those distribution effects. For the  $^{19}\text{F}$  NMR shifts, only

the dependence on the CS stoichiometry can be seen clearly while the smaller ranges within this trend depend on different equipollent effects. Therefore, it becomes more difficult to split those dependencies up.

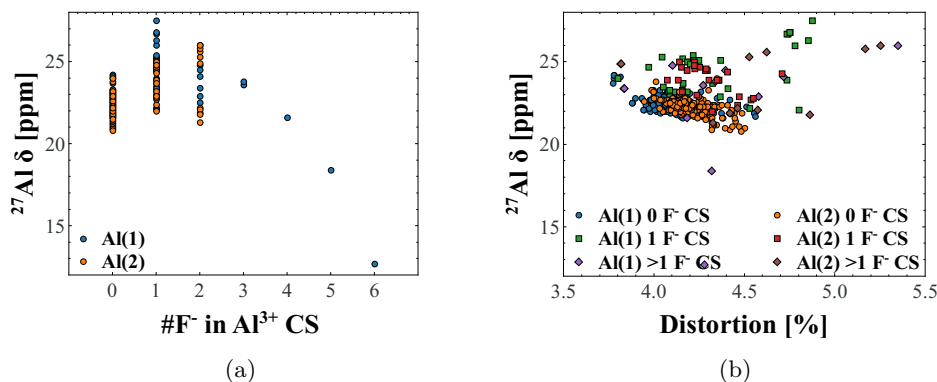


**Figure 4.8:**  $^{27}\text{Al}$  NMR shifts of selected fluorinated structures of the aluminium hydroxide bayerite - (a) in dependence on the CS stoichiometry and (b) in dependence on the distortion of the corresponding CS (VASP-DFT, PBE/PAW, 600.0 eV energy cut-off, D3-BJ).

Going from one aluminium hydroxide to the other, the  $^{27}\text{Al}$  NMR shifts of bayerite, shown in figure 4.8, look very similar to the ones of gibbsite. That is of course due to the very similar structure, where the slices are just displaced a bit against each other. Again, the  $^{27}\text{Al}$  NMR shifts show a negative parabolic shape depending on the amount of fluoride in the aluminium CS with mediocre spreads of them for the low fluorination degrees (see figure 4.8(a)). Likewise in gibbsite, the increasing amount of fluoride increasingly weakens the band interaction effect, which results in an increasing shielding of the aluminium centres while overwriting the deshielding electron density effect resulting from the more electronegative fluoride ions. Revisiting the spread of the  $^{27}\text{Al}$  NMR shifts for the low fluorination degrees of the aluminium CSs, figure 4.8(b) shows again similar but yet one different trend compared the  $^{27}\text{Al}$  NMR shifts of gibbsite. It can be seen that for the aluminium centres labelled with (1), the trends are similar to the ones of gibbsite, while the fluorinated aluminium centres labelled with (2) provide a reversed trend compared to gibbsite. This shows

that the increased *para*-effect, due to distortion, can not overwrite the effect of the more favourable intraslice hydrogen bonds for the aluminium centres labelled with (2). This is due to the different orientations of the hydrogen bonds of the two differently labelled aluminium centres in bayerite.

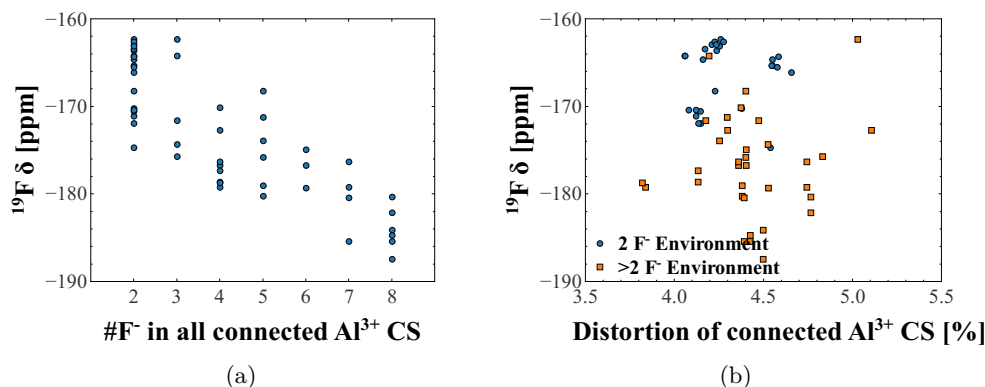


**Figure 4.9:**  $^{19}\text{F}$  NMR shifts of selected fluorinated structures of the aluminium hydroxide bayerite - (a) in dependence on the combined CS stoichiometry of the connected aluminium centres and (b) in dependence on the average distortion of the corresponding aluminium CSs (VASP-DFT, PBE/PAW, 600.0 eV energy cut-off, D3-BJ).

Moving once more from the  $^{27}\text{Al}$  NMR shifts to the  $^{19}\text{F}$  NMR shifts of bayerite (see figure 4.9), the fluoride ions are again always doubly coordinated and therefore, figure 4.9(a) starts again at “2”. Taking a closer look at figure 4.9(a), it can be seen that again a quite linearly decreasing trend of the  $^{19}\text{F}$  NMR shifts in dependence on the amount of fluoride in the connected aluminium CS is found. As it was discussed for the  $^{19}\text{F}$  NMR shifts of gibbsite, this results from the weakening of the deshielding band interaction effect with increasing amounts of fluoride. Since the electron density effect on the fluoride ions is less strong than for the aluminium centres, this effect plays a very minor role, so there is no increase in the  $^{19}\text{F}$  NMR shifts for small fluorination degrees which would otherwise result from a stronger competition of the anions. Once more, the  $^{19}\text{F}$  NMR shifts are spread noticeably within the different amounts of fluoride in their environment. Thus, those spreads are again plotted against the averaged distortion of the connected aluminium CSs (see figure 4.9(b)).

As for gibbsite, two groups of  $^{19}\text{F}$  NMR shifts can be identified within the “2 F $^-$  Environment”: one around  $-163$  ppm and the other around  $-171$  ppm. This is again evidence for a stronger differentiation between the two different aluminium centres, as it is indicated by their  $^{27}\text{Al}$  NMR shifts. For the higher fluorinated environments, trends become much harder to see because of the smaller sample size per fluorination degree and the anyhow more complex interplay of smaller effects on the  $^{19}\text{F}$  NMR shifts within a given fluorination degree. Thus, those shifts are plotted again as a second group just for completion.

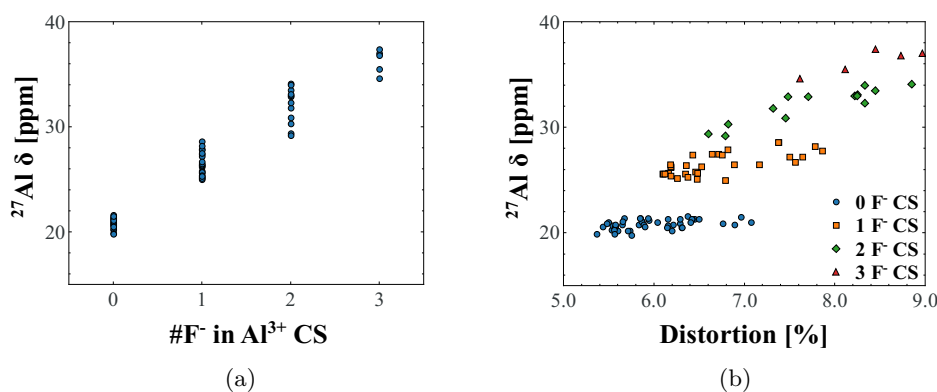


**Figure 4.10:**  $^{27}\text{Al}$  NMR shifts of selected fluorinated structures of the aluminium oxohydroxide diaspore - (a) in dependence on the CS stoichiometry and (b) in dependence on the distortion of the corresponding CS (VASP-DFT, PBE/PAW, 600.0 eV energy cut-off, D3-BJ).

Leaving the aluminium hydroxides behind and going to the aluminium oxohydroxides, diaspore will be the first one to look at. It provides a structure without slices but a very important hydrogen bonding region. Starting with the  $^{27}\text{Al}$  NMR shifts of diaspore, seen in figure 4.10, there are very different trends to observe this time. At first, by looking at figure 4.10(a), it can be seen that this time the  $^{27}\text{Al}$  NMR shifts increase almost linearly with an increasing amount of fluoride ions in their respective aluminium CSs. As mentioned for the two aluminium hydroxides previously, there are two strong and competing effects to affect the  $^{27}\text{Al}$  NMR shifts: the electron density effect and the band interaction effect. Since in diaspore the band gap is larger

by  $\approx 0.7$  eV as in the aluminium hydroxides, the band interaction effect is not only smaller, but is also less sensitive to variations of the band gap. Thus, the electron density effect plays the dominant role for this crystalline system. That is why the  $^{27}\text{Al}$  NMR shifts increase linearly, since each added fluoride ion pulls more electron density out of the aluminium centres. Hence, the shielding decreases, which corresponds of course to an increase in the  $^{27}\text{Al}$  NMR shift. As for the aluminium hydroxides, a spread of the  $^{27}\text{Al}$  NMR shifts can be observed for each fluorination degree. Therefore, the  $^{27}\text{Al}$  NMR shifts are plotted against the distortion of the corresponding aluminium CSs (see figure 4.10(b)) to analyse this spreading. It can be seen that for diaspore there are remarkably good linear trends to be found in dependence on the aluminium CS distortion. For each fluorination degree the increase of the distortion leads to an increase of the  $^{27}\text{Al}$  NMR shifts, while the slope of those linear increases gets larger with oncreasing amount of fluoride ions. In diaspore, the distortion results in weaker hydrogen bonds of the hydroxide groups, which then leads to a stronger electron withdrawing effect of those groups, and by association, this results in higher  $^{27}\text{Al}$  NMR shifts. The increase of the slope of those trends is due to the higher amount of fluoride ions in the aluminium CSs, which results in stronger electron withdrawing effects with increasing distortion than for the hydroxide groups.

Moving forward to the  $^{19}\text{F}$  NMR shifts of diaspore, seen in figure 4.11, they are plotted against the amount fluoride ions in their environment at first. The corresponding figure 4.11(a) starts with “3”, because this time the singly charged ligands are triply coordinated, so the summation of fluoride ions of the three corresponding aluminium CSs results in at least three. At first, the much more deshielded nature of the fluoride ions in diaspore compared to their counterparts in the aluminium hydroxides should be mentioned. This simply results from the triple coordination of those anions in diaspore, as opposed their double coordination in the previous crystalline systems. By increasing the amount of fluoride ions in the three connected aluminium CSs, the  $^{19}\text{F}$  NMR shifts increase as well because the selected fluoride ion has to

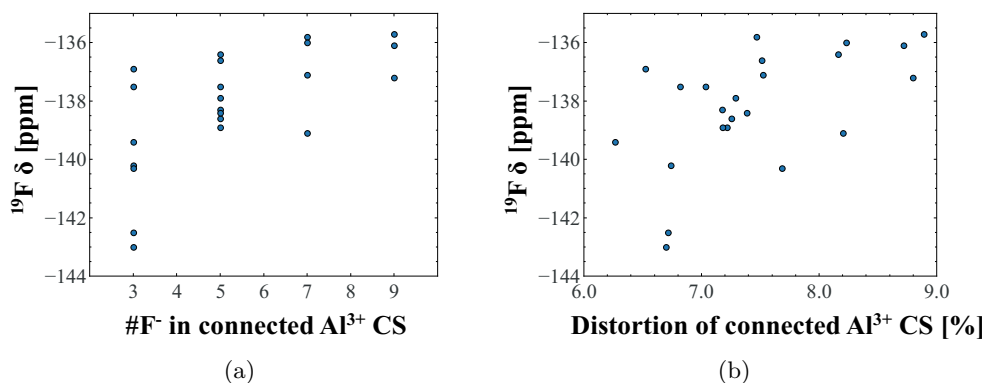


**Figure 4.11:**  $^{19}\text{F}$  NMR shifts of selected fluorinated structures of the aluminium oxohydroxide diaspoire - (a) in dependence on the combined CS stoichiometry of the connected aluminium centres and (b) in dependence on the average distortion of the corresponding aluminium CSs (VASP-DFT, PBE/PAW, 600.0 eV energy cut-off, D3-BJ).

compete with an increasing amount of stronger electron withdrawing anions, so gets less electron density from the aluminium centre than before. This results in a deshielding of the considered fluoride ions and, by association, in higher  $^{19}\text{F}$  NMR shifts. Trying to explain the spread of the  $^{19}\text{F}$  NMR shifts within each fluorination degree by plotting them against the averaged distortion of the connected aluminium CSs (see figure 4.11(b)), does not result in any clear trends. Even the fractionation in the different fluorination degrees, as it was done previously, does not result in any convincing trends. This indicates that the  $^{19}\text{F}$  NMR shifts of diaspoire depend much stronger on competing effects, than the aluminium hydroxides. Nonetheless, one might argue that there is a somewhat increasing trend of the  $^{19}\text{F}$  NMR shifts with increasing distortion, but since the data points are that widely distributed, this trend can only be vaguely assumed, which rules out any attempts to explain this possible trend.

Finalising the NMR analysis of the bulk materials with boehmite, the corresponding  $^{27}\text{Al}$  NMR shifts are shown in figure 4.12. This aluminium oxohydroxide provides again a sliced structure and again doubly coordinated singly charged anions. By looking at the  $^{27}\text{Al}$  NMR shifts plotted against the aluminium CS stoichiometry, shown in figure 4.12(a), it can be seen that the  $^{27}\text{Al}$  NMR shifts decrease again with increasing

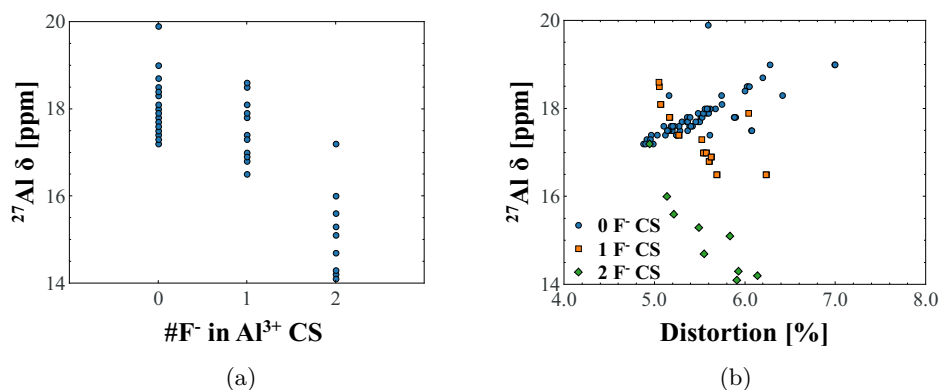


**Figure 4.12:**  $^{27}\text{Al}$  NMR shifts of selected fluorinated structures of the aluminium oxohydroxide boehmite - (a) in dependence on the CS stoichiometry and (b) in dependence on the distortion of the corresponding CS (VASP-DFT, PBE/PAW, 600.0 eV energy cut-off, D3-BJ).

amount of fluoride ions, as it was seen for the aluminium hydroxides. Furthermore, it seems that the trend of this decline of the  $^{27}\text{Al}$  NMR shifts is not really linearly but looks like the decreasing part of a negative parabolic shape. Since the aluminium centres only provide the possibility of a maximum of two fluoride ions per CS, there is only a very limited span of different fluorination degrees, which makes a clarification of this trend more difficult. Nonetheless, it is assumed that the trend is part of a negative parabolic shape. Following this assumption, the trend of the  $^{27}\text{Al}$  NMR shifts of boehmite looks very similar to the ones of gibbsite and bayerite, but it misses the increasing nature of the those crystalline systems for the  $^{27}\text{Al}$  NMR shifts with few to none fluoride ions. This is a result of the oxide backbone of the individual slices, which seems to approximately mimic the effect of the first fluoride ions by weakening the band interaction effect and provides an overall weaker electron density effect. Thus, the fluorination of those aluminium centres results in a further weakening of the band interaction effect and a comparably weak electron density effect. Therefore, the  $^{27}\text{Al}$  NMR shifts decrease progressively. In order to tackle the spread of the  $^{27}\text{Al}$  NMR shifts of each fluorination degree, they are again plotted against the distortion of the corresponding aluminium CSs (see figure 4.12(b)). While the unfluorinated alu-



minium centres show an increase in their  $^{27}\text{Al}$  NMR shifts with increasing distortion of their CSs, the reverse is true for the fluorinated aluminium centres. Additionally, the decreasing trend gets stronger with an increasing amount of fluoride ions in the aluminium CSs. Since in boehmite the slices are much closer together than in the aluminium hydroxides gibbsite and bayerite, the interslice hydrogen bonds of boehmite are shorter and, by association, stronger. This results in more “rigid” hydrogen bonds. With increasing distortion, those stronger and more “rigid” hydrogen bonds become weaker, so the electron withdrawing effects of the hydroxide groups increase, and by association, the  $^{27}\text{Al}$  NMR shifts increase. With addition of the fluoride ions this trend is increasingly reversed. This is due to the fact that in boehmite the selected trends are in the region where the weakening of the band structure effect overwrites the electron density effect. Whereas, in gibbsite and bayerite those finer trends were analysed in the region of a stronger electron density effect, so the trends are different here. In fact, since the band interaction effect is weakened that much already, the fluorinated aluminium CSs also seem to be more sensible to minor changes like the distortion of them. The fluoride ions not only increasingly weaken the band interaction effect but also increase the sensitivity of  $^{27}\text{Al}$  NMR shifts of connected aluminium CSs with respect to slight geometric changes if the band interaction effect is already considerably weakened. Thus, distortions of the aluminium CSs result in a further weakened band interaction effect and therefore, in stronger shielded  $^{27}\text{Al}$  NMR shifts. This also explains the stronger declining  $^{27}\text{Al}$  NMR shifts for the higher fluorination degree, because those CSs have to deal with this sensitisation of the band interaction effect twice.

Moving from the  $^{27}\text{Al}$  NMR shifts to the  $^{19}\text{F}$  NMR shifts for the last time in this bulk material section, the calculated  $^{19}\text{F}$  NMR shifts of boehmite can be seen in figure 4.13. Starting with the  $^{19}\text{F}$  NMR shift dependence on the amount of fluoride in the environment, figure 4.13(a) shows a general declining trend of the  $^{19}\text{F}$  NMR shifts, but due to the very huge spread, it can not be stated if the trend is linear or of

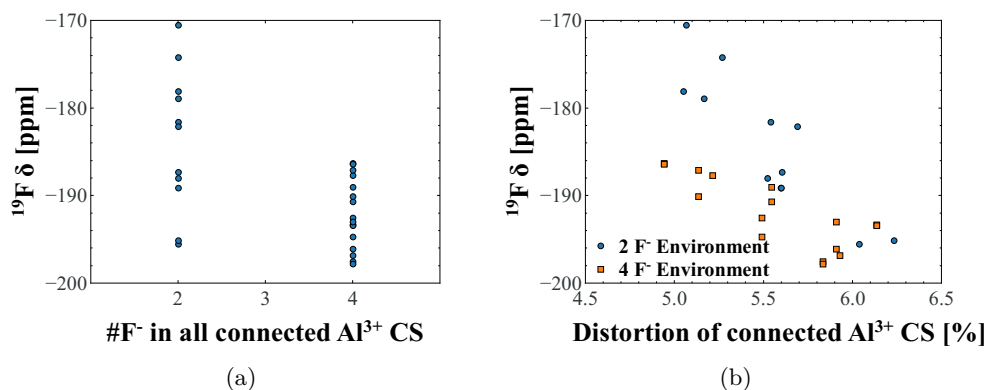


**Figure 4.13:**  $^{19}\text{F}$  NMR shifts of selected fluorinated structures of the aluminium oxhydroxide boehmite - (a) in dependence on the combined CS stoichiometry of the connected aluminium centres and (b) in dependence on the average distortion of the corresponding aluminium CSs (VASP-DFT, PBE/PAW, 600.0 eV energy cut-off, D3-BJ).

higher order. The declining trend results from the increasing weakening of the band interaction effect, as it was discussed for the  $^{27}\text{Al}$  NMR shifts previously, since this effect of course influences both, the anions and the cations at the same time. Thus, the electron density effect, which would result in more deshielded  $^{19}\text{F}$  NMR shifts due to the increasing competition for the electron density of the aluminium centres with increasing amount of fluoride ions, seems to be overruled by the band interaction effect. In order to deal with the high spread of the  $^{19}\text{F}$  NMR shifts within each fluorination degree, they were plotted against the averaged distortion of the connected aluminium CSs (see figure 4.13(b)). It can be seen that the spread of the  $^{19}\text{F}$  NMR shifts mainly results from the distortion of the related aluminium CSs, because two very good linear trends are observable. The decreasing trend results from the same effects which were already been seen for the  $^{27}\text{Al}$  NMR shifts previously. While the “2 F<sup>-</sup> Environment” shows a very steep decrease, the “4 F<sup>-</sup> Environment”’s decrease is less sensitive to the averaged distortion. For the  $^{27}\text{Al}$  NMR shifts it was seen that they became more sensitive to the distortion of their corresponding aluminium CSs with an increasing amount of fluoride ions because both fluoride ions impacted the respective aluminium centre simultaneously with the same strength. Regarding the  $^{19}\text{F}$  NMR

shifts, however, those effects of additional fluoride ions are weakened, because the first CS of the considered fluoride ions does not change, only the second one changes. Therefore, the difference in the steepness of those trends for the  $^{19}\text{F}$  NMR shifts can not be explained with the same effects, which influenced the steepness of the trends of the  $^{27}\text{Al}$  NMR shifts, at least not to the same extent. More importantly, another effect seems to kick in here to decrease the steepness of the “4  $\text{F}^-$  Environment”s trend. It is possible that the additional fluoride ions weaken the sensitisation effect of the considered fluoride ion and thus, the sensitivity of the  $^{19}\text{F}$  NMR shifts on the distortion is decreased. For the  $^{27}\text{Al}$  NMR shifts this was maybe also the case, but due to the doubling of this effect the sum of both weakened sensitisation effects could have been higher than the non-weakened one alone. Thus, for the  $^{27}\text{Al}$  NMR shifts an increasing sensitivity on the distortion is observed, while for the  $^{19}\text{F}$  NMR shifts an decreasing sensitivity is found.

Summarising, the explanation of NMR trends is very complex and involves a lot of opposing and correlated effects. The interplay of the electron density effect and the band interaction effect together with the stoichiometry of the aluminium CSs showed the strongest impact on the NMR shifts of both studied ionic species. For the aluminium hydroxides and boehmite, the theoretically obtained stoichiometry trends support the experimentally found ones [54] quite well. But regarding the results of diaspore, it was seen that the band gap strongly interferes in the different effects’ strengths, which adds another dimension to consider and changed the direction of the previous trend. To unravel the coherences of structure and NMR shifts further, experimentalists are often interested in the shapes of CSs, which is why the distortion values of the aluminium CSs were considered. In many cases it indeed influenced the NMR shifts noticeably but is also some times opposed by other effects of the same strength or many smaller effects which are not identified or quantified yet. That is why the issue of connecting NMR shifts to structural and energetic properties is so interesting. This attempt of unravelling it only scratches the surface of its

complexity, so it should be preferably regarded as a springboard for further and more intense studies, rather than a closed investigation. Nonetheless, the results and the corresponding trends showed that theoretical examinations are of major importance to riddle this issue step by step and quantify the different effects and their correlation to each other.

## 4.2 $\alpha$ -Aluminium Oxide Surfaces

In this section, the focus is laid on different  $\alpha$ -Al<sub>2</sub>O<sub>3</sub> surfaces, their terminations, their surface energies, the influence of hydration, and how fluoride doping impacts these properties. Based on the work of Choi *et al.* [85], Leeuw *et al.* [86], Marmier *et al.* [87], and Kurita *et al.* [88], seven different surfaces are considered. Choi *et al.* found five different surfaces in sapphire cavities using transmission electron microscopy (TEM) measurements. Later Leeuw *et al.* investigated those findings using atomistic simulation techniques, which are based on the Born model of solids [214]. Marmier *et al.* then expanded the work of Leeuw and used periodic DFT calculations utilising the PBE functional. Their respective results for the three investigations of the surface energies can be summarised in Wulff plots (see figure 4.14).

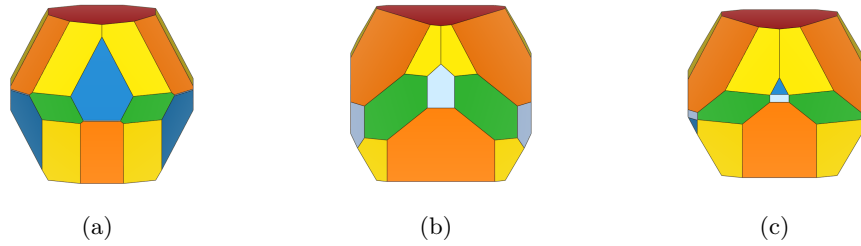


**Figure 4.14:** Wulff plots from the obtained vacuum surface energies for  $\alpha$ -Al<sub>2</sub>O<sub>3</sub> with the space group  $R\bar{3}c$  derived from the results of (a) Choi *et al.*, (b) Leeuw *et al.*, and Marmier *et al.* - red = (0001), orange = ( $\bar{1}\bar{1}02$ ), yellow = ( $11\bar{2}3$ ), green = ( $11\bar{2}0$ ), blue = ( $10\bar{1}1$ ), and lightblue = ( $10\bar{1}0$ ).

None of them investigated or at least did not really mention the stability of all different terminations of those surfaces. Whereas, Kurita *et al.* did so for three of the by now seven considered surfaces utilising periodic DFT and the PBE functional again. They studied the (0001), the ( $\bar{1}\bar{1}02$ ), and the ( $11\bar{2}0$ ) surface cuts regarding the different possible terminations and determined the most stable one. In order to complete this study of the plain surfaces of  $\alpha$ -Al<sub>2</sub>O<sub>3</sub>, the remaining four surfaces, which Kurita *et al.* did not study, are investigated. The results are compared with the previous ones, and a new Wulff plot is created.

To identify the most stable termination of each surface cut, the surface energies for each of them are calculated via the formalism mentioned in subsection 2.2.2 [Surface Energies](#) utilising [equation \(2.92\)](#) for the aluminium-rich as well as the oxygen-rich environment. Sticking to the most recent surface energy ranking by Marmier *et al.*, the number of different terminations for each surface cut is listed as follows: (0001) – 3, (1102) – 5, (1123) – 6, (1120) – 6, (1011) – 5, (1010) – 3 and (2243) – 8. Since Kurita *et al.* already checked the terminations of (0001), (1102) and (1120), the focus of this work is laid on the four remaining surfaces (see [figure 4.15](#)).

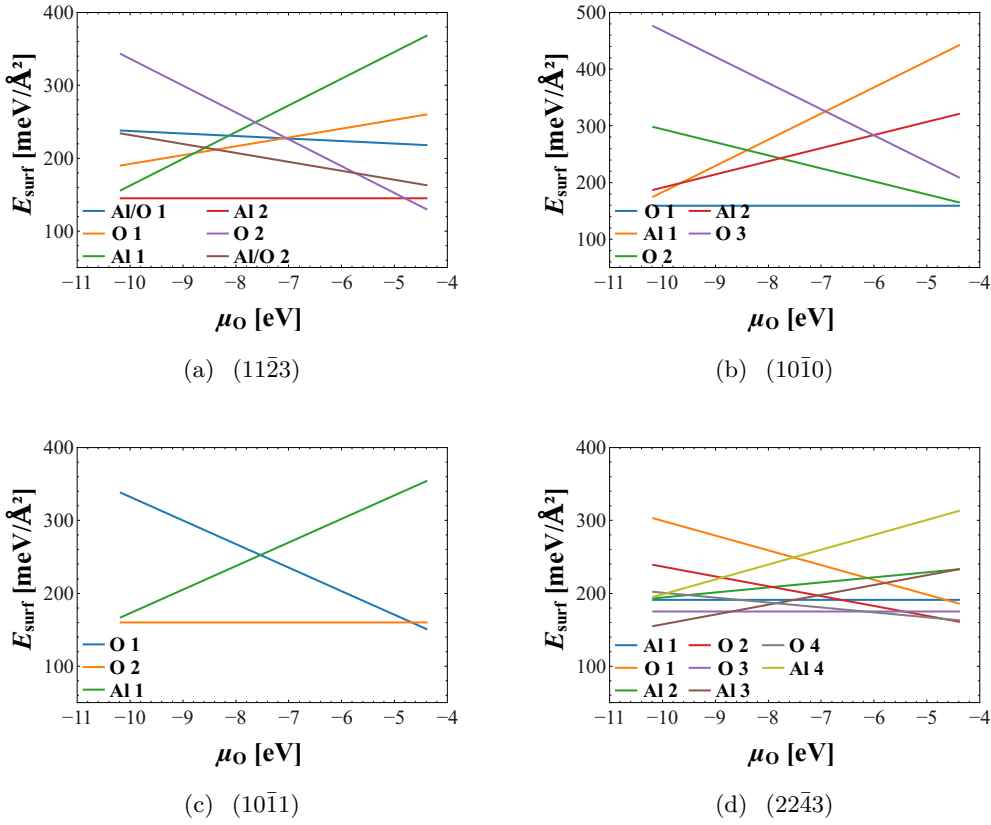


**Figure 4.15:** Surface energies for different terminations of the considered surface cuts in the aluminium-rich (left) and in the oxygen-rich environment (right) (VASP-DFT, PBE/PAW, 600.0 eV energy cut-off, D3-BJ).

Considering the aluminium-rich environment, this study reveals the (1123) surface to be aluminium terminated, the (1010) surface to be oxygen terminated, the (1011)

surface to be oxygen terminated as well, and the  $(22\bar{4}3)$  surface to be aluminium terminated again. Together with the three surfaces investigated by Kurita and *et al.*, the aluminium terminated  $(0001)$  surface, the oxygen terminated  $(1\bar{1}02)$  surface, and the also oxygen terminated  $(11\bar{2}0)$  surface, this leads to the seven surface structures, shown in figure 4.17, their summarised surface energies, presented in table 4.5, and the resulting Wulff plot, shown in figure 4.16.

**Table 4.5:** Comparison of surface energies calculated in this work with previously obtained theoretical and experimental data (VASP-DFT, PBE/PAW, 600.0 eV energy cut-off, D3-BJ).

Face	this work		Marmier [87]		Leeuw [86]		Choi [85]
	[meV/Å <sup>2</sup> ]	[%]	[meV/Å <sup>2</sup> ]	[%]	[meV/Å <sup>2</sup> ]	[%]	[%]
(0001)	130	1.00	124	1.00	151	1.02	1.00
(1 $\bar{1}$ 02)	131	1.01	127	1.03	149	1.00	1.05
(11 $\bar{2}$ 3)	145	1.15	140	1.14	177	1.19	1.06
(11 $\bar{2}$ 0)	149	1.14	146	1.18	167	1.13	1.12
(10 $\bar{1}$ 1)	159	1.23	160	1.30	198	1.34	1.07
(10 $\bar{1}$ 0)	160	1.23	160	1.29	179	1.20	1.16
(22 $\bar{4}$ 3)	155	1.19	173 <sup>a</sup>	1.40	218 <sup>a</sup>	1.47	-

<sup>a</sup> different termination - instead of aluminium terminated, their surface is oxygen terminated

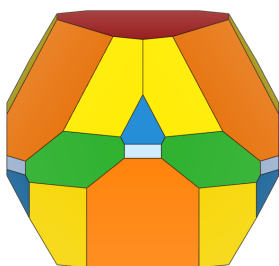


**Figure 4.16:** Wulff plot from the obtained surface energies for  $\alpha$ -Al<sub>2</sub>O<sub>3</sub> with the space group R $\bar{3}c$  - red =  $(0001)$ , orange =  $(1\bar{1}02)$ , yellow =  $(11\bar{2}3)$ , green =  $(11\bar{2}0)$ , blue =  $(10\bar{1}1)$ , and light blue =  $(10\bar{1}0)$ .

terminated cut (see figure 4.15(d)). Unfortunately, Marmier did not mention which termination of the  $(22\bar{4}3)$  surface was studied, but with the obtained results of this

From table 4.5 it can be seen that the absolute values are in very good agreement with previous calculations of Marmier *et al.* [87] and Leeuw *et al.* [86]. For the  $(22\bar{4}3)$  surface this work found a different termination to be more stable than the one studied previously. Leeuw considered the  $(22\bar{4}3)$  surface to be oxygen terminated (see “Table VI.” [86]), which is assumed to be the “O 3”

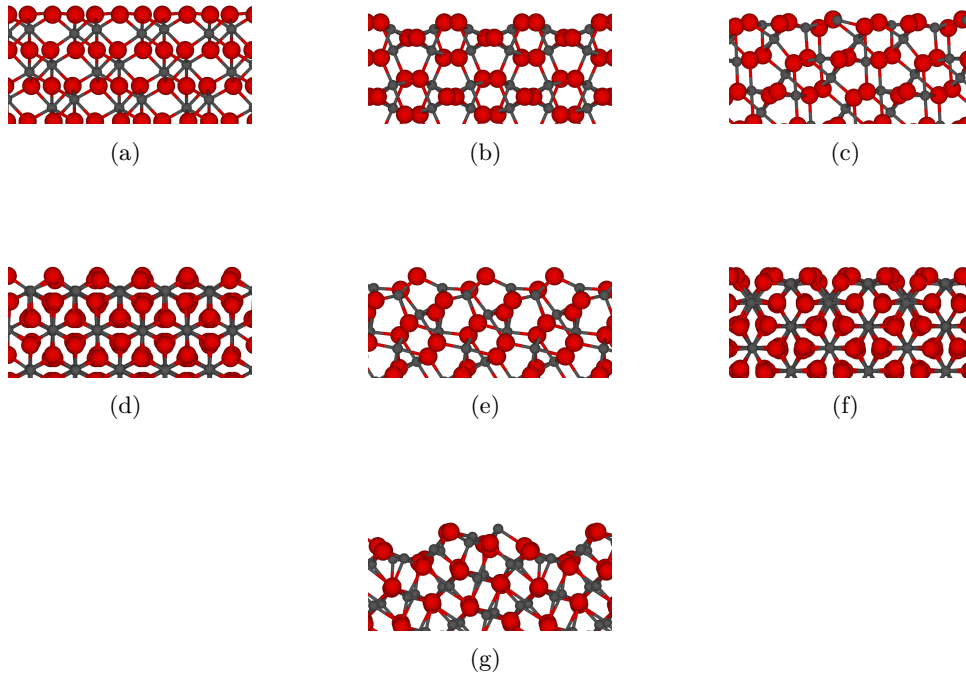


**Figure 4.17:** Side view structure depictions of the most stable terminations of each plain cut surface of  $\alpha\text{-Al}_2\text{O}_3$ ; (a) (0001) (please note that the terminating aluminium ion relaxed towards the surface and is now hidden by the oxygen ions), (b)  $(1\bar{1}02)$ , (c)  $(11\bar{2}3)$ , (d)  $(11\bar{2}0)$ , (e)  $(10\bar{1}0)$ , (f)  $(10\bar{1}1)$ , and (g)  $(22\bar{4}3)$  - gray = aluminium and red = oxygen (VASP-DFT, PBE/PAW, 600.0 eV energy cut-off, D3-BJ).

work being very similar to the ones of Marmier, it is assumed that he investigated the “O 3” termination (this work:  $175 \text{ meV}/\text{\AA}^2$ ; Marmier:  $173 \text{ meV}/\text{\AA}^2$ ) as well. As it can be seen in [figure 4.15\(d\)](#), the “O 3” terminated  $(22\bar{4}3)$  surface is the only one which provides a stoichiometric slab. Taking a second look at [figure 4.15](#) and the work of Kurita *et al.* [88], it can be seen that the assumption “the most stable termination has to be stoichiometric” would be very reasonable since for all other surface cuts this turns out to be the case. Unfortunately, this is not true for the  $(22\bar{4}3)$  surface cut; on the other hand, the  $(22\bar{4}3)$  surface it still does not occur in the Wulff plot, despite the this more stable termination.

In [figure 4.16](#) it can be seen that there are three surfaces which cover the majority of the Wulff plot’s surface area: the aluminium terminated (0001) surface (red), the



oxygen terminated ( $1\bar{1}02$ ) surface (orange), and the aluminium terminated ( $11\bar{2}3$ ) surface (yellow). That is why this work focuses on those three surfaces from now on.

### 4.2.1 Hydration of $\alpha$ -Aluminium Oxide Surfaces

Since under ambient conditions and even with only very small amounts of water the plain surfaces of corundum will be hydrated to form much more stable hydroxide bearing surfaces, those hydrated surfaces are very important. For the most stable (0001) surface both, experimental [90–93] and theoretical [87, 95–100] investigations were already made to determine the actual structure of its hydrated surface. The process of hydrating the plain aluminium terminated (0001) surface leads to the ablation of the terminating aluminium layer by forming  $\text{Al}(\text{OH})_3$ . Per UC, this hydration reaction looks as follows:

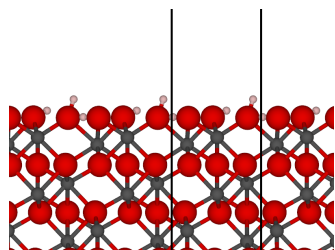
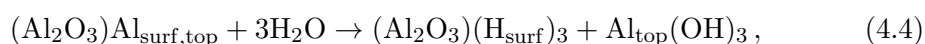


**Figure 4.18:** Side view structure depiction of the hydrated (0001) surface - gray = aluminium, red = oxygen, white = hydrogen, and black line = unit cell boundary (VASP-DFT, PBE/PAW, 600.0 eV energy cut-off, D3-BJ).

where the three water molecules leave a hydrogen ion on the surface each, which form hydroxide groups with the first oxygen layer of the (0001) surface. This led to the hydrated (0001) surface, which is seen in figure 4.18. It shows that two of the three hydroxide groups are nearly in plane with the oxygen layer itself to form stabilising hydrogen bonds within

the surface. After the hydration, the surface stays very smooth and now provides only hydroxide groups as topmost layer.

For the most abundant ( $1\bar{1}02$ ) surface, there are fewer previous investigations, nonetheless, there are both, experimental [101, 102] and theoretical [87, 103–105]

studies, to tackle the investigation of its hydrated structure. Especially Mason *et al.* investigated this very intensively [104] with different terminations as well as different modi of the water adsorption, namely dissociative and molecular. But since experiments can not determine the position of hydrogen atoms that easy, they were not able to strictly differentiate between those two modi. Despite this problem, the fundamental hydration of the  $(1\bar{1}02)$  surface within a UC involves the adsorption of two water molecules in order to fill the CSs of two fivefold coordinated aluminium centres (see figure 4.17(b)). Depending on the two possible adsorption modi, the two corresponding reaction formulas are as follows:

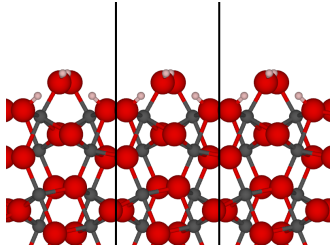


**Figure 4.19:** Side view structure depiction of the hydrated  $(1\bar{1}02)$  surface - gray = aluminium, red = oxygen, white = hydrogen, and black line = unit cell boundary (VASP-DFT, PBE/PAW, 600.0 eV energy cut-off, D3-BJ).

the surface with the purely dissociatively adsorbed water molecules, seen in figure 4.19, is considered in the upcoming investigations. The resulting hydroxides are again oriented in a way that they stabilise each other. While the two hydroxide groups located in the surface valley stabilise the higher lying hydroxide groups, the upper two hydroxide groups stabilise each other even further. This time, the resulting hydrated

Calculations performed for this work show that in contrast to the studies performed by Mason *et al.*, the dissociative only adsorption (see equation (4.5)) results in a more stable structure than the mixed one (see equation (4.6)). This stabilisation accounts for 0.18 eV per UC, which corresponds to a 4 meV/Å<sup>2</sup> increase in the surface energy. Thus, only

( $1\bar{1}02$ ) surface provides a very rough and channel-like surface shape.

The hydrated structure of the third stable and second most abundant ( $11\bar{2}3$ ) surface was only previously investigated by Marmier *et al.* [87]. As mentioned beforehand in section 4.2  $\alpha$ -Aluminium Oxide Surfaces, the plain ( $11\bar{2}3$ ) surface provides an aluminium termination, where the topmost aluminium ions are triply coordinated (see figure 4.17(c)). This is the same structure motif which is provided by the plain (0001) surface (see figure 4.17(a)). Therefore, it is assumed that one part of the hydration of the ( $11\bar{2}3$ ) surface's UC involves the formation of  $\text{Al}(\text{OH})_3$ , as formulated in equation (4.4). Thus, three hydrogen ions are present at the surface, which will form hydroxide groups with the topmost oxygen ions. Regarding the second and third aluminium layer, it can be seen that the aluminium ions of them are only fivefold coordinated (see figure 4.17(c)). That is why, it is assumed that those two under-coordinated aluminium ions per UC are adsorbing one water molecule each to fill their CS, which would follow the formulation of equation (4.5) or equation (4.6).

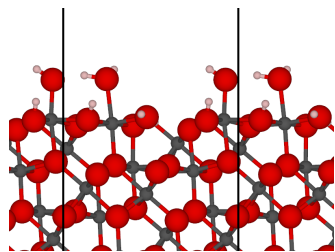


**Figure 4.20:** Side view structure depiction of the hydrated ( $11\bar{2}3$ ) surface - gray = aluminium, red = oxygen, white = hydrogen, and black line = unit cell boundary (VASP-DFT, PBE/PAW, 600.0 eV energy cut-off, D3-BJ).

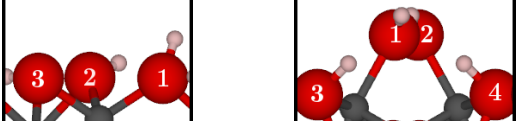
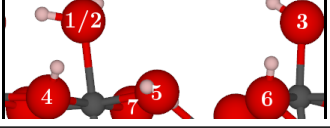
possibilities per UC to arrange the five hydrogen ions in order to form the corresponding hydroxide groups. Thus, those possibilities are studied in terms of their stability. The most stable hydrated ( $11\bar{2}3$ ) surface, which is 0.88 eV per UC more stable than the next stable one, is shown in figure 4.20. Interestingly, the dissociated starting arrangement of this structure relaxes by re-formation of an adsorbed water

Under the hypothesis that the adsorption of water molecules on the under-coordinated aluminium ions is processed dissociatively, there are two immediately formed hydroxide groups (to fill the CSs) and in total five hydrogen ions. Since the topmost oxygen ions are not in the same layer but strictly provide six different ones, there are now six different

molecule, which is also very close to the structure proposal of Marmier *et al.* [87]. This hydrated  $(11\bar{2}3)$  surface now provides again a rough surface with channel-like features but also exhibits a molecularly adsorbed water molecule at the surface.

To ensure that the found hydrated surfaces are stable minima,  $\Gamma$  phonon wavenumber analyses, as explained in subsection 2.1.6 [Normal Mode and Phonon Wavenumbers](#), are performed for all of them. They confirm the stability of the three found hydrated surface structures of  $(0001)$ ,  $(1\bar{1}02)$ , and  $(11\bar{2}3)$  with the OH stretch wavenumbers shown in [table 4.6](#).

**Table 4.6:**  $\Gamma$  phonon wavenumbers of the three hydrated surfaces  $(0001)$ ,  $(1\bar{1}02)$  and  $(11\bar{2}3)$  - fixing all ion positions except the considered hydrogen ion - gray = aluminium, red = oxygen, and white = hydrogen (VASP-DFT, PBE/PAW, 600.0 eV energy cut-off, D3-BJ).

OH Stretch Wavenumbers [ $\text{cm}^{-1}$ ] (Water: 3758.9)						
<b>(0001)</b>						
1	2	3				
3626.4	3556.7	3493.9				
<b>(1<math>\bar{1}02</math>)</b>						
1	2	3	4			
3300.0	3302.6	2593.6	2594.4			
<b>(11<math>\bar{2}3</math>)</b>						
1	2	3	4	5	6	7
2398.9	3660.6	3690.8	3617.6	3332.8	3614.7	3116.2

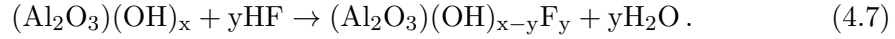
They show a quite clear trend of the wavenumbers of the hydrated  $(0001)$  surface depending on the orientation of the hydroxide groups and, by association, on the strength of the hydrogen bonding. The more the hydroxide groups point out of the surface plane, which corresponds to a decrease of the hydrogen bonding strength, the higher is the wavenumber. For the hydrated  $(1\bar{1}02)$  surface, the rough and channel-like structure provides two differently coordinated hydroxide groups. Two of them, the ones at the hills of the channels ((1) and (2)), are terminal hydroxide groups while the other two in the valley ((3) and (4)) are triply coordinated. Additionally, the hydrox-

ide groups (1) and (2) donate hydrogen bonds to each other, so they form hydrogen bonds from and to singly coordinated hydroxide groups resulting in wavenumbers of  $\approx 3301 \text{ cm}^{-1}$ . Whereas, the hydroxide groups (3) and (4) form hydrogen bonds from triply to singly coordinated hydroxide groups, and by association, the wavenumber drops down significantly to  $\approx 2594 \text{ cm}^{-1}$ , due to a very good acceptor ( $\text{CN} = 1$ ) and an already weak bond of the donating hydroxide group ( $\text{CN} = 3$ ). In case of the hydrated (11 $\bar{2}$ 3) surface, the CNs range from one to three, a molecular adsorbed water molecule is observable, and hydrogen bonds with different strengths are provided as well. Again, there is a comparably very small wavenumber of  $2398.8 \text{ cm}^{-1}$  for an OH stretching mode (1), this time, from a singly coordinated water molecule to a singly coordinated hydroxide group. The four wavenumbers with  $> 3600 \text{ cm}^{-1}$  are provided by hydroxide groups/water, which do not donate hydrogen bonds. Since (4) and (6) are both triply coordinated, their wavenumbers are lower than the one of (3) and the second water wavenumber (2). Concerning the wavenumbers of (5) and (7), they are smaller than the previous ones, because they donate hydrogen bonds but, this time, to doubly coordinated acceptors, which explains their higher wavenumber than the one for (1). The difference between (5) and (7) results from the fact that the former donates its hydrogen bond to an hydroxide group, while the latter donates it to an oxide ion, which is of course a better acceptor than the hydroxide group.

To sum those results up, different trends and their corresponding strengths can be observed. The strongest influence on the OH stretch wavenumbers comes from the formation of hydrogen bonds and the CN of the hydrogen bond acceptor: the lower the CN, the lower the wavenumber. Secondly, the CN of the donating hydroxide group/water influences the wavenumber of the OH stretch moderately: the higher the CN, the lower the wavenumber. And finally, the wavenumbers are also influenced by the nature of the hydrogen bond acceptor: oxide ions as acceptors result in smaller wavenumbers than hydroxide groups as acceptors.

### 4.2.2 Fluorination of Hydrated $\alpha$ -Aluminium Oxide Surfaces

The fluorination of those hydrated surfaces is done by exchanging hydroxide groups with fluoride ions following this reaction scheme:



If not otherwise stated, the term “(reaction) energy” in this subsection will always represent the Gibbs free (reaction) energy.

Starting again with the (0001) surface, in its hydrated form now, there are three symmetrically equivalent hydroxide groups at the surface and therefore, only one possible arrangement of fluoride ions for each fluorination degree is necessary (see [figure 4.21](#)). Please note that symmetrically equivalent here of course only considers the oxygen ions of the hydroxide groups, which are far more rigidly incorporated to the system than the hydrogen ion of the hydroxide groups. Therefore, the hydrogen ions can easily relax to stabilise the surface after the fluorination.

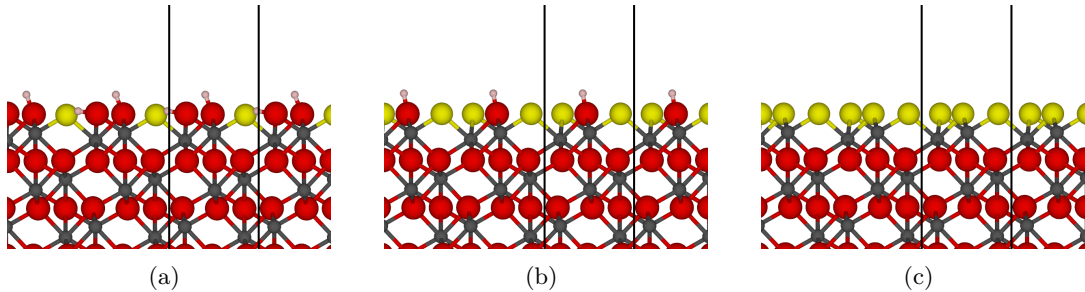


**Figure 4.21:** Side view structure depictions of the fluorinated (0001) surfaces - gray = aluminium, red = oxygen, yellow = fluorine, white = hydrogen, and black line = unit cell boundary (VASP-DFT, PBE/PAW, 600.0 eV energy cut-off, D3-BJ).

To ensure that the fluorinated surfaces are stable minima,  $\Gamma$  phonon wavenumber calculations are performed again. They do not only provide once more the OH stretch wavenumbers of the remaining hydroxide groups but also enable the calculation of energies at various temperatures. This was done by using the formulations of subsection 2.1.5 [Statistical Thermodynamics](#) and adding the contributions of enthalpy

and entropy to the total electronic energy of the systems. Additionally, the same is done for water and hydrogen fluoride to enable the calculation of reaction energies at different temperatures.

**Table 4.7:** Reaction energies  $G_{\text{rea}}$  for the fluorination reaction of the hydrated (0001) surface in a stepwise approach and per introduced fluoride ion in a one-step reaction (VASP-DFT, PBE/PAW, 600.0 eV energy cut-off, D3-BJ).

[eV]	Reaction	0 K	10 K	300 K	1273 K	1773 K
$G_{\text{rea}}$ stepwise	0 > 1	-0.630	-0.622	-0.649	-0.712	-0.724
	1 > 2	-0.236	-0.254	-0.296	-0.472	-0.545
	2 > 3	-0.330	-0.317	-0.333	-0.325	-0.299
$G_{\text{rea}}$ per $\text{F}^-$	0 > 1	-0.630	-0.622	-0.649	-0.712	-0.724
	0 > 2	-0.433	-0.438	-0.473	-0.592	-0.635
	0 > 3	-0.399	-0.398	-0.426	-0.503	-0.523

As it can be seen in [table 4.7](#), the thermodynamics favour the fluorination reaction of this surface all the way down to a fully fluorinated surface. Even the stepwise reaction pathway shows exergonic reactions for each step. While the first fluorination releases a significant amount of energy, the amount of energy released during the second step drops down to only one third compared to the previous one. This results from the loss of stabilisation via hydrogen bonding. In the singly fluorinated (0001) surface (see [figure 4.21\(a\)](#)), there is still the hydrogen bond in-plane with the surface, which stabilises this structure. Whereas, the remaining hydroxide group in the doubly fluorinated (0001) surface (see [figure 4.21\(b\)](#)) is pointing outwards the surface and, by association, do not further stabilise the surface. During the third fluorination step, there is no such stabilisation loss coming from hydrogen bonding, so the energy release rises again but only slightly, which indicates a decreasing preference of fluoride ions on this surface with an increasing amount of them. Nonetheless, the fluorination of the (0001) surface is thermodynamically favourable at various temperatures and for all fluorination degrees. Additionally, all fluorination reactions preserve very smooth surface without any reconstructions.

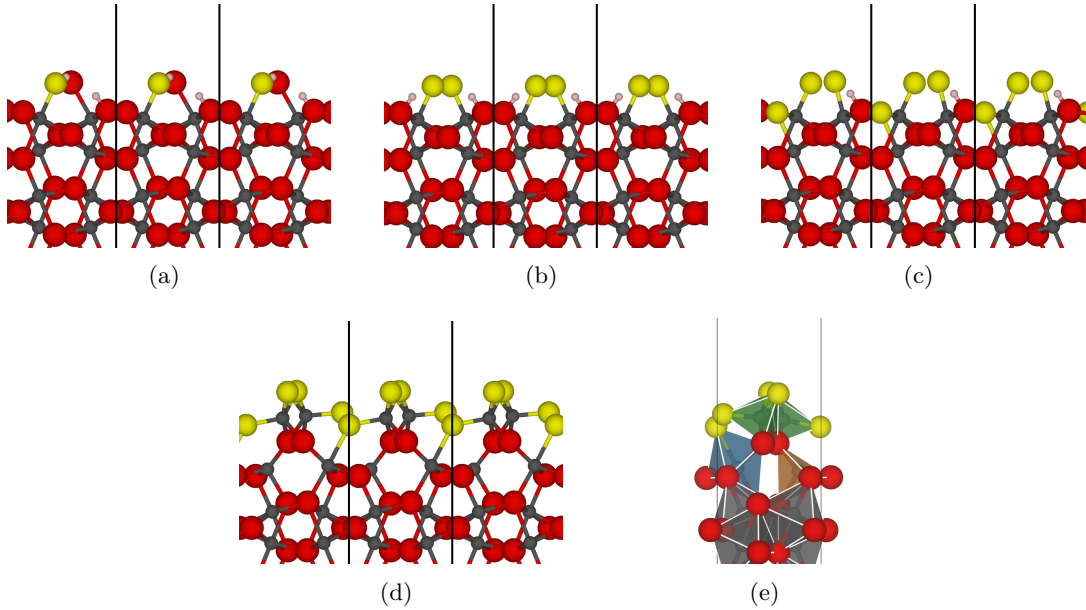


**Figure 4.22:** Side view structure depictions of the fluorinated ( $1\bar{1}02$ ) surfaces and a clarification of the **CS** of the reconstructed fourfold fluorinated one - gray = aluminium, red = oxygen, yellow = fluorine, white = hydrogen, black line = unit cell boundary, gray **CS** = 6, green/blue **CS** = 5, and orange **CS** = 4 (VASP-DFT, PBE/PAW, 600.0 eV energy cut-off, D3-BJ).

Going to the rough, channel-like hydrated ( $1\bar{1}02$ ) surface, the two different heights and the corresponding **CNs** play a very important role. Since this hydrated surface of the ( $1\bar{1}02$ ) cut is build very regularly, it provides two pairs of equivalent hydroxide groups: the top pair as well as the bottom pair. Due to this circumstance, the amount of possible structures per fluorination degree is decreased here as well and results in two possible **UC** structures for one and three fluoride ions and in three possible structures for two fluoride ions per **UC**. The most stable structures of each fluorination degree are shown in figure 4.22 and are used in the following studies.

Taking a closer look at figure 4.22(a), which is  $\approx 1.27$  eV more stable than the fluorination of an hydroxide group located in the valley, it can be seen that one hydrogen ion leaves its hydroxide group (left in the channel valley). Due to the periodicity, the addressed hydroxide group is also bound to the aluminium centre which gets fluorinated. Therefore, the Brønsted acidity of this hydroxide group increases enough to



enable the re-formation of a molecularly adsorbed water molecule at the position (2), which was slightly unfavourable for the hydrated surface itself. Unfortunately, the re-formed water molecule is not easily recognisable in [figure 4.22\(a\)](#). For the second fluorination step, the top position is again more favoured for the fluorination reaction, than the one of the two valley positions and is in fact  $\approx 0.04$  eV more stable. Taking the two previous results into account, the triply fluorinated UC now only have one reasonable fluoride arrangement left, since it would be very unlikely to fluorinate the two hydroxide groups in the valley of the channels first. Nonetheless, both possibilities were analysed, and indeed, the structure shown in [figure 4.22\(c\)](#) is favoured by  $\approx 0.34$  eV.

The fourfold fluorinated surface reconstructs itself during the optimisation due to the repulsive fluoride-fluoride interaction and the lack of stabilising hydrogen bonds. This reconstruction results in a variety of CS and CN changes. As it can be seen in [figure 4.22\(e\)](#), those include the formation of a tetrahedrally coordinated aluminium center (orange), a distorted trigonal bipyramidal aluminium centre with only one fluoride ion (blue), and two distorted trigonal bipyramidal aluminium centres with three fluoride ions directly at the surface (green). Since the former two are deeper in the surface, they do not expose under-coordinated sites, whereas the latter two do so with one free site at each aluminium centre.

Taking a look at the reaction energies  $G_{\text{rea}}$  for the fluorination of the hydrated  $(1\bar{1}02)$  surface, it can be seen that the first two fluorination steps are thermodynamically favourable for the system. The fluorination of the hydroxide groups located in the valley of the channel-like surface structure is not only more difficult to access, but it is a very endergonic process as well, which can be seen in the stepwise fluorination of the doubly fluorinated surface to the triply fluorinated one. Due to its reconstruction, the fourfold fluorinated surface becomes more stable and, by association, decreases the amount of needed energy for this reaction step. Nonetheless, the only possibility to fully fluorinate the surface thermodynamically advantageous is by doing it in

**Table 4.8:** Reaction energies  $G_{\text{rea}}$  for the fluorination reaction of the hydrated ( $1\bar{1}02$ ) surface in a stepwise approach and per introduced fluoride ion in a one-step reaction (VASP-DFT, PBE/PAW, 600.0 eV energy cut-off, D3-BJ).

[eV]	Reaction	0 K	10 K	300 K	1273 K	1773 K
$G_{\text{rea}}$ stepwise	0 > 1	-0.470	-0.422	-0.450	-0.565	-0.603
	1 > 2	-0.186	-0.196	-0.232	-0.358	-0.422
	2 > 3	0.312	0.279	0.231	0.001	-0.102
	3 > 4	0.143	0.173	0.117	-0.060	-0.128
$G_{\text{rea}}$ per $\text{F}^-$	0 > 1	-0.470	-0.422	-0.450	-0.565	-0.603
	0 > 2	-0.328	-0.309	-0.341	-0.467	-0.513
	0 > 3	-0.115	-0.113	-0.151	-0.254	-0.376
	0 > 4	-0.050	-0.042	-0.084	-0.248	-0.314

one-step, where the first two favourable reaction steps can compensate the last two unfavourable ones. Otherwise, the stepwise approach should allow an easy way to form a very well described, channel-like mixed surface of fluoride ions and hydroxide groups, where the fluoride ions will sit on the hills while the hydroxide ions remain in the valleys.

The hydrated ( $11\bar{2}3$ ) surface provides again a rough surface with isles of higher lying surface ligands. Assuming a dissociation of the molecularly adsorbed water molecule during the fluorination reaction, there are seven hydroxide groups available per UC to be fluorinated. Due to the lack of symmetry between those groups, there are much more possible structures for each fluorination degree than for the previous ones. Fortunately, the results of the previous two surfaces revealed in both cases that a continuous fluorination of the hydrated surface provides the most stable structures. Thus, the amount of possible structures per fluorination degree can be decreased and result in seven singly fluorinated surface structures, six doubly fluorinated surface structures, etc. Within all fluorination degrees, the most stable structures (see [figure 4.23](#)) are  $\approx 200$  meV more stable than the second stablest structure.

It can be seen that the molecularly adsorbed water remains at the surface until there is no other possibility to fluorinate the surface while the terminal hydroxide group is

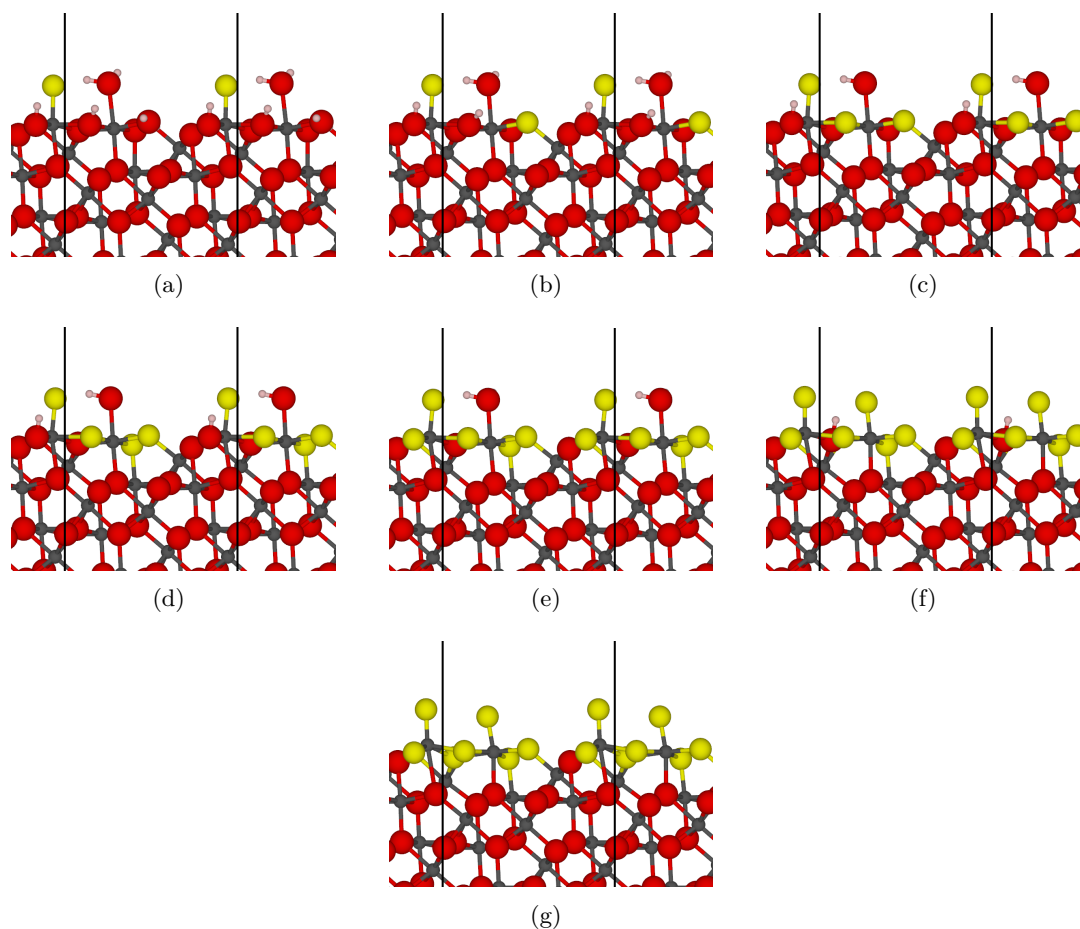


**Figure 4.23:** Side view structure depictions of the fluorinated  $(11\bar{2}3)$  surfaces - gray = aluminium, red = oxygen, yellow = fluorine, white = hydrogen, and black line = unit cell boundary (VASP-DFT, PBE/PAW, 600.0 eV energy cut-off, D3-BJ).

fluorinated in the first step already (see figure 4.23(a)). Additionally, figure 4.23(b) shows that the fluorination proceeds at the hydroxide groups located in the valley and that the fluorination of the aluminium centre carrying the water molecule is more favourable than the one with the first fluoride ion. Once there is no other option to fluorinate the surface without dissociating the water molecule, it is split and fluorinated at the resulting isle-site hydroxide group. This again confirms the preference of terminal hydroxide groups for the fluorination reaction. Interestingly, this surface does not reconstruct itself once it is fully fluorinated, which is due to fact that the top most aluminium CS orientations do not encourage such a possible

reconstruction. Since those two octahedral CSs are oriented in a corner-up way, the four ligands in the middle are more rigidly incorporated in the CS network and a reconstruction of those CSs would result in a more dramatic change of the structure.

**Table 4.9:** Reaction energies  $G_{\text{rea}}$  for the fluorination reaction of the hydrated  $(11\bar{2}3)$  surface in a stepwise approach and per introduced fluoride ion in a one-step reaction (VASP-DFT, PBE/PAW, 600.0 eV energy cut-off, D3-BJ).

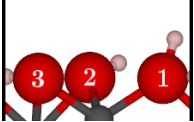
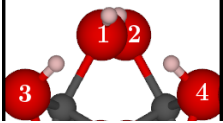
[eV]	Reaction	0 K	10 K	300 K	1273 K	1773 K
$G_{\text{rea}}$ stepwise	0 > 1	-0.598	-0.570	-0.610	-0.721	-0.755
	1 > 2	-0.370	-0.364	-0.375	-0.386	-0.372
	2 > 3	-0.169	-0.183	-0.221	-0.362	-0.417
	3 > 4	-0.137	-0.121	-0.145	-0.202	-0.211
	4 > 5	0.022	0.001	-0.033	-0.163	-0.212
	5 > 6	0.644	0.635	0.590	0.431	0.367
	6 > 7	0.244	0.212	0.158	-0.088	-0.200
$G_{\text{rea}}$ per $\text{F}^-$	0 > 1	-0.598	-0.570	-0.610	-0.721	-0.755
	0 > 2	-0.484	-0.467	-0.493	-0.553	-0.564
	0 > 3	-0.379	-0.372	-0.402	-0.490	-0.515
	0 > 4	-0.318	-0.310	-0.338	-0.418	-0.439
	0 > 5	-0.250	-0.247	-0.277	-0.367	-0.393
	0 > 6	-0.101	-0.100	-0.132	-0.234	-0.267
	0 > 7	-0.052	-0.056	-0.091	-0.213	-0.257

The first fluorination of the hydrated  $(11\bar{2}3)$  surface provides again a significant amount of energy over the whole temperature range because it is again a terminal substitution, as it was the case for the first fluorination of the hydrated  $(1\bar{1}02)$  surface. Additionally, since only a weaker hydrogen bond from the molecularly adsorbed water molecule to the terminal hydroxide group is removed, the exergonic energy for this first fluorination is higher than the one for the hydrated  $(1\bar{1}02)$  surface. The subsequent fluorination of the hydroxide groups located in the valley provides smaller exergonic energies with a decreasing trend for higher fluorination degrees. Differences of the reaction energies for the fluorination of the valley-site hydroxide groups between the  $(1\bar{1}02)$  and the modified  $(11\bar{2}3)$  surfaces as well as reaction energies for the fluorinated  $(11\bar{2}3)$  surfaces themselves result from the fluoride-fluoride repulsion, the

loss of hydrogen bonds, and different CNs of the substituted hydroxide groups. While for the doubly and triply fluorinated ( $1\bar{1}02$ ) surfaces the hydroxide groups are close to already fluorinated positions, they only provide weak hydrogen bonds to fluoride ions and are triply coordinated along with it. The valley-site hydroxide groups of the increasingly fluorinated ( $11\bar{2}3$ ) surfaces provide more nuanced combinations of those properties. Thus, their reaction energies can be exergonic especially for the doubly coordinated substituted hydroxide groups. The noticeable difference between the triply coordinated hydroxide groups of the modified ( $1\bar{1}02$ ) and the modified ( $11\bar{2}3$ ) surfaces might again result from the orientation and location of the corresponding aluminium CSs within the considered surface. For the last two reactions, the molecularly adsorbed water molecule is dissociated, which of course results in a very high endergonic reaction energy for the sixth fluorination. The seventh fluorination step is now simply a fluorination of a triply coordinated valley-site hydroxide group and therefore provides a relatively mediocre endergonic reaction energy. In the second part of [table 4.9](#) it can be seen that the one step reaction approach can again compensate the thermodynamically unfavourable last two reaction steps, which provides again the possibility to partially and also fully fluorinate the surface with favourable thermodynamics depending on the initial amount of the fluorinating agent.

Since  $\Gamma$  phonon wavenumber calculations are used to verify the found fluorinated structures, the OH stretch wavenumbers are obtained handily as well (see [table 4.10](#)). Starting with the fluorinated (0001) surfaces and remembering [table 4.6](#), it can be seen that the first fluorination step increases the OH stretch wavenumber of the formerly bend hydroxide group (2) while the wavenumber for (3) only decreases slightly. Considering that (2) now provides an angle of  $69^\circ$  (measured against the surface plane) while (1) provided an angle of  $61^\circ$ , which would already result in an wavenumber increase, the influence of the fluorination on the OH stretch wavenumbers can not be definitely stated. The decrease of the wavenumber for (3) should mainly result from the stronger hydrogen bonding due to a small turn of this group's orientation.

**Table 4.10:**  $\Gamma$  phonon wavenumbers of the fluorinated surfaces (0001), ( $1\bar{1}02$ ) and ( $11\bar{2}3$ ) - fixing all ion positions except the considered hydrogen ion; notation X-Y-Z: where X represents up (1) and down (2), Y stands for front (1) and back (2), and Z expresses left (1), middle (2), and right (3) (VASP-DFT, PBE/PAW, 600.0 eV energy cut-off, D3-BJ).

# $F^-$	OH Stretch Wavenumbers [ $cm^{-1}$ ]						
	<b>(0001)</b>						
	1	2	3				
1		3676.5	3467.3				
2		3733.3					
<b>(<math>1\bar{1}02</math>)</b>							
	1	2	3	4			
1		3102.7	2923.5 <sup>a</sup>	3418.0			
2			3213.5	3213.7			
3				3183.0			
<b>(<math>11\bar{2}3</math>)</b>							
	1	2	3	4	5	6	7
1	2976.6	3660.6		3613.9	3376.0	3595.0	3135.1
2	2949.3	3644.3		3515.2		3590.7	3215.1
3	2983.1	3609.7				3584.2	3269.7
4	2977.9	3618.2				3582.1	
5	2946.0	3620.9					
6	3305.6 <sup>b</sup>						

<sup>a</sup> second hydrogen at (2) due to re-formation of molecularly adsorbed water

<sup>b</sup> after dissociation and fluorination this hydroxide groups is located in the valley at (8)

Going to the doubly fluorinated (0001) surface, the angle of (2) increases again to  $78^\circ$ , so does the OH stretch wavenumber as well. Summarising those results for the differently fluorinated (0001) surfaces, the direct impact of the fluoride ions on the OH stretch wavenumbers could not be seen clearly yet.

For the fluorinated ( $1\bar{1}02$ ) surface the first fluorination increases the Brønsted acidity of (3), and by association, (2) and the hydrogen from (3) re-form a water molecule. This results in a decrease of the OH stretch wavenumber (2) due to the now two bound hydrogen ions. At the same time, the OH stretch wavenumber of the hydrogen previously bound to (3) increases because its hydrogen bonding is now weakened. The second hydroxide group located in the valley shows a strongly increased OH stretch

wavenumber because there is now only a very weak hydrogen bond acceptor with the fluoride ion. Since the second fluorination of the hydrated ( $1\bar{1}02$ ) surface resulted in a very symmetric mixed modified surface, this symmetry is also seen in the OH stretch wavenumbers of the two remaining hydroxide groups in the valley. Their wavenumbers decrease by around  $200\text{ cm}^{-1}$  compared to (4) of the singly fluorinated ( $1\bar{1}02$ ) surface because the increasing amount of the fluoride ions in their corresponding aluminium CS increases their Brønsted acidity and, by association, lowers the strength of those bonds. The same effect is observed for the triply fluorinated ( $1\bar{1}02$ ) surface where the OH stretch wavenumber is lowered further.

Going on to the fluorinated ( $11\bar{2}3$ ) surfaces, looking at [table 4.10](#), and remembering [table 4.6](#), it can be seen that the hydrogen bonding hydrogen of the molecularly adsorbed water molecule first increases its OH stretch wavenumber by  $\approx 600\text{ cm}^{-1}$ , then stays roughly the same, and then increases again by  $\approx 250\text{ cm}^{-1}$ . The first increase due to the first fluorination, results from the much weaker hydrogen bond acceptor fluoride, compared to the hydroxide group. Up to the fifth fluorination, the corresponding bond strength is not much influenced by further substitutions. With the sixth fluorination the water molecule has to be dissociated and the resulting hydroxide group (8), now located in the valley, increases the OH stretch wavenumber, but remains quite small for an hydroxide group without hydrogen bonding. This is due to the very high amount of fluoride surrounding this hydroxide group which, by association, becomes more Brønsted acidic. The second hydrogen of the molecularly adsorbed water molecule (2) only provides very slight changes of its OH stretch wavenumber. It first decreases a little bit with increasing fluorination due to the increasing Brønsted acidity resulting from the stronger electron withdrawing nature of the fluoride ions and then increases again by an even smaller amount until it is substituted for the sixth fluorination degree. Since the later occurring increase of the OH stretch wavenumber is very small, this can be attributed to the surface relaxation and the corresponding increasing distortion of the CS, which comes along with

a weaker *para*-effect of the two opposing ligands. The OH stretch wavenumbers of (6) simply decreases progressively during the fluorination reactions due to its increasing Brønsted acidity. Looking at (7) and its OH stretch wavenumbers, a small and then two mediocre increases are observed. Firstly, the small increase of  $\approx 20 \text{ cm}^{-1}$  might result from the combination of different even smaller influences, like the distortion of the connected aluminium CSs or a changed competition of the ligands of those CSs. The two mediocre increases are due to the fact that with the second fluorination this hydroxide group gets its hydrogen bond donor substituted, which strengthens the bond in this hydroxide group. And secondly, for the third fluorination the hydrogen bond acceptor of (7) gets its *para*-ligand substituted which results in stronger competition of those ligands and, by association, in a weaker hydrogen bond acceptor capability and, finally, in a weaker hydrogen bonding of (7). Regarding (4), its decreasing OH stretch wavenumber is again linked to its increasing Brønsted acidity due to the increasing amount of fluoride in the corresponding aluminium CS. As a last point, the increase of the OH stretch wavenumber of (5) might be explained by the summation of smaller influences, as it was the case for the first wavenumber change of (6).

To sum the influence of fluoride ions on the OH stretch wavenumbers of surface hydroxide groups up, the more fluoride is present in the surface, the stronger the hydroxide groups Brønsted acidity gets, so the smaller the wavenumbers are. Furthermore, the fluoride ions much weaker capability to act as a hydrogen bond acceptor leads to an increase of the corresponding hydroxide groups OH stretch wavenumber. Finally, smaller wavenumber changes can occur due to slight changes in the distortion of the corresponding aluminium CSs and/or due to changes in the competition of the ligands in those CSs, which can result from weakening or strengthening other hydrogen bonds.



### 4.2.3 NMR Shifts of $\alpha$ -Aluminium Oxide Surfaces

Similar to the bulk materials, the surfaces are studied with regard to their NMR shifts as well. Thus, the  $^{27}\text{Al}$  NMR shifts and  $^{19}\text{F}$  NMR shifts of the plain and modified (hydrated or fluorinated) surfaces are calculated and will be looked at in this subsection.

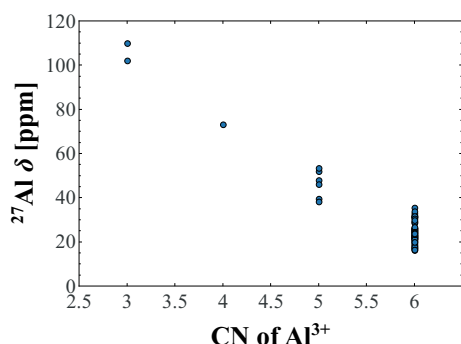


**Figure 4.24:**  $^{27}\text{Al}$  NMR shifts of the plain and modified  $\alpha\text{-Al}_2\text{O}_3$  surfaces in dependence on the CN of the corresponding aluminium centre (VASP-DFT, PBE/PAW, 600.0 eV energy cut-off, D3-BJ).

Starting with the  $^{27}\text{Al}$  NMR shifts, firstly, they are plotted against the CN of their corresponding aluminium centre, shown in figure 4.24. A very clear linear trend is observable with a spread of  $\approx 100$  ppm. As it was shown by Copéret *et al.* [213] and seen for the bulk materials, the band interaction effect plays a huge role for the  $^{27}\text{Al}$  NMR shifts in dependence on their CN. The very drastic influence of this effect during the CN

change of the aluminium centres results mainly from the strong structural change of those aluminium CS. By changing the geometry of the CS, the occupation of the bands can change and, by association, the interaction between them and the unoccupied ones which is very crucial for the paramagnetic part of NMR shifts, becomes much more different. Copéret *et al.* [213] showed for clusters that with a decreasing CN the increasing deshielding effect results from the orbital interaction which becomes stronger between occupied orbitals and unoccupied orbitals. Accordingly, the band interaction effect is strongest for the triply coordinated aluminium centres of the plain surface cuts of (0001) and (11 $\bar{2}$ 3), while it decreases with an increasing CN.

Since the strong CN dependence, shown in figure 4.24, showed also spreads of the  $^{27}\text{Al}$  NMR shifts, those spreads are further investigated in more detail (see figure 4.25).

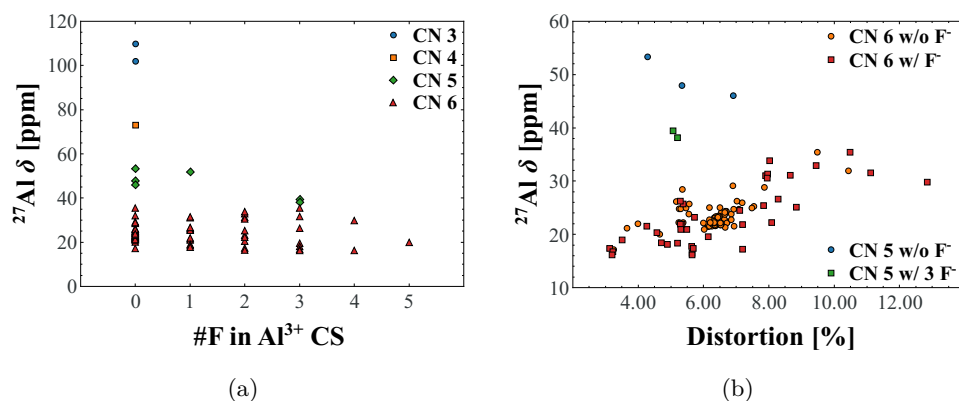


**Figure 4.25:**  $^{27}\text{Al}$  NMR shifts of the plain and modified  $\alpha\text{-Al}_2\text{O}_3$  surfaces - (a) in dependence on the CS stoichiometry and (b) in dependence on the distortion of the corresponding CS (VASP-DFT, PBE/PAW, 600.0 eV energy cut-off, D3-BJ).

Firstly, the  $^{27}\text{Al}$  NMR shifts are plotted against the fluoride amount of the corresponding aluminium CSs in figure 4.25(a). Since all aluminium centres from the top surface to the middle of the slab models UC are taken into account, there is a very dense region of  $^{27}\text{Al}$  NMR shifts for the unfluorinated octahedrally coordinated aluminium centres of  $\approx 23$  ppm, which corresponds to the aluminium centres in the inner part of the slab models UCs. Thus, the remaining  $^{27}\text{Al}$  NMR shifts correspond to the surface aluminium centres where there are now terminal fluoride ions and surface fluoride ions with less neighbours, which was of course not the case in the bulk materials gibbsite, bayerite, diasprore and boehmite. That is why the previously observed trends can not be identified here as well. It can be seen that for aluminium centres with  $\text{CN} = 5$  the  $^{27}\text{Al}$  NMR shifts show the possibility of a linearly or parabolically decreasing trend, while the octahedrally coordinated aluminium centres are heavily spread within the different fluorination degrees and provide the possibility of a linear trend with near zero negative slope. The decreasing trend for the fivefold coordinated aluminium centres results from the stronger band interaction effect and the weakening of this effect with increasing amounts of fluoride. Since the band interaction effect is stronger for those under-coordinated aluminium centres, the weakening of the band interaction

effect can compensate the strengthening of the electron density effect of the terminal and surface fluoride ions, so this trend looks similar to the ones of the clearly sliced bulk materials gibbsite, bayerite and boehmite. Regarding the octahedrally coordinated aluminium centres, there seems to be no dependence of the  $^{27}\text{Al}$  NMR shifts on the fluorination degree. But considering the previous results of the bulk materials and the results of the fivefold coordinated aluminium centres, it can be stated that the band interaction effect and the electron density effect are cancelling each other out this time. With an overall weaker band interaction effect for those fully coordinated aluminium centres, it is no longer able to turn the stronger electron density effect of the terminal and surface fluoride ions, and by association, the trend looks very flat. In order to tackle the spreads of the different fluorination degrees for the five- and sixfold coordinated aluminium centres, their  $^{27}\text{Al}$  NMR shifts are plotted against the distortion (see section 3.1 [Distortion of Cation Coordination Spheres](#) again) of the corresponding aluminium CSs in [figure 4.25\(b\)](#). It can be seen that for the fivefold coordinated aluminium centres without fluoride ions there is a decreasing trend of the  $^{27}\text{Al}$  NMR shifts with increasing distortion. Since for these aluminium centres the band interaction is quite strong, it is also very sensible to comparably small changes. Thus, a more distorted CS of an aluminium centre results in a stronger weakening of this effect and, by association, in a more shielded  $^{27}\text{Al}$  NMR shift. Considering the sixfold coordinated aluminium centres, the band interaction effect is weaker while the electron density effect is stronger due to terminal and surface fluoride ions and oxide ions in the aluminium CS. While the stronger band interaction effect could compensate this stronger electron density effect for the fivefold coordinated aluminium centres, it is not strong enough for the sixfold coordinated ones. Due to this, a stronger distortion results in a weaker para-effect and, by association, in a stronger electron withdrawing of the anions. Therefore, the corresponding aluminium centres are more deshielded which then results in a higher  $^{27}\text{Al}$  NMR shift.

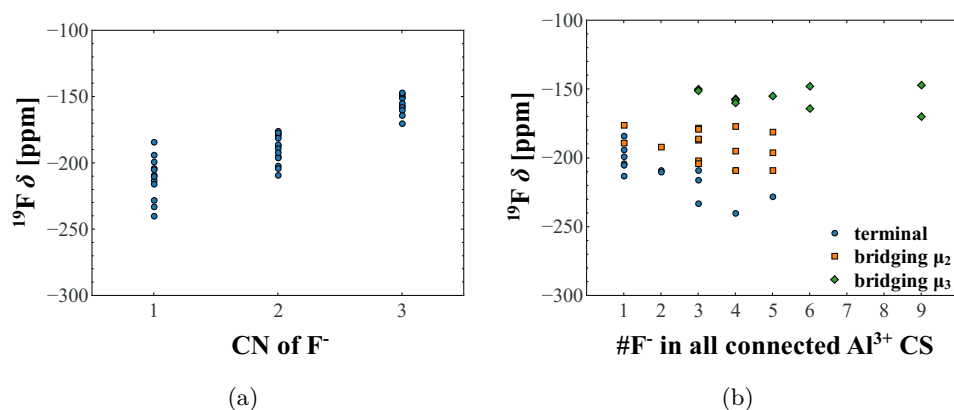


**Figure 4.26:**  $^{19}\text{F}$  NMR shifts of the fluorinated  $\alpha\text{-Al}_2\text{O}_3$  surfaces - (a) in dependence on the CN of the considered fluoride ion and (b) in dependence on the combined CS stoichiometry of the connected aluminium centres (VASP-DFT, PBE/PAW, 600.0 eV energy cut-off, D3-BJ).

Moving from the  $^{27}\text{Al}$  NMR shifts to the  $^{19}\text{F}$  NMR shifts of the plain and modified surfaces, figure 4.26 shows them and their found trends. In figure 4.26(a) it can be seen that the CN of the fluoride ions plays an important role and provides a linear increase of the  $^{19}\text{F}$  NMR shifts with increasing CN. This increase results mainly from the electron density effect, because the higher the CN, the more electron density of the fluoride is shared with the surrounding aluminium centres. Therefore, the electron density at the fluoride ion decreases with increasing CN and thus, the  $^{19}\text{F}$  NMR shifts increase. Since it can be seen in figure 4.26(a) that there are quite drastic spreads for the different CNs, they are further studied by plotting them against the summed up fluoride ions of all connected aluminium centres, which is seen in figure 4.26(b). It shows that for the three different binding motifs of the fluoride ions the  $^{19}\text{F}$  NMR shifts decline with an increasing amount of fluoride ions. This decline results from the band interaction effect, which gets weakened with an increasing amount of fluoride ions, as it was seen for gibbsite, bayerite and boehmite as well. While the decline of the  $^{19}\text{F}$  NMR shifts is comparably strong for the terminal fluoride ions, it gets weaker with increasing CN of those fluoride ions. Due to the decreasing effect of each fluoride ion itself with increasing CN, the impact of the surrounding fluoride ions declines

as well, because the connection to the bridging aluminium centre becomes weaker if more aluminium ions are connected to the considered fluoride ions. Thus, the slopes of those three trends decrease with increasing CN.

## 4.3 Water Adsorption on Modified $\alpha$ -Aluminium Oxide Surfaces

This section focuses on the interaction of molecular water with the hydrated and fluorinated surfaces described in the previous section 4.2  $\alpha$ -Aluminium Oxide Surfaces. To do so, different amounts of water molecules, up to three, are put on truncated surface within a UC. The exact procedure and the corresponding computational approach can be looked up in subsection 2.2.4 Surface Scans. These truncations lead to the following atomic region thicknesses for the (0001), the (1 $\bar{1}$ 02), and the (11 $\bar{2}$ 3) surface: ten atomic layers with four fixed ones, ten plus one atomic layers with five fixed ones, and 22 plus two atomic layers with twelve fixed ones, respectively. In order to evaluate the interaction of water with the surfaces, the adsorption energy is calculated via equation (2.95), which is shown here again for convenience:

$$E_{\text{ads}} = E_{\text{slab}+\text{H}_2\text{O}} - E_{\text{slab}} - E_{\text{H}_2\text{O}} \quad (4.8)$$

Please remember that the adsorption energy surfaces always represent a  $2 \times 2 \times 1$  SC although mainly UCs are used for the calculations. This is done for a better comparability with the few cases where actually SCs are calculated and for a better clearness regarding the edges of the UCs.

### 4.3.1 The (0001) Surface

Keeping the order introduced in section 4.2  $\alpha$ -Aluminium Oxide Surfaces the same, the hydrated and fluorinated surfaces of the (0001) cut are the first ones to consider. In order to classify this study of the adsorption of water on modified  $\alpha$ -aluminium oxide (0001) surfaces in contrast to the work of Wirth *et al.* [98] some aspects need to be addressed. Since Wirth *et al.* used four differently fluorinated UC in one  $2 \times 2 \times 1$  SC, there is completely different interaction with each other. So the fully fluorinated

UC right next to the singly fluorinated UC has of course a drastic impact on the latter's hydroxide groups with the adsorbing water molecule. With adsorption of the second water molecules on the mixed SC, one UC is already nearly blocked by the first water molecule. Although their work already gave a great insight in the influence of surface fluoride ions on the adsorption of water molecules on modified  $\alpha$ -aluminium oxide (0001) surfaces, this work will extend their study in a more systematic way. Thus, the effects of the differently fluorinated surfaces, the already adsorbed water molecules, and the spheres of influence of them will be studied in more detail.

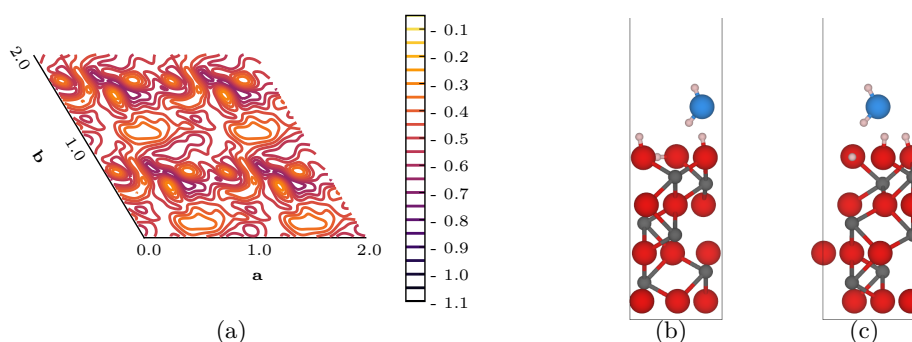


**Figure 4.27:** The first water molecule on the UC of the hydrated (0001) surface; (a) adsorption energy surface [eV], (b) side view structure depiction along  $a$ , and (c) side view structure depiction along  $b$  - gray = aluminium, red = oxygen, white = hydrogen, and light blue = first water oxygen (VASP-DFT, PBE/PAW, 600.0 eV energy cut-off, D3-BJ).

Looking at the adsorption energy surface of the first water molecule that adsorbs on the hydrated (0001) surface in figure 4.27(a), it can be seen that there is no clear pattern which would represent the underlying surface structure. Even the positioning of the three hydroxide groups can not be tracked with this visualisation of the adsorption energies. This is due to the comparable ease with which the hydroxide groups can change their orientation to suit the approaching water molecule the best way possible in order to form favourable hydrogen bonds. Thus, the first water molecule adsorbs quite favourably on the hydrated (0001) surface with an average adsorption energy of  $-0.48$  eV per UC. The best possible adsorption energy is reached, if it adsorbs directly between the three hydroxide groups on the surface. Doing so, it donates one

hydrogen bond to the hydroxide group which is oriented in-plane with the surface, while at the same time the water molecule accepts two hydrogen bonds from the two outwards pointing hydroxide groups (see figure 4.27(b) and figure 4.27(c)). Hence, a trigonal pyramidal  $O_4$  structure motif is formed which is then basally connected via hydrogen bonds to the next ones and, finally, results in an adsorption energy of  $-0.65$  eV.

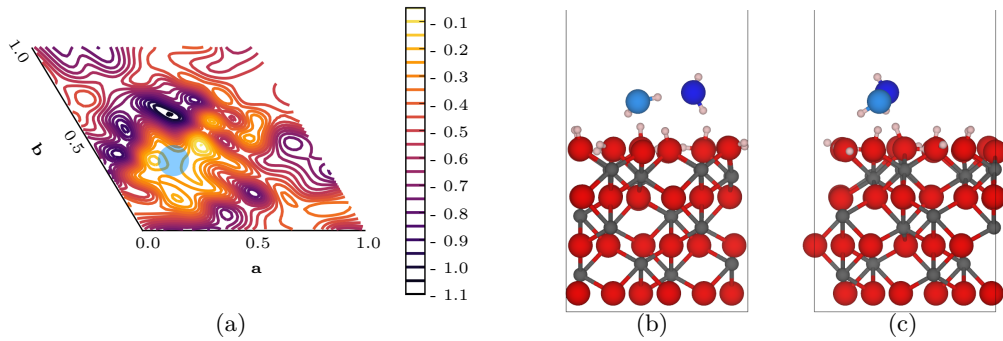


**Figure 4.28:** The second water molecule on a  $2 \times 2 \times 1$  SC of the hydrated (0001) surface; (a) adsorption energy surface [eV], (b) side view structure depiction along  $a$ , and (c) side view structure depiction along  $b$  - gray = aluminium, red = oxygen, white = hydrogen, light blue = first water oxygen, and blue = second water oxygen (VASP-DFT, PBE/PAW, 600.0 eV energy cut-off, D3-BJ).

In order to tackle the influence of the firstly adsorbed water molecule on the adsorption of a second one, the surface is extended from a single UC to a  $2 \times 2 \times 1$  SC. This is done by combining a UC bearing one already water molecule and three UC with no added water molecules, resulting in 0.25 water molecules per UC before the adsorption procedure. Thus, there should be enough space, regarding the periodicity, between the already adsorbed water molecules that only one water molecule affects the second ones adsorption. In figure 4.28(a) the position of the firstly adsorbed water molecule is indicated with a light blue circle. It can be seen that the adsorption directly on top of this water molecule is comparably unfavourable. Although favourable hydrogen bonds can be formed, there is only one hydrogen bond possible if the second water molecules stacks with the first one. That is why a very favourable adsorption around the first water molecule can be seen. By adsorbing near the first



water molecule but still on the surface, more hydrogen bonds can be formed, and the second water molecule can donate and accept them at the same time, as it is seen in figure 4.28(b) and figure 4.28(c). Doing so, the trigonal  $O_4$  pyramids are broken up, and the second water molecule now bridges this opened edge across the previous hydrogen bond accepting hydroxide group of the surface. Hence, a three legged sawhorse-shaped like hydrogen bond network with root-like hydrogen bonds within the surface is formed. This results in a more favourable minimum adsorption energy of  $-0.95$  eV compared to the adsorption of the first water molecule while the average adsorption energy only slightly decreases to  $-0.51$  eV. Comparing figure 4.27(a) with figure 4.28(a), no clear statement can be made on the range of the influence of the first water molecule because the outer areas of the second adsorption energy surface do not clearly resemble the ones of the first one. This is again due to the comparable ease with which the surface hydroxide groups can adapt their orientation together with the slight mobility of the firstly adsorbed water molecule. Nonetheless, the area of more favourable adsorption around the first water molecule extends over slightly more than one UC.

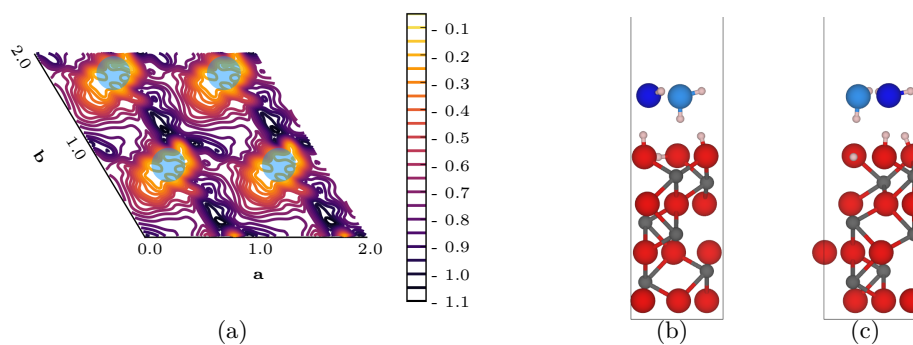


**Figure 4.29:** The second water molecule on the UC of the hydrated (0001) surface; (a) adsorption energy surface [eV], (b) side view structure depiction along  $a$ , and (c) side view structure depiction along  $b$  - gray = aluminium, red = oxygen, white = hydrogen, light blue = first water oxygen, and blue = second water oxygen (VASP-DFT, PBE/PAW, 600.0 eV energy cut-off, D3-BJ).

Keeping figure 4.28(a) in mind, the focus returns back to the UC by adding a second water molecule on the hydrated (0001) surface to evaluate the coverage de-

pendence in more detail. Looking at [figure 4.29\(a\)](#), it can be seen that the previously mentioned help of the first water molecule (light blue circle) is now of course much stronger due to the smaller UC and their now overlapping spheres of influence. Thus, the adsorption between the firstly adsorbed water molecules (see [figure 4.29\(b\)](#) and [figure 4.29\(c\)](#)) becomes even more favourable with a decreased minimum adsorption energy of  $-1.02$  eV. The second water molecule adsorption leads to the formation of regular hexagons with the firstly adsorbed water molecules. Two of the six edges also form squares with two hydroxide groups of the surface, so the hexagons are connected to the surface. It can also be seen that the area of unfavourable adsorption on top of the first molecule shrinks down compared to the one in [figure 4.28\(a\)](#), which results from the overlapping spheres of influence of the first water molecules as well. Furthermore, due to the very good adaptability of the hydroxide groups and the firstly adsorbed water molecules, the average adsorption energy for the second water molecule also decreases noticeably to  $-0.63$  eV.

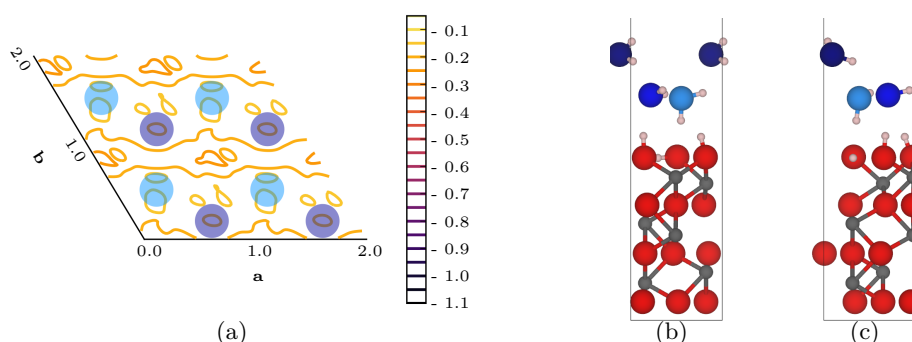


**Figure 4.30:** The third water molecule on the UC of the hydrated (0001) surface; (a) adsorption energy surface [eV], (b) side view structure depiction along  $a$ , and (c) side view structure depiction along  $b$  - gray = aluminium, red = oxygen, white = hydrogen, light blue = first water oxygen, blue = second water oxygen, and dark blue = third water oxygen (VASP-DFT, PBE/PAW, 600.0 eV energy cut-off, D3-BJ).

Adding a third water molecule to the hydrated (0001) surface (see [figure 4.30](#)), things become different. At first, a look at [figure 4.30\(a\)](#) reveals again the very coordinated distribution of the first two water molecules (light blue and blue circles) on the surface. The third water molecule can no longer adsorb directly on the surface

due to the steric hindrance caused by the first two water molecules. Thus, the third water molecule can only adsorb on the previously formed water network, so this process does not allow a high number of formed hydrogen bonds since those are already in use for the water network on the surface. The third water molecule is only able to donate a single comparably weak hydrogen bond itself (see figure 4.30(b) and figure 4.30(c)), which results in no significant change of the hydrogen bond network itself but results in a fivefold coordinated water molecule (the accepting one). Such highly coordinated oxygen atoms/ions are not as unusual as it sounds, even in small organo-aluminium clusters four- and fivefold coordinated oxygen atoms/ions are known [215, 216]. That is why the adsorption of the third water molecule in the middle the formed water hexagons only results in an adsorption energy of  $-0.26$  eV, while the average adsorption energy increases as well to unfavourable  $-0.18$  eV. The results therefore indicate that the first monolayer of water is completed with two water molecules per UC instead of three water molecules, which would correspond to the adsorption of one water molecule per surface hydroxide group. This common connection between the surface hydroxide groups and the amount of water to form a monolayer does not apply here, because the hydroxide groups are too dense and prevent the adsorption of the third water molecule by steric hindrances.

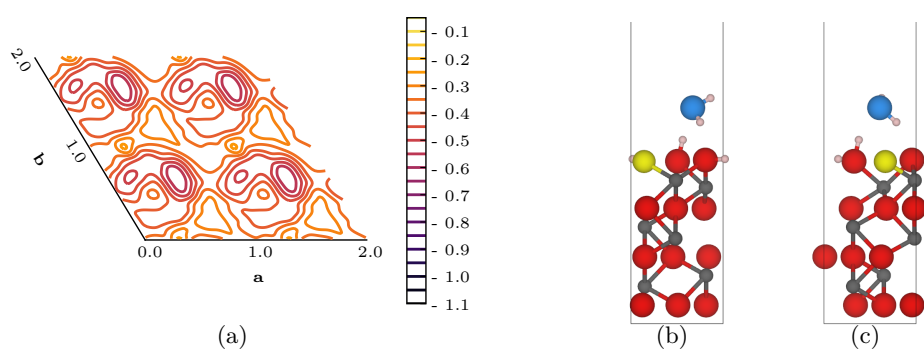


**Figure 4.31:** The first water molecule on the UC of the singly fluorinated (0001) surface; (a) adsorption energy surface [eV], (b) side view structure depiction along  $a$ , and (c) side view structure depiction along  $b$  - gray = aluminium, red = oxygen, yellow = fluorine, white = hydrogen, and light blue = first water oxygen (VASP-DFT, PBE/PAW, 600.0 eV energy cut-off, D3-BJ).

Going from the hydrated (0001) surface to the singly fluorinated one, [figure 4.31](#) shows the results of the adsorption of the first water molecule on its UC. Firstly, a more distinct pattern is to be seen in [figure 4.31\(a\)](#) as compared to [figure 4.27\(a\)](#). A quite unfavourable adsorption site directly on top of the fluoride ion ( $0.66a$  and  $0.14b$ ) can be identified and a favourable adsorption site nearly on top of the outwards pointing hydroxide group ( $0.6a$  and  $0.67b$ ), which is also part of a pincer-like shaped area. The center of the pincer-like shaped area is the exact position of the outwards pointing hydroxide group. In [figure 4.31\(b\)](#) and [figure 4.31\(c\)](#) it can be seen why the adsorbing water molecule does not want to sit directly on top of this hydroxide group. By tilting a bit away it accepts the hydrogen bond of the considered hydroxide group while also donating a hydrogen bond to the in-plane pointing hydroxide group, which results in a minimum adsorption energy of  $-0.59$  eV. Doing so, it also forms  $180^\circ$  rotated “V”s on the surface, where the “legs” are connected via hydrogen bonding as well. The unfavourable adsorption on the fluoride ions position simply results from the formation of only very weak hydrogen bonds to fluoride ions and the lack of favourable hydrogen bonds to oxide ions (remember the results [table 4.4](#)). Considering this, the average adsorption energy increases, compared to the first water molecule on the hydrated (0001) surface, to  $-0.39$  eV.

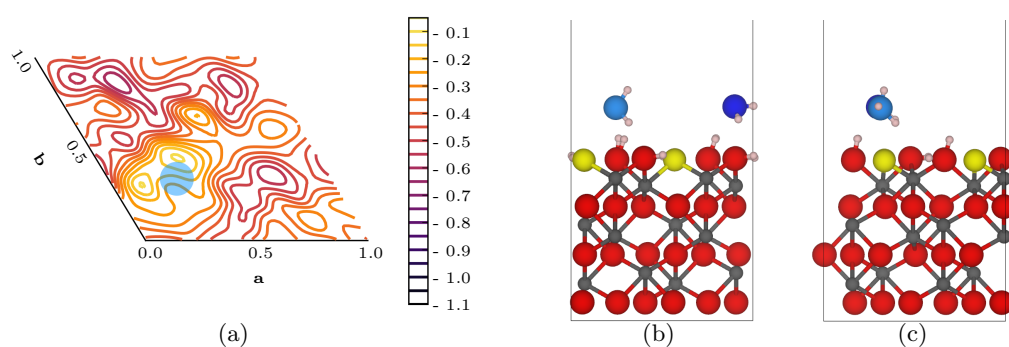


**Figure 4.32:** The second water molecule on a  $2 \times 2 \times 1$  SC of the singly fluorinated (0001) surface; (a) adsorption energy surface [eV], (b) side view structure depiction along  $a$ , and (c) side view structure depiction along  $b$  - gray = aluminium, red = oxygen, yellow = fluorine, white = hydrogen, light blue = first water oxygen, and blue = second water oxygen (VASP-DFT, PBE/PAW, 600.0 eV energy cut-off, D3-BJ).

Increasing again the space between the firstly adsorbed water molecules by using a  $2 \times 2 \times 1$  SC to adsorb the second water molecule, [figure 4.32](#) shows the results of this study. Comparing [figure 4.31\(a\)](#) with [figure 4.32\(a\)](#), it can be seen that, first of all, the adsorption on top of the first water molecule is again unfavourable but that the unfavourable adsorption sites on top of the fluoride positions remain observable as well. Furthermore, the remaining three favourable adsorption sites on top of the outwards pointing hydroxide groups are still recognisable as wells as parts of the pincer-like shaped areas. Combining this, the loss of only one highly adaptable hydroxide group on the surface results in a much more recognisable adsorption energy surface than it was case for the first two adsorption energy surfaces for the hydrated (0001) surface. Due to this, the second water molecule adsorbs at a similar position as the first water molecule, with a slightly larger tilt towards the first water molecules to also form a hydrogen bond with that one (see [figure 4.32\(b\)](#) and [figure 4.32\(c\)](#)). Hence, a minimum adsorption energy of  $-0.62$  eV is obtained. The difference of  $\approx 0.33$  eV compared to the minimum adsorption energy resulting from [figure 4.28\(a\)](#) confirms the importance of hydrogen bonding with the surface and the already adsorbed water molecule. Considering the resulting hydrogen bond network, the two adsorbed water molecules form a complete sawhorse this time, and again they have root-like hydrogen bonds within the surface. Based on the quite high recognisability of [figure 4.31\(a\)](#) and [figure 4.32\(a\)](#), it is not surprising that the average adsorption energy is also similar with  $-0.39$  eV.

Going back to the UC of the singly fluorinated (0001) surface, the second water molecule is added, and the results are shown in [figure 4.33](#). Looking at [figure 4.33\(a\)](#), it can be seen that again the spheres of influence of the first water molecule overlap to further increase the likelihood to adsorb the second water molecule. Since now all desirable adsorption sites are filled compared to [figure 4.32\(a\)](#), the second water molecule positions itself between the previously adsorbed water molecules and directly on top of the remaining hydroxide group as well. But instead of accepting a

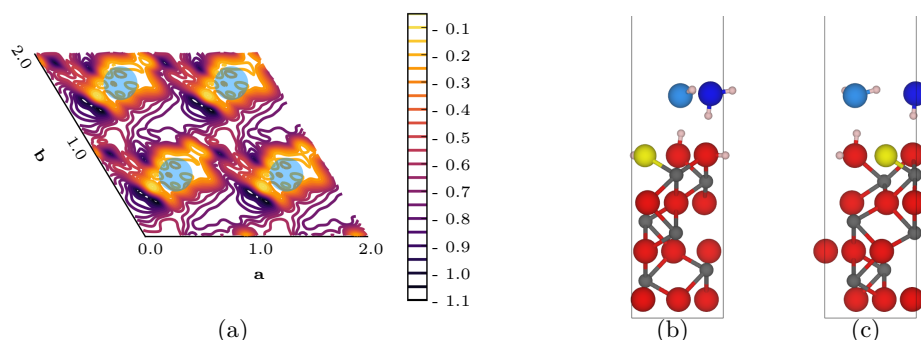


**Figure 4.33:** The second water molecule on the UC of the singly fluorinated (0001) surface; (a) adsorption energy surface [eV], (b) side view structure depiction along  $a$ , and (c) side view structure depiction along  $b$  - gray = aluminium, red = oxygen, yellow = fluorine, white = hydrogen, light blue = first water oxygen, and blue = second water oxygen (VASP-DFT, PBE/PAW, 600.0 eV energy cut-off, D3-BJ).

hydrogen bond from the last hydroxide group, it donates a hydrogen bond to it while at the same time accepting and donating hydrogen bonds to the already adsorbed water molecules (see figure 4.33(b) and figure 4.33(c)). Thus, the most favourable position for the second water molecule to adsorb is located at  $0.1a$  and  $0.9b$ , where the adsorption energy reaches its minimum with  $-0.98$  eV. The resulting hydrogen bond network is the same, as it was seen for the hydrated (0001) surface with two water molecules per UC, the water molecules form regular hexagons with squares connecting them to the surface. Taking a second look at figure 4.33(a), it can be seen that the fluorinated position, at  $0.67a$  and  $0.14b$ , is still clearly observable, although, the overlapping spheres of influence of the first water molecule makes this area more likely for adsorption. Due to this, the average adsorption energy for the second water molecule on the singly fluorinated (0001) surfaces UC is higher than its counterpart for the hydrated surface and provides only  $-0.56$  eV.

Finalising the investigation of the singly fluorinated (0001) surface, the results of the addition of the third water molecule on the UC are shown in figure 4.34. As it was seen already for figure 4.30(a), figure 4.34(a) reveals a very ordered network of previously adsorbed water molecules. Likewise, the network consists of water molecules forming hexagons which are connected to the surface via donated and accepted hydrogen

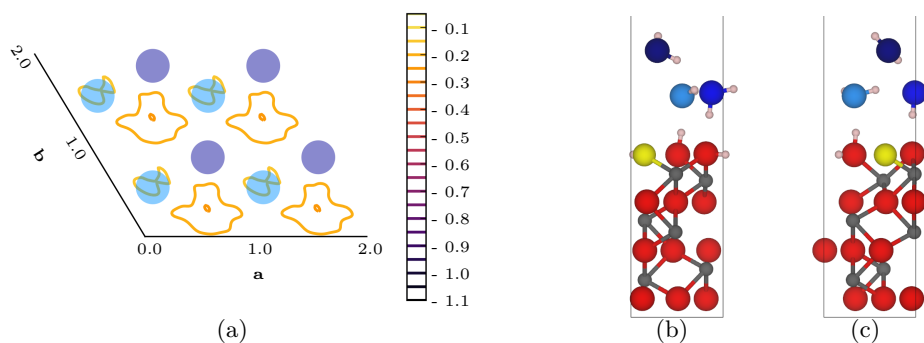


**Figure 4.34:** The third water molecule on the UC of the singly fluorinated (0001) surface; (a) adsorption energy surface [eV], (b) side view structure depiction along  $a$ , and (c) side view structure depiction along  $b$  - gray = aluminium, red = oxygen, yellow = fluorine, white = hydrogen, light blue = first water oxygen, blue = second water oxygen, and dark blue = third water oxygen (VASP-DFT, PBE/PAW, 600.0 eV energy cut-off, D3-BJ).

bonds while the water molecules themselves are connected via hydrogen bonds as well. Again, steric hindrance prevent the third water molecule to adsorb directly at the surface, at the same time, the adsorption on top of an existing water molecule remains the most unfavourable position to adsorb. Therefore, the third water molecule adsorbs in the middle of a hexagon by donating a hydrogen bond (see figure 4.34(b) and figure 4.34(b)), which results in a minimum adsorption energy of  $-0.25$  eV. This adsorption energy is nearly the same as the one resulting from figure 4.30(a) which indicates that the third water molecule on the hydrated and singly fluorinated (0001) surfaces behaves in the same way. Indeed, the hydrogen bond network is the same, even the fivefold coordinated water molecule in the hexagon, and by preventing the adsorption directly on the surface due to steric hindrance, the position of the fluoride ion does not play any role for adsorption of the third water molecule. Therefore, it is no surprise that the average adsorption energy provides the same value of  $-0.18$  eV, as for the hydrated one.

Starting with the doubly fluorinated (0001) surface, the results of the addition of the first water molecule are seen in figure 4.35. The adsorption energy surface in figure 4.35(a) shows stepped lines of unfavourable adsorption sites following the orientation of  $b$  at around  $0.9a$ . They are the result of the now two fluorinated

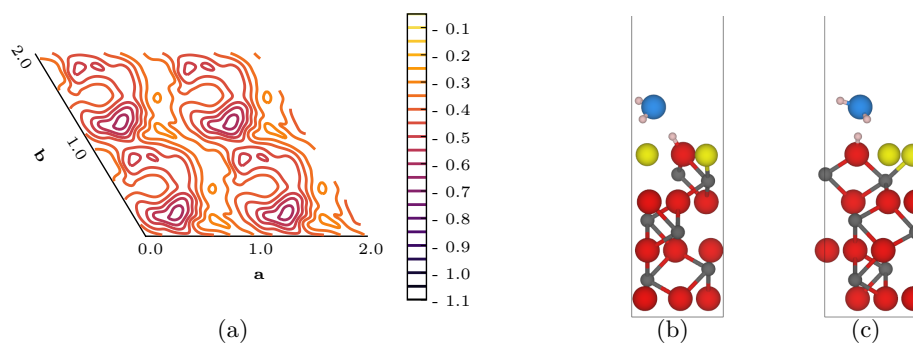


**Figure 4.35:** The first water molecule on the UC of the doubly fluorinated (0001) surface; (a) adsorption energy surface [eV], (b) side view structure depiction along  $a$ , and (c) side view structure depiction along  $b$  - gray = aluminium, red = oxygen, yellow = fluorine, white = hydrogen, and light blue = first water oxygen (VASP-DFT, PBE/PAW, 600.0 eV energy cut-off, D3-BJ).

positions at the surface and represent the extension of the smaller triangular shaped plateau at  $0.66a$  and  $0.14b$  in figure 4.31(a). Between those stepped lines pincer-like shaped favourable adsorption sites are located, where the remaining hydroxide group of the surface is located in the middle. Considering the starting orientation of this hydroxide group, only one pincer-half provides a comparably good adsorption energy of  $-0.61$  eV. As it is seen in figure 4.35(b) and figure 4.35(c), the water molecule adsorbs near the remaining hydroxide group to accept its hydrogen bond while it also donates a weak hydrogen bond to a fluoride ion of the surface. Considering the shape of the resulting hydrogen bond network, there is only one tilted and  $180^\circ$  rotated “V” per UC. Condensing the adsorption energies for the whole UC in the average adsorption energy, a value of  $-0.42$  eV is obtained, which is slightly lower than the one resulted from figure 4.31(a). This is due to the increasing Brønsted acidity of the remaining hydroxide groups with increasing amounts of fluorides.

Increasing the space between the already adsorbed water molecules once more by adsorbing the second water molecule firstly on a  $2 \times 2 \times 1$  SC, the results are shown in figure 4.36. In figure 4.36(a) it can be seen that the somewhat ordered adsorption energy surface of figure 4.35(a) is overthrown by the sphere of influence of the firstly adsorbed water molecule and only the upper right part slightly reminds on the pin-



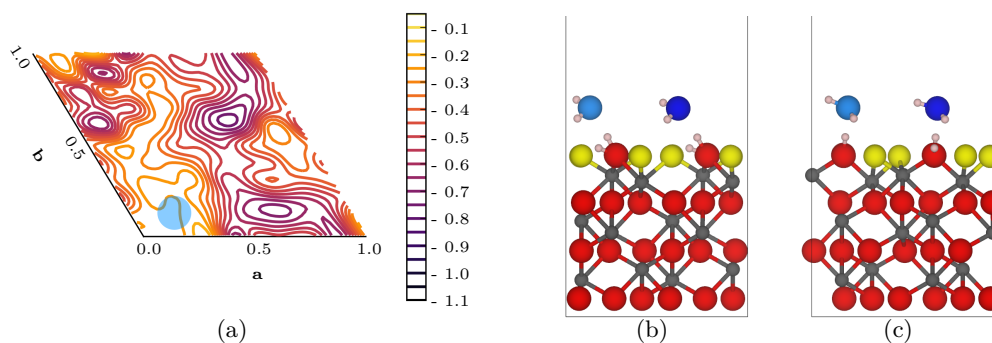


**Figure 4.36:** The second water molecule on a  $2 \times 2 \times 1$  SC of the doubly fluorinated (0001) surface; (a) adsorption energy surface [eV], (b) side view structure depiction along  $a$ , and (c) side view structure depiction along  $b$  - gray = aluminium, red = oxygen, yellow = fluorine, white = hydrogen, light blue = first water oxygen, and blue = second water oxygen (VASP-DFT, PBE/PAW, 600.0 eV energy cut-off, D3-BJ).

cer-like shaped motif seen earlier. All three free hydroxide groups can be identified in figure 4.36(a) while the most favourable of them to “capture” the second water molecule is the farthest away from the firstly adsorbed water molecule. As it can be seen in figure 4.36(b) and figure 4.36(c), the second water molecule adsorbs there in the same way the first water molecule did, and by association, there is no change in the hydrogen bond network. Due to the formation of repetitive and comparably weak hydrogen bonds between those two water molecules, the minimum adsorption energy drops to  $-0.74$  eV while the average adsorption energy drops down to  $-0.44$  eV as well. The latter is due to at least weak hydrogen bonding to the firstly adsorbed water molecule, which can adjust its position more freely now since it is only bound to one hydroxide group that can adapt its orientation and is otherwise only bound by weak interactions with the fluoride ions of the surface.

Lowering the distance between the firstly adsorbed water molecules again by using the UC of the doubly fluorinated (0001) surface, the results for the adsorption of the second water molecule are shown in figure 4.37. Once more, the firstly adsorbed water molecules’ overlapping spheres of influence result in very favourable adsorption sites between them (see figure 4.37(a)) due to the donation and acceptance of hydrogen bonds by the second water molecule. Furthermore, it can be clearly seen that the

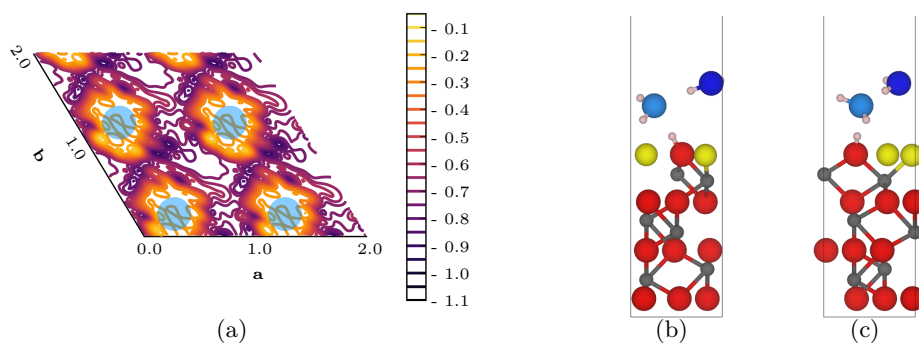


**Figure 4.37:** The second water molecule on the UC of the doubly fluorinated (0001) surface; (a) adsorption energy surface [eV], (b) side view structure depiction along  $a$ , and (c) side view structure depiction along  $b$  - gray = aluminium, red = oxygen, yellow = fluorine, white = hydrogen, light blue = first water oxygen, and blue = second water oxygen (VASP-DFT, PBE/PAW, 600.0 eV energy cut-off, D3-BJ).

adsorption directly on the existing water molecules remains unfavourable. The second water molecule adsorbs at  $0.82a$  and  $0.88b$ , almost on top of a fluoride, at least laterally, since it is further away from the surface than the previously adsorbed water molecules (see figure 4.37(b) and figure 4.37(c)). By forming chains of hydrogen bonding along the short diagonal of the UC between the two water molecules per UC and simultaneous connection of those chains via weak (stretched) hydrogen bonds, the adsorption of the second water molecule reveals a minimum adsorption energy of  $-0.93$  eV. Considering the resulting hydrogen bond network, stretched chair-like  $O_6$ -rings are formed, which stand on three on their head standing “V”s each. Each line of the letter “V” and other letters later represents a formed hydrogen bond. Due to the spheres of influence’s overlap, the average adsorption energy drops down to  $-0.55$  eV compared to the one resulted from figure 4.36(a).

Increasing the amount of water on the doubly fluorinated (0001) surface with the addition of a third water molecule per UC, the investigation leads to the results shown in figure 4.38. In figure 4.38(a) it can be seen that the adsorption on top of the first water molecule is not as hindered, as it was the case for the previous surfaces with already two adsorbed water molecules. Thus, figure 4.38(a) does not show the same smooth adsorption energy surface and instead provides one which is very similar to

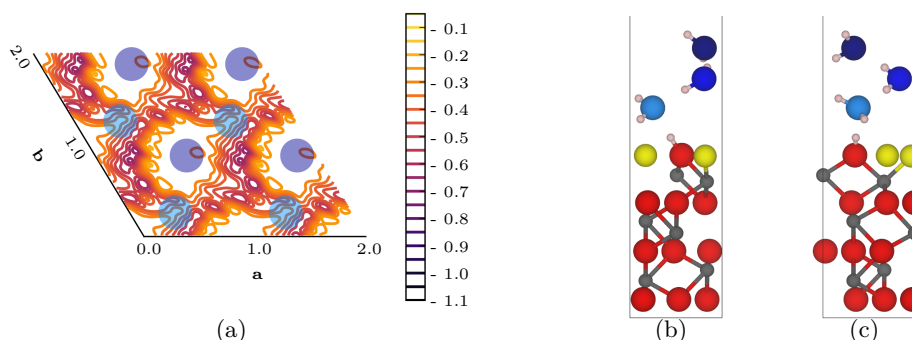


**Figure 4.38:** The third water molecule on the UC of the doubly fluorinated (0001) surface; (a) adsorption energy surface [eV], (b) side view structure depiction along  $a$ , and (c) side view structure depiction along  $b$  - gray = aluminium, red = oxygen, yellow = fluorine, white = hydrogen, light blue = first water oxygen, blue = second water oxygen, and dark blue = third water oxygen (VASP-DFT, PBE/PAW, 600.0 eV energy cut-off, D3-BJ).

the ones for the adsorption of the second water molecule. This is due to the different height of the already two adsorbed water molecules. Since steric effects hinder the third water molecule to adsorb directly on the surface and combining this with the extent of the spheres of influence from the previously adsorbed water molecules, the third one effectively only “sees” those two water molecules. Therefore, the adsorption on top of the second one is unfavourable, as it was seen previously, while the adsorption on top the first one is more favoured. This is due to the third water molecule now sitting between the second ones with a reasonable distance to the first one, so that it is not sterically hindered that much. In figure 4.38(b) and figure 4.38(c) it can be seen that the third water molecule forms again chains of hydrogen bonding with the second water molecule resulting in a network of hydrogen bonds between all three water molecules, which consists of deep bathtub-like shaped  $O_8$ -rings standing on two  $180^\circ$  rotated “V”s each. The resulting minimum adsorption energy increases to  $-0.63$  eV and the average adsorption energy increases to  $-0.37$  eV, compared to the second water molecules on this surface modification.

Starting to finalise the investigation of water adsorption on modified (0001) surfaces, figure 4.39 shows the results of the adsorption of the first water molecule on the triply fluorinated (0001) surface. It reveals the fundamental difference of this adsorption

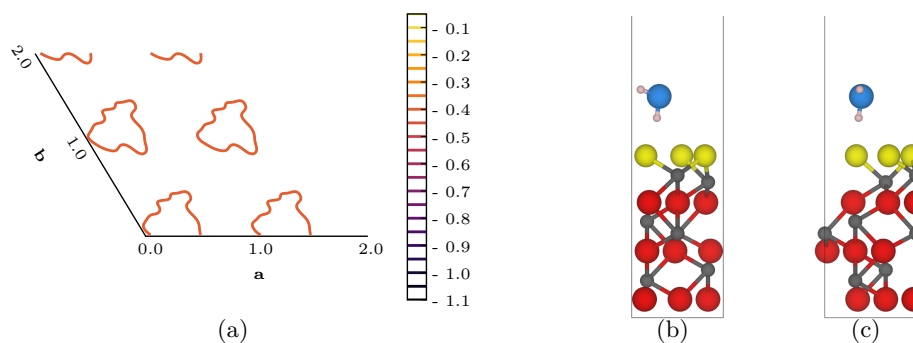


**Figure 4.39:** The first water molecule on the UC of the triply fluorinated (0001) surface; (a) adsorption energy surface [eV], (b) side view structure depiction along  $a$ , and (c) side view structure depiction along  $b$  - gray = aluminium, red = oxygen, yellow = fluorine, white = hydrogen, and light blue = first water oxygen (VASP-DFT, PBE/PAW, 600.0 eV energy cut-off, D3-BJ).

energy surface (see figure 4.39(a)) to the other ones. This time, it is extremely smooth and provides only values ranging from  $-0.41$  eV to  $-0.36$  eV. That is of course simply due to the very smooth surface provided by the now fully fluorinated UC and the associated lack of adaptable hydroxide groups. As it can be seen in figure 4.39(b) and figure 4.39(c), the first water molecule can only donate one very weak hydrogen bond to the surface, which results in an increased minimum adsorption energy of  $-0.41$  eV and an increased average adsorption energy of  $-0.39$  eV.

Unfortunately, the investigation of the second water molecules' adsorption on a  $2 \times 2 \times 1$  SC of the triply fluorinated (0001) surface shows many convergence issues due to its strong reliance on the formation of otherwise highly adaptable hydrogen bonds to the surface. This challenge is even worsened by the size of the SC and the associated computational effort for the structure optimisation. Since it is very unlikely to obtain new insights in the size of the first water molecules' sphere of influence on this triply fluorinated (0001) surface's SC, the completion of the needed but very expensive calculation is waived to save otherwise needed computer resources.

Adding the second water molecule on the UC of the triply fluorinated (0001) surface, the calculations lead to the results seen in figure 4.40. The adsorption energy surface in figure 4.40(a) shows an unfavourable adsorption on top the first water molecule but

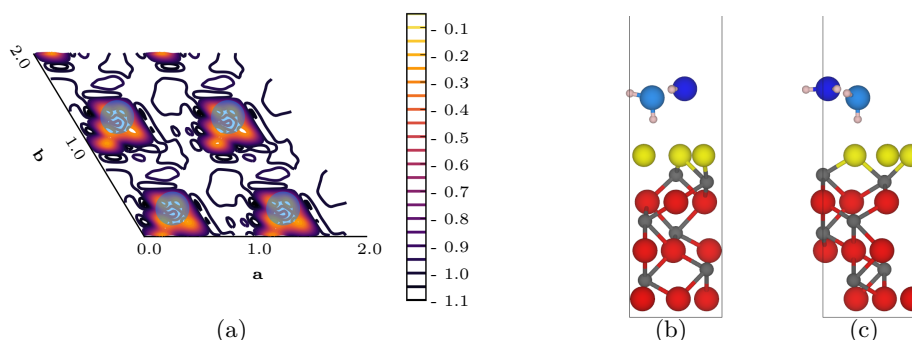


**Figure 4.40:** The second water molecule on the UC of the triply fluorinated (0001) surface; (a) adsorption energy surface [eV], (b) side view structure depiction along  $a$ , and (c) side view structure depiction along  $b$  - gray = aluminium, red = oxygen, yellow = fluorine, white = hydrogen, light blue = first water oxygen, and blue = second water oxygen (VASP-DFT, PBE/PAW, 600.0 eV energy cut-off, D3-BJ).

also a very drastic increase of the area of favourable adsorption around it for the second water molecule. This results from the comparably very high mobility of the first water molecule on the triply fluorinated surface (see again [figure 4.39\(a\)](#)) which can easily adapt its position to different adsorption positions of the second water molecule. The heavy decrease in the adsorption energy within this area results from the formation of three very strong hydrogen bonds between the two water molecules while there is only a very weak one to the surface (see [figure 4.40\(b\)](#) and [figure 4.40\(c\)](#)). Therefore, the system gains much more energy during the formation of those hydrogen bonds and forms again the already seen water hexagons, whose sole connection to the surface are the mentioned weak hydrogen bonds to surface fluoride ions. Thus, the minimum adsorption energy obtained is  $-1.02$  eV, the best adsorption energy so far, while the average adsorption energy drops significantly to  $-0.89$  eV.

Increasing the water content the last time for the investigation of modified (0001) surfaces, [figure 4.41](#) shows the results of the adsorption of the third water molecule on the triply fluorinated (0001) surface. In [figure 4.41\(a\)](#) the previously discussed hexagon structure of the already adsorbed water molecules can be seen very easily. Furthermore, a mediocre average adsorption energy of  $-0.37$  eV is provided by this quite smooth adsorption energy surface. This is due to the very good possibility to

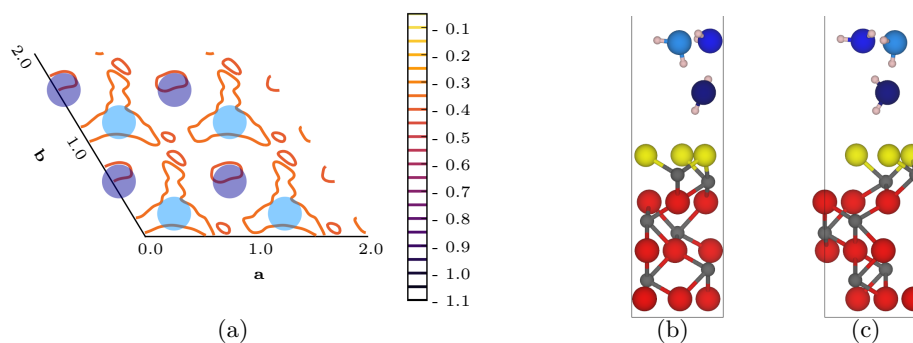


**Figure 4.41:** The third water molecule on the UC of the triply fluorinated (0001) surface; (a) adsorption energy surface [eV], (b) side view structure depiction along  $a$ , and (c) side view structure depiction along  $b$  - gray = aluminium, red = oxygen, yellow = fluorine, white = hydrogen, light blue = first water oxygen, blue = second water oxygen, and dark blue = third water oxygen (VASP-DFT, PBE/PAW, 600.0 eV energy cut-off, D3-BJ).

form hydrogen bonds between the third water molecule and water molecules of the hexagon. But interestingly, the most favourable adsorption site, with  $-0.41$  eV in the middle of such a hexagon, provides a very structural change. First of all, this position is the most likely to adsorb due the very good and continuous interaction with the water hexagon and the lack of steric hindrance of those in order to minimise the distance to the surface. However, the adsorption of the third water molecule does not stop on top of such a hexagon, instead, it penetrates the hexagon and forms a weak hydrogen bond to the surface fluoride. At the same time during the structure optimisation, the whole honeycomb-like water structure is lifted upwards and shifted, so that two edges of each hexagon are placed above the thirdly adsorbed water molecules (see figure 4.41(b) and figure 4.41(c)). Those findings implicate that the honeycomb-like water structure prefers a larger distance to the fluorinated surface which corresponds to a favouritism of minimising the interaction with this fully fluorinated surface. The only connection to the surface is mediated by the third water molecule.

In order sum things up so far, table 4.11 condenses the important adsorption energies and a short description of the adsorbing water molecule's binding for each modified surface and added water molecule. Unsurprisingly, the formation of hydrogen bonds was the main driving force for a favourable adsorption of water molecules.

**Table 4.11:** Three notable adsorption energies resulting from each adsorption energy surface and a short adsorption site description for the water adsorption on modified (0001) surfaces (VASP-DFT, PBE/PAW, 600.0 eV energy cut-off, D3-BJ).

$\text{H}_2\text{O}$	<b>F/UC</b>	$E_{\text{ads,MAX}}$	$E_{\text{ads,MIN}}$	$\bar{E}_{\text{ads}}$	<b>Positioning</b>
		[eV]	[eV]	[eV]	
1. on UC	0	-0.31	-0.65	-0.48	above 3 OH
	1	-0.25	-0.59	-0.39	above 2 OH
	2	-0.28	-0.61	-0.42	above OH+F
	3	-0.36	-0.41	-0.39	above 3 F
2. on SC	0	-0.15	-0.95	-0.51	on OH; near 1.
	1	-0.12	-0.62	-0.29	above 2 OH; near 1.
	2	-0.21	-0.74	-0.44	above OH+F
	3	—	—	—	—
2. on UC	0	-0.21	-1.02	-0.63	on OH; among 2 1.
	1	-0.20	-0.98	-0.56	above OH; among 2 1.
	2	-0.24	-0.93	-0.55	above 2 1.; distant 1.
	3	-0.36	-1.02	-0.89	among 3 1.
3. on UC	0	-0.13	-0.26	-0.18	above 3 1.+3 2.
	1	-0.13	-0.25	-0.18	above 3 1.+3 2.
	2	-0.25	-0.63	-0.37	above 2 2.
	3	-0.32	-0.41	-0.37	beneath 1.+2.

It was shown that in all cases the adsorption on top of an already adsorbed water molecule provided the most unfavourable adsorption energy which also depended on the strength of the formed hydrogen bonds between them and, by association, resulted in maximum adsorption energies ranging from  $-0.36$  eV to  $-0.12$  eV. The adsorption on top of surface fluoride ions was unfavourable due to fluoride being an inferior hydrogen bond acceptor. Nonetheless, with increasing amounts of fluoride ions in the surface structure, the remaining hydroxide groups became more and more Brønsted acidic, which decreased the adsorption energy on them and provided an opposed trend to the decrease of possible stronger hydrogen bonds to other hydroxide groups. Regarding the spheres of influence's sizes from the firstly adsorbed water molecules, it was seen that those areas are of similar extent and close to the size of a (0001) UC, which corresponds to  $\approx 20 \text{ \AA}^2$ . This area also depended of course on the mobility or

adaptability of the first water molecule on the surface, namely how strongly it was locked in its position. Due to this and the therefore overlapping spheres of influence, the adsorption of the second water molecule on the UC was mainly directed by the previously adsorbed water molecule. The adsorption of the third molecule was, in case of the (0001) surface, nearly decoupled from the actual surface composition, because the previously two adsorbed water molecules defined how and where the third one could adsorb due to their orientations and steric demands on the surface. However, the surface composition “only” had an impact on the value of the adsorption energy by influencing the strength of the interaction of the first two water molecules with itself.

Regarding a possible fluoride protective coat, the triply fluorinated (0001) surface showed that the adsorption of water provides a very similar average adsorption energy but a very thin deviation of the maximum and minimum adsorption energies as well. Thus, the adsorption of water was only possible via very weak hydrogen bonds to fluoride ions or the formation of a stable hydrogen bond network for higher amounts of water. This was especially underlined by the hydrogen bond network found after adsorption of the third water molecule on the triply fluorinated (0001) surface.

### 4.3.2 The (1 $\bar{1}$ 02) Surface

Shifting the focus of the water adsorption investigation to the (1 $\bar{1}$ 02) surface, please be reminded that this surface structure exhibits a wavy surface with channel-like structure motifs as described in subsection 4.2.1 [Hydration of  \$\alpha\$ -Aluminium Oxide Surfaces](#) and subsection 4.2.2 [Fluorination of Hydrated  \$\alpha\$ -Aluminium Oxide Surfaces](#).

Starting with the first water molecule on the hydrated (1 $\bar{1}$ 02) surface UC, the obtained results can be seen in [figure 4.42](#). The adsorption energy surface in [figure 4.42\(a\)](#) resembles the actual surface structure remarkably well. While the adsorption on channel hills is comparably unfavourable, due to a very exposed position which is accompanied by poor possibilities to form hydrogen bonds without breaking



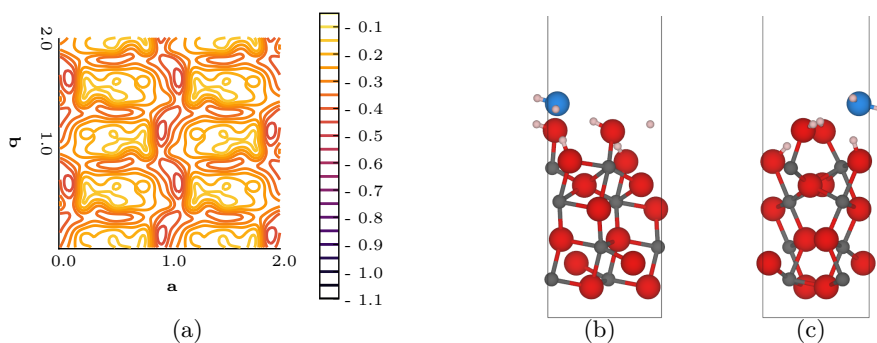


**Figure 4.42:** The first water molecule on the UC of the hydrated ( $1\bar{1}02$ ) surface; (a) adsorption energy surface [eV], (b) side view structure depiction along  $a$ , and (c) side view structure depiction along  $b$  - gray = aluminium, red = oxygen, white = hydrogen, and light blue = first water oxygen (VASP-DFT, PBE/PAW, 600.0 eV energy cut-off, D3-BJ).

existing ones, the adsorption in the channel valleys is more preferred. This is a result of the very good possibilities to accept and donate hydrogen bonds despite the increased sterical hindrance. As it was already seen for the modified (0001) surfaces, the positions of the surface hydroxide groups mainly dictate the position of the water adsorption. In figure 4.42(b) and figure 4.42(c) it can be seen that the first water molecule adsorbs nearly directly on a valley-site hydroxide group by accepting its hydrogen bond and donating one back to a hill-site hydroxide group, which together overcome the sterical hindrance within the channel valleys. The formed hydrogen bond network results mainly from the surface hydroxide groups, it consists of flat zigzag chains containing the hill-site hydroxide groups. These chains are stabilised by the valley-site hydroxide groups, while the adsorbing water molecule intercalates in such a stabilisation and forms a  $\approx 150^\circ$  rotated “V”. This adsorption site reveals the minimum adsorption energy of  $-0.48$  eV while the favourable and unfavourable adsorption sites average themselves out to  $-0.28$  eV. Both values are  $\approx 200$  meV higher than the one resulting from figure 4.27(a) for the adsorption of the first water molecule on the hydrated (0001) surface. Thus, the hydrated ( $1\bar{1}02$ ) surface is less favourable to adsorb water molecules than the hydrated (0001) surface.

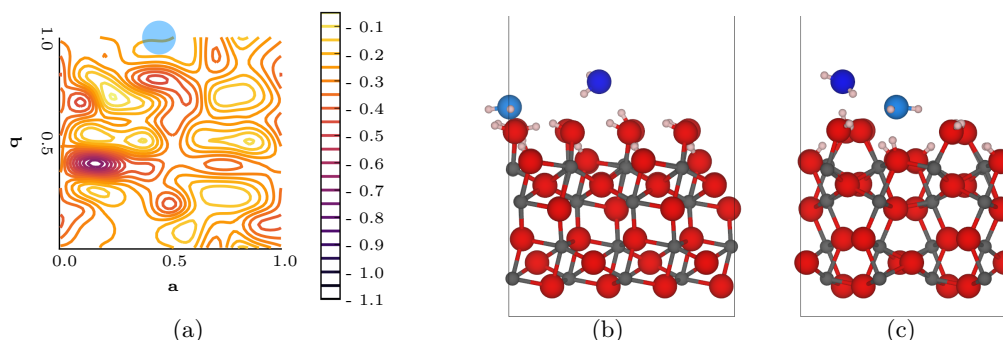


**Figure 4.43:** The second water molecule on a  $2 \times 2 \times 1$  SC of the hydrated  $(1\bar{1}02)$  surface; (a) adsorption energy surface [eV], (b) side view structure depiction along  $a$ , and (c) side view structure depiction along  $b$  - gray = aluminium, red = oxygen, white = hydrogen, light blue = first water oxygen, and blue = second water oxygen (VASP-DFT, PBE/PAW, 600.0 eV energy cut-off, D3-BJ).

By increasing the space between the firstly adsorbed water molecules using a  $2 \times 2 \times 1$  SC, the calculations lead to the results shown in figure 4.43. In figure 4.43(a) it can be seen that the right hand side adsorption positions do not change that much as a result of the first adsorbed water molecule, only in a comparably small area around it, the adsorption energy surface shows differences. For the left hand side, some motifs remain observable as well while there is a very drastic change showing the most favourable adsorption site. Due to mutual stabilisation of the hill-site hydroxide groups, the first water molecule can expand its sphere of influence further along those hydrogen bond chains. This results in an increased likelihood to adsorb the second water molecule between those hill-site hydroxide groups along those chains. Shown in figure 4.43(b) and figure 4.43(c), the second water molecule adsorbs directly on the hill of the channel-like surface. It is therefore interfering in the stabilisation chain to stabilise its position there and forming a  $180^\circ$  rotated “V” of hydrogen bonds on the hill. This is only possible because the first water molecule influenced this whole chain of stabilisation of the left hand side hill-sites by bending downwards slightly and donating a second hydrogen bond to the right hand side hill-site zigzag chain and, by association, bridging them. The resulting minimum adsorption energy is  $-0.68$  eV and much stronger than a possible adsorption of the first water molecule on the same

position. Due to the quite small sphere of influence of the first water molecule, the unfavourable adsorption on top of it, and the new favourable adsorption site, the average adsorption energy stays nearly the same compared to the one resulting from [figure 4.42\(a\)](#) and provides a value of  $-0.27$  eV.

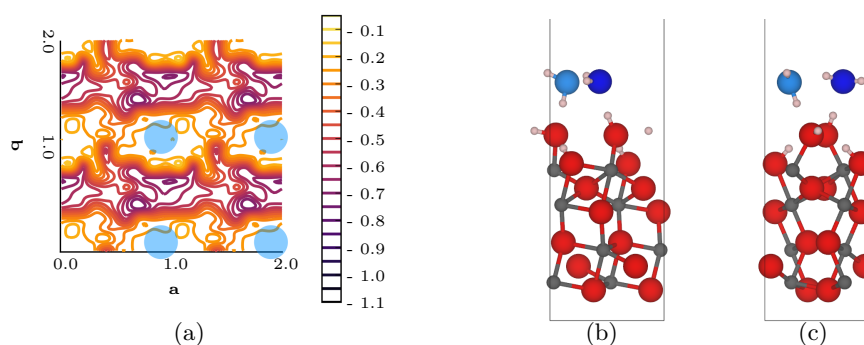


**Figure 4.44:** The second water molecule on the UC of the hydrated  $(1\bar{1}02)$  surface; (a) adsorption energy surface [eV], (b) side view structure depiction along  $a$ , and (c) side view structure depiction along  $b$  - gray = aluminium, red = oxygen, white = hydrogen, light blue = first water oxygen, and blue = second water oxygen (VASP-DFT, PBE/PAW, 600.0 eV energy cut-off, D3-BJ).

Decreasing again the distance between the firstly adsorbed water molecules by going back to the UC and letting the second water molecule adsorb there, the obtained results are shown in [figure 4.44](#). The first water molecule's overlapping spheres of influence result in rows of favourable and unfavourable adsorption sites crossed to the channel-like structure of the surface itself (see [figure 4.44\(a\)](#)). While the unfavourable adsorption positions simply result from the unfavourable adsorption on top of the first water molecule or between them on the hills, the favourable ones result from the influence of the first water molecule along the hydrogen bonding chains of the hills and the second valley-site hydroxide group. Interestingly, the most favourable adsorption site is located on the slope between the hill-site and the valley-site. At this position the second water molecule pushes the first one out of the valley by steric demands and pulls it out by forming hydrogen bonds (see [figure 4.44\(b\)](#) and [figure 4.44\(c\)](#)). During this, the valley-site hydroxide groups stabilise again the hill-site ones while the two water molecules per UC together with the hill-site hydroxide groups form

sheared bathtub-like shaped  $O_{10}$ -rings, where the edges represent the hydrogen bonds. This three dimensional network results in the very favourable adsorption site with a minimum adsorption energy of  $-0.70$  eV. Whereas, the previously mentioned rows of favourable and unfavourable adsorption sites combine themselves to an average adsorption energy of  $-0.40$  eV.

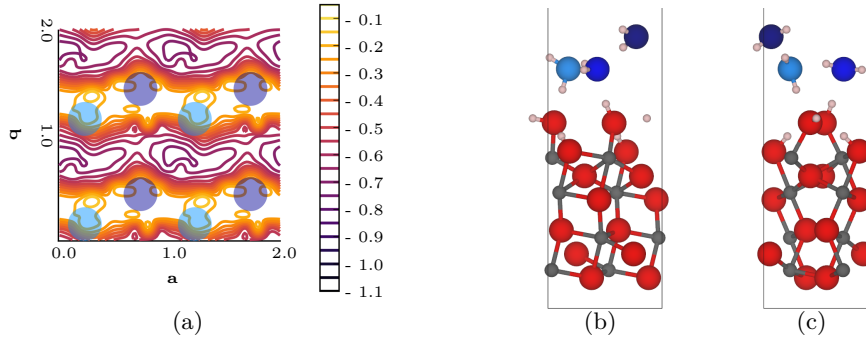


**Figure 4.45:** The third water molecule on the UC of the hydrated  $(1\bar{1}02)$  surface; (a) adsorption energy surface [eV], (b) side view structure depiction along  $a$ , and (c) side view structure depiction along  $b$  - gray = aluminium, red = oxygen, white = hydrogen, light blue = first water oxygen, blue = second water oxygen, and dark blue = third water oxygen (VASP-DFT, PBE/PAW, 600.0 eV energy cut-off, D3-BJ).

Increasing the amount of water on the  $(1\bar{1}02)$  surface UC to three water molecules, figure 4.45 shows the results of this investigation. Taking a look at figure 4.45(a), it can be seen that again rows of favourable and unfavourable adsorption sites appear. This time, they are straight forward to be explained. While the unfavourable adsorption rows result from the adsorption on the edges of the bathtub-like shaped  $O_{10}$ -rings and, by association, limit the possibilities to form hydrogen bonds, the favourable ones are the result of an adsorption between those bathtub edges, so more opportunities to form hydrogen bonds are given. Hence, the third water molecule's most favourable adsorption site (see figure 4.45(b) and figure 4.45(c)) results from the acceptance and donation of one hydrogen bond each, which together stretch along the smallest diagonal of the bathtub-like shaped  $O_{10}$ -rings and leads to a minimum adsorption energy of  $-0.72$  eV and an average adsorption energy of  $-0.42$  eV. At the same time, the adsorption of the third water molecule is not only a simple bridging of the

bathtub-like shaped  $O_{10}$ -ring but also leads to the formation of helical structures with the cross section of a regular  $O_5$ -ring. Those helical structures include the two hill-site hydroxide groups per UC and are therefore incorporated in the surface structure while the helices are also connected with each other via hydrogen bonds between the shifted rings of them. Furthermore, if only the water molecules are considered by leaving the hydroxide groups aside, they form flat and shallow bathtub-like  $O_8$ -rings with the third water molecule providing the only two peaks of those rings.

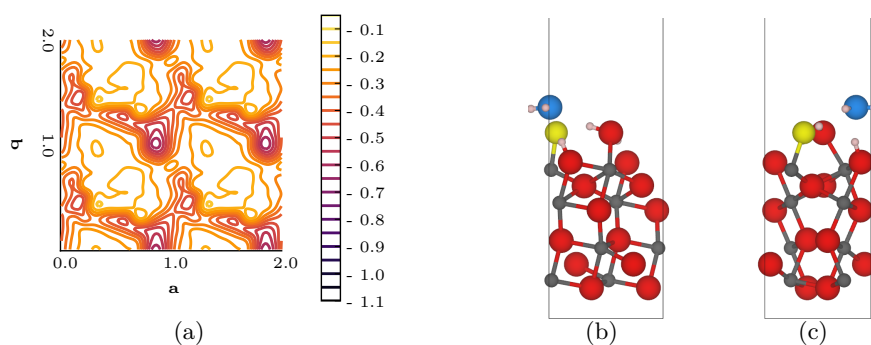


**Figure 4.46:** The first water molecule on the UC of the singly fluorinated  $(1\bar{1}02)$  surface; (a) adsorption energy surface [eV], (b) side view structure depiction along  $a$ , and (c) side view structure depiction along  $b$  - gray = aluminium, red = oxygen, yellow = fluorine, white = hydrogen, and light blue = first water oxygen (VASP-DFT, PBE/PAW, 600.0 eV energy cut-off, D3-BJ).

Going to the singly fluorinated  $(1\bar{1}02)$  surface and the adsorption of water on it, figure 4.46 shows the obtained results for the first water molecule on the UC. Looking at figure 4.46(a), an obvious change due to the first fluorination step can be seen. While in figure 4.42(a) there were rectangularly shaped areas of unfavourable adsorption, pairs of them form a larger unfavourable adsorption area now. Although the first fluoride was introduced at  $0.37a$  and  $0.06b$ , a thin line of favourable adsorption sites can be seen very closely to it. This is due to the possibility to accept a hydrogen bond from the remaining hill-site hydroxide group in this line. Nonetheless, the first water molecule prefers to adsorb at the valley-site hydroxide groups, which would otherwise stabilise the introduced fluoride ion. Due to the fluorination and the periodicity, this hydroxide group becomes more Brønsted acidic, so the adsorption on

it is more favourable resulting in a decreased adsorption energy of  $-0.60$  eV. In this position, the first water molecule is only able to accept one hydrogen bond, donating one back to the remaining hill-site hydroxide group, and donating a weak one to the fluoride ion (see [figure 4.46\(b\)](#) and [figure 4.46\(c\)](#)). Thus, the hydrogen bond network consists of zigzag chains of the water molecule and the two hill-site anions, which proceed diagonal to the channels. Those chains are stabilised by both valley-site hydroxide groups: one is stabilising the water molecule while the other is stabilising the hill-site hydroxide group. Although the area of unfavourable adsorption is increased, the decrease of the adsorption energy in the favourable domains results in an overall nearly the same average adsorption energy of  $-0.29$  eV.

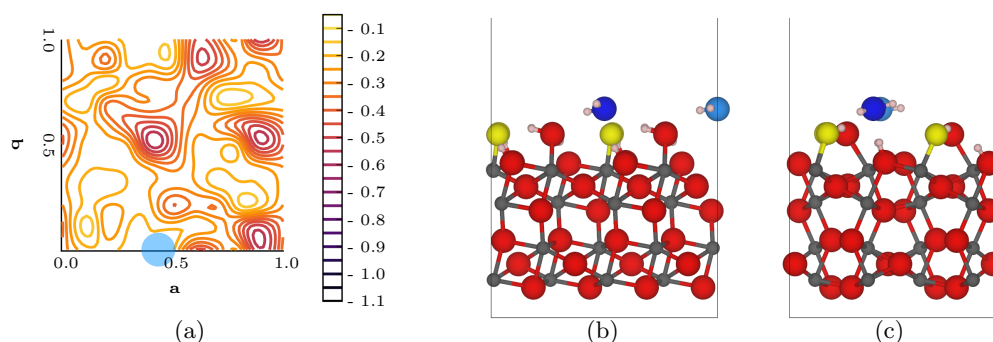


**Figure 4.47:** The second water molecule on a  $2 \times 2 \times 1$  SC of the singly fluorinated  $(1\bar{1}02)$  surface; (a) adsorption energy surface [eV], (b) side view structure depiction along  $a$ , and (c) side view structure depiction along  $b$  - gray = aluminium, red = oxygen, yellow = fluorine, white = hydrogen, light blue = first water oxygen, and blue = second water oxygen (VASP-DFT, PBE/PAW, 600.0 eV energy cut-off, D3-BJ).

Increasing the distance of the firstly adsorbed water molecules once more by utilising a  $2 \times 2 \times 1$  SC of the singly fluorinated  $(1\bar{1}02)$  surface, [figure 4.47](#) shows the results for the adsorption of the second water molecule on it. From [figure 4.47\(a\)](#) it can be seen that the first water molecule extended the unfavourable adsorption area in the lower left hand side and kept the translational equivalent positions very favourable while introducing or enhancing a new one at the top of this figure. Nonetheless, the translational equivalent adsorption positions remain the most favourable ones with a slight preference to the one in same valley, as it can be seen in [figure 4.47\(b\)](#)

and figure 4.47(c). The second water molecule therefore forms the same hydrogen bonding motifs as the first one resulting in a very similar minimum adsorption energy of  $-0.57$  eV. But this time, both water molecules lack the hydrogen bonding to the fluoride ions due to mutual interaction via the hill. This results in the breaking of the previously seen hydrogen bond zigzag chain and the formation of “Y”-shaped structures which are underpinned at the bottom part from a valley hydroxide group. While those structure motifs are formed on the left hand side, regarding figure 4.47(c), on the right hand side there are “Z”-shaped formations stabilising the hill-sites by the valleys hydroxide groups. For the average adsorption energy of  $-0.28$  eV the changes are even smaller, because the newly introduced improvements and deteriorations of adsorption sites cancel each other out.

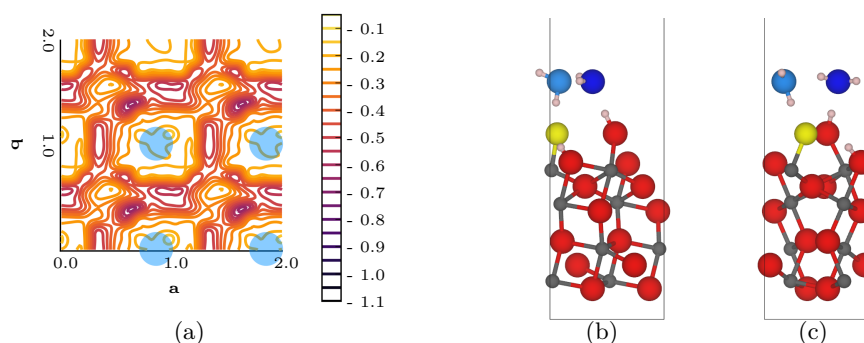


**Figure 4.48:** The second water molecule on the UC of the singly fluorinated  $(1\bar{1}02)$  surface; (a) adsorption energy surface [eV], (b) side view structure depiction along  $a$ , and (c) side view structure depiction along  $b$  - gray = aluminium, red = oxygen, yellow = fluorine, white = hydrogen, light blue = first water oxygen, and blue = second water oxygen (VASP-DFT, PBE/PAW, 600.0 eV energy cut-off, D3-BJ).

Going back to the UC of the singly fluorinated  $(1\bar{1}02)$  surface and adding the second water molecule, the calculations lead to the results seen in figure 4.48. Looking at figure 4.48(a), it can be seen that the closer distance of the firstly adsorbed water molecules results in a grid-like shaped area of favourable adsorption, where grid spaces represent the unfavourable adsorption on the first water molecule. Due to the steric demands of it within the valley, the second water molecule is unlikely to adsorb at the second valley-site hydroxide and instead adsorbs near the slope of the hill via accepting

an hydrogen bond of the remaining hill-site hydroxide group. As it was already seen for the hydrated ( $1\bar{1}02$ ) surface, it pulls out the first water molecule and stabilises it by forming zigzag chains of hydrogen bonds (see [figure 4.48\(b\)](#) and [figure 4.48\(c\)](#)). Since the fluoride ion interrupts the hill-site hydrogen bond chains, the previously seen sheared bathtub-like shaped  $O_{10}$ -rings can not be formed this time. Thus, the formed zigzag chains crossing the channels “stand” on hydrogen bonds from and to the hills. The resulting minimum adsorption energy increases slightly to  $-0.63$  eV, due to the missing hydrogen bond from the substituted hydroxide group. Because of the overlapping spheres of influence of the first water molecules, the average adsorption energy decreases to  $-0.33$  eV, which is a bit higher than for the hydrated ( $1\bar{1}02$ ) surface.

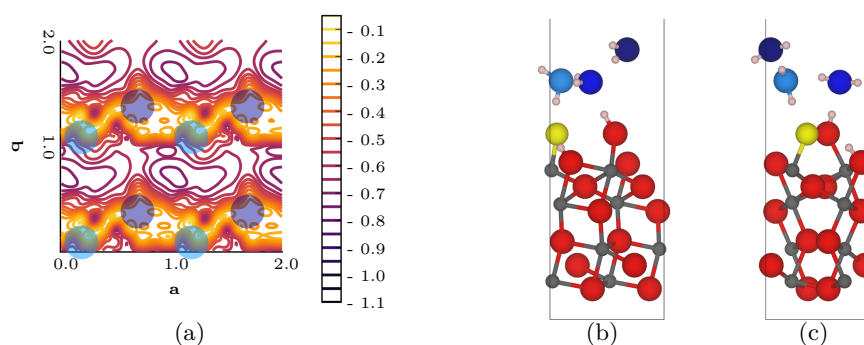


**Figure 4.49:** The third water molecule on the UC of the singly fluorinated ( $1\bar{1}02$ ) surface; (a) adsorption energy surface [eV], (b) side view structure depiction along  $a$ , and (c) side view structure depiction along  $b$  - gray = aluminium, red = oxygen, yellow = fluorine, white = hydrogen, light blue = first water oxygen, blue = second water oxygen, and dark blue = third water oxygen (VASP-DFT, PBE/PAW, 600.0 eV energy cut-off, D3-BJ).

Increasing once more the amount of added water in the UC to three, the results for the singly fluorinated ( $1\bar{1}02$ ) surface are shown in [figure 4.49](#). Comparing [figure 4.49\(a\)](#) with [figure 4.48\(a\)](#), it can be seen that the grid-like shaped area of favourable adsorption turns into row shaped areas. This is of course due to unfavourable adsorption on the already adsorbed water molecules, which are closely arranged in zigzag chains. However, between those zigzag chains the adsorption is very favourable due to the very good formation of hydrogen bonds by bridging two chains with one another (see



figure 4.49(b) and figure 4.49(c)). The resulting flat and shallow bathtub-like shaped  $O_8$ -rings, which build up the three dimensional network of water molecules connected via hydrogen bonds, give rise to a decreased minimum adsorption energy of  $-0.72$  eV. Due to the expansion of the favourable adsorption area, the average adsorption energy decreases as well and is now  $-0.47$  eV.

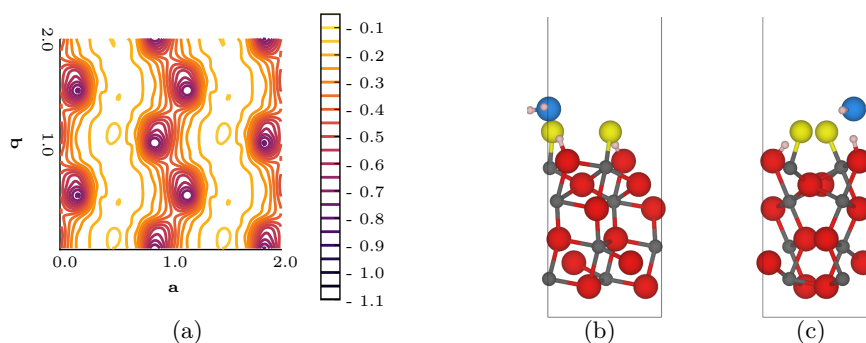


**Figure 4.50:** The first water molecule on the UC of the doubly fluorinated ( $1\bar{1}02$ ) surface; (a) adsorption energy surface [eV], (b) side view structure depiction along  $a$ , and (c) side view structure depiction along  $b$  - gray = aluminium, red = oxygen, yellow = fluorine, white = hydrogen, and light blue = first water oxygen (VASP-DFT, PBE/PAW, 600.0 eV energy cut-off, D3-BJ).

Looking at the doubly fluorinated ( $1\bar{1}02$ ) surface, figure 4.50 shows the results for the adsorption of the first water molecule in the surfaces UC. The adsorption energy surface, seen in figure 4.50(a), reveals very well ordered and interesting adsorption areas. With the fluorination of both hill-site hydroxide groups the channel-like structure is now also very well reflected in the adsorption energy surface of water. It exhibits quite unfavourable adsorption sites along the hills of the surface while the adsorption in the valleys decreases further. Of course, the adsorption of the first water molecule is most preferred above one of the two remaining hydroxide groups in the valley and provides a minimum adsorption energy of  $-0.70$  eV. At this position (see figure 4.50(b) and figure 4.50(c)) the water molecule only accepts one hydrogen bond and donates a weak one to a fluoride ion, but due to the increasing Brønsted acidity of the remaining hydroxide groups, the adsorption energy decreases steadily. Considering the hydrogen bond network, “Z”-shaped motifs are formed where the sec-

ond corner (water molecule) is underpinned by a hydrogen bond from the valley-site hydroxide group. However, the average adsorption energy of  $-0.30$  eV stays roughly the same compared to the hydrated and singly fluorinated cases, which emphasises the unfavourable adsorption possibilities of water on the hill-site fluoride ions.

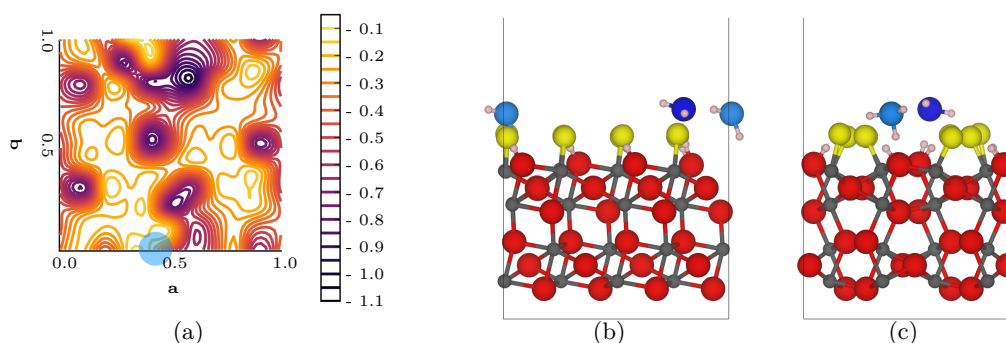


**Figure 4.51:** The second water molecule on a  $2 \times 2 \times 1$  SC of the doubly fluorinated ( $1\bar{1}02$ ) surface; (a) adsorption energy surface [eV], (b) side view structure depiction along  $a$ , and (c) side view structure depiction along  $b$  - gray = aluminium, red = oxygen, yellow = fluorine, white = hydrogen, light blue = first water oxygen, and blue = second water oxygen (VASP-DFT, PBE/PAW, 600.0 eV energy cut-off, D3-BJ).

Regarding the adsorption of the second water molecule on the  $2 \times 2 \times 1$  SC of the doubly fluorinated ( $1\bar{1}02$ ) surface, figure 4.51 shows the obtained results. Looking at figure 4.51(a), it can be seen that the resemblance with figure 4.50(a) is quite high while the sphere of influence of the first water molecule is comparably small but quite influencing. By overlapping this sphere of influence with the favourable adsorption sites of the surface itself, the second water molecule is most likely to adsorb at  $0.6a$  and  $0.8b$ . As it can be seen in figure 4.51(b) and figure 4.51(c), the second water molecule accepts one hydrogen bond from the underlying hydroxide group and one from the firstly adsorbed water molecule at this position. By accepting one hydrogen bond from the first water molecule, the latter becomes slightly more Brønsted basic, which results in the deprotonation of the surface and the formation of a hydronium ion. Therefore, the resulting minimum adsorption energy drops even further to  $-0.98$  eV, compared to the one resulting from figure 4.50 while the average adsorption decreases as well to  $-0.38$  eV due to the very good overlap of effects from the first water molecule

and the surface itself. Regarding the hydrogen bond network, the adsorption at this position results in the formation of a twisted sawhorse structure motif.

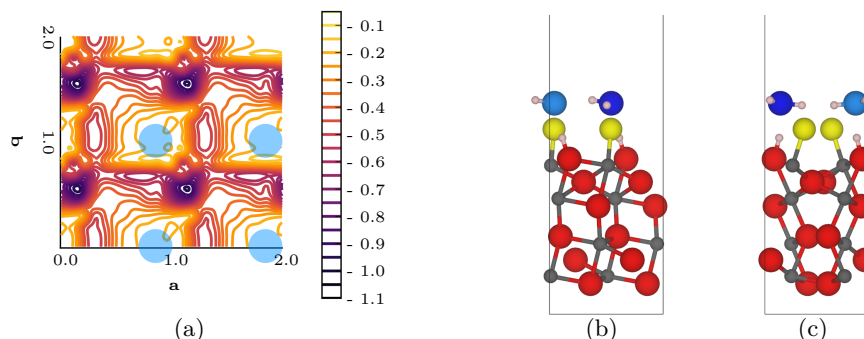


**Figure 4.52:** The second water molecule on the UC of the doubly fluorinated  $(1\bar{1}02)$  surface; (a) adsorption energy surface [eV], (b) side view structure depiction along  $a$ , and (c) side view structure depiction along  $b$  - gray = aluminium, red = oxygen, yellow = fluorine, white = hydrogen, light blue = first water oxygen, and blue = second water oxygen (VASP-DFT, PBE/PAW, 600.0 eV energy cut-off, D3-BJ).

Decreasing the space between the firstly adsorbed water molecules by focusing again on the UC of the doubly fluorinated  $(1\bar{1}02)$  surface, the results of the second water molecule's adsorption are shown in figure 4.52. It can be seen from figure 4.52(a) that the overlap of the firstly adsorbed water molecule's spheres of influence interrupt the area of unfavourable adsorption. Therefore, a grid-like area of favourable adsorption is generated again, as it was shown in figure 4.48 for the second water molecule on the singly fluorinated UC of the  $(1\bar{1}02)$  surface. This sometimes tripled overlap results in the most favourable adsorption position being located at  $0.1a$  and  $0.5b$  where the second water molecule adsorbed nearly directly on the last remaining hydroxide group in the valley. While accepting a hydrogen bond from this hydroxide group and from the firstly adsorbed water molecule, it also donates one to the first water molecule and to a hill-site fluoride (see figure 4.52(b) and figure 4.52(c)) which leads to the minimum adsorption energy of  $-0.88$  eV. This time, the resulting zigzag chain of the adsorbed water molecules is formed in the valley itself and is stabilised by donating hydrogen bonds from the water molecules to the fluoride ions in the hills. Combining the effect of the increased Brønsted acidity of the valley-site hydroxide groups and the

fact that the water molecules form zigzag chains of hydrogen bonds with each other, the sterical hindrance, which previously helped to push those chains atop the surface hills, is overcome and leads to this comparably very low adsorption energy. Besides, the impact of those factors on the average adsorption energy is relatively small and results in  $-0.39$  eV.

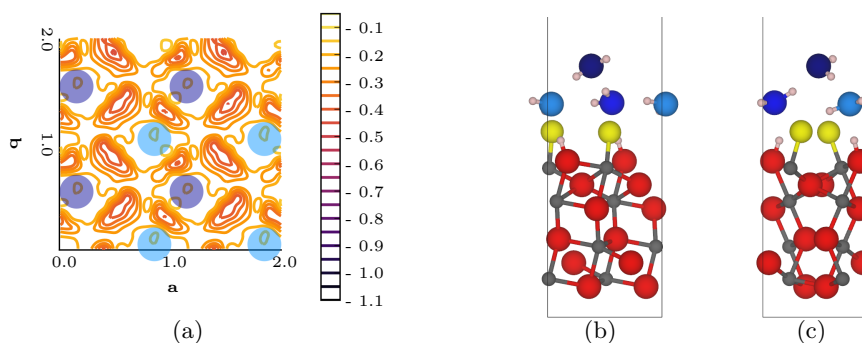


**Figure 4.53:** The third water molecule on the UC of the doubly fluorinated ( $1\bar{1}02$ ) surface; (a) adsorption energy surface [eV], (b) side view structure depiction along *a*, and (c) side view structure depiction along *b* - gray = aluminium, red = oxygen, yellow = fluorine, white = hydrogen, light blue = first water oxygen, blue = second water oxygen, and dark blue = third water oxygen (VASP-DFT, PBE/PAW, 600.0 eV energy cut-off, D3-BJ).

Going to the investigation of the adsorption of the third water molecule on the ( $1\bar{1}02$ ) surface's UC, figure 4.53 shows the corresponding results. Taking a look at figure 4.53(a), the position and orientation change of the formed zigzag chains by the previously adsorbed water molecules is revealed immediately. Since the zigzag chain is now located in the valley, there are no rows of favourable or unfavourable adsorption areas, because the third water molecule has to come much closer to the surface than before (previous adsorption of the third water molecule) and, by association, seems to be repelled by the hill-site fluoride ions. Therefore, only positions with a good resulting hydrogen bond network are able to provide reasonable adsorption energies, so the adsorption energy surface looks patchy. Nonetheless, the third water molecule adsorbs most favourably between two zigzag chains to bridge those two chains with each other via hydrogen bonding (see figure 4.53(b) and figure 4.53(c)), which results in a minimum adsorption energy of  $-0.42$  eV. Interestingly, nearly the same shaped

shallow bathtub-like  $O_8$ -rings are formed, as it was seen for the third water molecule on the singly fluorinated surface. This time, the sole difference is that the third water molecule is farther away in  $z$ -direction than it was the case previously. By revisiting [figure 4.53\(a\)](#) and remembering the reasons for that patchy look, it is no surprise that the average adsorption energy increases noticeably to  $-0.24$  eV.

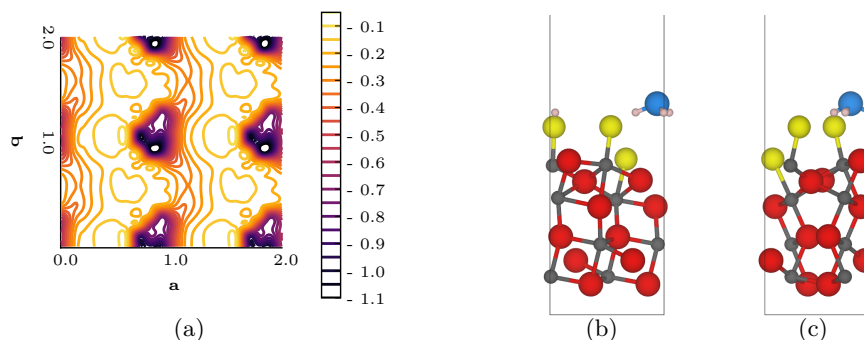


**Figure 4.54:** The first water molecule on the UC of the triply fluorinated  $(1\bar{1}02)$  surface; (a) adsorption energy surface [eV], (b) side view structure depiction along  $a$ , and (c) side view structure depiction along  $b$  - gray = aluminium, red = oxygen, yellow = fluorine, white = hydrogen, and light blue = first water oxygen (VASP-DFT, PBE/PAW, 600.0 eV energy cut-off, D3-BJ).

Increasing the amount of fluoride ions to three per UC of the  $(1\bar{1}02)$  surface, the results for the adsorption of the first water molecule are shown in [figure 4.54](#). From [figure 4.54\(a\)](#) it can be seen that the third fluoride ion decreases the area of favourable adsorption noticeably, but at the same time, it decreases the adsorption energy of the favourable adsorption site as well, which leads to an average adsorption energy of  $-0.30$  eV. The only favourable position to adsorb the first water molecule is the remaining hydroxide group, which is located in the valley. By looking at [figure 4.54\(b\)](#) and [figure 4.54\(c\)](#), it is revealed that due to the further increasing Brønsted acidity of the hydroxide group, the adsorbing water molecule is protonated and stabilised not only ionically but also by donating three weak hydrogen bonds to the surrounding fluoride ions. This stabilisation of the formed hydronium ion provides the most favourable adsorption energy for the modified  $(1\bar{1}02)$  surfaces of  $-1.02$  eV. At the same time, peaking zigzag chains are formed between the adsorbed water molecule

and one of the hill-site fluoride ions, which are then connected to the second hill-site fluoride as well.

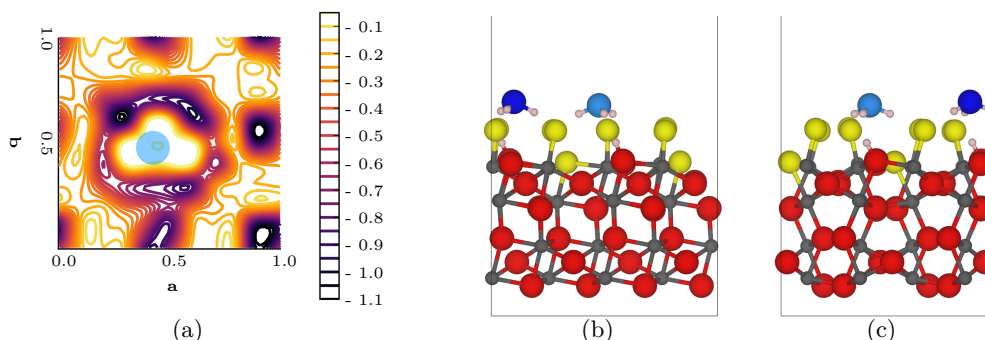


**Figure 4.55:** The second water molecule on a  $2 \times 2 \times 1$  SC of the triply fluorinated ( $1\bar{1}02$ ) surface; (a) adsorption energy surface [eV], (b) side view structure depiction along  $a$ , and (c) side view structure depiction along  $b$  - gray = aluminium, red = oxygen, yellow = fluorine, white = hydrogen, light blue = first water oxygen, and blue = second water oxygen (VASP-DFT, PBE/PAW, 600.0 eV energy cut-off, D3-BJ).

Using a  $2 \times 2 \times 1$  SC of the ( $1\bar{1}02$ ) surface for the adsorption of the second water molecule, the sphere of influence of the firstly adsorbed water molecule is investigated, and the obtained results are shown in figure 4.55. In figure 4.55(a) it can be seen that for the triply fluorinated ( $1\bar{1}02$ ) surface the best resemblance of the first two adsorption energy surfaces is found. That is not only due to the lack of favourable adsorption positions but also because the firstly adsorbed water molecule can not move that freely on the surface any longer, so its sphere of influence becomes smaller than the ones before. Besides, the adsorption on the first water molecule is considerably hindered again while the near environment is enhanced to adsorb the second water molecule, which results in an average adsorption energy of  $-0.38$  eV. Interestingly, the second water molecules favours to adsorb at the most distant possible site, which results in a minimum adsorption energy of  $-1.08$  eV. Since it adsorbs on this more remote position, the bonding and interaction situation is nearly the same (see figure 4.55(b) and figure 4.55(c)), as it was seen for the first molecule. Regarding the resulting hydrogen bond network, due to the larger distance between the now two hydronium ions, they can not form chains of hydrogen bonds. Instead, they simply form “Y”-

shaped motifs of hydrogen bonds, where the hydronium ion in the middle is more elevated. The slight decrease of the most favourable adsorption energy results from the possible formation of weak hydrogen bonds to fluoride ions whose performance is slightly influenced by the first water molecule. While for the more close adsorption positions the surrounding fluoride ions are already accepting hydrogen bonds from the first hydronium ion, the fluoride ions around the more distant adsorption position do not and thus, the adsorption on it becomes more favourable.

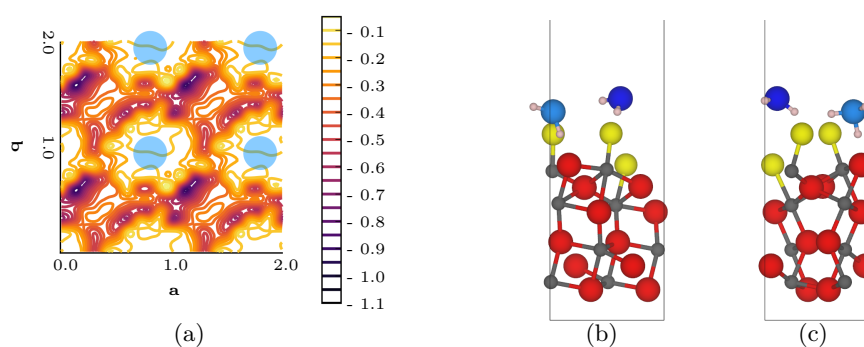


**Figure 4.56:** The second water molecule on the UC of the triply fluorinated  $(1\bar{1}02)$  surface; (a) adsorption energy surface [eV], (b) side view structure depiction along  $a$ , and (c) side view structure depiction along  $b$  - gray = aluminium, red = oxygen, yellow = fluorine, white = hydrogen, light blue = first water oxygen, and blue = second water oxygen (VASP-DFT, PBE/PAW, 600.0 eV energy cut-off, D3-BJ).

Decreasing the distance between the firstly adsorbed water molecules by using again the UC of the triply fluorinated  $(1\bar{1}02)$  surface, the results of the adsorption of the second water molecule can be seen in figure 4.56. As figure 4.56(a) shows, the adsorption energy surface provides once more a unfavourable adsorption very close to or on top of the first water molecule while only one favourable position for the second water molecule is revealed again. Since the first water molecule is pretty rigidly bound to its position, it can not adapt that easily to the second one in order to improve its orientation, so the formation of chains is not as easy as previously. As it can be seen in figure 4.56(b) and figure 4.56(c), the second water molecule accepts one of the hydrogen bonds previously donated to a fluoride ion by the first water molecule and donates one hydrogen bond to a fluoride ion itself and one to the first water molecule

via a more stretched hydrogen bond. At the same time, the first water molecule is rotating a bit to stabilize its position on the surface by pointing one hydrogen ion back towards the surface hydroxide groups position. Therefore, with the quite elongated hydrogen bond, the formation of zigzag chains similar to the ones of the doubly fluorinated ( $1\bar{1}02$ ) surface is possible. This improvement of the hydrogen bonding on this surface results in a minimum adsorption energy of  $-0.84$  eV while the average adsorption energy of  $-0.31$  eV rises to its maximum, compared to the adsorption of the second water molecule on the other surface's UCs.

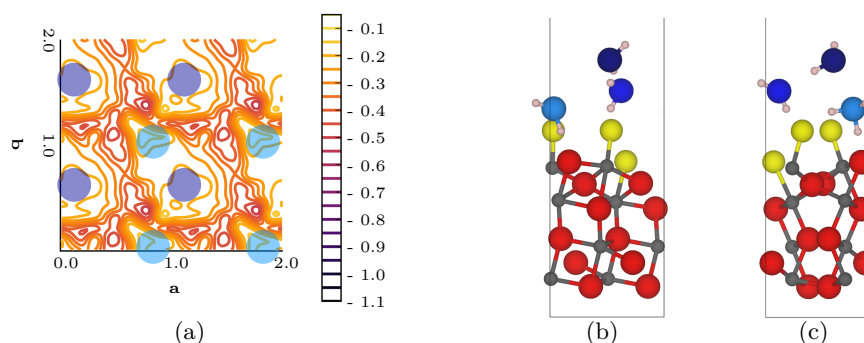


**Figure 4.57:** The third water molecule on the UC of the triply fluorinated ( $1\bar{1}02$ ) surface; (a) adsorption energy surface [eV], (b) side view structure depiction along *a*, and (c) side view structure depiction along *b* - gray = aluminium, red = oxygen, yellow = fluorine, white = hydrogen, light blue = first water oxygen, blue = second water oxygen, and dark blue = third water oxygen (VASP-DFT, PBE/PAW, 600.0 eV energy cut-off, D3-BJ).

Increasing the amount of water on the UC even further with the adsorption of the third water molecule, the calculations provide the results shown in figure 4.57. From figure 4.57(a) it can be seen that it looks very similar to the adsorption energy surface for the third water molecule on the doubly fluorinated ( $1\bar{1}02$ ) surface. The small difference in the distance between the first water molecule and the second water molecule in the lower right, compared the doubly fluorinated surface case, prevents the adsorption of the third water molecule above this “edge” due to steric hindrance. Due to this resemblance, the minimum and the average adsorption energies are both only slightly lower than the doubly fluorinated case with  $-0.49$  eV and  $-0.28$  eV, respectively. Looking at figure 4.57(b) and figure 4.57(c), it can be seen that the



third water molecule donates and accepts a hydrogen bond from the second water molecule, and by association, water chains crossing the channels are formed. Due to this better possibility to form zigzag chains, the previous chains, using a quite elongated hydrogen bond, are broken up to allow for a better adaptation for the formation of the new chains. Using the first hydronium ion only as a kind of spacer and connector to the surface structure, this implicates the possibility that the fourth water molecule might adsorb similarly to the third one on the previous  $(1\bar{1}02)$  surfaces to form alike network structures.

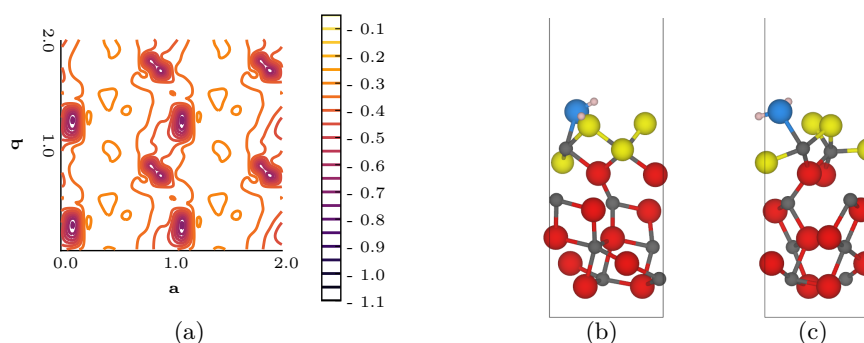


**Figure 4.58:** The first water molecule on the UC of the fourfold fluorinated  $(1\bar{1}02)$  surface; (a) adsorption energy surface [eV], (b) side view structure depiction along  $a$ , and (c) side view structure depiction along  $b$  - gray = aluminium, red = oxygen, yellow = fluorine, white = hydrogen, and light blue = first water oxygen (VASP-DFT, PBE/PAW, 600.0 eV energy cut-off, D3-BJ).

Coming to the last modified  $(1\bar{1}02)$  surface, namely the fourfold fluorinated one, the results for the investigation of the adsorption of the first water molecule on the UC are shown in figure 4.58. As discussed in subsection 4.2.2 Fluorination of Hydrated  $\alpha$ -Aluminium Oxide Surfaces, the fourfold fluorinated  $(1\bar{1}02)$  surface underwent a reconstruction during the structure optimisation, so it exhibits free coordination sites of the two topmost aluminium centres. Thus, the adsorption energy surface, seen in figure 4.58(a), indicates those positions by a comparably quite low minimum adsorption energy of  $-0.70$  eV. Since the first water molecule completes the CS of one aluminium centre, the orientation of it only allows for one weak additional hydrogen bond to a fluoride ion. For the positions where it would not fill a aluminium centres CS, it orien-

tates itself in way to form two hydrogen bonds to the surface fluoride ions, favourably with terminal ones, which results in the somehow unexpected good adsorption energies outside of the most favourable positions. Due to this, the average adsorption energy with  $-0.36$  eV is also noticeably lower than previous ones for the adsorption of the first water molecule. Therefore, it seems that two hydrogen bonds to surface fluoride ions, particularly terminal ones, provide a better stabilisation of the water molecule on the surface than one hydrogen bond from a hydroxide of the surface. Please note that the contradiction to the results of the aluminium (oxo)hydroxides (see table 4.4) is avoided by the fact that, this time, terminal fluoride ions play a major role, which were absent in those bulk materials. Furthermore, the quite strong effects of this difference in the CN of anions was already seen for the NMR shifts (see subsection 4.1.2 Fluoride Depending NMR Shifts in Aluminium (oxo)hydroxides and subsection 4.2.3 NMR Shifts of  $\alpha$ -Aluminium Oxide Surfaces) and the OH stretch frequencies as well (see subsection 4.2.1 Hydration of  $\alpha$ -Aluminium Oxide Surfaces and subsection 4.2.2 Fluorination of Hydrated  $\alpha$ -Aluminium Oxide Surfaces).

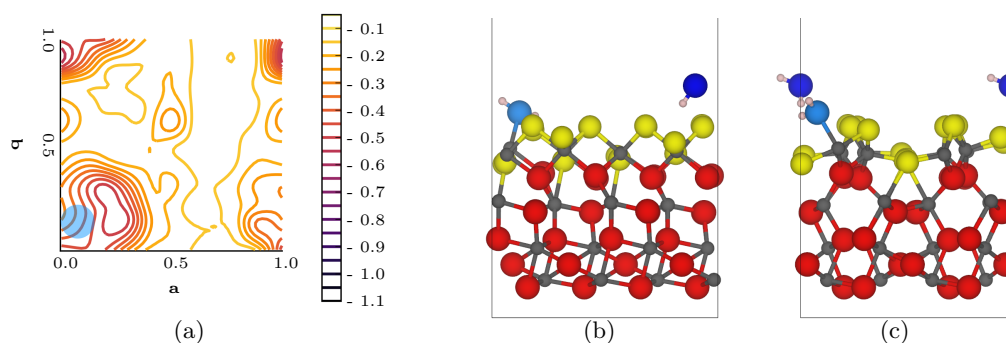


**Figure 4.59:** The second water molecule on a  $2 \times 2 \times 1$  SC of the fourfold fluorinated  $(1\bar{1}02)$  surface; (a) adsorption energy surface [eV], (b) side view structure depiction along  $a$ , and (c) side view structure depiction along  $b$  - gray = aluminium, red = oxygen, yellow = fluorine, white = hydrogen, light blue = first water oxygen, and blue = second water oxygen (VASP-DFT, PBE/PAW, 600.0 eV energy cut-off, D3-BJ).

Using a  $2 \times 2 \times 1$  SC of the fourfold fluorinated  $(1\bar{1}02)$  surface, the distances between the firstly adsorbed water molecules become larger, which leads to the results shown in figure 4.59. From figure 4.59(a) it can be seen that the right hand side of

this adsorption energy surface again exhibits the unfavourable adsorption on top of the hill-site fluoride ions. Otherwise, the very favourable adsorption positions to fill the under-coordinated CSs of the topmost aluminium centres are gone or at least became less favourable due to surface relaxations. Instead, the adsorption close to the firstly adsorbed water molecule becomes very favourable and results in a noticeable relaxation of the fluoride ions in the surface, which results in a change of orientation of the first water molecule. Afterwards, it stabilises a valley-site fluoride ion instead of a hill-site one. In figure 4.59(b) and figure 4.59(c) it can be seen that the second water molecule accepts a hydrogen bond from the firstly adsorbed one and also donates a weak hydrogen bond to a terminal fluoride ion of the former valley, which results in a minimum adsorption energy of  $-0.57$  eV. Regarding the formation of a hydrogen bond network, only parts of zigzag chains are formed from the anions, where one end (the second water molecule) is underpinned by donating a hydrogen bond to an underlying fluoride ion. Due to the otherwise comparably unfavourable adsorption of the second water molecule on this surface, the average adsorption energy reaches the highest value for all SCs of the  $(1\bar{1}02)$  surfaces with  $-0.22$  eV.

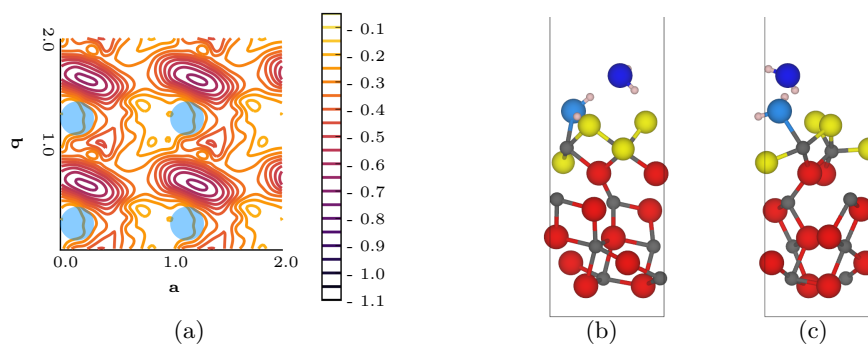


**Figure 4.60:** The second water molecule on the UC of the fourfold fluorinated  $(1\bar{1}02)$  surface; (a) adsorption energy surface [eV], (b) side view structure depiction along  $a$ , and (c) side view structure depiction along  $b$  - gray = aluminium, red = oxygen, yellow = fluorine, white = hydrogen, light blue = first water oxygen, and blue = second water oxygen (VASP-DFT, PBE/PAW, 600.0 eV energy cut-off, D3-BJ).

Going back to the UC of the  $(1\bar{1}02)$  surface for the adsorption of the second water molecule, the results of this investigation can be seen in figure 4.60. By taking a

first look at [figure 4.60\(a\)](#), it is revealed that again the favourable adsorption of the second water molecule is dominated by the influence of the firstly adsorbed water molecules while the free areas of the fourfold fluorinated ( $1\bar{1}02$ ) surface are unlikely to be adsorbed at. Shifting the attention to [figure 4.60\(b\)](#) and [figure 4.60\(c\)](#), it can be seen that the second water molecule accepts a hydrogen bond from the first one while it donates a hydrogen bond to a hill-site fluoride ion itself, which then resulted in a minimum adsorption energy of  $-0.66$  eV. Since the firstly adsorbed molecules are much closer together using a **UC**, the relaxation of the surface fluoride ions is prevented, and by association, both water molecules now stabilise only hill-site fluoride ions while the second unsaturated aluminium **CS** of the **UC** remains fivefold coordinated. For the hydrogen bond network this results in a tilted,  $180^\circ$  rotated “V”-shaped motif, where one end (the first water molecule) expands this motif for one hydrogen bond to a fluoride ion. Due to the comparably large areas of favourable adsorption, the average adsorption energy decreases again to  $-0.35$  eV, compared to the one resulting from [figure 4.59](#).

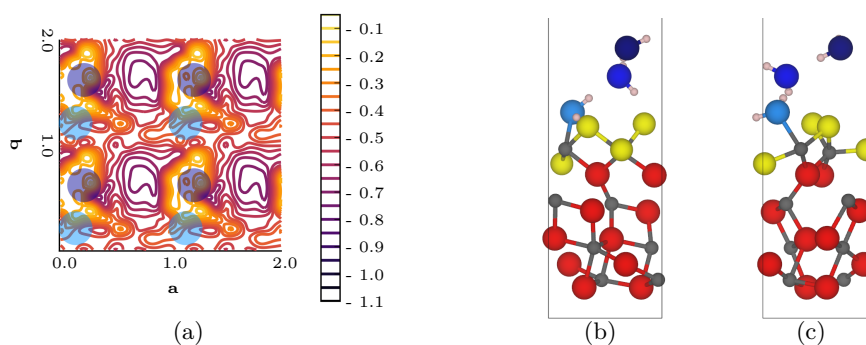


**Figure 4.61:** The third water molecule on the **UC** of the fourfold fluorinated ( $1\bar{1}02$ ) surface; (a) adsorption energy surface [eV], (b) side view structure depiction along *a*, and (c) side view structure depiction along *b* - gray = aluminium, red = oxygen, yellow = fluorine, white = hydrogen, light blue = first water oxygen, blue = second water oxygen, and dark blue = third water oxygen (VASP-DFT, PBE/PAW, 600.0 eV energy cut-off, D3-BJ).

Increasing the amount of water the last time to three molecules per **UC** for the ( $1\bar{1}02$ ) surface, the results for the fourfold fluorinated surface are shown in [figure 4.61](#). From [figure 4.61\(a\)](#) it can be seen that again the favourable and unfavourable adsorp-

tion sites tend to form rows, as it was seen, for example, in [figure 4.49\(a\)](#). However, the rows are not really closed and are rotated as well this time, which leads to an average adsorption energy of  $-0.46$  eV. Furthermore, it seems that the adsorption on top of the first water molecule is also favoured now, which is in contrary to all other observations this far. But looking at [figure 4.61\(b\)](#) and [figure 4.61\(c\)](#) indicates that this is only due to the adsorption of the third water molecule way above the first one since the most stable adsorption position exhibits this motif of being farther away from the surface as well. To obtain the minimum adsorption energy of  $-0.73$  eV, the third water molecule adsorbs between two secondly adsorbed water molecules by accepting and donating one hydrogen bond each and bridging them. Thus a zigzag chain is formed again, as it was the case for the third water molecule on the triply fluorinated  $(1\bar{1}02)$  surface. But since the zigzag chain is formed further away from the hill-site fluorides this time, the water molecule is not repelled that much, and by association, the adsorption energy is lower than for the triply fluorinated  $(1\bar{1}02)$  surface. In contrast to the triply fluorinated  $(1\bar{1}02)$  surface, the chains on this modified  $(1\bar{1}02)$  surface are not only connected to the surface via the first water molecule, but instead use the firstly water molecules as well as hydrogen bonds to a hill-site fluorides to connect to the surface. As it was seen many times before, the adsorption of the third water molecules depends almost solely on the previously adsorbed water molecules.

In order to sum up the results of the  $(1\bar{1}02)$  surface, the most important adsorption energies and a short description of the adsorbing water molecule's binding for each modified surface and added water molecule are shown in [table 4.12](#). It can be seen that the maximum adsorption energy roughly stayed in the range of  $-100$  to  $-200$  meV per water molecule and unit cell with two exceptions. Firstly, the second water molecule on the [SC](#) of the triply fluorinated  $(1\bar{1}02)$  surface provided a much higher maximum adsorption energy, which is due to a very unfavourable adsorption on top of the hydronium ion. In the second case, the adsorption of the first water molecule on the reconstructed fourfold fluorinated  $(1\bar{1}02)$  surface provided a lower maximum

**Table 4.12:** Three notable adsorption energies resulting from each adsorption energy surface and a short adsorption site description for the water adsorption on modified (1102) surfaces - fourfold fluorinated surface is separated to highlight its reconstruction (VASP-DFT, PBE/PAW, 600.0 eV energy cut-off, D3-BJ).

$\text{H}_2\text{O}$	F/UC	$E_{\text{ads,MAX}}$	$E_{\text{ads,MIN}}$	$\bar{E}_{\text{ads}}$	Positioning
		[eV]	[eV]	[eV]	
1. on UC	0	-0.14	-0.48	-0.28	on valley OH; near hill OH
	1	-0.17	-0.60	-0.29	on valley OH; among hill F+OH
	2	-0.13	-0.70	-0.30	on valley OH; among 2 hill F
	3 <sup>a</sup>	-0.11	-1.02	-0.30	on valley OH; among 3 hill F
	4	-0.29	-0.70	-0.36	filling Al CS; near hill F
2. on SC	0	-0.09	-0.68	-0.27	above 2 hill OH
	1	-0.13	-0.57	-0.28	on valley OH; near hill OH
	2	-0.14	-0.98	-0.38	on valley OH; among 1.+hill F
	3 <sup>a</sup>	-0.00	-1.08	-0.38	on valley OH; among 3 hill F
	4	-0.11	-0.57	-0.22	above 1.+hill F
2. on UC	0	-0.16	-0.70	-0.40	on hill OH; among 2 1.
	1	-0.14	-0.63	-0.33	on valley OH; among 2 1.
	2	-0.17	-0.88	-0.39	on valley OH; among 2 1.+F
	3	-0.11	-0.84	-0.31	above 2 1.+hill F
	4	-0.19	-0.66	-0.35	above 1.+hill F
3. on UC	0	-0.13	-0.72	-0.42	above 1.+2.
	1	-0.17	-0.72	-0.47	above 1.+2.
	2	-0.15	-0.42	-0.24	above 1.+2.
	3	-0.14	-0.49	-0.28	above 2 2.
	4	-0.18	-0.73	-0.46	above 2 2.

<sup>a</sup> hydronium ion was formed due to surface deprotonation

adsorption energy because the water molecule stabilises the reconstructed surface by filling one aluminium centre's CS. Furthermore, due to this reconstruction (see also subsection 4.2.2 Fluorination of Hydrated  $\alpha$ -Aluminium Oxide Surfaces), the fourfold fluorinated (1 $\bar{1}$ 02) surface was in all cases an exception to all possible trends for these modifications of the (1 $\bar{1}$ 02) surface. Regarding the spheres of influence of the firstly adsorbed water molecules, it was seen that indeed the previously mentioned area of  $\approx 20 \text{ \AA}^2$  for the (0001) surface cut was observed, but they also depended heavily

on the hydrogen bond network of the surface itself because it could propagate their influence farther away. It can also be seen from nearly all three notable adsorption energies that the hydrated and the singly fluorinated ( $1\bar{1}02$ ) surfaces seemed to behave similarly, while the doubly and the triply fluorinated surfaces did so as well. This was due to very similar adsorption motifs and positions of the first and the second water molecule of those two pairs. The distinct differences in the described hydrogen bond networks often resulted from comparably small structural differences and adjustments to the higher amount of fluoride on the surface. Additionally, this similarity can also be seen very nicely by looking at [figure A.13](#) to [figure A.16](#) in the section [A.3 Surfaces](#), where the adsorption energy surfaces are shown again in a more comparable fashion.

Besides that, the doubly fluorinated ( $1\bar{1}02$ ) surface provided a very interesting adsorption pattern for the first water molecule. Due to the two fluoride ions on the hill, the adsorption was only possible in the channels. Taking yet again a look at [figure 4.50\(a\)](#), it can also be seen that the barrier between two most favourable adsorption sites along the channel was lower than the one crossing the hill. Thus, it might be possible, with very small amounts of water, to obtain water trickles on the surface with a distinct distance to each other. Going forward and regarding the formation of a hydronium ion on the triply fluorinated ( $1\bar{1}02$ ) surface, this modification might be usable as a heterogeneous Brønsted acidic catalyst. Furthermore, regarding a possible fluoride protective coat, the fully fluorinated ( $1\bar{1}02$ ) surface provided a growing hydrogen bond network which tends to avoid interactions with the surface itself. Only the reconstruction enabled this surface to provide a weak point for the interaction with water. Other than that, the interaction with water was quite low and additional water molecules preferred to interact only with already adsorbed water molecules. The adsorption energy of water molecules on the fully fluorinated surface indeed decreased, but the surface's relaxation due to water adsorption was very low and for the fully fluorinated case it resulted in a less favourable adsorption of the second water molecule (see [figure 4.59](#)). Additionally a good adsorption of

water does not inherently mean that the surface is less protected from dissolution by water, the water might just adsorb favourably on the surface without changing the surface structure. To really study the dissolution of the modified surfaces, molecular dynamics (MD) calculations are necessary to study the kinetics for such a process, at least thermodynamics (see subsection 4.2.2 [Fluorination of Hydrated  \$\alpha\$ -Aluminium Oxide Surfaces](#)) indicated that surface fluoride ions increase the surfaces' stability. Thus, fluorinating the  $(1\bar{1}02)$  surface and overcoming the challenges introduced by its reconstruction, a fluoride protective coat might be possible but further studies are needed.

### 4.3.3 The $(11\bar{2}3)$ Surface

Shifting once more the focus of the water adsorption investigation, the  $(11\bar{2}3)$  surface is in the spotlight for this section. Remembering subsection 4.2.1 [Hydration of  \$\alpha\$ -Aluminium Oxide Surfaces](#) and subsection 4.2.2 [Fluorination of Hydrated  \$\alpha\$ -Aluminium Oxide Surfaces](#), it can be recalled that the  $(11\bar{2}3)$  surface provides a much larger UC than the previous two surface cuts and resembles structural elements of the  $(1\bar{1}02)$  surface as well. It also provides terminal ligands, but this time, they are farther away from each other, which should lower the steric hindrance in the valleys. Furthermore, due to the larger UC, studying the firstly adsorbed water molecule's sphere of influence on the larger SC would be too demanding, compared to the new insight it would bring. Thus, only UCs are considered for this surface and its modifications.

Starting with the adsorption of the first water molecule on the hydrated  $(11\bar{2}3)$  surface, [figure 4.62](#) shows the results of the corresponding calculations. Looking at [figure 4.62\(a\)](#), it can be seen that the adsorption on top of the two terminal ligands (molecularly adsorbed water molecule through hydration) is quite unfavourable, while the adsorption between them is very likely. At those positions, the first water molecule comes closer to the actual surface and into the surface's valley. The most favourable adsorption position allows the formation of three hydrogen bonds, two are donated



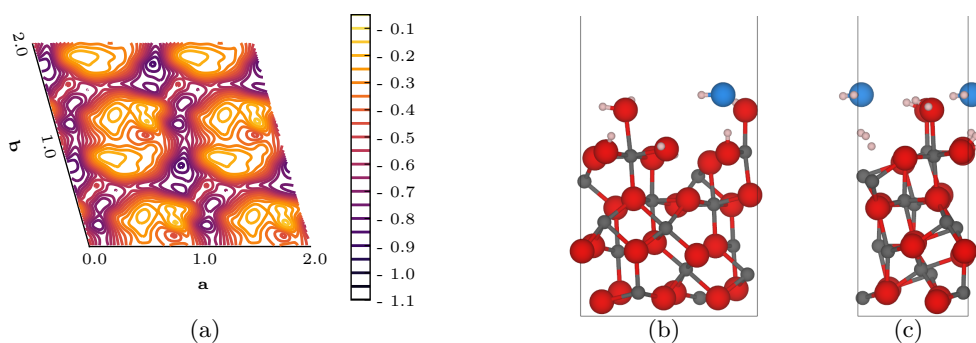


**Figure 4.62:** The first water molecule on the UC of the hydrated  $(11\bar{2}3)$  surface; (a) adsorption energy surface [eV], (b) side view structure depiction along  $a$ , and (c) side view structure depiction along  $b$  - gray = aluminium, red = oxygen, white = hydrogen, and light blue = first water oxygen (VASP-DFT, PBE/PAW, 600.0 eV energy cut-off, D3-BJ).

from the surface to the water molecule while it donates one back to the surface itself. As it can be seen in figure 4.62(b) and figure 4.62(c), this involves one hydroxide group from the surface's valley and the terminal hydroxide group twice. Regarding the formed hydrogen bond network, a zigzag chain along  $a$  is formed, which is stabilised via the water ligand and one valley hydroxide group. This leads to a minimum adsorption energy of  $-0.84$  eV. Combining the favourable and unfavourable adsorption sites into the average adsorption energy, a value of  $-0.45$  eV is obtained. This is only slightly higher than the one resulting from figure 4.27(a) of the hydrated (0001) surface and much lower than the one for the hydrated  $(1\bar{1}02)$  surface.

Increasing the amount of water by adsorbing the second water molecule on the hydrated  $(11\bar{2}3)$  surface, the obtained results of this investigation can be seen in figure 4.63. The adsorption energy surface in figure 4.63(a) shows that once more the adsorption on top of the previously adsorbed water molecule is unfavourable due to the lack of possible hydrogen bonds. Thus, the area of unfavourable adsorption increases, so the average adsorption energy increases as well and provides a value of  $-0.38$  eV. Trying to maximise its hydrogen bonding, the second water molecule adsorbs most favourably between the two terminal ligands and the firstly adsorbed water molecule. In this position it donates two hydrogen bonds and accepts two

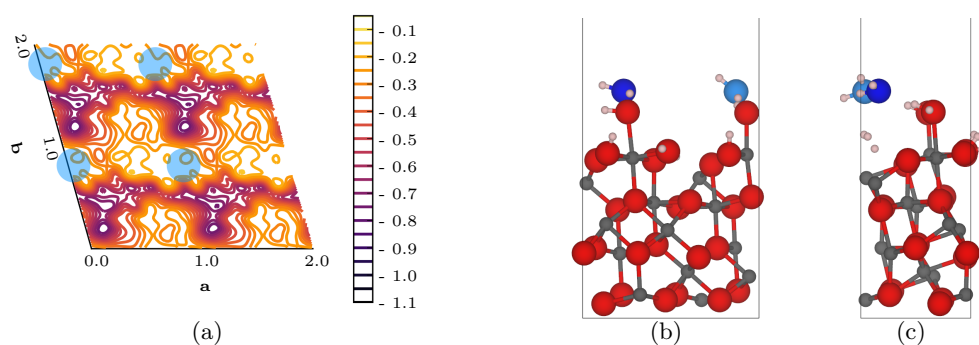


**Figure 4.63:** The second water molecule on the UC of the hydrated  $(11\bar{2}3)$  surface; (a) adsorption energy surface [eV], (b) side view structure depiction along  $a$ , and (c) side view structure depiction along  $b$  - gray = aluminium, red = oxygen, white = hydrogen, light blue = first water oxygen, and blue = second water oxygen (VASP-DFT, PBE/PAW, 600.0 eV energy cut-off, D3-BJ).

hydrogen bonds at the same time (see figure 4.63(b) and figure 4.63(c)), which results in a minimum adsorption energy of  $-0.75$  eV. The increased minimum adsorption energy results from the weaker hydrogen bonds, compared to the hydrogen bonds of the first water molecule with the terminal hydroxide group, involving the water ligand of the surface. Nonetheless, a very interesting hydrogen bond network results from this adsorption position. Both water molecules now bridge two terminal ligands along  $a$ , resulting in two zigzag chains, which are interconnected and thus, forming a “ $\beta$ -sheet”-like shaped structure (see figure A.45(b)).

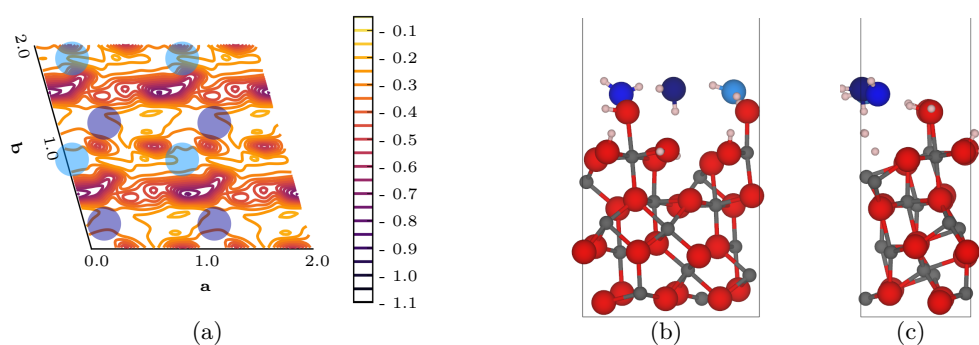


**Figure 4.64:** The third water molecule on the UC of the hydrated  $(11\bar{2}3)$  surface; (a) adsorption energy surface [eV], (b) side view structure depiction along  $a$ , and (c) side view structure depiction along  $b$  - gray = aluminium, red = oxygen, white = hydrogen, light blue = first water oxygen, blue = second water oxygen, and dark blue = third water oxygen (VASP-DFT, PBE/PAW, 600.0 eV energy cut-off, D3-BJ).

Considering the third water molecule on the hydrated  $(11\bar{2}3)$  surface, [figure 4.64](#) shows the results of this adsorption process. Taking a first look at [figure 4.64\(a\)](#), it is seen that a broad row of unfavourable adsorption has formed which is only interrupted by two positions of favourable adsorption, resulting in a further increased average adsorption energy of  $-0.34$  eV. Those two positions result from the possible adsorption on top of one of the terminal ligands and bridging the first two water molecules via hydrogen bonds. But there are other, more favourable adsorption positions for the third water molecule. The most favourable one can be seen in [figure 4.64\(b\)](#) and [figure 4.64\(c\)](#) where it adsorbs between the first two water molecules by forming a water chain along  $b$ . Doing so involves the donation and acceptance of two hydrogen bonds each while the second water molecule turns one of its donating hydrogen bonds to the water ligand away and donates it to the third water molecule. This results in a stronger hydrogen bond than before. Therefore, the minimum adsorption energy remains low with a value of  $-0.72$  eV. Looking at the resulting hydrogen bond network on the surface, the “ $\beta$ -sheet”-like shaped structure is expanded by enlarging one half of the tetragons to pentagons, which also bridge to the next “ $\beta$ -sheet”-like shaped structure motif (see [figure A.45\(c\)](#)).

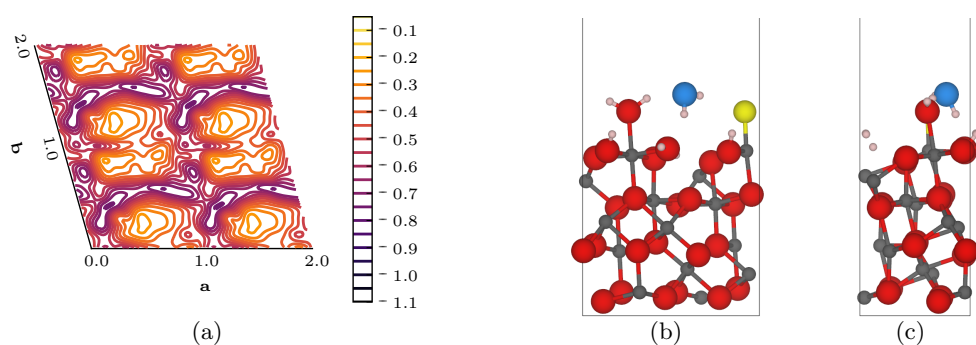


**Figure 4.65:** The first water molecule on the UC of the singly fluorinated  $(11\bar{2}3)$  surface; (a) adsorption energy surface [eV], (b) side view structure depiction along  $a$ , and (c) side view structure depiction along  $b$  - gray = aluminium, red = oxygen, yellow = fluorine, white = hydrogen, and light blue = first water oxygen (VASP-DFT, PBE/PAW, 600.0 eV energy cut-off, D3-BJ).

Going to the fluorinated  $(11\bar{2}3)$  surfaces, [figure 4.65](#) shows the results of the first water molecule's adsorption on the singly fluorinated  $(11\bar{2}3)$  surface. Taking a look at [figure 4.65\(a\)](#), it seems like the area of favourable adsorption is increased, compared to the one in [figure 4.62\(a\)](#). On the other hand, it can be seen that the favourable adsorption sites become slightly less attractive for the first water molecule to adsorb on. Nonetheless, the resulting average adsorption energy decreases slightly to  $-0.48$  eV. Furthermore, the position of the firstly introduced fluoride ion, at the former terminal hydroxide position, is not as recognisable, as it was the case for the  $(0001)$  and the  $(1\bar{1}02)$  surfaces. Regarding the most favourable adsorption position with an adsorption energy of  $-0.74$  eV, the first water molecule positions itself between the two different terminal ligands, unlike it did for the hydrated  $(11\bar{2}3)$  surface, where it positioned itself between two occurrences of the same terminal ligand. Due to the terminal fluoride ion, the water ligand can orient itself more freely than before and, by association, can adjust itself better to the approaching first adsorbing water molecule, which explains the increased area of favourable adsorption. Therefore, this enhances the adsorption between the two different terminal ligands. As it can be seen in [figure 4.65\(b\)](#) and [figure 4.65\(c\)](#), the first adsorbing water molecule accepts a hydrogen bond from the water ligand while donating one hydrogen bond to a valley hydroxide group and a quite weak one to the terminal fluoride ion. Featuring this weak (elongated) hydrogen bond to the terminal fluoride ion, the resulting hydrogen bond network forms a mixed zigzag chain along  $b$ , which "stands" on bonds to aluminium centres and one hydrogen bond to the  $(11\bar{2}3)$  surface's valley. Without considering this weak hydrogen bond to the terminal fluoride ion, the hydrogen bond network would resemble a tilted "Z"-like shaped structure if the hydrogen bonds within the valley are considered as well (see [figure A.45\(a\)](#)).

Increasing the amount of water on the singly fluorinated  $(11\bar{2}3)$  surface to two, [figure 4.66](#) shows the results of this investigation. In [figure 4.66\(a\)](#) it is revealed that the adsorption on top of the firstly adsorbed water molecule is again unfavourable

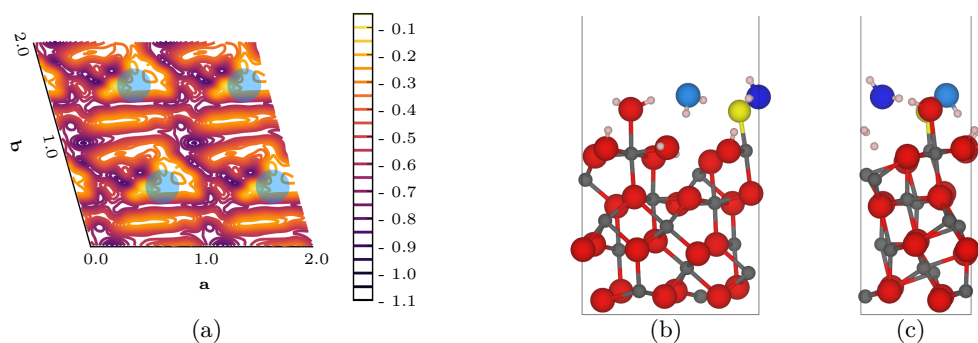


**Figure 4.66:** The second water molecule on the UC of the singly fluorinated  $(11\bar{2}3)$  surface; (a) adsorption energy surface [eV], (b) side view structure depiction along  $a$ , and (c) side view structure depiction along  $b$  - gray = aluminium, red = oxygen, yellow = fluorine, white = hydrogen, light blue = first water oxygen, and blue = second water oxygen (VASP-DFT, PBE/PAW, 600.0 eV energy cut-off, D3-BJ).

while, at the same time, the area of favourable adsorption increases due to the new possibilities to form hydrogen bonds. That is why the average adsorption energy does not change, compared to the one with one water molecule already adsorbed, and provides a value of  $-0.48$  eV. As figure 4.66(b) and figure 4.66(c) indicate, the adsorption of the second water molecule results in the formation of various hydrogen bonds and results in a minimum adsorption energy of  $-0.85$  eV. It positions itself between two terminal fluoride ions, where it accepts two hydrogen bonds from the valley hydroxide groups, one from the water ligand, which was previously donated to the terminal fluoride ion, and by donating one hydrogen bond to the terminal fluoride ion. Thus, the oxygen atom of the second water molecule is “fivefold coordinated” with hydrogen atoms and features a square pyramidal “CS”. The same structure motif of a  $\mu_5$ -O was also found by Kemnitz *et al.* [215], although, they observed it in a fluorinated aluminium oxide-*iso*-propoxide cluster. Nonetheless, the resulting hydrogen bond network represents a mixed chain featuring the two terminal ligands and both adsorbed water molecules and is directed along  $b$ . Within those mixed chains, the first water molecule bridges the wider gap between the two terminal ligands while the second water molecule bridges them via a horizontal peak near their narrower gap.

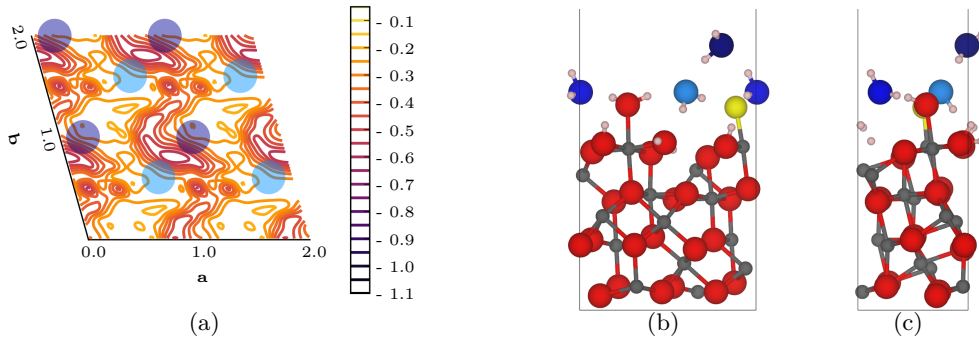


**Figure 4.67:** The third water molecule on the UC of the singly fluorinated  $(11\bar{2}3)$  surface; (a) adsorption energy surface [eV], (b) side view structure depiction along  $a$ , and (c) side view structure depiction along  $b$  - gray = aluminium, red = oxygen, yellow = fluorine, white = hydrogen, light blue = first water oxygen, blue = second water oxygen, and dark blue = third water oxygen (VASP-DFT, PBE/PAW, 600.0 eV energy cut-off, D3-BJ).

Finalising the adsorption of water on the singly fluorinated  $(11\bar{2}3)$  surface by adding the third water molecule, the results are shown in figure 4.67. From the adsorption energy surface in figure 4.67(a) it can be seen that the previously discussed mixed zigzag hydrogen bond chain, formed with the secondly adsorbed water molecule, is resembled quite well as the unfavourable adsorption area. This leads to a noticeably increased average adsorption energy of  $-0.33$  eV. Furthermore, the most favourable adsorption position with an energy of  $-0.59$  eV results mainly from the possible acceptance of a hydrogen bond by the third water molecule from the secondly adsorbed water molecule,, as it can be seen in figure 4.67(b) and figure 4.67(c). They show that the third water molecule not only accepts this one hydrogen bond but also donates one itself to the first water molecule. Additionally, it is revealed that the third water molecule can not be influenced by the surface directly, and by association, its adsorption solely depends on the previously adsorbed water molecules. Regarding the formed hydrogen bond network, due to the bridging of the mixed chains along  $b$  via the third water molecule, flat  $O_{10}-F_2$ -rings are formed where only the third water molecules are out of plane (see figure A.46(c)).

Increasing the amount of fluoride on the  $(11\bar{2}3)$  surface to two, the investigation of the first water molecule on it yields the results shown in figure 4.68. Comparing the

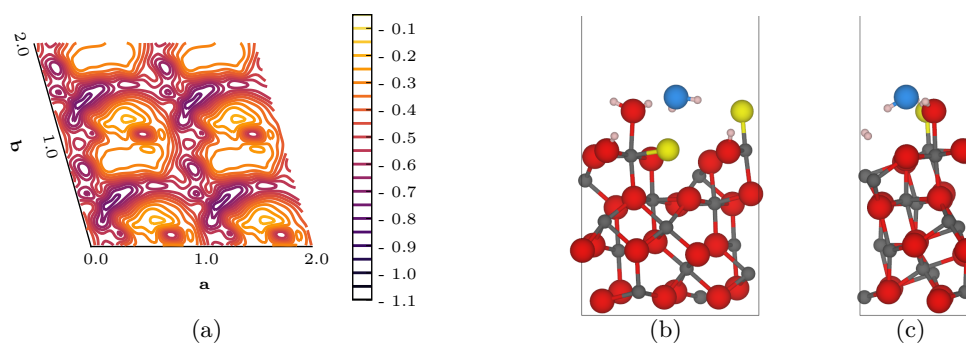


**Figure 4.68:** The first water molecule on the UC of the doubly fluorinated  $(11\bar{2}3)$  surface; (a) adsorption energy surface [eV], (b) side view structure depiction along  $a$ , and (c) side view structure depiction along  $b$  - gray = aluminium, red = oxygen, yellow = fluorine, white = hydrogen, and light blue = first water oxygen (VASP-DFT, PBE/PAW, 600.0 eV energy cut-off, D3-BJ).

new adsorption energy surface in figure 4.68(a) with the ones in figure 4.62(a) for the hydrated and in figure 4.65(a) for the singly fluorinated, it can be seen that the second fluorination nearly has no influence on the adsorption of the first water molecule. That is because the substituted hydroxide group in the valley was not involved in any interaction of the previously adsorbing water molecules and the former modified  $(11\bar{2}3)$  surfaces. Thus, only minor changes can be identified comparing figure 4.68(a) with figure 4.65(a), even the most favourable adsorption site is very similar and is just on the other side of the terminal ligand's positions. Therefore, it is not surprising that the minimum and average adsorption energies,  $-0.74$  eV and  $-0.44$  eV, respectively, are quite similar to the ones of the singly fluorinated  $(11\bar{2}3)$  surface's first water adsorption. The formed hydrogen bond network is very similar as well and provides again a mixed zigzag chain along  $b$  featuring a weak (elongated) hydrogen bond to the terminal fluoride ion. Whereas, it shows just a lying spread "V" without considering this weak hydrogen bond. Nonetheless, the adsorbing water molecule is tilted towards the valley fluoride ion and, by association, donating a second weak hydrogen bond within this hydrogen bond network.

Adding the second water molecule to the doubly fluorinated  $(11\bar{2}3)$  surface reveals the findings shown in figure 4.69. Due to the positioning of the firstly adsorbed water

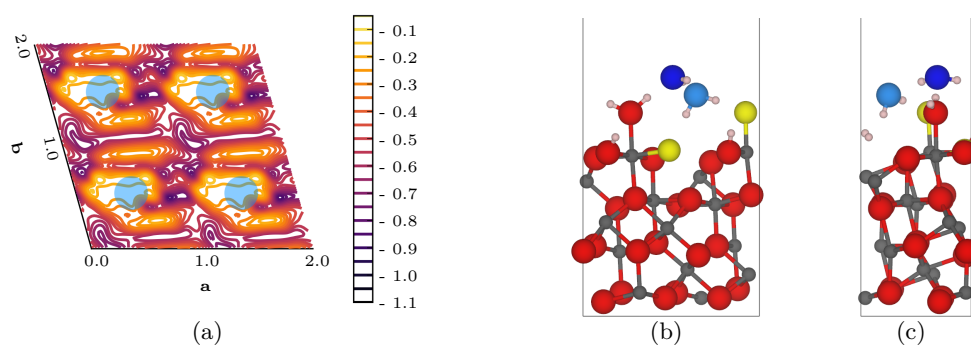


**Figure 4.69:** The second water molecule on the UC of the doubly fluorinated  $(11\bar{2}3)$  surface; (a) adsorption energy surface [eV], (b) side view structure depiction along  $a$ , and (c) side view structure depiction along  $b$  - gray = aluminium, red = oxygen, yellow = fluorine, white = hydrogen, light blue = first water oxygen, and blue = second water oxygen (VASP-DFT, PBE/PAW, 600.0 eV energy cut-off, D3-BJ).

molecule, the adsorption energy surface in figure 4.69(a) looks different compared to the one in figure 4.66(a) from the singly fluorinated  $(11\bar{2}3)$  surface. But a rotation of this plot by  $180^\circ$  would improve the resemblance, so similarity of those two modified  $(11\bar{2}3)$  surfaces is seen clearly. That is why, the minimum and average adsorption energies are again nearly the same and provide values of  $-0.82$  eV and  $-0.44$  eV, respectively. Besides, the formed hydrogen bond network paints a completely different picture for the doubly fluorinated  $(11\bar{2}3)$  surface. Due to the different positioning of the first water molecule, the second one pushes it in the direction of the valley, where it strengthens its hydrogen bond to the valley fluoride ion while the second water molecule positions itself close to the water ligand (see figure 4.69(b) and figure 4.69(c)). Thus, the hydrogen bond network now features a net-like shaped structure of crossing mixed zigzag chains along  $a$  and  $b$ , respectively. While the one along  $b$  is built by the two terminal ligands and both water molecules, the one along  $a$  only consists of the two water molecules. Since a net-like structure is revealed, the single meshes represent  $O_8F_2$ -rings shaped like an “opened double-folded piece of paper” (see figure A.47(b)).

With the third water molecule on the doubly fluorinated  $(11\bar{2}3)$  surface, the investigation of this modified version ends while the obtained results are presented in figure 4.70. Looking at figure 4.70(a), it can be seen that the previously adsorbed wa-



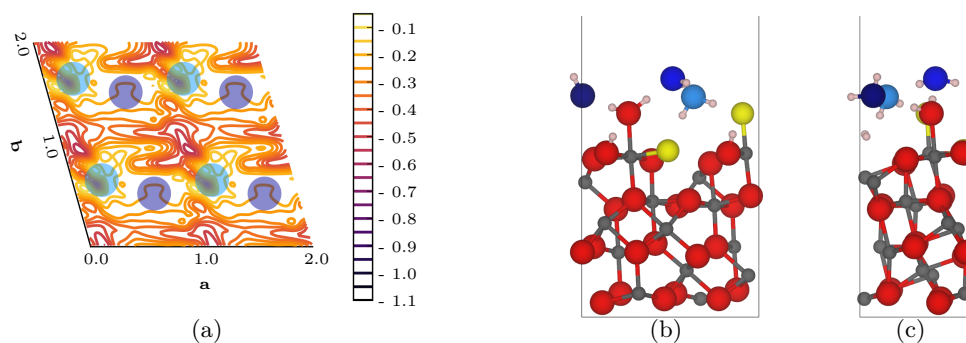


**Figure 4.70:** The third water molecule on the UC of the doubly fluorinated  $(11\bar{2}3)$  surface; (a) adsorption energy surface [eV], (b) side view structure depiction along  $a$ , and (c) side view structure depiction along  $b$  - gray = aluminium, red = oxygen, yellow = fluorine, white = hydrogen, light blue = first water oxygen, blue = second water oxygen, and dark blue = third water oxygen (VASP-DFT, PBE/PAW, 600.0 eV energy cut-off, D3-BJ).

ter molecules provides a quite large area of unfavourable adsorption for the third one. This area nearly forms a row across the doubly fluorinated  $(11\bar{2}3)$  surface's structure along  $a$ . Unsurprisingly, the average adsorption energy increases drastically by around 170 meV to  $-0.27$  eV. From figure 4.70(a) it can also be seen that there is only one suitable position for the third water molecule to adsorb onto the surface. It adsorbs between the two terminal ligands of the surface but not between them in  $b$  direction, as it was shown before, but rather between them in a diagonal  $a + b$  direction. Thus, the water ligand adjusts its orientation to suit the third water molecule by breaking its hydrogen bond to the terminal fluoride ion and, by association, breaking the chain in  $b$  direction. Interestingly, the third water molecule bridges along  $a + b$ , so the chains along  $a$  are connected again. The resulting sheared net-like structure features  $O_{10}F_2$ -rings, which provide a crown-like shape. Interestingly, the third water molecule again exhibits the structure motif of a “fivefold coordinated CS”. The formation of this hydrogen bond network results in a minimum adsorption energy of  $-0.55$  eV.

Going to the triply fluorinated  $(11\bar{2}3)$  surface, the adsorption of the first water molecules leads to the results shown in figure 4.71. From figure 4.71(a) it can be seen that the area of unfavourable adsorption is slightly extended with a small hook around  $0.9a$  and  $0.5b$ , which is exactly the position of the newly introduced fluoride

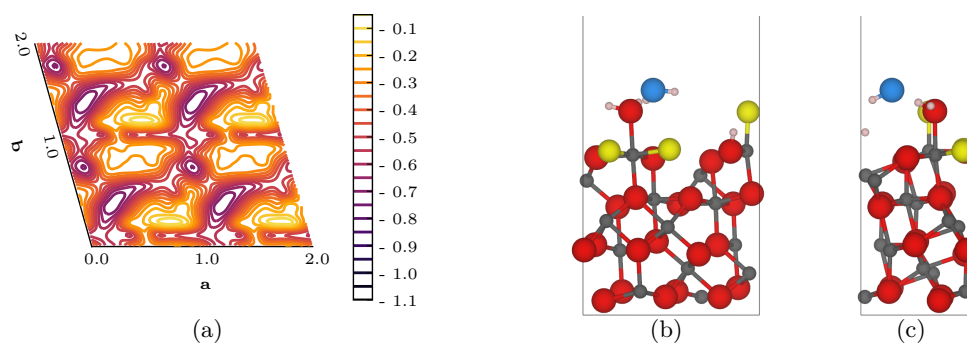


**Figure 4.71:** The first water molecule on the UC of the triply fluorinated  $(11\bar{2}3)$  surface; (a) adsorption energy surface [eV], (b) side view structure depiction along  $a$ , and (c) side view structure depiction along  $b$  - gray = aluminium, red = oxygen, yellow = fluorine, white = hydrogen, and light blue = first water oxygen (VASP-DFT, PBE/PAW, 600.0 eV energy cut-off, D3-BJ).

ion. Due to this, the average adsorption energy increases to  $-0.40$  eV. Furthermore, the resulting area of favourable adsorption looks like one half of a pincer in each UC and features mainly two beneficiary adsorption sites. The most favourable one is located near  $0.3a$  and  $0.4b$  and provides a minimum adsorption energy of  $-0.74$  eV by accepting and donating one hydrogen bond from and to the water ligand (see figure 4.71(b) and figure 4.71(c)). At this position, the first water molecule adsorbs between two water ligands along  $a$  and, by association, forms chains of hydrogen bonding along this direction. Within those chains, the water ligand also provides a hydrogen bond to the terminal fluoride ion.

Adsorbing the second water molecule on the triply fluorinated  $(11\bar{2}3)$  surface, figure 4.72 presents the results of this investigation. In figure 4.72(a) it can be clearly seen that, this time, a row of unfavourable adsorption is formed, which is due to the weakened adsorption on the water ligand and the firstly adsorbed water molecule. Thus, the average adsorption energy of this adsorption energy surface is increased, compared to its two predecessors for the adsorption of the second water molecule, and reaches a value of  $-0.39$  eV. The most favourable adsorption site is located near the terminal fluoride ion and nearly on top of a valley hydroxide group, which is shown in figure 4.72(b) and figure 4.72(c). In this position, the second water molecule accepts

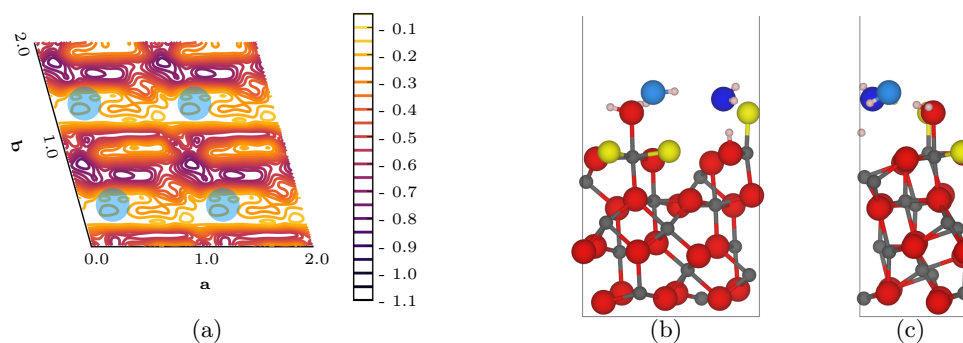


**Figure 4.72:** The second water molecule on the UC of the triply fluorinated  $(11\bar{2}3)$  surface; (a) adsorption energy surface [eV], (b) side view structure depiction along  $a$ , and (c) side view structure depiction along  $b$  - gray = aluminium, red = oxygen, yellow = fluorine, white = hydrogen, light blue = first water oxygen, and blue = second water oxygen (VASP-DFT, PBE/PAW, 600.0 eV energy cut-off, D3-BJ).

a hydrogen bond from the valley while donating one to the terminal fluoride ligand itself. Therefore, the hydrogen bond network is slightly extended beyond the terminal fluoride ion. Interestingly, this position of the two adsorbed water molecules allows the formation of a honeycomb-like shaped hydrogen bond network if one considers very stretched hydrogen bonds of  $2.7 \text{ \AA}$ . Hence, this might be a quite distorted version of the distinct honeycomb-like shaped water structures on the modified  $(0001)$  surfaces and might result in very similar hydrogen bond networks further on.

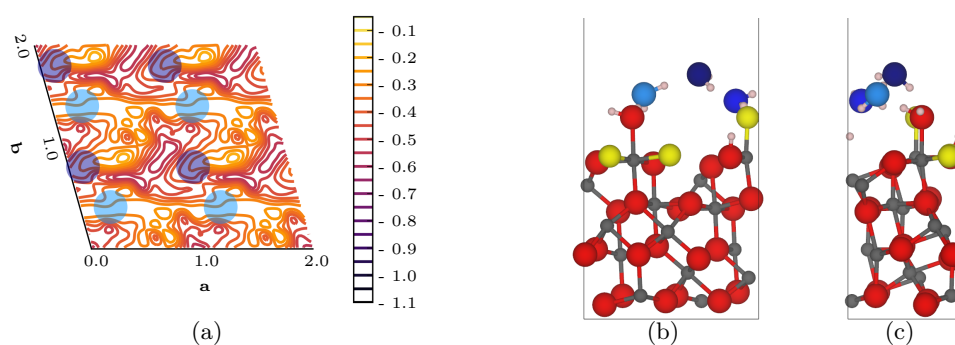


**Figure 4.73:** The third water molecule on the UC of the triply fluorinated  $(11\bar{2}3)$  surface; (a) adsorption energy surface [eV], (b) side view structure depiction along  $a$ , and (c) side view structure depiction along  $b$  - gray = aluminium, red = oxygen, yellow = fluorine, white = hydrogen, light blue = first water oxygen, blue = second water oxygen, and dark blue = third water oxygen (VASP-DFT, PBE/PAW, 600.0 eV energy cut-off, D3-BJ).

Closing the investigation of the water adsorption on the triply fluorinated ( $11\bar{2}3$ ) surface with the third water molecule, the results shown in [figure 4.73](#) are obtained. Looking at the adsorption energy surface in [figure 4.73\(a\)](#), the previously addressed possible honeycomb-like shaped structure can not be identified in this diagram. This is due to the fact that parts of this structure motif are not the adsorbed water molecules but the terminal ligands of the surface. Besides, a comparably small area of favourable adsorption can be identified and results in the lowest average adsorption energy for the third water molecule so far by providing a value of  $-0.37$  eV. As it can be seen in [figure 4.73\(b\)](#) and [figure 4.73\(c\)](#), the third water molecule adsorbs above the previous ones and laterally in between them and the terminal ligands. Therefore, it donates one hydrogen bond to the water ligand while accepting one from the second water molecule, which is fourfold coordinated now. The resulting minimum adsorption energy is  $-0.58$  eV. This quite good adsorption energy, despite the larger distance to the surface itself, results from the very interesting formed hydrogen bond network. Due to the bridging of the second water molecule and the water ligand by the third water molecule, the second water molecule is able to close the distance to the first water molecule and, by association, shortens the previously quite long hydrogen bonds of the possible honeycomb-like shaped structure. Unfortunately, not all hydrogen bonds are adjusted in favour of the honeycomb-like shaped structure, so this possible structure is completely discarded and three new rings are formed. The first one is a planar  $O_2F$ -ring, the second represents a shallow bathtub-like shaped  $O_4F_2$ -ring, and the third one depicts a bathtub-like shaped  $O_6F$ -ring (see [figure A.48\(c\)](#)).

By further fluorination of the ( $11\bar{2}3$ ) surface and analysing the water adsorption on it, [figure 4.74](#) shows the results of the first water molecule's adsorption on the fourfold fluorinated ( $11\bar{2}3$ ) surface. Looking at [figure 4.74\(a\)](#) reveals that the areas of unfavourable adsorption become more and more connected and, by association, shrink the area of favourable adsorption. On the other hand, due to the increasing Brønsted acidity of the surface hydroxide groups, the remaining favourable adsorption sites

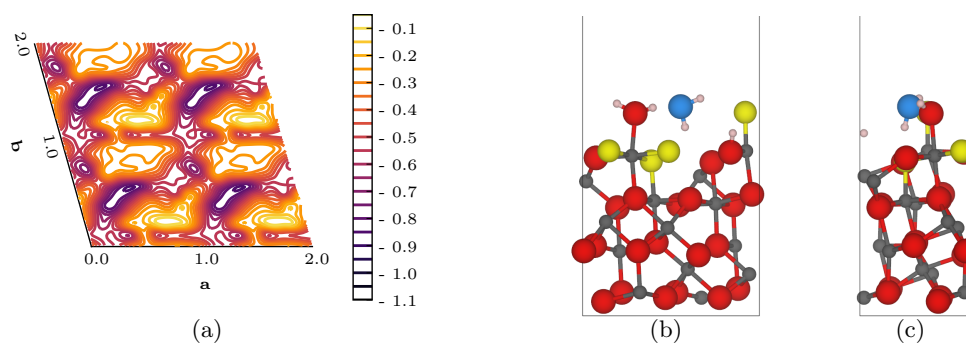


**Figure 4.74:** The first water molecule on the UC of the fourfold fluorinated  $(11\bar{2}3)$  surface; (a) adsorption energy surface [eV], (b) side view structure depiction along  $a$ , and (c) side view structure depiction along  $b$  - gray = aluminium, red = oxygen, yellow = fluorine, white = hydrogen, and light blue = first water oxygen (VASP-DFT, PBE/PAW, 600.0 eV energy cut-off, D3-BJ).

become better, which ultimately leads to a minimum adsorption energy of  $-0.83$  eV and an average adsorption energy of  $-0.42$  eV. With the help of [figure 4.74\(b\)](#) and [figure 4.74\(c\)](#), it can be seen that, interestingly enough, the first water molecule adsorbs not only between the two terminal ligands in way that it bridges the wider gap, but it is also not on top the more acidic valley hydroxide group. Instead, it donates one hydrogen bond to two competing acceptors, one oxide ion and one fluoride ion in the  $(11\bar{2}3)$  surface's valley. Regarding the formed hydrogen bond network, a chain along  $b$  is formed, which “stands” on the “competed” hydrogen bond to the valley.

Doubling the amount of water on the fourfold fluorinated  $(11\bar{2}3)$  surface, the obtained results can be seen in [figure 4.75](#). From [figure 4.75\(a\)](#) it can be seen that the firstly adsorbed water molecule hinders the adsorption of the second one and the area of favourable adsorption located above the surface's valley remains quite small. The resulting average adsorption energy provides a value of  $-0.40$  eV and is nearly the same as for the triply fluorinated  $(11\bar{2}3)$  surface. Regarding the most favourable adsorption position above the valley, [figure 4.75\(b\)](#) and [figure 4.75\(c\)](#) show that the second water molecules adsorbs near the water ligand. There it accepts one hydrogen bond from the water ligand while donating two hydrogen bonds to the firstly adsorbed

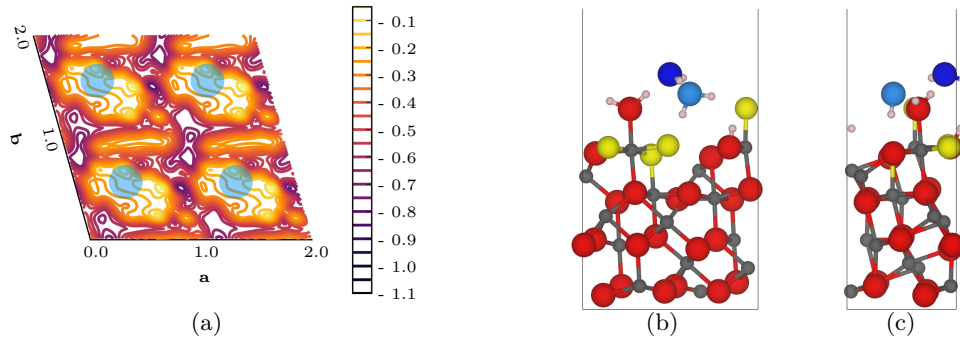


**Figure 4.75:** The second water molecule on the UC of the fourfold fluorinated  $(11\bar{2}3)$  surface; (a) adsorption energy surface [eV], (b) side view structure depiction along  $a$ , and (c) side view structure depiction along  $b$  - gray = aluminium, red = oxygen, yellow = fluorine, white = hydrogen, light blue = first water oxygen, and blue = second water oxygen (VASP-DFT, PBE/PAW, 600.0 eV energy cut-off, D3-BJ).

water molecule, resulting in a minimum adsorption energy of  $-0.77$  eV. Additionally, it displaces the first water molecule in a way that the previous hydrogen bond mixed chain along  $b$  shows a horizontal peak with the first water molecule while incorporating the second water molecule as well. Furthermore, the water molecules now form a second chain themselves along  $a$ , resulting once more in a net-like hydrogen bond network. This time, the single meshes form again  $O_8F_2$ -rings shaped like an “opened double-folded piece of paper” (see figure A.18(e)), as it was seen for the second water molecule on the doubly fluorinated  $(11\bar{2}3)$  surface as well.

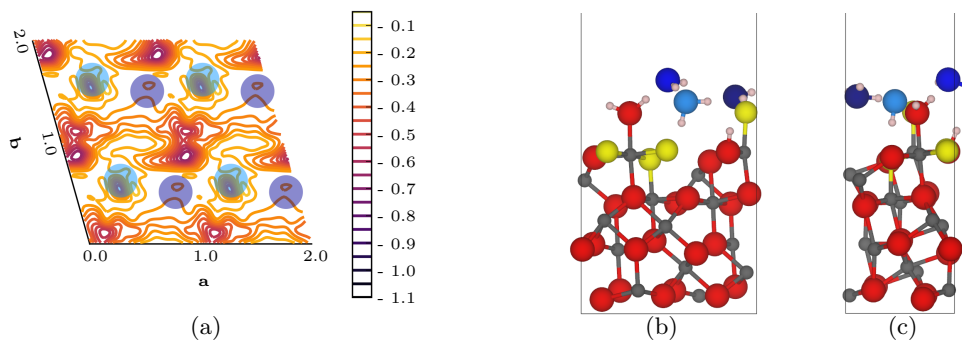


**Figure 4.76:** The third water molecule on the UC of the fourfold fluorinated  $(11\bar{2}3)$  surface; (a) adsorption energy surface [eV], (b) side view structure depiction along  $a$ , and (c) side view structure depiction along  $b$  - gray = aluminium, red = oxygen, yellow = fluorine, white = hydrogen, light blue = first water oxygen, blue = second water oxygen, and dark blue = third water oxygen (VASP-DFT, PBE/PAW, 600.0 eV energy cut-off, D3-BJ).

Increasing the amount of adsorbed water on the fourfold fluorinated  $(11\bar{2}3)$  surface to three, the results of this investigation can be seen in figure 4.76. Taking a first look at the adsorption energy surface in figure 4.76(a), it can be seen that this time the already adsorbed water molecules and the terminal ligands provide an extensive net of unfavourable adsorption positions while only two small spots remain for a favourable adsorption of the third water molecule. Looking at figure 4.76(b) and figure 4.76(c) reveals the most stable adsorption site for the third water molecule where it accepts the hydrogen bond from the quite Brønsted acidic remaining valley hydroxide group and donates two hydrogen bonds to the terminal fluoride ions. Therefore, this position results in the second lowest minimum adsorption energy of  $-0.65$  eV for the adsorption of the third water molecule. Regarding the formed hydrogen bond network, due to the third water molecule, a second chain along  $a$  formed, which splits the  $O_8F_2$ -rings in two smaller rings. The smaller one now shows a  $180^\circ$  rotated bathtub-like shaped  $O_4F_2$ -ring while the larger one represents again an “opened double-folded piece of paper”-shaped  $O_6F_2$ -ring (see figure A.49(c)).

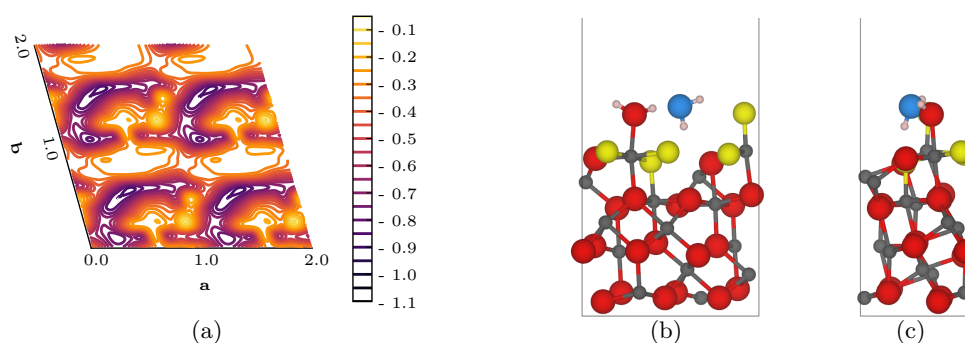


**Figure 4.77:** The first water molecule on the UC of the fivefold fluorinated  $(11\bar{2}3)$  surface; (a) adsorption energy surface [eV], (b) side view structure depiction along  $a$ , and (c) side view structure depiction along  $b$  - gray = aluminium, red = oxygen, yellow = fluorine, white = hydrogen, and light blue = first water oxygen (VASP-DFT, PBE/PAW, 600.0 eV energy cut-off, D3-BJ).

Coming to the last fluorinated  $(11\bar{2}3)$  surface where the water ligand is present, figure 4.77 shows the results for the adsorption of the first water molecule on the fivefold fluorinated  $(11\bar{2}3)$  surface. Comparing figure 4.74(a) with figure 4.77(a), they

both show very similar features of the favourable and unfavourable adsorption sites. However, the fivefold fluorinated  $(11\bar{2}3)$  surface is able to connect those areas since the valley hydroxide group responsible for the otherwise favourable adsorption position is gone. On the other hand, the increasing amount of fluoride helps to make the hydrogen bonding to the water ligand more likely and stronger and results in an overall slightly decreasing average adsorption energy ( $-0.45$  eV), although, the area of unfavourable adsorption increases. Looking at [figure 4.77\(b\)](#) and [figure 4.77\(c\)](#), it can be seen that the most favourable adsorption position for the first water molecule is again between the two terminal ligands. It adsorbs there by bridging the wider gap between the terminal ligands, which is exactly the same position the first water molecule on the fourfold fluorinated  $(11\bar{2}3)$  surface adsorbed at. Unsurprisingly, the minimum adsorption energy is nearly the same and provides a value of  $-0.85$  eV. By accepting one hydrogen bond from the water ligand while donating one hydrogen bond to the terminal fluoride ion and one “competed” hydrogen bond to the surface’s valley, the first water molecule on the fivefold fluorinated  $(11\bar{2}3)$  surface provides exactly the same hydrogen bond network, as it was shown for the fourfold fluorinated  $(11\bar{2}3)$  surface.

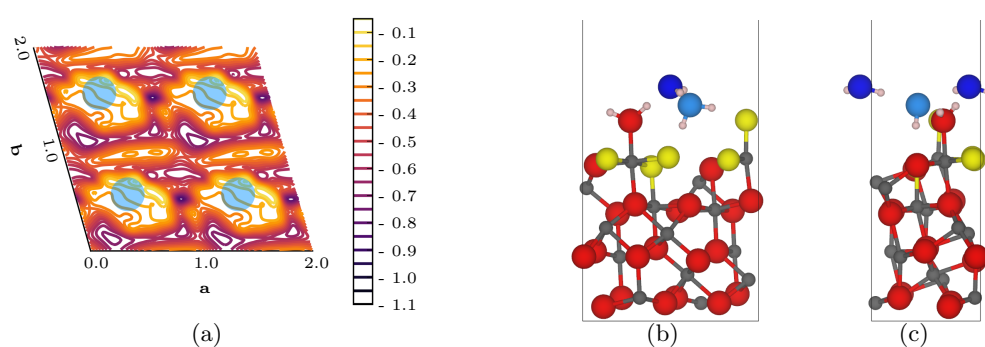


**Figure 4.78:** The second water molecule on the UC of the fivefold fluorinated  $(11\bar{2}3)$  surface; (a) adsorption energy surface [eV], (b) side view structure depiction along  $a$ , and (c) side view structure depiction along  $b$  - gray = aluminium, red = oxygen, yellow = fluorine, white = hydrogen, light blue = first water oxygen, and blue = second water oxygen (VASP-DFT, PBE/PAW, 600.0 eV energy cut-off, D3-BJ).



Investigating the adsorption of the second water molecule on the fivefold fluorinated  $(11\bar{2}3)$  surface leads to the results shown in figure 4.78. Again, the comparison with the fourfold fluorinated  $(11\bar{2}3)$  surface shows an astonishing similarity of those two fluorination degrees. The adsorption energy surface in figure 4.78(a) provides a vast resemblance of its predecessor’s one, so the average adsorption energy provides the same value of  $-0.40$  eV. Interestingly, the most favourable adsorption position on the fivefold fluorinated  $(11\bar{2}3)$  surface is somewhat isolated at  $0.9a$  and  $0.5b$  between the two areas of unfavourable adsorption. This is due to the competition between good hydrogen bonding and less steric hindrance the second water has to face while there is no “help” from a hydroxide group left in the surface valley. At this position, it accepts one hydrogen bond from the water ligand and donates two hydrogen bonds to the firstly adsorbed water molecule, resulting in a minimum adsorption energy of  $-0.80$  eV. Finally, it is not surprising that the formed hydrogen bond network is also the same, as compared to the one formed on the fourfold fluorinated  $(11\bar{2}3)$  surface. Again, there is a net-like structure formed by two hydrogen bond chains along  $a$  and  $b$ , respectively, which consists of “opened double-folded piece of paper”-shaped  $O_8F_2$ -rings (see figure A.50(b)).

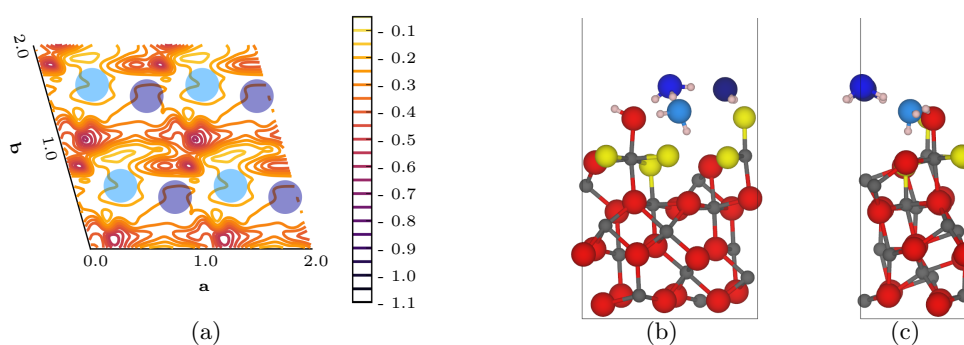


**Figure 4.79:** The third water molecule on the UC of the fivefold fluorinated  $(11\bar{2}3)$  surface; (a) adsorption energy surface [eV], (b) side view structure depiction along  $a$ , and (c) side view structure depiction along  $b$  - gray = aluminium, red = oxygen, yellow = fluorine, white = hydrogen, light blue = first water oxygen, blue = second water oxygen, and dark blue = third water oxygen (VASP-DFT, PBE/PAW, 600.0 eV energy cut-off, D3-BJ).

Increasing the amount of adsorbed water on the fivefold fluorinated  $(11\bar{2}3)$  surface by adding a third water molecule, [figure 4.79](#) shows the results of the corresponding calculations. While the adsorption energy surface in [figure 4.79\(a\)](#), the average adsorption energy with  $-0.27$  eV, and the most favourable adsorption position of the third water molecule are nearly the same, compared to the fourfold fluorinated  $(11\bar{2}3)$  surface, the involved hydrogen bonds differ dramatically. As it is indicated in [figure 4.79\(b\)](#) and [figure 4.79\(c\)](#), the second water molecule gets protonated and is a hydronium ion now while the water ligand becomes a terminal hydroxide group, resulting in a minimum adsorption energy of  $-0.58$  eV. This is only possible because the high amount of surface fluoride ions increases the Brønsted acidity so much that the water ligand is able to be deprotonated. Hence, the hydrogen bond network changes dramatically as well. The second water molecule is shifted slightly along  $a$ , and by association, the hydrogen bond chain along  $a$  is broken up. Furthermore, the third water molecule bridges again the terminal fluoride ions, and two new seven membered rings are formed. The first one's topview shows a “church-like” shape, whose sides are up-folded. In contrast, the second one represents a bathtub-like shape of a somewhat regular heptagon (see [figure A.50\(c\)](#)).

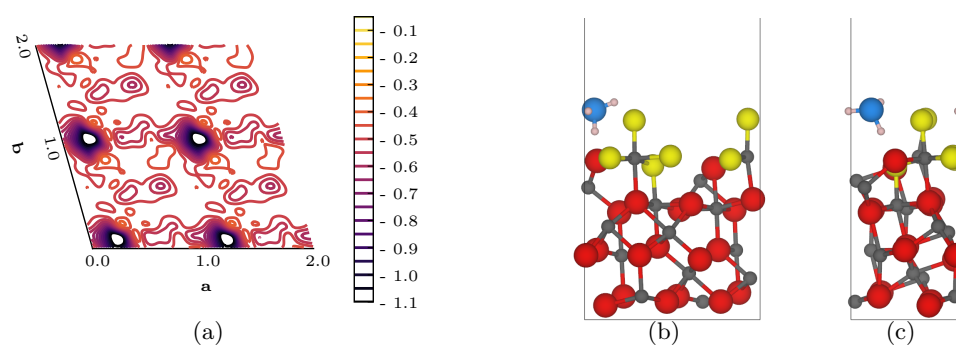


**Figure 4.80:** The first water molecule on the UC of the sixfold fluorinated  $(11\bar{2}3)$  surface; (a) adsorption energy surface [eV], (b) side view structure depiction along  $a$ , and (c) side view structure depiction along  $b$  - gray = aluminium, red = oxygen, yellow = fluorine, white = hydrogen, and light blue = first water oxygen (VASP-DFT, PBE/PAW, 600.0 eV energy cut-off, D3-BJ).

Since the sixth fluorination of the  $(11\bar{2}3)$  surface included the dissociation of the terminal water ligand and the subsequent fluorination of the obtained terminal hydroxide group, the adsorption of the first water molecule on the sixfold fluorinated  $(11\bar{2}3)$  surface provides the results shown in [figure 4.80](#). By looking at [figure 4.80\(a\)](#) it can be seen immediately that there is a drastic change in the  $(11\bar{2}3)$  surface's ability to adsorb the first water molecule. Providing two terminal fluoride ions, whose corresponding aluminium CSs are significantly fluorinated, results in a largely decreased average adsorption energy of  $-0.53$  eV. This results from the formation of seemingly very good hydrogen bonds of the adsorbing water molecule to those terminal fluoride ions. It is very important to highlight the underlying structure motifs which enable the surprisingly good hydrogen bond acceptance of them. In contrast to the fluorinated aluminium hydroxide, aluminium oxohydroxides, and the  $(0001)$  surfaces, the considered fluoride ions are at terminal positions here. Additionally, they are also part of highly fluorinated aluminium CSs, which was not the case for the terminal fluoride ions of the fluorinated  $(1\bar{1}02)$  surfaces. While the second structural characteristic has only a slightly increasing influence on the acceptor qualities of the fluoride ions, their own CN is very important, which was also seen previously, for example, for the OH stretch frequencies in subsection 4.2.2 [Fluorination of Hydrated  \$\alpha\$ -Aluminium Oxide Surfaces](#). Terminal fluoride ions are much better hydrogen bond acceptors than bridging fluoride ions. Furthermore, up until this point nearly all adsorption investigations for the first water molecule involved the prior breaking or at least weakening of existing hydrogen bonds, which partly stabilised the surface structure. By breaking or weakening those stabilisations, the “real” or “pure” adsorption energy is compensated by that amount of energy and a higher adsorption energy is obtained. Combining those considerations explains the unexpected low adsorption energies for the adsorption of the first water molecule on this surface. Besides, the most favourable adsorption site for the first water molecule ( $-1.18$  eV) is provided mainly by the last remaining hydroxide within the  $(11\bar{2}3)$  surface's valley. Due to the

high amount of fluoride ions in the surface, the Brønsted acidity of this hydroxide ion is quite high and, by association, results in the protonation of the adsorbing water molecule. As it can be seen in [figure 4.80\(b\)](#) and [figure 4.80\(c\)](#), the hydronium ion donates three hydrogen bonds, one of course to the former hydroxide group in the valley and two to the two different terminal fluoride ions, resulting in “T” shaped hydrogen bond network.

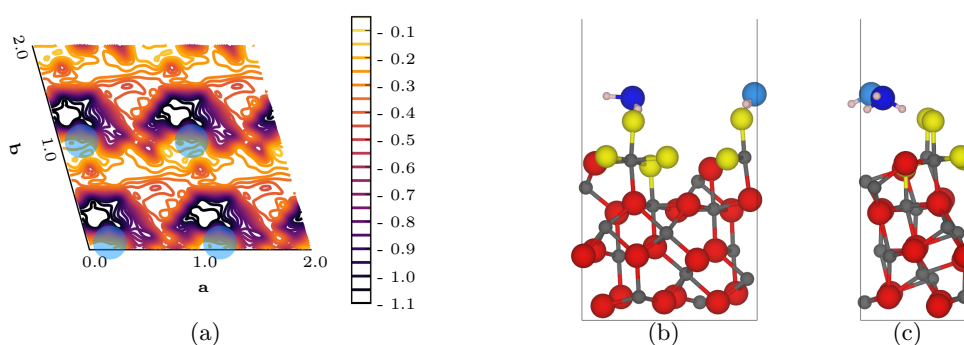


**Figure 4.81:** The second water molecule on the UC of the sixfold fluorinated  $(11\bar{2}3)$  surface; (a) adsorption energy surface [eV], (b) side view structure depiction along  $a$ , and (c) side view structure depiction along  $b$  - gray = aluminium, red = oxygen, yellow = fluorine, white = hydrogen, light blue = first water oxygen, and blue = second water oxygen (VASP-DFT, PBE/PAW, 600.0 eV energy cut-off, D3-BJ).

Increasing the amount of water on the sixfold fluorinated  $(11\bar{2}3)$  surface, [figure 4.81](#) shows the results of the adsorption of the second water molecule. Looking at the adsorption energy surface in [figure 4.81\(a\)](#) shows that the previously lowered adsorption energies are back at “normal” levels because the firstly adsorbed water molecule enables again the compensation of the “real” adsorption energies by breaking and weakening of already existing hydrogen bonds. At the same time, the formed hydronium ion, in combination with the terminal fluoride ions, provides an increased area of favourable adsorption for the second water molecule with also very low adsorption energies, resulting in an only very slightly increased average adsorption energy of  $-0.51$  eV. From [figure 4.81\(b\)](#) and [figure 4.81\(c\)](#) it can be seen that at the most favourable adsorption position both water molecules now compete for the hydrogen ion from the former hydroxide group in the valley resulting in a minimum adsorption

energy of  $-1.17$  eV. Furthermore, both of them bridge two terminal fluoride ions, resulting in two mixed zigzag chains of hydrogen bonds along  $a$ , which are connected with each other via the contested hydrogen ion. The formed  $O_4F_2$ -rings provide bathtub-like shape provide once more a “ $\beta$ -sheet”-like shaped structure.

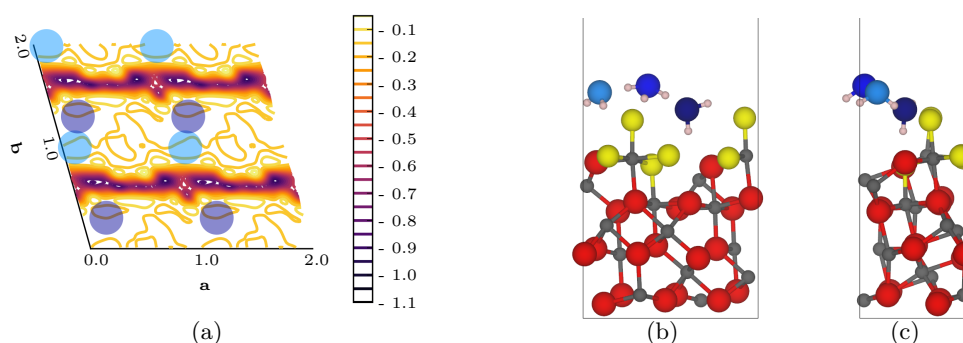


**Figure 4.82:** The third water molecule on the UC of the sixfold fluorinated  $(11\bar{2}3)$  surface; (a) adsorption energy surface [eV], (b) side view structure depiction along  $a$ , and (c) side view structure depiction along  $b$  - gray = aluminium, red = oxygen, yellow = fluorine, white = hydrogen, light blue = first water oxygen, blue = second water oxygen, and dark blue = third water oxygen (VASP-DFT, PBE/PAW, 600.0 eV energy cut-off, D3-BJ).

Finalising the sixfold fluorinated  $(11\bar{2}3)$  surface with the adsorption of the third water molecule, the obtained results are presented in figure 4.82. From figure 4.82(a) it can be seen that an adsorption on top of the formed “ $\beta$ -sheet”-like shaped structure is unfavourable while an adsorption between two of those structure motifs is very favourable. The resulting two rows of favourable and unfavourable adsorption positions yield an increased average adsorption energy of  $-0.24$  eV. Comparing figure 4.81(b) and figure 4.81(c) with figure 4.82(b) and figure 4.82(c), it can be seen that for the most favourable adsorption position of the third water molecule, with an energy of  $-0.91$  eV, the first two water molecules are pulled away along  $b$  from their position. Since the third water molecule adsorbs at its position via donating one hydrogen bond to the  $(11\bar{2}3)$  surface’s valley and donating a second one to a terminal fluoride ion, its position is quite fixed. Thus the previous two water molecules adjust their positions to maximise their interaction with the third water molecule. The resulting hydrogen bond network presents a highly distorted net-like structure where

the single meshes consist of  $O_8F_4$ -rings, which do not provide an easy to compare shape but are quite flat with peaking edges and corners. Concerning the minimum adsorption energy, a value of  $-0.91$  eV is obtained.

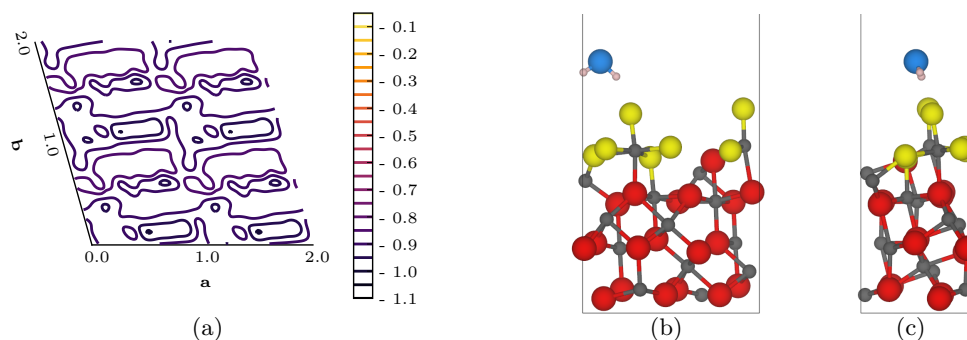


**Figure 4.83:** The first water molecule on the UC of the sevenfold fluorinated  $(11\bar{2}3)$  surface; (a) adsorption energy surface [eV], (b) side view structure depiction along  $a$ , and (c) side view structure depiction along  $b$  - gray = aluminium, red = oxygen, yellow = fluorine, white = hydrogen, and light blue = first water oxygen (VASP-DFT, PBE/PAW, 600.0 eV energy cut-off, D3-BJ).

Coming to the last considered and modified surface of this work, the adsorption of the first water molecule on the sevenfold fluorinated  $(11\bar{2}3)$  surface provides the results shown in figure 4.83. From figure 4.83(a) it can be seen that the effect described for the first water molecule on the sixfold fluorinated  $(11\bar{2}3)$  surface is even stronger for this modification. Since in the sixfold fluorinated  $(11\bar{2}3)$  surface the remaining hydroxide group also provided hydrogen bonds to the terminal fluoride ions, their weakening by the adsorption of the first water molecule compensated the “real” adsorption energy. This is no longer possible for the fully fluorinated  $(11\bar{2}3)$  surface, so the adsorption of the first water molecule provides very low values, which result in an average adsorption energy of  $-0.89$  eV. In figure 4.83(b) and figure 4.83(c) it can be seen that the most favourable adsorption site ( $-0.99$  eV) involves the donation of one hydrogen bond each to the two terminal fluoride ions by the adsorbing first water molecule. Regarding the resulting hydrogen bond network,  $180^\circ$  rotated “V”s on top the terminal fluoride ligands are found.

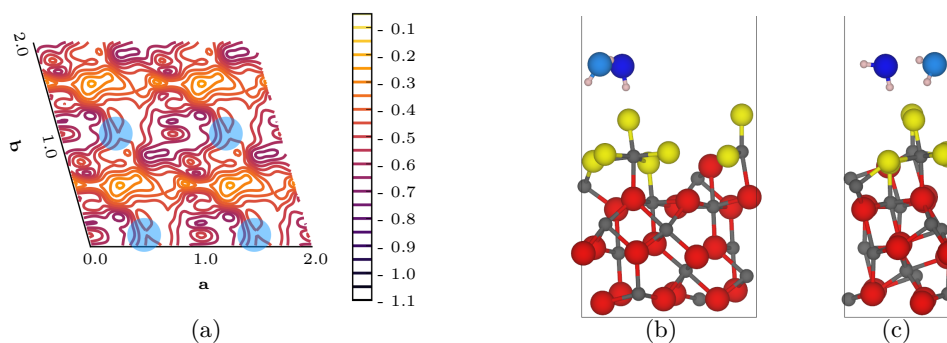


**Figure 4.84:** The second water molecule on the UC of the sevenfold fluorinated  $(11\bar{2}3)$  surface; (a) adsorption energy surface [eV], (b) side view structure depiction along  $a$ , and (c) side view structure depiction along  $b$  - gray = aluminium, red = oxygen, yellow = fluorine, white = hydrogen, light blue = first water oxygen, and blue = second water oxygen (VASP-DFT, PBE/PAW, 600.0 eV energy cut-off, D3-BJ).

For the adsorption of the second water molecule on the sevenfold fluorinated  $(11\bar{2}3)$  surface, the obtained results can be seen in figure 4.84. Since the breaking and weakening of existing hydrogen bonds in order to adsorb the second water molecule happens once more, the adsorption energy in figure 4.84(a) reveals again increased adsorption energies. This results in an increased average adsorption energy of  $-0.49$  eV. For most favourable adsorption position of the second water molecule, the first one has to adjust its position in order to allow the donation of a favourable hydrogen bond to a terminal fluoride ion (see figure 4.84(b) and figure 4.84(c)). Additionally, this adjustment yields a zigzag chain along  $a$  as hydrogen bond network, consisting of only the two water molecules. Those chains are then stabilised by one hydrogen bond of each water molecule to the terminal fluoride ions, resulting in a minimum adsorption energy of  $-0.66$  eV.

Lastly, the adsorption of the third water molecule on the sevenfold fluorinated  $(11\bar{2}3)$  surface yields the results shown in figure 4.85. The adsorption energy surface in figure 4.85(a) shows that the distinct pattern seen in figure 4.82(a) is smoothed out this time. Nonetheless, the areas of unfavourable adsorption directly on top of the already adsorbed water molecules can be identified as well as the favourable adsorption areas between the previously formed water zigzag chains. But since the unfavourable

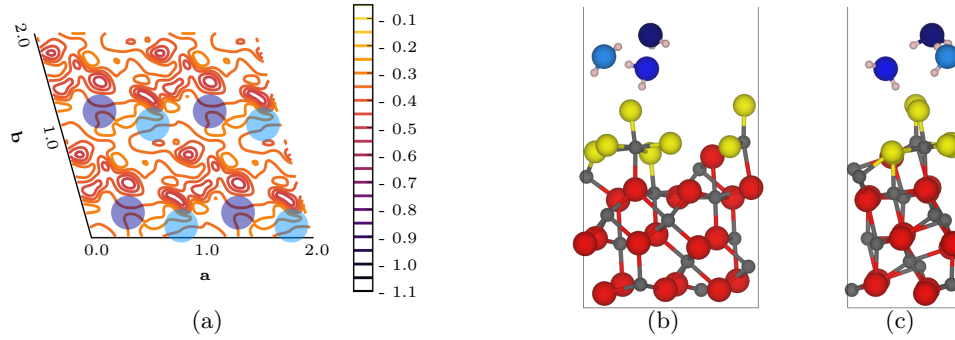


**Figure 4.85:** The third water molecule on the UC of the sevenfold fluorinated  $(11\bar{2}3)$  surface; (a) adsorption energy surface [eV], (b) side view structure depiction along  $a$ , and (c) side view structure depiction along  $b$  - gray = aluminium, red = oxygen, yellow = fluorine, white = hydrogen, light blue = first water oxygen, blue = second water oxygen, and dark blue = third water oxygen (VASP-DFT, PBE/PAW, 600.0 eV energy cut-off, D3-BJ).

adsorption sites's energies are lowered, compared to the ones for the sixfold fluorinated  $(11\bar{2}3)$  surface, the average adsorption energy is decreased to  $-0.36$  eV. However, the third water molecule adsorbs close to one edge of the existing zigzag chain and intercalates in it by accepting and donating one hydrogen bond each to the two previously adsorbed water molecules. Thus, the length of one zigzag chain's stage is increased to three water molecules while the second one still contains two of them. Lastly, this results in the minimum adsorption energy of  $-0.53$  eV.

In order to sum up the obtained results for the modified  $(11\bar{2}3)$  surfaces, table 4.13 contains the three most interesting adsorption energies and a short description of the adsorbing water molecule's binding for each water on each modified  $(11\bar{2}3)$  surface. It can be seen that the maximum adsorption energy provided the lowest value of  $\approx 240$  meV, which was comparable to the previous lowest values for the maximum adsorption energy. But again two notable exceptions are revealed: the adsorption of the first water molecule on the sixfold and sevenfold fluorinated  $(11\bar{2}3)$  surfaces. In both cases, the exceptional values are based on the fact that for these modified  $(11\bar{2}3)$  surfaces the adsorption of the first water molecule did not require the breaking or substantial weakening of already existing hydrogen bonds. Thus, the "real" adsorption energy was obtained by only forming new hydrogen bonds, instead of reorienting pre-



### 4.3 Water Adsorption on Modified $\alpha$ -Aluminium Oxide Surfaces

**Table 4.13:** Three notable adsorption energies resulting from each adsorption energy surface and a short adsorption site description for the water adsorption on modified (11 $\bar{2}$ 3) surfaces (**V** = valley, **H** = hill, H<sub>2</sub>O = terminal water ligand) (VASP-DFT, PBE/PAW, 600.0 eV energy cut-off, D3-BJ).

<b>H<sub>2</sub>O F/UC</b>	$E_{\text{ads,MAX}}$	$E_{\text{ads,MIN}}$	$\bar{E}_{\text{ads}}$	<b>Positioning</b>	
	[eV]	[eV]	[eV]		
1.	0	-0.18	-0.84	-0.45	on <b>V</b> OH; among 2 <b>H</b> OH
	1	-0.24	-0.74	-0.48	near <b>V</b> OH; among <b>H</b> F+H <sub>2</sub> O
	2	-0.21	-0.74	-0.44	among <b>H</b> F+H <sub>2</sub> O
	3	-0.12	-0.74	-0.40	among 2 H <sub>2</sub> O
	4	-0.10	-0.83	-0.42	above <b>V</b> O+ <b>V</b> F; among <b>H</b> F+H <sub>2</sub> O
	5	-0.15	-0.85	-0.45	above <b>V</b> O+ <b>V</b> F; among <b>H</b> F+H <sub>2</sub> O
	6 <sup>a</sup>	-0.43	-1.18	-0.53	near <b>V</b> OH; among 2 <b>H</b> F
	7	-0.81	-0.99	-0.89	above 2 <b>H</b> F
2.	0	-0.18	-0.75	-0.38	on <b>V</b> OH; among 1.+2 H <sub>2</sub> O
	1	-0.21	-0.85	-0.48	near 2 <b>V</b> OH; among <b>H</b> F+H <sub>2</sub> O
	2	-0.18	-0.82	-0.44	among 2 1.+ H <sub>2</sub> O
	3	-0.14	-0.78	-0.39	near <b>V</b> OH+ <b>H</b> F
	4	-0.11	-0.77	-0.40	among 2 1.+H <sub>2</sub> O
	5	-0.10	-0.80	-0.40	among 2 1.+H <sub>2</sub> O
	6	-0.15	-1.16	-0.51	among 1.+2 <b>H</b> F
	7	-0.24	-0.66	-0.49	above <b>H</b> F; among 2 1.
3.	0	-0.20	-0.72	-0.34	on <b>V</b> OH; among 1.+2.+H <sub>2</sub> O
	1	-0.19	-0.59	-0.33	above 1.+2.
	2	-0.13	-0.55	-0.27	on 2 <b>V</b> OH; among <b>H</b> F+H <sub>2</sub> O
	3	-0.17	-0.58	-0.37	above 1.+2.+ <b>H</b> F
	4	-0.16	-0.65	-0.28	on <b>V</b> OH; among 2 <b>H</b> F
	5 <sup>a</sup>	-0.14	-0.58	-0.27	among 2.+2 <b>H</b> F
	6	-0.09	-0.91	-0.24	above <b>V</b> OH+ <b>V</b> F; among 2.+ <b>H</b> F
	7	-0.28	-0.53	-0.36	above 1.+2.

<sup>a</sup> hydronium ion was formed due to surface deprotonation

existing ones. Additionally, the impact of the fluoride ions' **CN** on their hydrogen bond accepting qualities was crucial as well in explaining this observations. In case of the modified (11 $\bar{2}$ 0) surfaces, the terminal fluoride ions often times accepted hydrogen bonds from at least the valley hydroxide groups while the corresponding aluminium **CS**s did not exceed a fluorination degree of two. For the six- and sevenfold fluorinated (11 $\bar{2}$ 3) surfaces, the corresponding aluminium **CS**s reached a fluorination degree of

three and four. Thus, the combination of the highly fluorinated aluminium CSs, the fluoride ions with terminal positioning, and the lack of compensatory energy loss by breaking or weakening already existing hydrogen bonds led to very low values of the three notable adsorption energies for these two  $(11\bar{2}3)$  surface modifications. Besides, it can be also seen from [table 4.13](#) that the minimum and the average adsorption energies provided varying changes going from the first to the second water molecule, but then increased in all cases going to the third water molecule. While the decrease resulted from more and better possibilities to form hydrogen bonds and favourable hydrogen bond networks, the adsorption of the third water molecule faced a more difficult balancing act. It had to weigh the possible formation of hydrogen bonds against the increasing steric hindrance on the surface. Therefore, it could adsorb above the previous water molecules to avoid the latter by also reducing the opportunities to form hydrogen bonds, or it forms a reasonable hydrogen bond network but forfeits energy gain during the adsorption by steric hindrances. Besides, as it was seen for the triply fluorinated  $(1\bar{1}02)$  surface, the fivefold and sixfold fluorinated  $(11\bar{2}3)$  surfaces were also able to protonate approaching water molecules, due to their increasing Brønsted acidity with increasing amounts of fluoride. While for the fivefold  $(11\bar{2}3)$  surface this occurred with the adsorption of the third water molecule, the sixfold fluorinated  $(11\bar{2}3)$  surface was able to protonate the first adsorbing water molecule.

Considering possible applications of those modified  $(11\bar{2}3)$  surfaces, the capability to protonate approaching water molecules makes the sixfold fluorinated  $(11\bar{2}3)$  surface quite interesting as a potential heterogeneous Brønsted acidic catalyst. Furthermore, the hydrated  $(11\bar{2}3)$  surface provided a chain solely from water molecules along the surface's valley. This could provide a similar behaviour as the doubly fluorinated  $(1\bar{1}02)$  surface, namely presenting channels of water, which might be used as molecular water trickles. Regarding, for example, a fluoride protective coat, it was seen that despite the very low adsorption energy of the first water molecule on the sevenfold fluorinated  $(11\bar{2}3)$  surfaces, the hydrogen bond network mainly resides above the

surface itself. It only used two hydrogen bonds to connect and anchor itself on the fully fluorinated surface. Therefore, a completely fluorinated  $(11\bar{2}3)$  surface might hinder the interaction of water with the surface enough that it would interact mainly with itself to achieve a more stable hydrogen bond network. This is in agreement with the findings for the other two investigated surfaces and supports a possible fluoride protective coating against corrosion by water.

#### 4.3.4 Summary of the Water Adsorption

Looking at the water adsorption on differently modified surfaces of the  $(0001)$ ,  $(1\bar{1}02)$  and  $(11\bar{2}3)$  surface cuts of  $\alpha$ -aluminium oxide revealed a complex interplay of different aspects to enhance or inhibit the water molecules' adsorption. In order to investigate the influence of fluoride ions on the adsorption of water, the focus was laid on a possible application, namely a fluoride protective coat against dissolution in water.

Studying the  $(0001)$  surface, which only provided doubly coordinated surface anions, it was seen that an increasing fluorination degree resulted in an increasing average adsorption energy for the water molecules. But due to the increasing fluorination degree, the adsorption on the remaining hydroxide groups in the mixed surfaces becomes more likely and provided decreasing minimum adsorption energies. This was attributed to the increasing Brønsted acidity of those hydroxide groups. Already in this rather simple and smooth surface cut two aspects were found that counteract each other. Nonetheless, the fully fluorinated  $(0001)$  surfaces resulted in an average adsorption energy of  $-0.39$  eV, which is higher than the doubled energy gain from forming two hydrogen bonds between water molecules ( $2 \cdot (-0.21$  eV) [216, 217]) while keeping the slight overbinding due to **D3-BJ** in mind. Since this is otherwise only a small difference, the main aspect that supports a fluoride protective coating is the fact that additionally adsorbed water molecules, on this fully fluorinated surface, rather formed hydrogen bonds with the previously adsorbed water molecules, than with the surface itself.

For the  $(1\bar{1}02)$  surface even more aspects came into play that influenced the adsorption energy of the water molecules. This surface cut not only provided a rough structure but also exhibited terminal fluoride ions during the fluorination process. The rough surface structure itself resulted in the competition of steric hindrance with more opportunities to form hydrogen bonds for the adsorbing water molecules within the channels. In addition, the terminal fluoride ions introduced another aspect to consider since they tended to accept hydrogen bonds much better than the bridging fluoride ions. Furthermore, the mixed surfaces of this cut always provided a self-stabilisation via the surface hydroxide groups which had to be broken in order to allow the water molecule to adsorb. Thus, the adsorption energies depended on many different and competing aspects, so monitoring only its value is not sufficient to judge on the protective nature of the doped fluoride ions. Additionally, the fully fluorinated  $(1\bar{1}02)$  surface reconstructs and this results in a decrease in the adsorption energy. But especially for the fully fluorinated surface it was seen that additional water molecules favour to adsorb more closely to already adsorbed ones than to the surface. This again emphasised the possibility of a protective coat against water.

For the modified  $(11\bar{2}3)$  surfaces with an even rougher atomic structure, the effects on the adsorption energies got even more complex with a molecularly adsorbed water ligand and a terminal fluoride ion after the first fluorination, which is not stabilised via hydrogen bonds. The roughness resulted in notably decreasing average adsorption energies for the first and second water molecules since due to the larger unit cell, they did not have to compete with each other for their hydrogen bonding. Especially for the six- and sevenfold fluorinated surfaces, the average adsorption energy of the firstly adsorbing water molecule dropped significantly because of the very good hydrogen accepting nature of the terminal fluoride ions and the lack of internal surface stabilisation that needed to be broken. Besides the very low adsorption energies, the surface structure did not relax notably during the adsorption and the interaction of further adsorbing water molecules was mainly focused on the molecularly adsorbed

water ligand, the terminal fluoride ions, and especially near the previously adsorbed water molecules. Thus, the adsorption energies might deceive the protective nature of the fluoride ions which is emphasized once more by the actual positions of the adsorbed water molecules.

Nonetheless, to really verify the assumed protective effect of the fluoride ions within the different surfaces, MD would be needed to complete these investigations.

## 4.4 Structure Motifs of Water

Since the previous section 4.3 [Water Adsorption on Modified  \$\alpha\$ -Aluminium Oxide Surfaces](#) provided a variety of different and interesting structure motifs of the adsorbed water molecules and were conducted at 0 K, this section will compare those motifs with structure motifs found in the different known ice phases and not liquid water. Here, motifs refer to hydrogen bond networks that form rings, chains, helices, ring-chains or in case of small amounts of adsorbed water, letter-shaped or similar motifs. It starts with the analysis of ice phases in order to work out the needed structure motifs. This is done via the approach discussed in subsection 2.2.5 [Analysis of Ice Structures](#).

### 4.4.1 Ice Phases

First of all, there are 18 different ice phases, which are named “ice” plus its number in Roman numerals. Since there are two phases named “ice **I**” (ice-**I<sub>h</sub>** and ice-**I<sub>c</sub>**), the counting goes up to **XVII** (17). Furthermore, some phases represent the low temperature and/or high pressure analogue of another one. Those linked phases do not show a change in the oxygen structure motifs, instead, their hydrogen bonding is different. While most ice phases show an unordered hydrogen bonding, still obeying the [ice rules](#) (four hydrogen bonds per oxygen; two donating and two accepting), their linked phases provide slightly denser versions of them and presenting an ordered hydrogen bonding. Hence, the number of considered ice phases can be decreased from 17 to eleven, because only oxygen atom structure motifs are of interest here. Those eleven ice phases are ice-**I<sub>h</sub>** [106, 107] (ice-**XI** [122, 123]), ice-**I<sub>c</sub>** [108, 109], ice-**II** [110], ice-**III** [111, 112] (ice-**IX** [112, 119]), ice-**IV** [113], ice-**V** [114] (ice-**XIII** [125]), ice-**VI** [115, 116] (ice-**XV** [126]), ice-**VII** [116, 117] (ice-**VIII** [116, 118]), ice-**X** [120, 121]), ice-**XII** [124] (ice-**XIV** [125]), ice-**XVI** [127], and ice-**XVII** [128–130], where phases in brackets represent the corresponding low temperature and/or high

pressure analogues. In nature only ice-**I<sub>h</sub>** and ice-**I<sub>c</sub>** are present where ice-**I<sub>c</sub>** only accounts for tiny fraction in the upper atmosphere, the remaining ice phases are artificial ice phases produced under high pressures and at low temperatures, or by degassing gas hydrates. Regarding the structure motifs, only ring sizes larger than six and other larger structure motifs will be shown in pictures. Smaller rings will be named according to their shape, because the shapes of those rings are more easy to imagine and very similar to their carbon counterparts. Since there are quite a few different ring sizes and shapes in most of the different ice phases, all of them will be depicted in section A.4 [Ice](#) while selected ones will also be shown in subsection 4.4.2 [Comparison of Water's Structure Motifs](#).

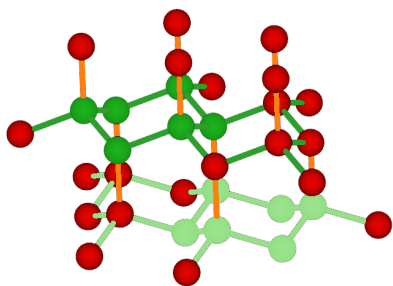


**Figure 4.86:** Macroscopic structure depiction of ice-**I<sub>h</sub>**; two sheets of chair-like shaped  $O_6$ -rings with interconnection to directly stack - hydrogen atoms are left out, red = oxygen, green = first sheet + representing  $O_6$ -ring, light green = second sheet + representing  $O_6$ -ring, and orange = connection between slices.

Starting with the structure of ice-**I<sub>h</sub>** (and ice-**XI**), this most abundant phase of solid water provides a sliced structure. Each slice represents a honeycomb-like shaped sheet of chair-like  $O_6$ -rings (see [figure 4.86](#)). Two slices are connected via the forth hydrogen bond in a way that the sheets stack up perfectly aligned. Thus, the two slices represent the two “different” layers of a hexagonal close-packed system. Within this well

and simply organised water network only  $O_6$ -rings can be found, which resemble the chair and bathtub conformations of its carbon analogues. The bathtub-like shaped  $O_6$ -rings are found between two orange slice-connections.

The second well and simply organised structure of ice-**I<sub>c</sub>** provides again a sliced structure with honeycomb-like shaped sheets of chair-like  $O_6$ -rings (see [figure 4.87\(a\)](#)) But this time, those sheets are shifted against each other and the water molecules now appear to be in a cubic close-packed-like system. This also gives rise to the formation

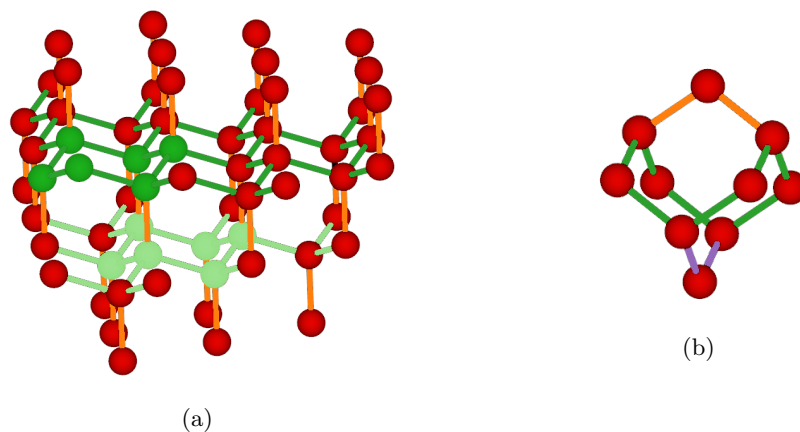


**Figure 4.87:** Macroscopic structure and substructure depiction of ice- $\text{I}_c$ ; (a) sliced structure and (b) substructure structure - hydrogen atoms are left out, red = oxygen, green = first slice + representing  $\text{O}_6$ -ring/ $\text{O}_8$ -ring, light green = second slice + representing  $\text{O}_6$ -ring, orange = connection between slices/first bridging, and purple = second bridging.

of a substructure, which is shown in [figure 4.87\(b\)](#). A deep bathtub-like shaped  $\text{O}_8$ -ring (green) can be seen which is bridged at two positions (orange and purple) by additional water molecules. Each bridge itself gives rise to two chair-like shaped  $\text{O}_6$ -rings (easiest seen with the purple bridge).

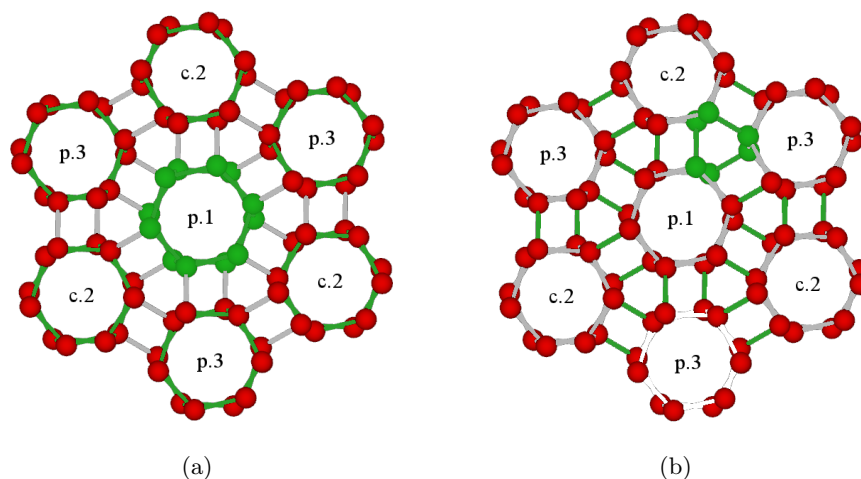


**Figure 4.88:** Macroscopic structure depictions of ice- $\text{II}$ , where p = planar, c = chair-like and digit = subplane number; (a) highlighting the stacked  $\text{O}_6$ -rings and (b) highlighting connecting corners - hydrogen atoms are left out, red = oxygen, and green highlighted substructures.



Leaving those well and simply organised structures behind, ice-**II** is the only phase of ice that provides an ordered hydrogen bonding at “low” pressures and “high” temperatures. First of all, its structure features a quite well organised looking macroscopic structure (see [figure 4.88](#)). As it can be seen in [figure 4.88\(a\)](#), ice-**II** provides  $O_6$ -rings which are twisted to each other going along the viewing axis. Those  $O_6$ -rings either have the shape of a planar  $O_6$ -ring or of a chair-like one. The position of them is alternating going along the viewing axis and also alternating in their lateral distribution. From the central  $O_6$ -ring to its directly underlying counterpart, two subplanes are passed as well. In [figure 4.88\(a\)](#) and [figure 4.88\(b\)](#) those subplanes are indicated. While the letter represents the shape of the  $O_6$ -ring (**p** = planar and **c** = chair-like), the number stands for the increasingly deep subplane. It can be seen that “p.1” is placed above three chair-like shaped  $O_6$ -rings while they are again positioned above three planar  $O_6$ -rings, ultimately, resulting in the shown assembly.

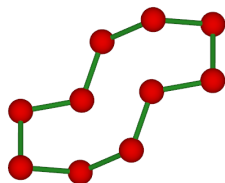


**Figure 4.89:** Structure depiction of the  $O_{10}$ -ring in ice-**II** connecting the previously shown  $O_6$ -rings (from top left oxygen of the lower left “c.2” to the top right oxygen of “p.1”) - hydrogen atoms are left out, red = oxygen, and green = hydrogen bonds.

In [figure 4.88\(b\)](#) the highlighted parts are not actual  $O_3$ -rings, but show, the connection between the  $O_6$ -rings. Within the space between those  $O_6$ -ring “subplanes”, “S”-shaped  $O_{10}$ -rings are formed (see [figure 4.89](#)), which connect the  $O_6$ -rings. The highlighted “triangles” in [figure 4.88\(b\)](#) result from the overlapping edges of those  $O_{10}$ -rings.

Distorted versions of them also connect the  $O_6$ -rings vertically. In addition to those  $O_{10}$ - and  $O_6$ -rings, ice-**II** also gives rise to twisted bathtub-like  $O_6$ -ring, two different  $O_8$ -rings, further six  $O_{10}$ -rings, and four  $O_{12}$ -rings (see [figure A.20](#) to [figure A.22](#)).

Looking at the structure of ice-**III** (and ice-**IX**), two interesting larger structure motifs can be identified. The first one, seen in [figure 4.90](#), shows two slices of the ice-**III** structure, how they are built up, and how they are connected. In [figure 4.90\(a\)](#) two

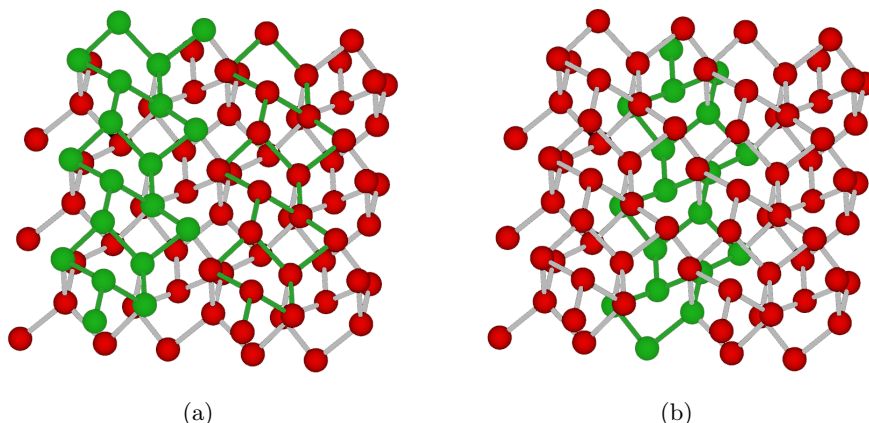


**Figure 4.90:** Macroscopic structure depictions of ice-**III**; (a) highlighting two chains of  $O_5$ -rings and (b) highlighting a chain of  $O_5$ -rings below the previous ones - hydrogen atoms are left out, red = oxygen, green highlighted substructures, and light gray = de-emphasised bonds.

chains made from edge sharing envelop-like  $O_5$ -rings are highlighted, which are part of the first slice. Those two chains are not connected to each other, but instead, the tips of those chains bind to the slice below (see [figure 4.90\(b\)](#)) and above. Thus, those connections between the chains generate the three dimensional structure of ice-**III**.

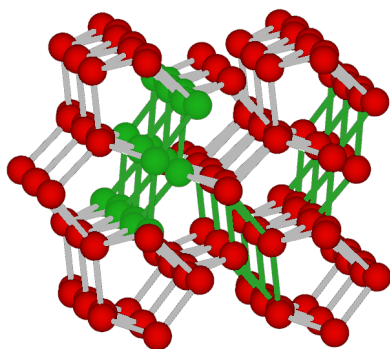


**Figure 4.91:** Macroscopic structure depiction of the fourfold helical structure motif in ice-**III** - hydrogen atoms are left out, red = oxygen, green = highlighted substructure, and light gray = de-emphasised bonds.

Viewing ice-**III** from another perspective, a second larger structure motif can be seen. Taking a look at [figure 4.91](#), it can be seen that within the previously discussed network of  $O_5$ -ring-chains, fourfold helical structures are observable as well. Their cross section shows a very narrow rhombus. Those fourfold helices come to existence through the slice interconnections, and by association, they appear quite often.

Apart from those larger structure motifs, ice-**III** provides one  $O_7$ -ring, one  $O_8$ -ring, one  $O_9$ -ring, and one  $O_{12}$ -ring, which can be seen in [figure A.23](#).

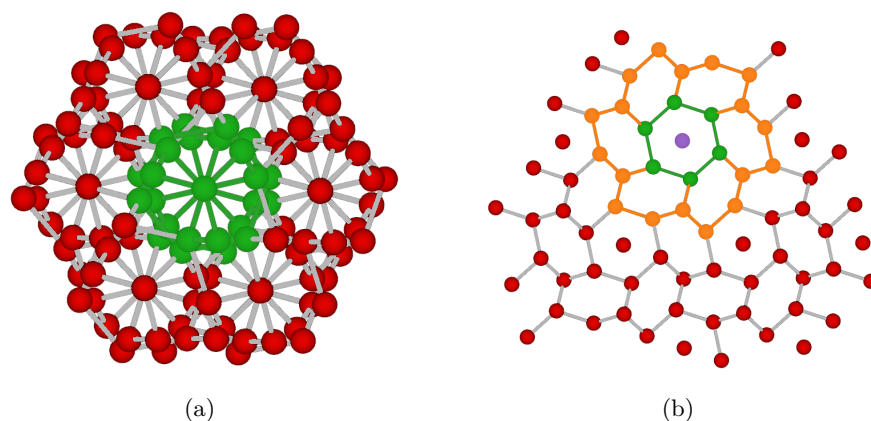


**Figure 4.92:** Macroscopic structure depictions of ice-**IV**; (a) highlighting an overlapping substructure and (b) slice of  $O_6$ -rings - hydrogen atoms are left out, red = oxygen, green = highlighted substructure/penetrated planar  $O_6$ -ring, orange = surrounding chair-like  $O_6$ -rings, purple = penetrating hydrogen bond, and light gray = de-emphasised bonds.

Going to ice-**IV**, its structure features again a very well organised looking macroscopic structure (see [figure 4.92](#)). The highlighted part in [figure 4.92\(a\)](#) resembles the overlap of a very interesting substructure, which can be seen in [figure 4.93](#). In [figure 4.92\(b\)](#) a single slice of ice-**IV** can be seen, whose stacking would result in the structure shown in [figure 4.92](#). Those slices consist of only  $O_6$ -rings, some planar ones (green) and many sheared chair-like ones (orange). The substructure highlighted in [figure 4.92\(a\)](#) shows a “barbell”-like shaped structure (see [figure 4.93\(a\)](#)), where the centrepiece (purple in [figure 4.92\(b\)](#)) penetrates a planar  $O_6$ -ring, shown in [figure 4.93\(b\)](#). A closer look at the ends of the “barbell” reveals that they are a sub-

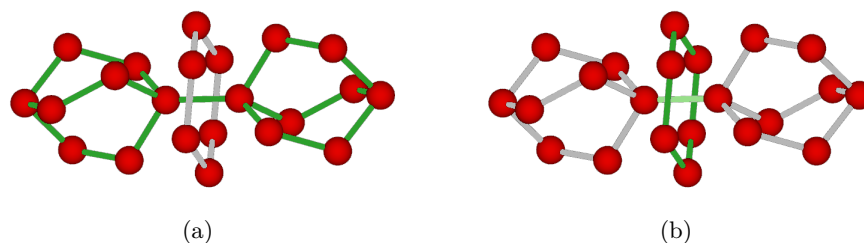


**Figure 4.93:** Structure depiction of the main substructure in ice-**IV**; (a) “barbell”-part and (b) penetrated  $O_6$ -ring - hydrogen atoms are left out, red = oxygen, green/light green = highlighted parts, and light gray = de-emphasised bonds.

structures of three twisted bathtub-like shaped  $O_6$ -rings. Those smaller substructures are also responsible for the chair-like  $O_6$ -rings in [figure 4.92\(b\)](#). By connecting one downwards pointing end with three upwards pointing ends of the “barbells”, three chair-like  $O_6$ -rings are formed.

Further connections between the substructures, in conjunction with the approach to analyse the different ice phases (see subsection 2.2.5 [Analysis of Ice Structures](#)), result in a variety of differently shaped  $O_n$ -rings. Hence, three  $O_8$ -rings, 15  $O_{10}$ -rings, and 13  $O_{12}$ -rings can be identified in ice-**IV**. All of them can be seen in [figure A.24](#) to [figure A.26](#).

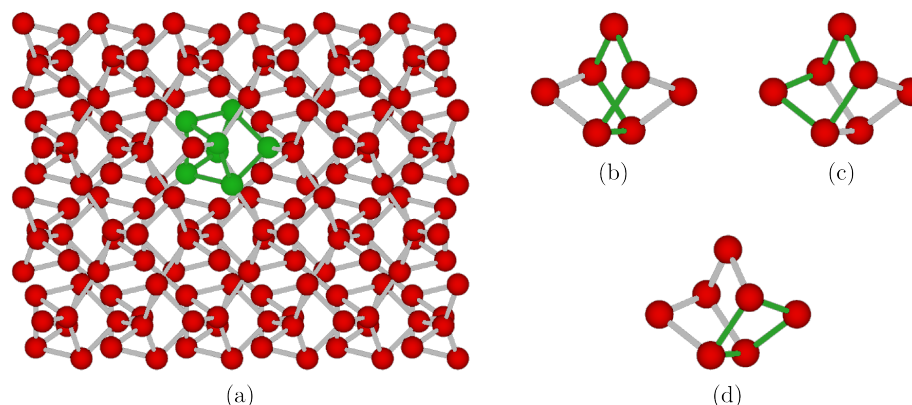


**Figure 4.94:** Macroscopic structure and substructure depictions of ice-**V**; (a) highlighting a smaller substructure, (b) first  $O_5$ -ring, (c) second  $O_5$ -ring, and (d)  $O_4$ -ring - hydrogen atoms are left out, red = oxygen, green highlighted substructures, and light gray = de-emphasised bonds.

The next ice phase to analyse is ice-**V** (and ice-**XIII**). Its macroscopic structure reveals two reoccurring substructures, depending on the viewing angle. In [figure 4.94](#) a comparably small but very frequent substructure can be seen. Taking a closer look at it shows that it is made of three different small  $O_n$ -rings, two different  $O_5$ -rings and one  $O_4$ -ring. Considering the shape of the small  $O_n$ -rings, the  $O_4$ -ring shows a very flat butterfly-like one while the two different  $O_5$ -rings provide two differently wide “opened” envelop-like shapes.

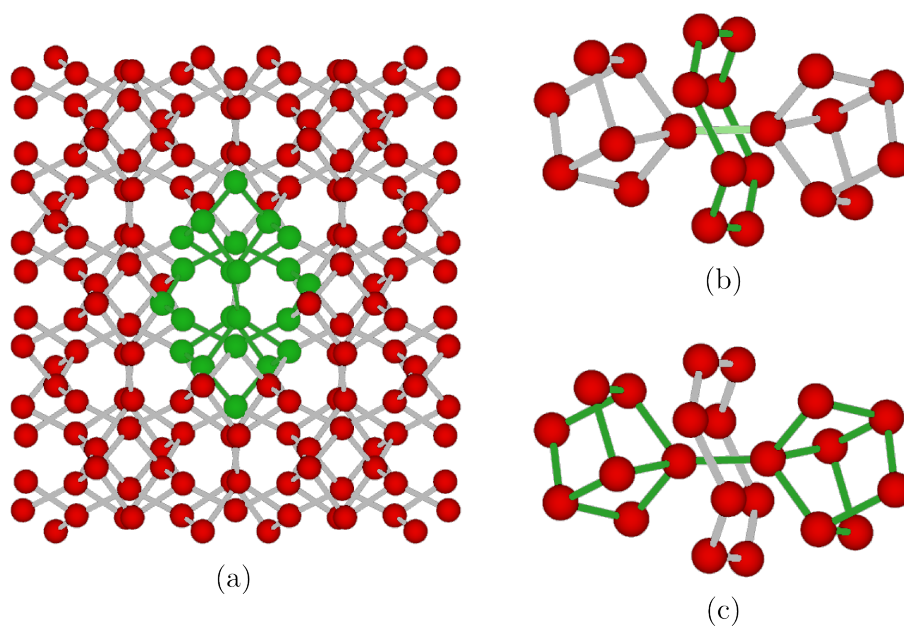


**Figure 4.95:** Macroscopic structure and substructure depictions of ice-**V**; (a) highlighting a larger substructure, (b) penetrated O<sub>8</sub>-ring, and (c) “barbell”-part - hydrogen atoms are left out, red = oxygen, green highlighted substructures, and light gray = de-emphasised bonds.

Regarding the second substructure, shown in [figure 4.95](#), it can be seen that this substructure is much larger than the previous one. As it was seen in [figure 4.93](#), the water molecules in this ice phase form again an “barbell”-like substructure. For the second time, the “barbell”’s centrepiece penetrates a ring of water molecules, this time an O<sub>8</sub>-ring.

The incorporation of the seen substructures in ice-**V** provides a variety of connection pathways between them. Adding the eased restrictions for the finding of O<sub>n</sub>-rings, explained in subsection 2.2.5 [Analysis of Ice Structures](#), ice-**V** yields the most structure motifs of all ice phases. In [figure A.27](#) to [figure A.31](#) the second O<sub>8</sub>-ring, two O<sub>9</sub>-rings, ten O<sub>10</sub>-rings, seven O<sub>11</sub>-rings, and 21 O<sub>12</sub>-rings can be viewed.

The next ice phase, ice-**VI** (and ice-**XV**), is even more interesting than its predecessors. It consists of strings of quite small substructures (see [figure 4.96\(a\)](#)) that spread and connect themselves with each other in the three spatial directions. Thus, they form a very regular three dimensional network. Interestingly, not one but two of

such networks are found in the structure of ice-**VI** and both are independent of each other, see [figure 4.96\(b\)](#).

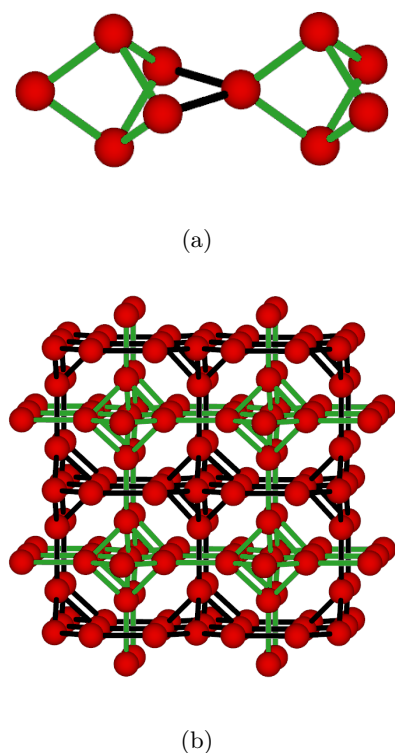


**Figure 4.96:** Macroscopic structure and substructure depictions of ice-**VI**; (a) highlighting subunits of the network's substructure (b) highlighting one independent network of hydrogen bonds - hydrogen atoms are left out, red = oxygen, green = highlighted substructures/first independent network, and black = connecting hydrogen bonds/second independent network.

for the last two ice phases ice-**IV** and ice-**V**. Nonetheless, three  $O_8$ -rings, one  $O_{10}$ -ring, and four  $O_{12}$ -rings can be found and are displayed in [figure A.32](#).

Hence this leads to a variety of different ring penetrations in order to make this structure of two intercalating but not connected networks work. Those required ring penetrations are depicted in [figure 4.97](#), where an  $O_8$ -ring is penetrated each time. While in two cases (see [figure 4.97\(a\)](#) and [figure 4.97\(b\)](#)) the penetrated  $O_8$ -rings provide shallow bathtub-like shapes and are penetrated by two bonds at the same time (see [figure 4.96\(a\)](#) the black bonds), in the other four cases (see [figure 4.97\(c\)](#) to [figure 4.97\(f\)](#)), the  $O_8$ -rings show flat shapes with two peaking water molecules and are penetrated by “only” one bond.

Since this ice phase provides two intercalating but independent networks, the amount of possible structure motifs, namely the sizes and shapes of the detectable  $O_n$ -rings, are much smaller than

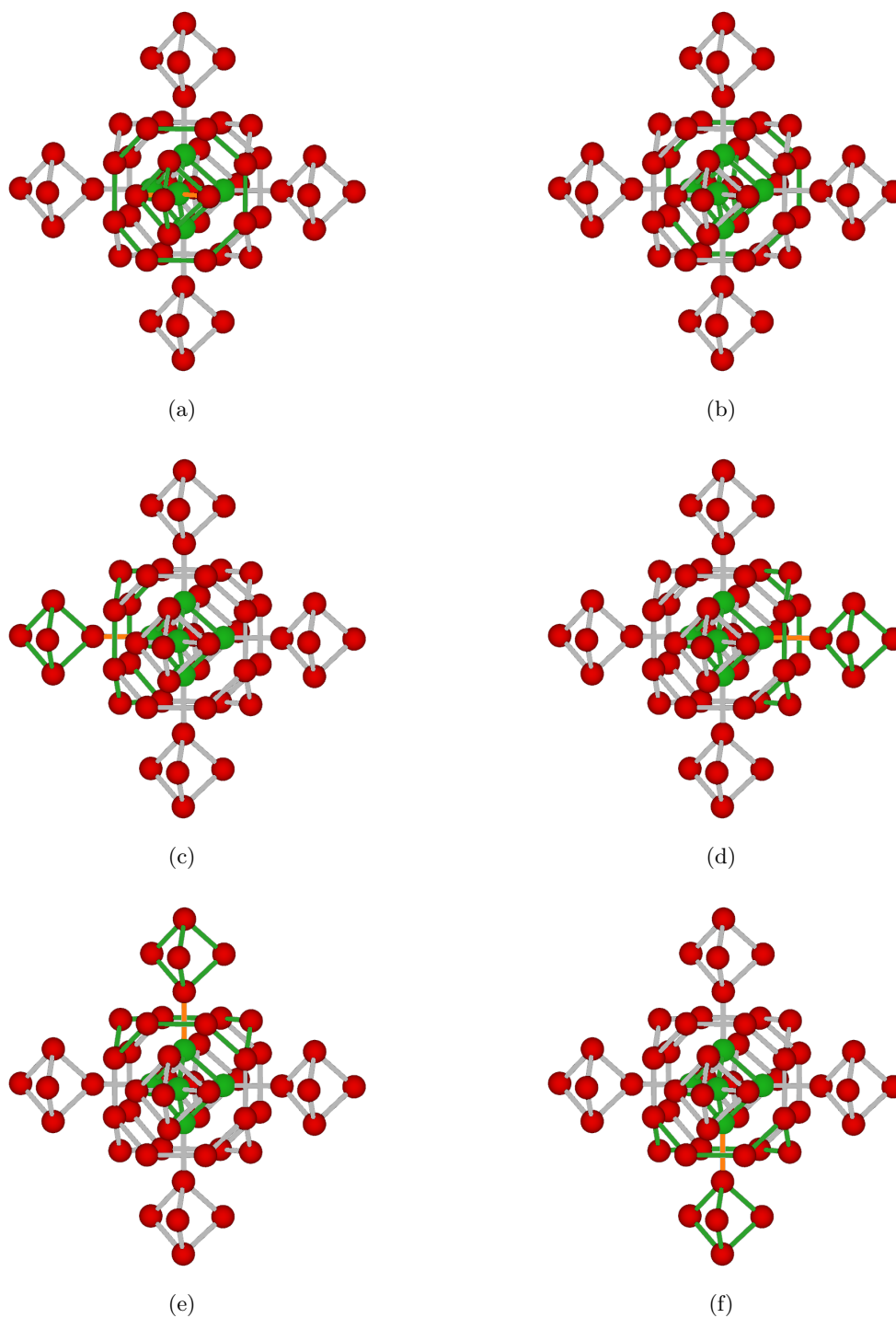


**Figure 4.97:** Structure depiction of a larger substructure in ice-VI; (a) - (f) large substructure with different penetration directions - hydrogen atoms are left out, red = oxygen, green/light green = highlighted parts, and light gray = de-emphasised bonds.

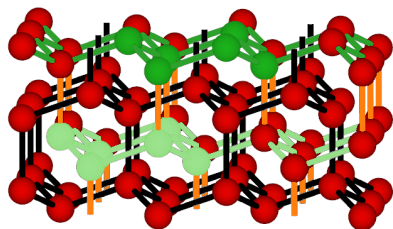


**Figure 4.98:** Macroscopic structure depiction of ice-**VII** with two intercalating but independent ice-**I<sub>c</sub>** networks and highlighting one of them - hydrogen atoms are left out, red = oxygen, green = first slice + representing O<sub>6</sub>-ring, light green = second slice + representing O<sub>6</sub>-ring, orange = connection between slices, and black = second independent ice-**I<sub>c</sub>** network.

Continuing the investigation of the different ice phases with ice-**VII** (and ice-**VIII** as well as ice-**X**), its structure features again two independent networks which are intercalating. This time, the single networks represent the same structure as ice-**I<sub>c</sub>**. Thus, it not surprising that the same structure motifs can be found here, as they were in ice-**I<sub>c</sub>**. The only new theme is the penetration of every

O<sub>6</sub>-ring in the structure. Therefore, ice-**VII** consists solely from O<sub>6</sub>-rings, which form two intercalating but independent ice-**I<sub>c</sub>** networks.

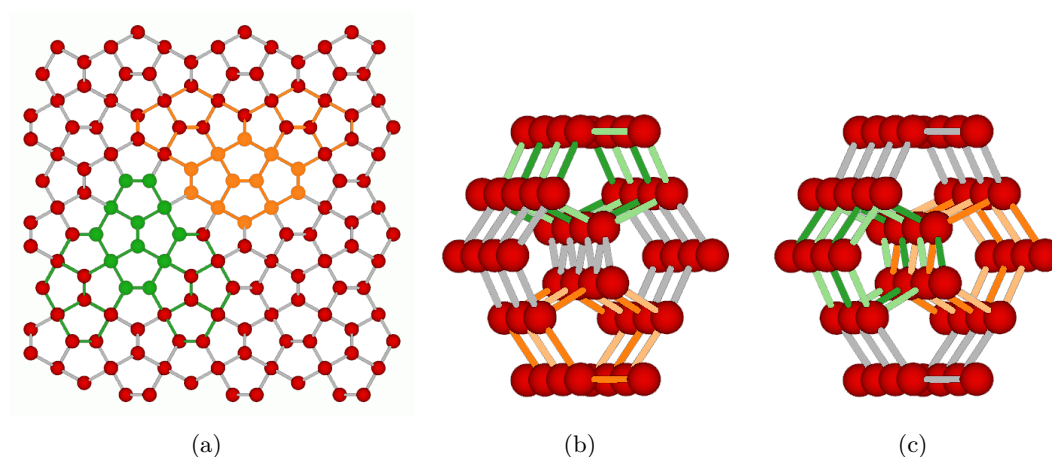


**Figure 4.99:** Macroscopic structure and substructure depictions of ice-**XII**; (a) highlighting two overlapping spreads of a larger substructure, (b) highlighting two double helices in (a)'s substructure, and (c) highlighting another two double helices in (a)'s substructure - hydrogen atoms are left out, red = oxygen, green/light green/orange/light orange = highlighted substructure, and light gray = de-emphasised bonds.

After this short but revealing look at ice-**VII**, ice-**XII** is the next ice phase to study. This structure seems to provide “sheets” made of envelop-like O<sub>5</sub>-rings, which can be seen in [figure 4.99\(a\)](#). Within those “sheets” of O<sub>5</sub>-rings, four of such O<sub>5</sub>-rings seem to form their own substructure, but the orientation of such substructures can have



two different orientations, as it is indicated in [figure 4.99\(a\)](#). By taking a closer look at those substructures (see [figure 4.99\(b\)](#) and [figure 4.99\(c\)](#)), it can be seen that ice-**XII** does not have sheets or slices, but it still shows a very regular three dimensional structure. The regularities result from the formation of fivefold double helices, which build up the whole structure of ice-**XII**. Each substructure consists of two times two opposing double helices.

Due to the high interconnectivity of such substructures with each other, the amount of possible  $O_n$ -rings increases again slightly compared to ice-**VI**. In ice-**XII** two  $O_7$ -rings, four  $O_8$ -rings, three  $O_9$ -rings, four  $O_{10}$ -rings, two  $O_{11}$ -rings, and five  $O_{12}$ -rings can be found, which are once more depicted in [figure A.33](#) and [figure A.34](#).

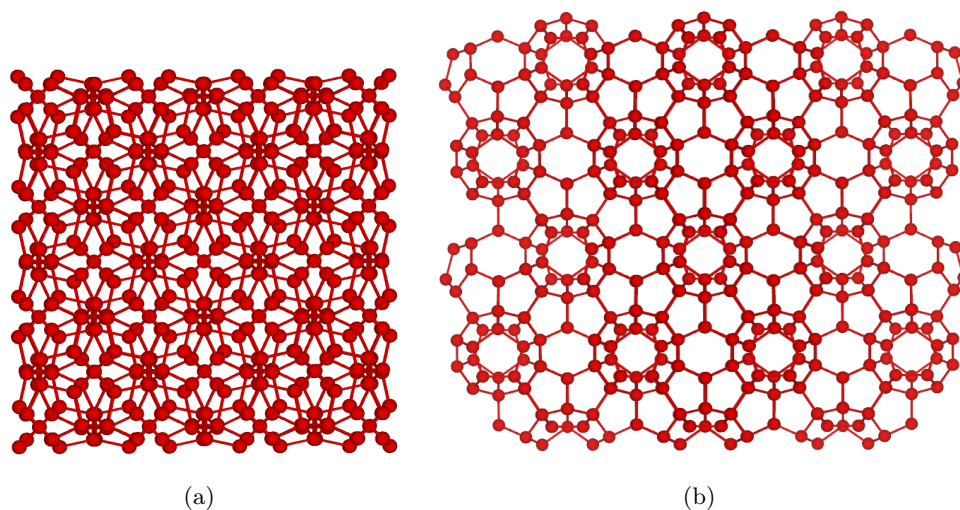


**Figure 4.100:** Macroscopic structure depictions of ice-**XVI**; with two different viewing angles - hydrogen atoms are left out and red = oxygen/bonds.

Looking at [figure 4.100](#) immediately reveals that the structure of ice-**XVI** is very well organised, and it might remind the proficient water enthusiast of a clathrate hydrate type-**II**, which is nothing but a porous ice network storing small non-polar molecules like hydrogen, nitrogen, oxygen, carbon dioxide, etc.

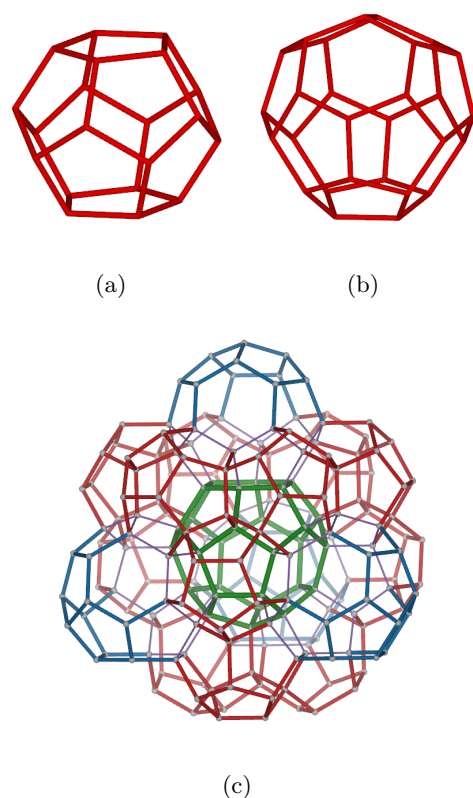


**Figure 4.101:** Substructure depictions of ice-**XVI**; (a) small cage with twelve O<sub>6</sub>-rings, (b) large cage with twelve O<sub>5</sub>-rings and four O<sub>6</sub>-rings, and (c) first “CS” of the large cage - hydrogen atoms are left out, oxygen atoms are left out as well for clarity, red = oxygen-oxygen bonds/non-overlapping small cage edges, green = central large cage edges, blue = non-overlapping large cage edges, and purple = overlapping cage edges.

Alongside the obvious planar O<sub>5</sub>- and O<sub>6</sub>-rings, the investigation for structure motifs in ice-**XVI** also yielded one O<sub>10</sub>-ring and three O<sub>12</sub>-rings, which can be seen in [figure A.35](#).

Within ice-**XVI** there are two different substructures which can be viewed as two differently sized cages or cavities: a smaller cage consisting of twelve edge-sharing O<sub>5</sub>-rings (see [figure 4.101\(a\)](#)) and a larger second one made from twelve and four edge-sharing O<sub>5</sub>- and O<sub>6</sub>-rings (see [figure 4.101\(b\)](#)). The face-sharing combination of both cages (see [figure 4.101\(c\)](#)) simply results in the structure of ice-**XVI** while this combination is easiest explained by looking at single large cage (green). Each O<sub>6</sub>-ring of it is shared with the next large cage (blue) while each O<sub>5</sub>-ring of it is shared with a small cage (red). Thus, the first “CS” of a large cage contains twelve small cages and four additional large cages. Please note that the four large cages in the “CS” are arranged tetrahedrally around the central one.

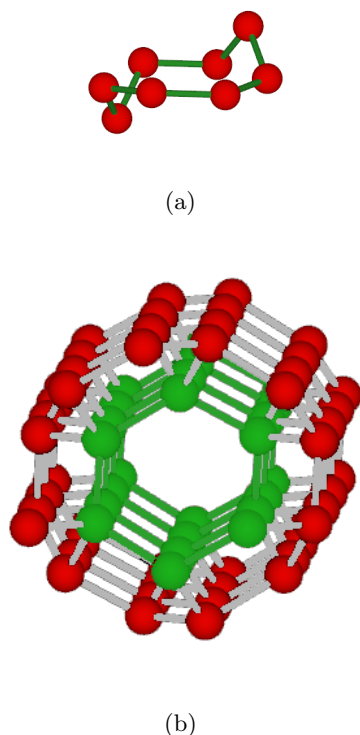


**Figure 4.102:** Substructure depictions of ice-**XVII**; (a)  $O_8$ -ring and (b) highlighted sixfold helix - hydrogen atoms are left out, red = oxygen, green highlighted substructure/hydrogen bonds, and light gray = de-emphasised bonds.

Finalising the investigation of the different ice phases, the structure of ice-**XVII** is the last one to look at. Like ice-**XVI** it is one of the low density ice phases and is obtained likewise by degassing a gas hydrate at low temperatures. First of all, the computer assisted analysis of ice-**XVII** could only find one  $O_8$ -ring, which is why it is shown here directly in [figure 4.102\(a\)](#). Furthermore, its porous structure features a sixfold helical substructure, which reoccurs quite often and can be seen in [figure 4.102\(b\)](#). Those helical structures represent the chambers which stored the gas molecules beforehand. The walls of those pipe-like substructures are sheets made of envelop-like  $O_5$ -rings (see [figure 4.103\(a\)](#)).

Those sheets were previously assumed as structure motifs in ice-**XII**, but it turned out to be a crossing of fivefold double helices. In ice-**XVII**, however, the sheets are not close enough to each other to form those double helices and thus, they connect to other ones in a more spread way by crossing each other at an angle of  $60^\circ$ , which can be seen in [figure 4.103\(b\)](#). Within this macroscopic depiction all substructures and their interplay in ice-**XVII** can be seen: the crossing  $O_5$ -ring-sheets (green and orange) as well as the sixfold helical substructure (purple), which results from two times two parallel proceeding sheets.

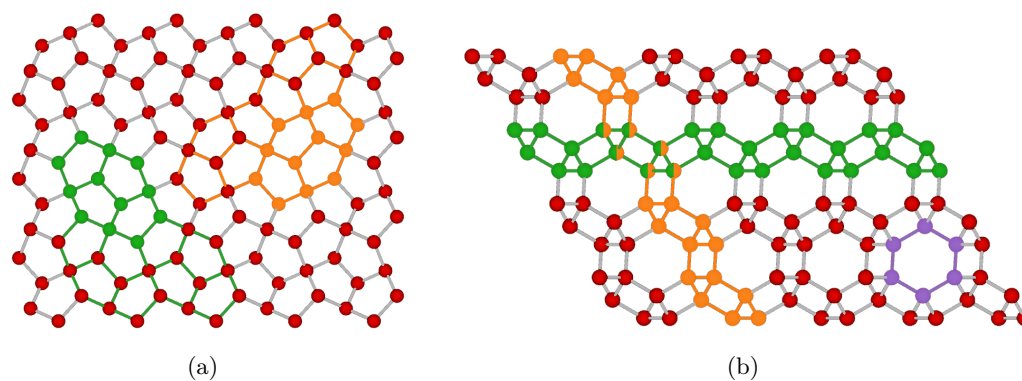


**Figure 4.103:** Macroscopic structure and substructure depiction of ice-**XVII**; (a) highlighting subunits in sheets made of envelop-like  $O_5$ -rings and (b) highlighting two crossing  $O_5$ -ring-sheets and the cross section of a sixfold helix - hydrogen atoms are left out, red = oxygen, green/orange/purple = highlighted substructure, and light gray = de-emphasised bonds.

#### 4.4.2 Comparison of Water's Structure Motifs

Now that the structure motifs of adsorbed and solid water are known, they can be compared in order to see if a given surface is potentially able to grow a specific ice phase. For this comparison only selected surface modification and water amount combinations will be taken, precisely those, which provide a clear identifiable and large enough structure motif. This includes helices, sheets, ring-chains and all ring motifs even if they contain fluoride ions. One very frequently occurring structure motif of adsorbed water molecules is the formation of zigzag chains. They are formed with or without the surface hydroxide groups as well as with or without fluoride ions. Unfortunately, those chains can not give any hint for a possible resemblance of them with structure motifs found in the different ice phases. Thus, they are left out from this more detailed comparison, otherwise, they would lead to very ambitious and speculative assumptions. Besides, every structure motif resulting from all combinations of surface modification and water amount can be seen in [figure A.36](#) to [figure A.52](#).

Please note that the used approach to investigate the adsorption of small amounts of water of course limits our considerations. First of all, the structure motifs of adsorbed water are always repeated laterally, due to the periodicity, providing only

sheets of water which is only very rarely the case for structure motifs of water in ice phases. To overcome this problem, selected UCs were taken to build up a supercell and were again structurally optimised to decrease the influence of this effect, but it provides no observable structural differences, because a minimum, at least locally, was already found. Additionally, the comparably small amount of water, especially the very small height of the water slice on the surface, also challenges the accuracy of this comparison. This should be kept in mind, while reading the following subsection.

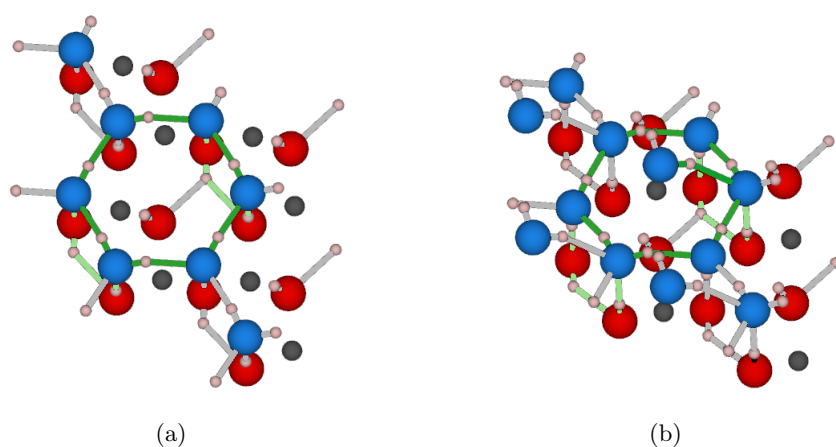


**Figure 4.104:** Depictions of structure motifs of adsorbed water, in different amounts, on a hydrated (0001) surface; (a) two water molecules per UC and (b) three water molecules per UC - gray = aluminium, red = oxygen, white = hydrogen, light blue = water oxygen, green/light green = highlighted structural motif, and light gray = de-emphasised bonds (VASP-DFT, PBE/PAW, 600.0 eV energy cut-off, D3-BJ).

Keeping the order of the analysed surface cuts and added amount of water as it was used in section 4.3 [Water Adsorption on Modified  \$\alpha\$ -Aluminium Oxide Surfaces](#), the first structure motif to look at is provided by the hydrated (0001) surface UC with two added water molecules (see [figure 4.104\(a\)](#)). It can be seen that the adsorbed water molecules form planar  $O_6$ -rings (green), which build up a honeycomb-like water slice on the surface. The single  $O_6$ -rings are connected to the surface via hydrogen bonds between each water molecule and the surface hydroxide groups, resulting in two “standing” planar  $O_4$ -rings per  $O_6$ -ring. The structure motif of a planar  $O_6$ -ring is found in ice-II, ice-IV, and ice-XVI but never in a honeycomb-like structure. While

ice-**XVI** is the least plausible ice phase to be formed via water adsorption due to its low density structure, ice-**II** and ice-**IV** seem to be more plausible but require quite a few adaptations. Regarding ice-**II**, three more or less small changes have to take place to make the found honeycomb-like structure be a part of this ice phase. At first, some of the planar  $O_6$ -rings have to reshape to chair-like planar  $O_6$ -rings. Secondly, several more have to merge with each other in pairs (elongate one shared bond) to form the  $O_{10}$ -rings shown in [figure 4.89](#). And finally, the slice have to “swell” in order to resemble the different subplanes indicated in [figure 4.88](#). For a better resemblance with ice-**IV**, the found honeycomb-like shaped slice has to change the shape of  $\frac{6}{7}$  of its planar  $O_6$ -rings to sheared chair-like ones. In both cases, the connection to the next forming slice have to fit as well.

Nonetheless, there are also other ice phases which are possible to be formed, based on the found structure motif of adsorbed water on this surface. Although ice-**I<sub>h</sub>**, ice-**I<sub>c</sub>**, and ice-**VII** do not provide planar  $O_6$ -rings, they provide slices of  $O_6$ -rings with chair-like subunits. Thus, it is possible that additional water molecules will result in the breaking of some of the hydrogen bonds to the surface in order to allow the shifting of planar  $O_6$ -rings to chair-like  $O_6$ -rings.

In general, the found honeycomb-like slice of adsorbed water on the hydrated (0001) surface might result in the growing of five different ice phases, ice-**I<sub>h</sub>**, ice-**I<sub>c</sub>**, ice-**II**, ice-**IV**, and ice-**VII**. In all cases several adjustments have to take place to resemble a single slice of the respective ice phase, but with enough added water the formation of that phase should overcome the bonding to the surface that forces the planar rings.

Unfortunately, the addition of a third water molecule per **UC** is not enough and does not change the shape of the  $O_6$ -rings, but it adds the water molecule directly on top of the ring’s middle (see [figure 4.104\(b\)](#)). This favours the formation of ice-**VII** with the addition of more water molecules, since the third water molecule is placed at the correct position for the first water molecule of the second ice-**I<sub>c</sub>** network’s formation in ice-**VII**. On the other hand, until now it is just a loosely oriented water molecule,

it might well be that it will orient itself in a way to allow the formation of the second slice of ice-**I<sub>h</sub>**, ice-**I<sub>c</sub>**, ice-**II** or ice-**IV** as well. Thus, the third water molecule does not really help here to work out the most possible and reasonable ice phase, which might grow on this surface.

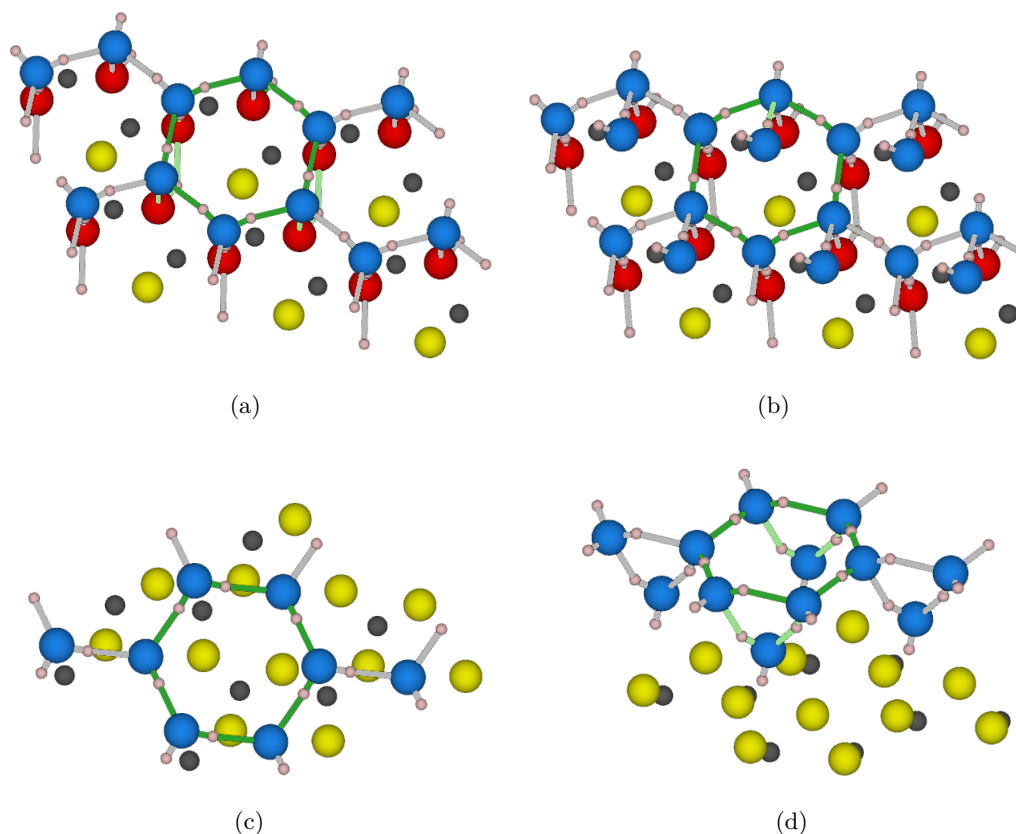


**Figure 4.105:** Depictions of structure motifs of adsorbed water, in different amounts, on a singly (first row) and triply (second row) fluorinated (0001) surface; (a) + (c) two water molecules per UC and (b) + (d) three water molecules per UC - gray = aluminium, red = oxygen, white = hydrogen, light blue = water oxygen, green/light green = highlighted structural motif, and light gray = de-emphasised bonds (VASP-DFT, PBE/PAW, 600.0 eV energy cut-off, D3-BJ).

Since the adsorbed water molecules on the singly and triply fluorinated (0001) surfaces form nearly the same honeycomb-like slices (see figure 4.105), the just mentioned issues and conclusions hold true for both of these fluorinated surfaces. The needed adjustments becomes even easier to be implemented due to the decreasing strength

of the connection to the surface. However, for the third water molecule per UC on the triply fluorinated (0001) surface, some additional points have to be made. Since the third water molecule lifts the honeycomb-like shaped slice further away from the surface, the needed adjustments mentioned for the hydrated (0001) surface become even more easier as they are already because of the weaker interactions to the surface. Thus, the triply fluorinated (0001) surface provides the highest possibility to grow one of ice phases ice-**I<sub>h</sub>**, ice-**I<sub>c</sub>**, ice-**II**, ice-**IV** and ice-**VII** on it, considering the three looked at modified (0001) surfaces so far.

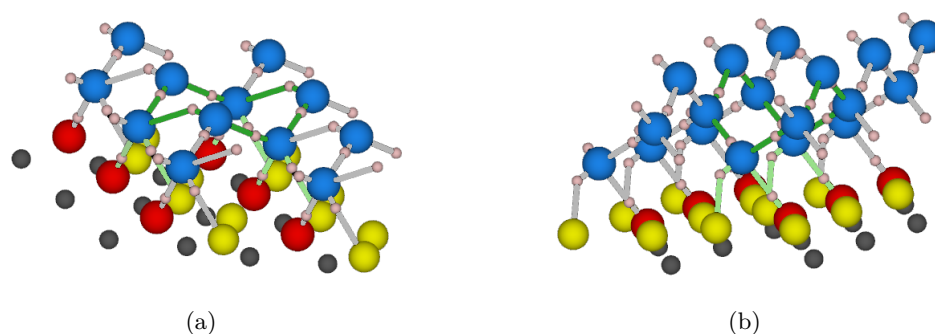


**Figure 4.106:** Depictions of structure motifs of adsorbed water, in different amounts, on a doubly fluorinated (0001) surface; (a) two water molecules per UC and (b) three water molecules per UC - gray = aluminium, red = oxygen, white = hydrogen, light blue = water oxygen, green/light green = highlighted structural motif, and light gray = de-emphasised bonds (VASP-DFT, PBE/PAW, 600.0 eV energy cut-off, D3-BJ).

Looking at the structure motifs of adsorbed water on a doubly fluorinated (0001) surface in figure 4.106, a clear and drastic difference compared to the other modified (0001) surfaces can be seen. This time, the adsorption of two water molecules per UC formed again a slice of O<sub>6</sub>-rings, but it only shows chair-like shaped ones. Interestingly, the generally weaker but selectively stronger interactions of the adsorbed water molecules with the surface keep the slice anchored to the surface but allow it to otherwise position it farther away from the surface. Although slices of ice-**II** and ice-**IV** are still possible to be formed via structural adjustments, the ice phases ice-**I<sub>h</sub>**, ice-**I<sub>c</sub>** and ice-**VII** are clearly favoured this time. This is underlined by the addition of



the third water molecule per UC (see figure 4.106(b)), where the resulting structure motif resembles nearly exactly the substructure of ice-**I<sub>c</sub>** in figure 4.87(b). While the purple part of ice-**I<sub>c</sub>**'s substructure is disconnectedly resembled with the remaining hydroxide group and one fluoride ion in the surface, the orange part is missing but is very likely to be added with the next adsorbed water molecule. Thus, the doubly fluorinated (0001) surface is most likely able to grow ice-**I<sub>c</sub>** or ice-**VII** in (001) direction on it.

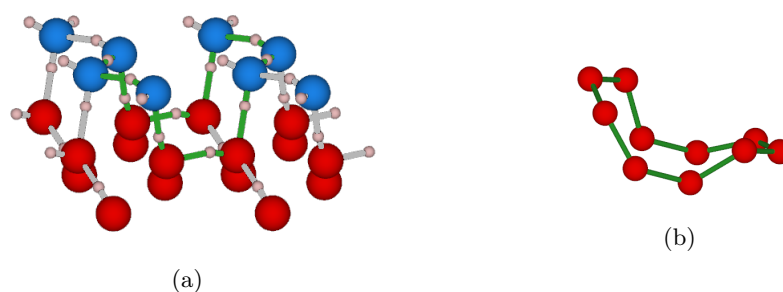


**Figure 4.107:** Depictions of structure motifs of adsorbed water on a hydrated ( $1\bar{1}02$ ) surface and the best matching structure motif in ice; (a) two water molecules per UC and (b) ice-**IV** mimicry - gray = aluminium, red = oxygen, white = hydrogen, light blue = water oxygen, green = highlighted structural motif/hydrogen bonds, and light gray = de-emphasised bonds (VASP-DFT, PBE/PAW, 600.0 eV energy cut-off, D3-BJ).

Leaving the flat (0001) surface behind and going to the wavy ( $1\bar{1}02$ ) surface, its hills and valleys gave rise to much different structure motifs. The first notable structure motif of water on the hydrated ( $1\bar{1}02$ ) surface results from the addition of two water molecules on the UC. It shows a network of  $O_{10}$ -rings which provide a deep bathtub-like shape without peaking water molecules. Going through the different structure motifs found in the different ice phases, one  $O_{10}$ -ring shows a very good agreement with structure motif of the adsorbed water molecules, the twelfth  $O_{10}$ -ring of ice-**IV** (see figure 4.107(b)). If quite a bit of reshaping would be allowed, the second most similar  $O_{10}$ -ring would be the fifth  $O_{10}$ -ring of ice-**V**, which can be seen in figure A.28(e).

Taking a second look at [figure 4.107\(a\)](#), one could also think that this O<sub>10</sub>-ring, involving the two hill-site hydroxide groups of the surface, might actually be a planar O<sub>6</sub>-ring consisting solely from water molecules which is halved due to the distance between two hills. Thus, the surface's structure and the quite strong hydrogen bonds from the surface to the water molecules seem to prevent the formation of such planar rings. Therefore, it might be possible for next water molecules to step by step overcome this surface restriction via decreasing distortions of their ideal ice phase positions. Hence, they might form one of the previously discussed ice phases for the modified (0001) surfaces: ice-**I<sub>h</sub>**, ice-**I<sub>c</sub>**, ice-**II**, ice-**IV** and ice-**VII** as well.

Adding the third water molecule on the hydrated ( $\bar{1}\bar{1}02$ ) surface's UC, the just addressed issue might be resolved. Looking at [figure 4.108](#) shows that it adsorbs above the O<sub>10</sub>-ring/possible O<sub>6</sub>-ring and bridges two corners. Considering the latter of the two mentioned ring sizes, this would again perfectly fit with the structure motifs provided by the hydrated and singly fluorinated (0001) surfaces with three added water molecules. Thus, the corresponding five ice phases are still in the competition for possibly being grown on this surface as well.

Besides, the bridging of the O<sub>10</sub>-ring by the third water molecule also gives rise to a completely different structure motif, a fivefold helical structure, seen in [figure 4.108\(b\)](#). And due to periodicity of the small UCs, they are also very close to each other, forming a horizontal zigzag chain between the single coils of two adjacent helices. Unfortunately, this structure motif can not be found in any of the studied eleven different ice phases. The most similar but still very different structure motif which can be observed in the ice phases is the fivefold double helix of ice-**XII**.

Finally, considering only the water molecules and neglecting the surface hydroxide groups, the three water molecules form a very shallow O<sub>8</sub>-ring with two peaking water molecules (see [figure 4.108\(c\)](#)). The most reasonable agreement of an ice phase structure motif with this O<sub>8</sub>-ring is found with the second O<sub>8</sub>-ring of ice-**IV**, seen in [figure 4.108\(d\)](#). To actually see the accordance of both, the latter has to be rotated

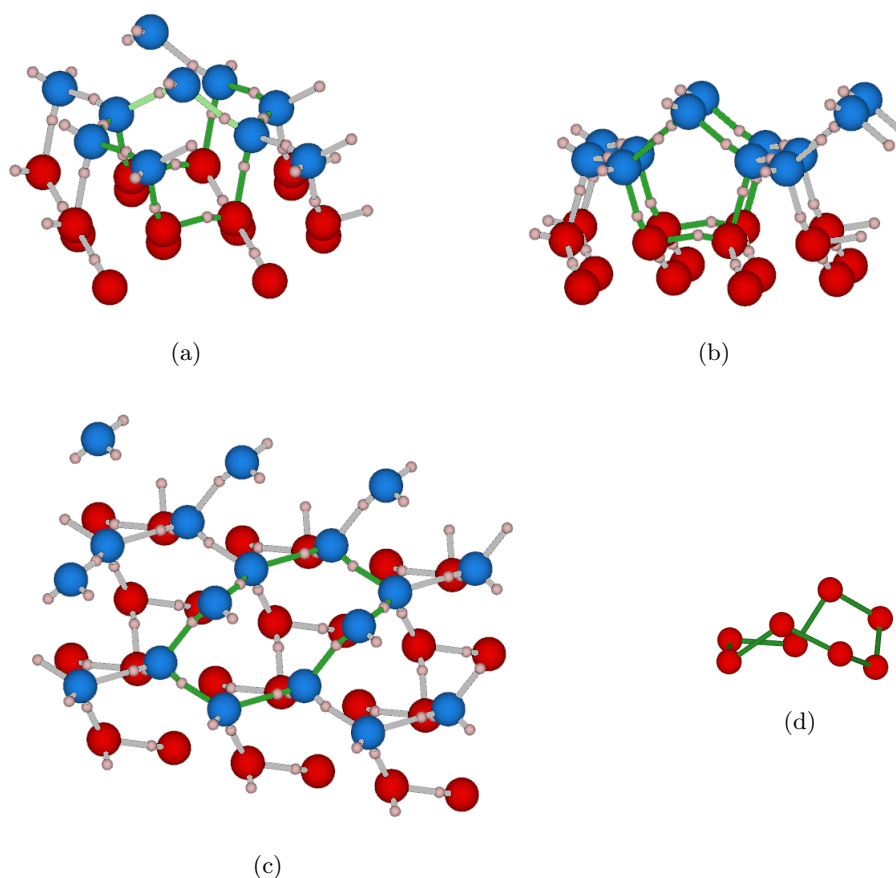


**Figure 4.108:** Depictions of structure motifs of adsorbed water on a hydrated ( $1\bar{1}02$ ) surface and the best matching structure motif in ice; (a) - (c) three water molecules per UC with different aspects highlighted, and (d) ice-**IV** mimicry of (c) - gray = aluminium, red = oxygen, white = hydrogen, light blue = water oxygen, green/light green = highlighted structural motif/hydrogen bonds, and light gray = de-emphasised bonds (VASP-DFT, PBE/PAW, 600.0 eV energy cut-off, D3-BJ).

by  $90^\circ$  clockwise around the “z”-direction and the new front-oxygen has to be moved upwards. So, with only one oxygen atom to be moved, the resemblance of both structure motifs is at least recognisable.

Despite the fact that three different structure motifs can be found for three water molecules on the hydrated ( $1\bar{1}02$ ) surface, only one motif shows a promising, although distorted, possibility to grow an actual ice phase. The firstly discussed bridged and cut  $O_6$ -ring closely resembles the found motifs for the modified (0001) surfaces, and by association, it might be able to grow ice-**I<sub>h</sub>**, ice-**I<sub>c</sub>**, ice-**II**, ice-**IV** or ice-**VII**, depending

on possible further adjustments with more added water molecules.

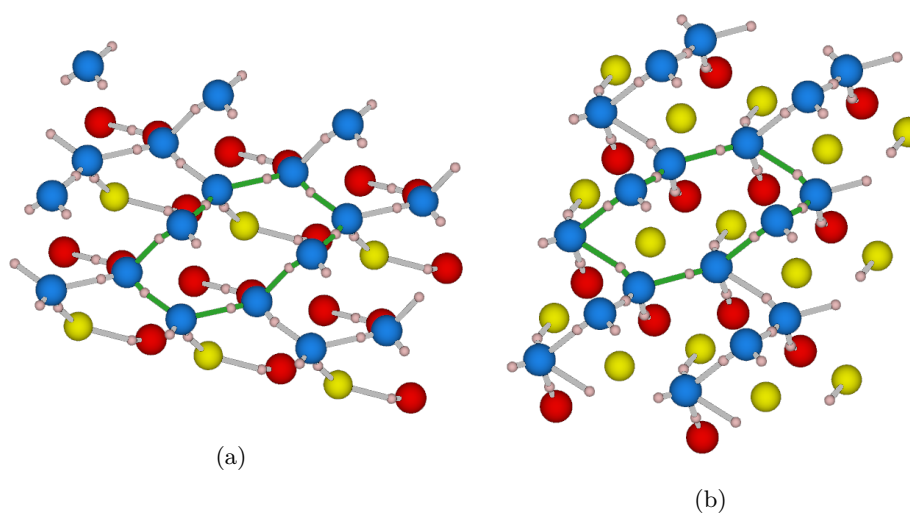


**Figure 4.109:** Depictions of structure motifs of adsorbed water on a singly and doubly fluorinated ( $1\bar{1}02$ ) surface; (a) three water molecules per singly fluorinated UC and (b) three water molecules per doubly fluorinated UC - gray = aluminium, red = oxygen, white = hydrogen, light blue = water oxygen, green = highlighted structural motif, and light gray = de-emphasised bonds (VASP-DFT, PBE/PAW, 600.0 eV energy cut-off, D3-BJ).

Going to the singly and doubly fluorinated versions of the ( $1\bar{1}02$ ) surface, three adsorbing water molecules on them form again a very flat  $O_8$ -ring with two peaking water molecules. Due to the introduced fluoride ion and the missing hydrogen bonds, two adsorbing water molecules only form chains of water on the surfaces, and the previously seen structure motif with three water molecules, the fivefold helix, is also neglected. Besides, the  $O_8$ -ring on those surfaces and the one on the hydrated ( $1\bar{1}02$ ) surface looks very similar, the same consideration regarding the underlying cut  $O_6$ -ring can be made. Thus, these surfaces might well be used as well to potentially grow ice-**I<sub>h</sub>**, ice-**I<sub>c</sub>**, ice-**II**, ice-**IV** or ice-**VII** on them, although, they start from a more distorted foundation than the structure motifs found on the (0001) surfaces. Other than that, the found  $O_8$ -rings agree best with the second  $O_8$ -ring in ice-**IV**, seen once more in figure 4.108(d).

Since the structure motifs on the triply and fourfold fluorinated ( $1\bar{1}02$ ) surfaces “only” result in chains and even smaller structure motifs, they will be solely shown in [figure A.43](#) and [figure A.44](#).

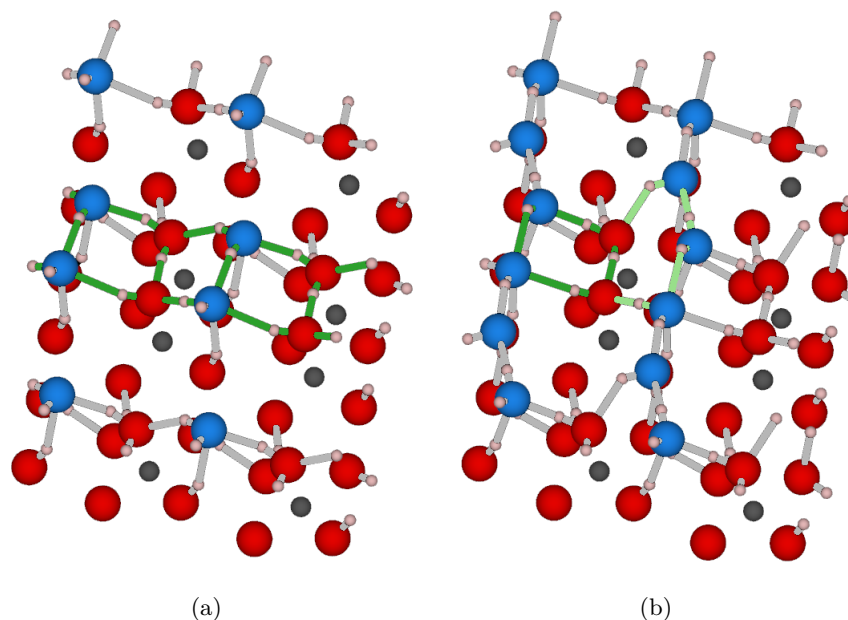


**Figure 4.110:** Depictions of structure motifs of adsorbed water on a hydrated ( $11\bar{2}3$ ) surface; (a) two water molecules per UC and (b) three water molecules per UC - gray = aluminium, red = oxygen, white = hydrogen, light blue = water oxygen, green = highlighted structural motif, and light gray = de-emphasised bonds (VASP-DFT, PBE/PAW, 600.0 eV energy cut-off, D3-BJ).

Moving on to the ( $11\bar{2}3$ ) surface, the first interesting structure motif is provided by the adsorption of two water molecules on the hydrated version of it, seen in [figure 4.110\(a\)](#). It can be seen that the two adsorbed water molecules position themselves between two terminal ligands each forming two interconnected zigzag chains and, by association, forming a  $\beta$ -sheet-like shaped structure made of  $O_4$ -rings.  $O_4$ -rings are only found in ice-**V**, but there they are available in small substructures only (see again [figure 4.94](#)). Besides, the  $O_4$ -rings in those smaller substructures of ice-**V** are also connected to each other to resemble an opened book, so “just” the succession of them is missing. Nonetheless, the agreement of those substructures, the  $\beta$ -sheet and the smaller substructure of ice-**V**, are too different to assume that ice-**V** might be grown

on the hydrated  $(11\bar{2}3)$  surface.

Interestingly, if one considers the chain of small rings as the structure motif, neglecting the size of them, one structure motif of a different ice phases comes into mind as well, the consecutive chains of ice-**III**'s envelop-shaped  $O_5$ -rings (see again [figure 4.90](#)). In both cases the chains are not connected to each other, only via secondary and shifted slices above and beneath them. Of course, there is the folded nature of the water's structure motif on the surface in contrast to the quite planar progression of the ring chains in ice-**III**, but the similarity is still surprisingly good.

Adding the third water molecules to the hydrated  $(11\bar{2}3)$  surface, the picture becomes more clear. Looking at [figure 4.110\(b\)](#) immediately reveals the formation of a  $O_5$ -ring within the  $\beta$ -sheets, which is alternating with a  $O_4$ -ring in the chain's progression. Although ice-**V** also provides  $O_5$ -rings, even within the smaller substructures as well, this "updated" structure motif on the surface seems to favour the substructure of ice-**III**. A even better agreement with the ice-**III**'s chains of  $O_5$ -rings might be achieved by shifting the water molecule located in the left water chain at the second position (from below) slightly to the right, while intercalating it in the lower hydrogen bond highlighted in green. This would break the water chain, which would otherwise connect the small-ring chains, and would result in the needed alternating orientation of the  $O_5$ -rings. Again, quite a few adjustments are needed for the observed structure motif to really resemble the most similar structure motif in ice-**III**. But with the addition of more water molecules, this might be achieved, and the hydrated  $(11\bar{2}3)$  surface might actually be used to grow ice-**III** on it.

The next structure motif on the  $(11\bar{2}3)$  surface to consider is the one resulting from adsorbing three water molecules on the singly fluorinated modification of it. It shows a quite broad but cornered  $O_{10}F_2$ -ring with two peaking water molecules, seen in [figure 4.111\(a\)](#). Since this structure motif is quite large and flat with only two exceptions, finding a reasonable match of the obtained structure motifs in ice is quite challenging. The most similar but still different motif is provided by first  $O_{12}$ -ring

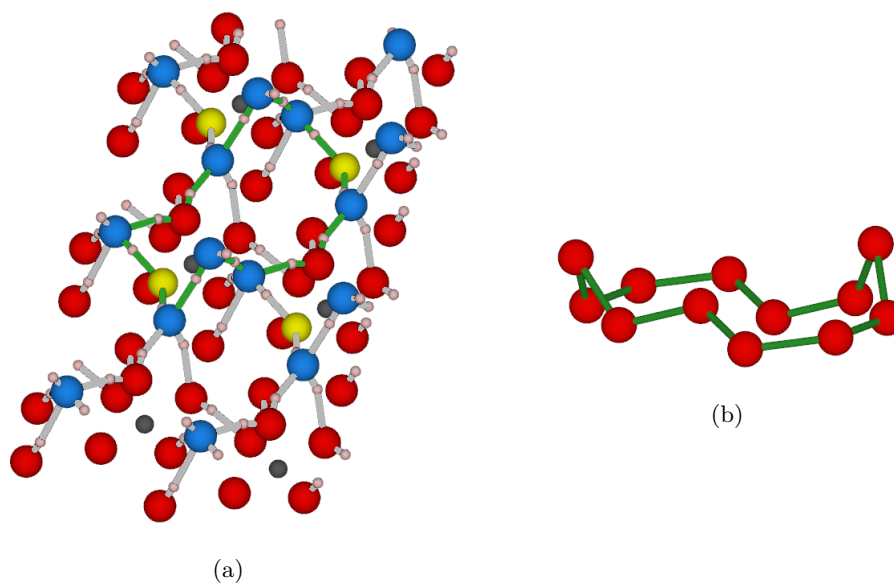


**Figure 4.111:** Depictions of structure motifs of adsorbed water on a singly fluorinated ( $11\bar{2}3$ ) surface and the best matching structure motif in ice; (a) three water molecules per UC and (b) ice-**V** mimicry - gray = aluminium, red = oxygen, yellow = fluorine, white = hydrogen, light blue = water oxygen, green/light green = highlighted structural motif, and light gray = de-emphasised bonds (VASP-DFT, PBE/PAW, 600.0 eV energy cut-off, D3-BJ).

of ice-**V**, seen in figure 4.111(b). By rotating the ice's motif by  $90^\circ$  clockwise, the resemblance can be seen a bit easier. Unfortunately, the adsorbed water's structure motif can not mimic the "S" character of the ice-**V**'s one and, by association, the likelihood to grow ice-**V** on this surfaces shrinks further. Nonetheless, the found similarity makes the found structure motif of adsorbed water on this surface modification more reasonable.

Going on the next structure motif to look at, two water molecules on the doubly fluorinated ( $11\bar{2}3$ ) surface provide a net-like shaped structure made by  $O_8F_2$ -rings, which can be seen in figure 4.112(a). Those rings look like opened double-folded pieces of paper. Interestingly, this structure motif resembles quite well two structure motifs found in two different ice phases. The highest agreement is reached with the fifth  $O_{10}$ -ring of ice-**V**, which can be seen in figure 4.112(b) while the other one is the twelfth  $O_{10}$ -ring of ice-**IV**. Although the adsorbed water's structure motif needs

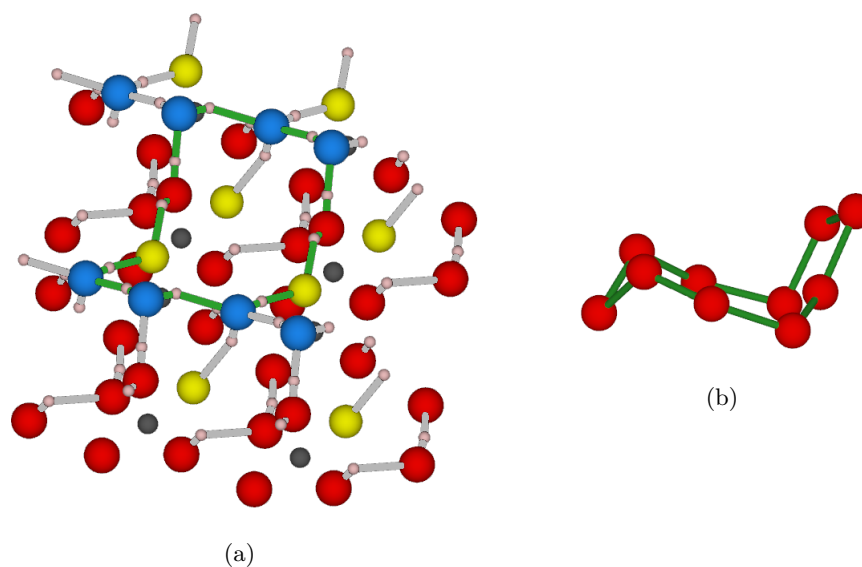


**Figure 4.112:** Depictions of structure motifs of adsorbed water on a doubly fluorinated ( $11\bar{2}3$ ) surface and the best matching structure motif in ice; (a) two water molecules per UC and (b) ice-V mimicry - gray = aluminium, red = oxygen, yellow = fluorine, white = hydrogen, light blue = water oxygen, green = highlighted structural motif, and light gray = de-emphasised bonds (VASP-DFT, PBE/PAW, 600.0 eV energy cut-off, D3-BJ).

some adjustments in order to really be similar with one of the two, its actual shape becomes more reasonable with those two structure motifs of ice. Nonetheless, none of the two ice phases is likely to be grown on the doubly fluorinated ( $11\bar{2}3$ ) surface due to the repetition of those rings on surface, which is not observable in the structures of ice-IV and ice-V.

By adding a third water molecule on the doubly fluorinated ( $11\bar{2}3$ ) surface, the adsorbed water's structure motif changes from a  $O_8F_2$ -ring to net-like slice of  $O_{10}F_2$ -rings (see figure 4.113(a)). With the exception of one prong, the new rings look like crowns, at least regarding the prongs. Their ring shapes look more like stylised bones than circles. Due to this, finding similar structure motifs in the different ice phases could not provide a reasonable mimicry. The most similar ones, regarding the prongs, were both found in ice-XVI: the first and the third  $O_{12}$ -ring (see the latter in figure 4.113(b)). Because of the quite bad similarity of the adsorbed water's structure motif with one of the ice phases' ones and the unlikeliness to grow the low density



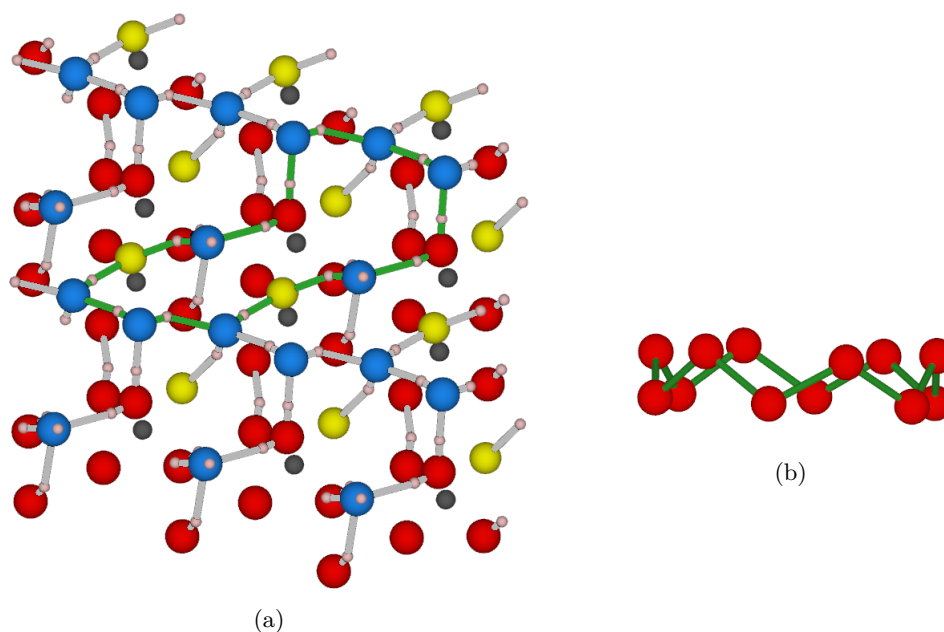


**Figure 4.113:** Depictions of structure motifs of adsorbed water on a doubly fluorinated ( $11\bar{2}3$ ) surface and the best matching structure motif in ice; (a) three water molecules per UC and (b) ice-**XVI** mimicry - gray = aluminium, red = oxygen, yellow = fluorine, white = hydrogen, light blue = water oxygen, green = highlighted structural motif, and light gray = de-emphasised bonds (VASP-DFT, PBE/PAW, 600.0 eV energy cut-off, D3-BJ).

ice-**XVI** on this surface, the doubly fluorinated ( $11\bar{2}3$ ) surface seems to be unable to grow any specific ice phase on it. Maybe this changes with the addition of more water molecules, but it seems to be quite unlikely.

Increasing the amount of fluoride on the ( $11\bar{2}3$ ) surface, the next adsorbed water's structure motif to look at is found on the triply fluorinated modification with two added water molecules. As it can be seen in figure 4.114(a), a zigzag chain along  $a$  consisting of a water molecule and the terminal water ligand is formed (green). This water ligand is also extends the hydrogen bond network further using the terminal fluoride ion and the other adsorbing water molecule. The position and orientation of the adsorbing water molecules nearly enables the formation of anion hexagons (light green). While the possible  $O_4F_2$ -ring only needs one more hydrogen bond, the  $O_5F$ -ring beneath of it needs two additional hydrogen bonds (one due to periodicity). Because the orientations of the free hydrogen atoms, which are needed for those

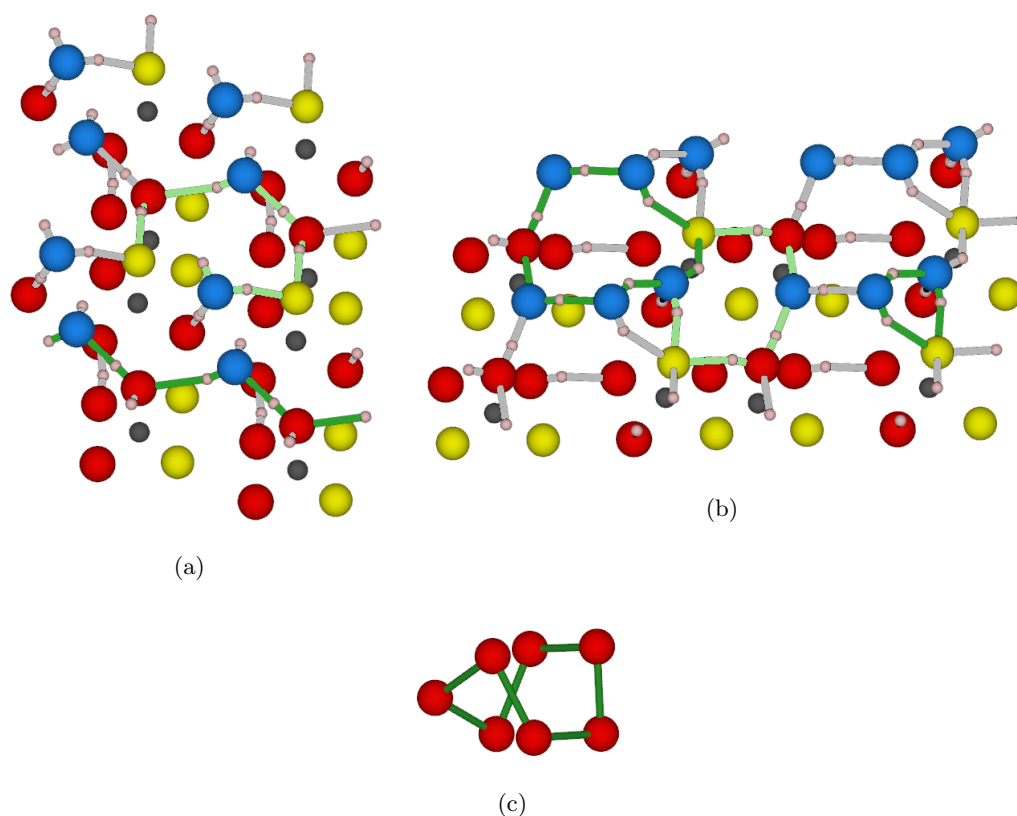


**Figure 4.114:** Depictions of structure motifs of adsorbed water on a triply fluorinated ( $11\bar{2}3$ ) surface and the best matching structure motif in ice; (a) two water molecules per UC, (b) three water molecules per UC, and (c) ice-**XII** mimicry for (b) - gray = aluminium, red = oxygen, yellow = fluorine, white = hydrogen, light blue = water oxygen, green/light green = highlighted structural motif, and light gray = de-emphasised bonds (VASP-DFT, PBE/PAW, 600.0 eV energy cut-off, D3-BJ).

additional hydrogen bonds, are quite promising, this triply fluorinated ( $11\bar{2}3$ ) surface might be able to provide a honeycomb-like shaped structure with the adsorbed water molecules. With this possible honeycomb-like shaped structure, it might be able to grow one of the same ice phases mentioned beforehand for the (0001) surface modifications: ice-**I<sub>h</sub>**, ice-**I<sub>c</sub>**, ice-**II**, ice-**IV**, and ice-**VII**. Nonetheless, the needed adjustments of the actual adsorbed water's structure motif are more substantial than for the (0001) surfaces and, by association, may need much more adsorbed water molecules to do so.

Unfortunately, adding the third water molecule does not help to form the desired honeycomb-like shaped structure, instead, it becomes somewhat worse with the formation of three differently sized rings (see [figure 4.114\(b\)](#)). Indeed, one hexagon (light green) formed, but along with it, also a triangle (right hand side green) and a heptagon (left hand side green) formed. The intercalation of the third water molecule between the two previously adsorbed ones is the reason for that quite unwanted formation of new ring sizes. Maybe further added water molecules can compensate for that later, but for now, only these three rings are present. Since the formed  $O_4F_2$ -ring provides a bathtub-like shaped structure and the triangular shape is also quite clear, the shape of the hexagon need to be clarified and be compared with ice phase structure motifs. The  $O_6F$ -ring shows a quite shallow bathtub-like shaped structure as well, which also provides a quite circular topview. Considering its best matching ice phase counterpart, the second  $O_7$ -ring of ice-**XII** provides the agreement (see [figure 4.114\(c\)](#)), although, it is much steeper than the adsorbed water's structure motif. Nonetheless, growing ice-**XII** on this triply fluorinated  $(11\bar{2}3)$  surface is very unlikely, only a step by step improvement of the possible honeycomb-like shaped structure on the surface with more water molecules might result in the possibility to grow ice-**I<sub>h</sub>**, ice-**I<sub>c</sub>**, ice-**II**, ice-**IV**, or ice-**VII** on it.

Adding another fluoride ion to the surface via substitution of an hydroxide groups, the now fourfold fluorinated  $(11\bar{2}3)$  surface is the next one to look for further adsorbing water's structure motifs. The first interesting structure motif is provided by adsorbing two water molecules on this surface (see [figure 4.115\(a\)](#)). It shows a net-like structure of  $O_8F_2$ -rings, which result from the crossing of two different hydrogen bond chains on the surface. Once more, the greater rings show the shape of an opened double-folded piece of paper, as it was seen already for the adsorption of two water molecules on the doubly fluorinated  $(11\bar{2}3)$  surface. Since those  $O_8F_2$ -rings look quite similar, the fifth  $O_{10}$ -ring of ice-**V** matches the adsorbing water's structure motif quite well. Nonetheless, the growing of ice-**V** on this surface seems quite unlikely due the net-like

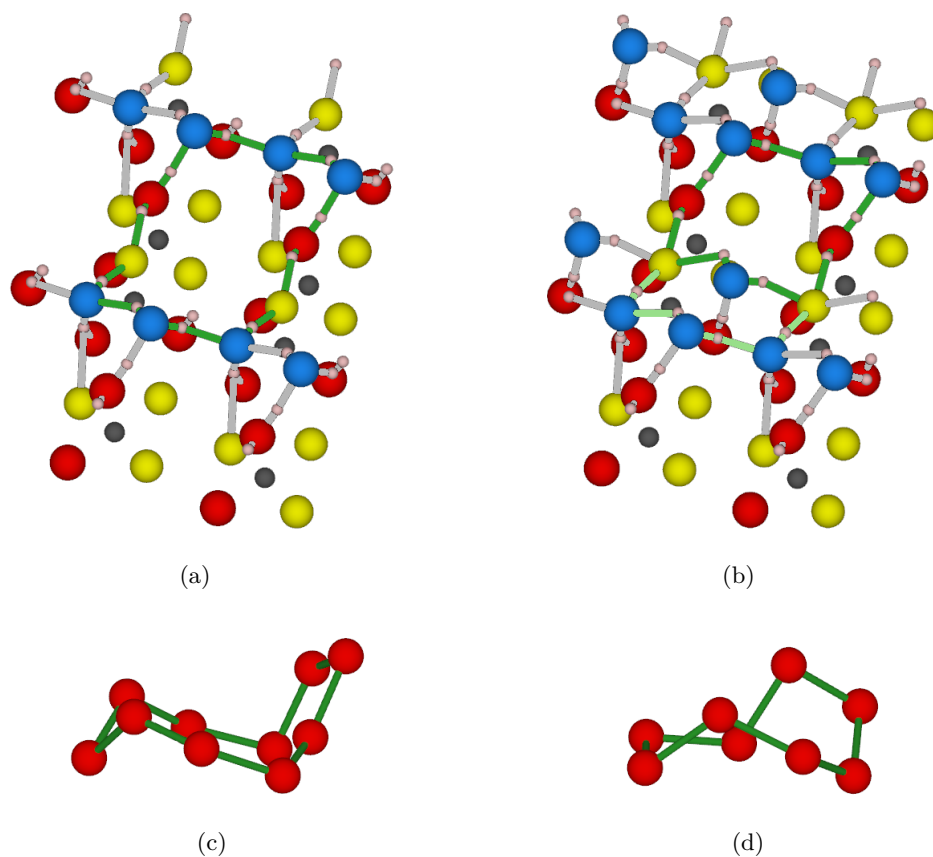


**Figure 4.115:** Depictions of structure motifs of adsorbed water on a fourfold fluorinated ( $11\bar{2}3$ ) surface and the best matching structure motifs in ice; (a) two water molecules per UC, (b) three water molecules per UC, (c) ice-V mimicry for (a), and (d) ice-IV mimicry for (b) - gray = aluminium, red = oxygen, yellow = fluorine, white = hydrogen, light blue = water oxygen, green/light green = highlighted structural motif, and light gray = de-emphasised bonds (VASP-DFT, PBE/PAW, 600.0 eV energy cut-off, D3-BJ).

structure providing these  $O_8F_2$ -rings, which is not present in this ice phase.

Adsorbing the third water molecules on this surface, the  $O_8F_2$ -rings are split into two new rings, which can be seen in [figure 4.115\(b\)](#). While the light green one shows a bathtub-like shaped  $O_4F_2$ -ring, the green one shows again the shape of an opened double-folded piece of paper, but this time, with a  $O_6F_2$ -ring. The best matching ice phase structure motif is provided by the second  $O_8$ -ring of ice-IV, although, ice-XII also provides a very reasonable match. To notice the similarity of both structure motifs shown in [figure 4.115](#), the ice phase representative need to be rotated clockwise by

90° around the “z”-direction and then flipped around the “x”-direction. Nonetheless, the growing of any specific ice phase seems to be quite unlikely due to the net-like structure involving the already adsorbed water molecules. The only possibility to make it happen is again the split of the  $O_6F_2$ -rings with the adsorption of the fourth water molecule between the two water ligands. This would result in a net-like structure of only hexagons, which again would resemble the honeycomb-like shaped sheets of water molecules on the (0001) surface. Therefore, with this surface structure, the fourfold fluorinated ( $11\bar{2}3$ ) surface might actually be able to grow ice-**I<sub>h</sub>**, ice-**I<sub>c</sub>**, ice-**II**, ice-**IV**, or ice-**VII** on it.

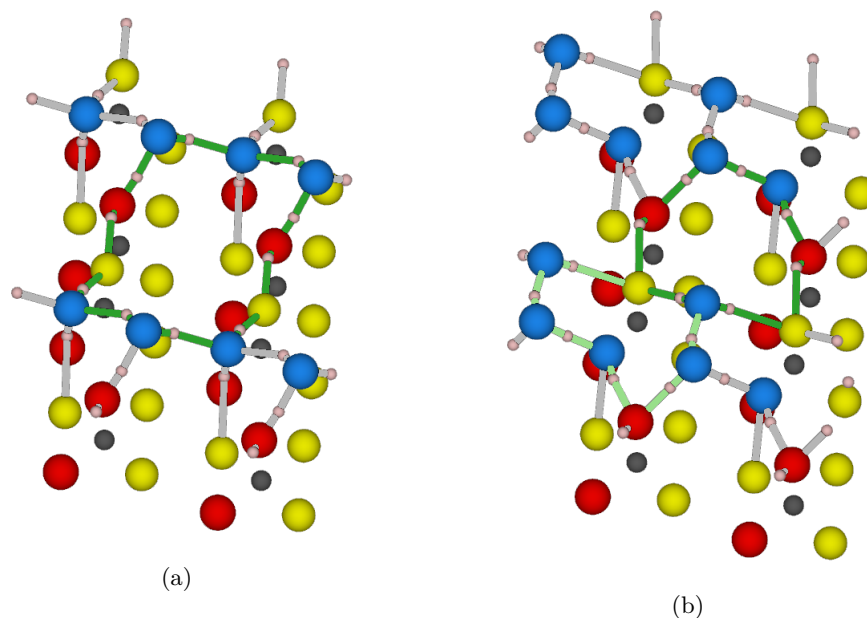


**Figure 4.116:** Depictions of structure motifs of adsorbed water on a fivefold fluorinated ( $11\bar{2}3$ ) surface; (a) two water molecules per UC and (b) three water molecules per UC - gray = aluminium, red = oxygen, yellow = fluorine, white = hydrogen, light blue = water oxygen, green/light green = highlighted structural motif, and light gray = de-emphasised bonds (VASP-DFT, PBE/PAW, 600.0 eV energy cut-off, D3-BJ).

Going on to the fivefold fluorinated ( $11\bar{2}3$ ) surface, the adsorption of two water molecules led to nearly exactly the same structure motif as provided on the fourfold fluorinated modification (see figure 4.116(a)). Thus, the same considerations and

matching ice structures can be found here as well.

The difference of these two  $(11\bar{2}3)$  surface modifications can be seen with the addition of the third water molecule. Due to the now missing hydroxide group within the surface's valley, the third water molecule is less fixed in its lateral positioning and, by association, adsorbs more closely to one of the already adsorbed water molecules. The resulting adjustment of them and the breaking of the  $O_8F_2$ -rings results in two differently shaped heptagons, which can be seen in [figure 4.116\(b\)](#). While the green one resembles a shallow, quite "regular" heptagon with the composition  $O_5F_2$ , the light green one shows again a shallow structure, but this time, the  $O_6F$ -ring provides a "church"-like topview. Unfortunately, both heptagons can not be matched with any of the structure motifs provided by the different ice phases without making quite drastic adjustments to their structures. Thus, the likelihood to grow a specific ice phase on this fivefold fluorinated  $(11\bar{2}3)$  surface is very small, at least by considering such small amounts of water on it.

Increasing the fluorination degree of the surface further, the adsorption of water on the sixfold fluorinated  $(11\bar{2}3)$  surface results in the structure motifs shown in [figure 4.117](#). The first one to look at is provided with the adsorption of two water molecules (see [figure 4.117\(a\)](#)), where two mixed zigzag chains are connected with each other. This results in the formation of a  $\beta$ -sheet-like structure motif (light green), which again consists of bathtub-like shaped  $O_4F_2$ -rings (green). Considering the former one, the best matching ice phase structure motif would be the chains of envelop-like shaped  $O_5$ -rings of ice-**III**. Unfortunately, the lack of hydrogen bonds due to the terminal fluoride ions prevents a possible adjustment of those  $O_4F_2$ -rings with the addition of more water molecules and, by association, prevents the growing of ice-**III** on this surface as well.

Adding the third water molecules to this surface modification, re-orientation of the previously adsorbed water molecules together with the new one results in a very distorted net-like structure, which features  $O_8F_4$ -rings (see [figure 4.117\(b\)](#)). Those large

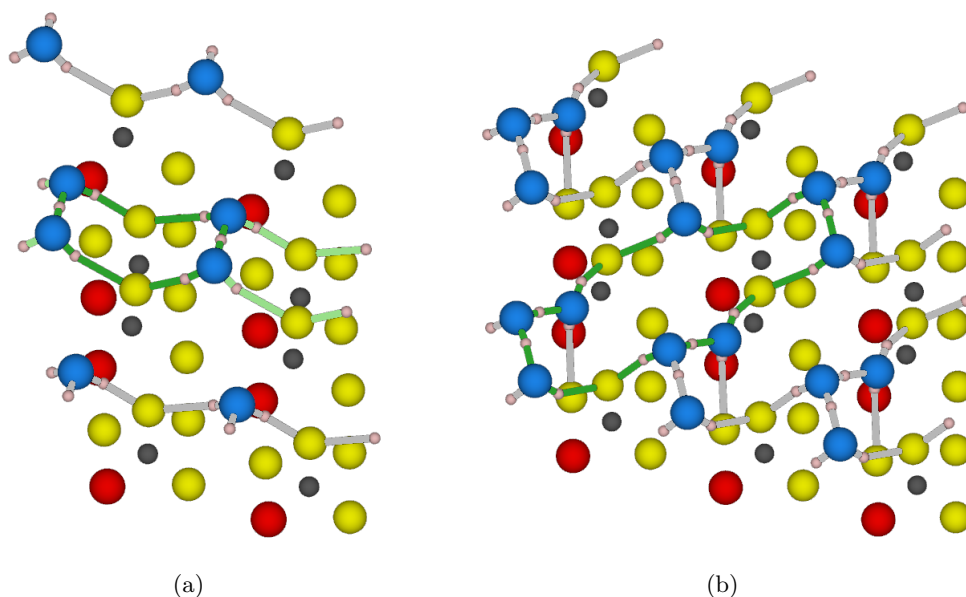


**Figure 4.117:** Depictions of structure motifs of adsorbed water on a sixfold fluorinated ( $11\bar{2}3$ ) surface; (a) two water molecules per UC and (b) three water molecules per UC - gray = aluminium, red = oxygen, yellow = fluorine, white = hydrogen, light blue = water oxygen, green/light green = highlighted structural motif, and light gray = de-emphasised bonds (VASP-DFT, PBE/PAW, 600.0 eV energy cut-off, D3-BJ).

rings are sheared drastically and, by association, well matching ice phase structure can not be found. So far, it seems to be very unlikely that this surface might be able to grow a specific ice phase on it.

Since the sevenfold fluorinated ( $11\bar{2}3$ ) surface only provides different zigzag chains as structure motifs for the different amounts of adsorbing water molecules, they will be solely shown in [figure A.52](#).

To sum things up so far, the comparison of adsorbing water's structure motifs on differently modified and cut surfaces of  $\alpha\text{-Al}_2\text{O}_3$  with the structure motifs found in different ice phases showed was constrained by the computational approach. Due to the comparably small UCs, only slice of water or slice-like structures incorporating terminal ligands were observable. Thus, the focus was directed to sliced ice phases, unlike ice-VI, ice-XII, ice-XVI, and ice-XVII. On all surfaces one structure motif tends to be preferred, the formation of honeycomb-like shaped structure motifs. While

the modified (0001) surfaces exhibit the best possibility to form them, the other two surface cuts provide obstructions to do due to their terminal and ligands and their rough surface structure. They prevented the adsorbing water molecules to position themselves at the needed locations and, by association, hindered the formation of the honeycomb-like shaped structure motifs. Due to this, the ice phases ice-**I<sub>h</sub>**, ice-**I<sub>c</sub>**, ice-**II**, ice-**IV**, and ice-**VII** are the most likely ones to be grown on the different surfaces. The actual phase depends on the further adsorption of additional water molecules and how they can influence the interaction of first water slice with the surface as well as overcome induced structural distortions of the considered ice phase. Despite the imposed constraints for the investigation of adsorbing water's structure motifs, the found larger rings were compared with rings found in the different ice phases, although, in almost every case the associated net-like structure is not observable in any ice phase. This provided very good to reasonable agreements with found rings in ice-**IV**, ice-**V**, ice-**XII**, and ice-**XVI**, which emphasises the reasonableness of those adsorbing water's structure motifs.



## Chapter 5

### Summary

The formation and dissolution of earth abundant materials/minerals always involves water and starts or end with molecular compounds in solution. By growing these molecular compounds and reaching the nanometer scale, so-called nanocrystals are formed. Investigating the molecular scale, I previously studied small aluminium clusters [216], which were based on experimental findings [215]. Thus, this work focused on the larger particles with a crystalline core. Attributed to their size, these nanostructures can be modelled with a bulk-like core and a surface-like shell for quantum chemical calculations. The interactions of such compounds with water were modelled by adsorbing water molecules on the selected surfaces and their modifications. Due to its huge abundance in the earth crust (8.10 % [219]) and its high range of possible applications, aluminium oxides, oxohydroxides, and hydroxides were chosen as compounds of choice for this study. Since in nature and most applications minerals are not found or used in their purest form but with impurities or dopants, this work also incorporated such defects. Because of its known influence on interactions with water, its abundance in the earth crust (0.05 % [219]), and its controllable incorporation via the fluorolytic sol-gel synthesis, fluoride ions were the dopants of choice within this work. Using the mentioned model enabled the investigation of different aspects for various applications.

In the first part, the study of possible aluminium hydroxides and oxohydroxides, namely gibbsite and bayerite as representatives of the former and diaspore and boehmite as representatives for the latter, was conducted. With this part the fluoride doping within the bulk was examined. Those crystal structures were modified with various amounts of fluoride ions via substitution of hydroxide groups in order to investigate the influence of this well known modifier of water interactions. At first, the applied computational approaches were verified by comparing results for the unfluorinated structures with experimentally obtained data (see section 4.1 [Aluminium \(oxo\)hydroxides](#)). This study revealed the importance of including dispersion corrections in order to account for the very important hydrogen bonds in these crystalline systems. During this examination of aluminium hydroxides and oxohydroxides, the fluoride ions' impact on the stability and the possible structural adjustment was analysed (see subsection 4.1.1 [Fluorinated Aluminium \(oxo\)hydroxide Structures](#)). To quantify the stability of the differently fluorinated crystal systems, the reaction energy for the corresponding fluorination reaction was calculated. This immediately showed that the sliced aluminium hydroxides exclusively provided thermodynamically favoured fluorination reaction while the two aluminium oxohydroxides showed solely thermodynamically unfavoured fluorination reactions. Thus, the former seem to be much more suitable as a reagent to remove fluoride ions from, for example, waste water. Additionally, for the quantification of the fluoride ions' impact on the structure of the systems, different parameters were proposed (see chapter 3 [Structure-Stability-Relation Parameters](#)) to cover different aspects of possible influences. This included short range parameters like the alteration of the cationic [CS](#) and the shifting of charge centres, for example, as well as long range parameters, like the anion distribution over the system and the remaining crystal symmetry after modification, were taken into account. Furthermore, structure specific parameters, which focus on the sliced structure of those aluminium hydroxides and oxohydroxides, for example, were also taken into account. The values of all different parameters were combined to

---

yield a single value describing the structure reasonably good, the structure parameter. By matching the change in stability with the change in the structural parameter for each of the 181 investigated structures via a careful and chemically intuitive weighting procedure, the strengths of the single parameters' influences were obtained. It turned out to be very important to treat the structure specific parameters individually for each crystalline system, because each of those systems demanded the parameters with different strengths. The confirmed weightings showed that the distortion of the cationic **CS**, the remaining symmetry of the crystalline system after modification and the stoichiometry differences of different slices are very important for the stability of the system. While the other parameters provide moderate, weak and negligible influences on the stability. Afterwards, the obtained weightings were tested by using them directly, without any adjustments for the calculation of the structure parameter for six structures of another crystalline aluminium hydroxide system, doyleite. For this system a much higher fluorination degree was chosen, to test the obtained weightings outside their fitting range. Comparing the change of the stability with the change in the structure parameter, a very good agreement was found. With those findings the foundation of the educational guess for aluminium oxide nanostructure cores becomes more substantiated and might enable more reasonable starting points for future investigations. For a better comparison of these theoretical results with experimental ones,  $^{27}\text{Al}$  and  $^{19}\text{F}$  NMR shifts were calculated for 63 selected structures (see subsection 4.1.2 **Fluoride Depending NMR Shifts in Aluminium (oxo)hydroxides**). Based on the obtained results, different trends were observed depending on the fluorination degree of the aluminium centre's **CS** and its distortion. They were explained in detail using the electron negativity, the effects of the distortion of the cationic **CS** itself and orbital influences according to Copéret *et al.*'s findings [213]. A comparison with the trends found by Kemnitz and co-workers [53, 54, 210, 211] showed a good agreement while differences were mainly attributed to structural differences of the sliced structures of the investigated aluminium hydroxides and oxohydroxides compared to the

experimentally studied non-sliced structures.

The second part of this work focused on the shell of such nanostructures by investigating different surface cuts of  $\alpha$ -aluminium oxide, corundum. In case of corundum, the fluorination of an already existing crystal would be thermodynamically unfavourable within the bulk structure but more likely on the surface. Thus, it not only served as a model for the nanostructure's shell, but also as the possibility to study possible aspects of the corrosion of this compound. As for the aluminium hydroxides and oxohydroxides, modelling the core of the nanostructures, the influence of fluoride ions on the stability and structural adjustments of the studied corundum surfaces was investigated. At first the detailed examination of different terminations per surface cut (see section 4.2 [\\(\alpha\\)-Aluminium Oxide Surfaces](#)) led to a well agreeing Wulff plot with previous studies. Based on this Wulff plot, the three most abundant and most stable surfaces were chosen for further investigations. To begin with, the three surface cuts were hydrated (see subsection 4.2.1 [Hydration of \\(\alpha\\)-Aluminium Oxide Surfaces](#)) to not only provide substitutable hydroxide groups but also to serve as a reference to previous results of, for example, Mason *et al.* [104]. By exchanging all formed hydroxide groups progressively with fluoride ions (see subsection 4.2.2 [Fluorination of Hydrated \\(\alpha\\)-Aluminium Oxide Surfaces](#)) and calculating the reaction energy with hydrogen fluoride at various temperatures, it was seen that the fluorination degree might stop prematurely if hydrogen fluoride is added stepwise. Furthermore, it was seen by  $\Gamma$  phonon frequency analyses of the OH bonds that an increasing amount of fluoride ions on the surface increases the Brønsted acidity of the remaining hydroxide groups as well. Regarding the structural changes during the fluorination, the repulsive interaction of the fluoride ions among themselves resulted for the fully fluorinated ( $1\bar{1}02$ ) surface in a reconstruction and thus, in the formation of two under-coordinated aluminium ions per UC. For the other surfaces and fluorination degrees, only minor relaxations took place during the  $\Gamma$  phonon frequency checked structure optimisation.  $^{27}\text{Al}$  and  $^{19}\text{F}$  NMR shifts were calculated, for all considered surface cuts and fluori-

---

nation degrees (see subsection 4.2.3 [NMR Shifts of  \$\alpha\$ -Aluminium Oxide Surfaces](#)), to allow for mutual comparison of theoretical and experimental results. The same trends as found for the bulk materials were obtained and could be explained with the same effects as well.

In order to study the nanostructure's interaction with water and the possible corrosion of corundum therewith the adsorption of water on the previously studied modified surface cuts of corundum was investigated. To get a full picture of the adsorption, potential energy surfaces on the modified surfaces were determined by adding water molecules (see section 4.3 [Water Adsorption on Modified  \$\alpha\$ -Aluminium Oxide Surfaces](#)) and increasing their amount up to three per UC. Since the unit cells of the (0001) and the ( $1\bar{1}02$ ) surface cuts are comparably small, the influence of the firstly adsorbed water molecule was studied by adding a second water molecule on a  $2 \times 2 \times 1$  supercell bearing only one water molecule. Due to this, the coverage of 1 to 3 molecules per UC was lowered to 0.5 per UC via adsorption of the second water molecule on the SC. Unsurprisingly, the water adsorption heavily depended on the formation of hydrogen bonds to the surface's hydroxide groups or to previously adsorbed water molecules, respectively. From the studies of the supercell surfaces, it was shown that the first water's sphere of influence is about  $20 \text{ \AA}^2$  and can be extended by a hydrogen bond network of the modified surfaces. During the adsorption of water on the variously modified different surfaces, it was seen that on some occasions water's oxygen atom was able to be part of five hydrogen bonds. The structural motif of a fivefold coordinated oxygen atom/ion was indeed already known to be present, for example, in clusters [215] but continues to be quite rare. Furthermore, it was shown that the increasing amount of fluoride ions on the surface increased the Brønsted acidity of the remaining hydroxide groups steadily, resulting in the formation of hydronium ions on certain occasions. This led to the assumption that comparably high amounts of fluoride ions in the corundum surfaces lead to the possibility of being a good heterogeneous acid-catalyst. Regarding the adsorption energies themselves, it was seen that

they depend on a complex interplay of different aspects, like steric hindrance, possibilities to form hydrogen bonds, hydrogen bond accepting and donating capabilities which are linked to the corresponding ion's CN, and the prior breaking of existing hydrogen bonds to adsorb. Thus, the average adsorption energies vary quite drastically between  $-0.18$  eV and  $-0.89$  eV while the minimum adsorption energies range from  $-0.25$  eV to  $-1.18$  eV, where the lowest values were found for the formation of an exceptional hydrogen bond network (six membered rings) or for the formation of hydronium ions. Additionally, the investigation of the first water molecule's adsorption on the six- and sevenfold fluorinated ( $11\bar{2}3$ ) surfaces (see subsection 4.3.3 [The \( \$11\bar{2}3\$ \) Surface](#)) showed very low average adsorption energies. This could be attributed to the strong hydrogen bonds formed with terminal fluoride ions and to the lack of hydrogen bonds that have to be weakened or broken in order form new hydrogen bonds with the adsorbing water molecule. In general, it was seen that doubly bound fluoride ions at the surface interact weaker with approaching water molecules and, consequently, those fluoride ions work as a protective coat against water. Although, terminal fluoride ions increase the interaction with water molecules due to the stronger hydrogen bonds to them, the surface's structure underwent less relaxation and seemed to be less influenced by the adsorbing water molecules. Nonetheless, the substitution of surface hydroxide groups with fluoride ions may cause the reconstruction of the surface, as it was seen for the fourfold fluorinated ( $1\bar{1}02$ ) surface (see subsection 4.3.2 [The \( \$1\bar{1}02\$ \) Surface](#)), and by association, can introduce new favourable adsorption sites for water molecules. Therefore, using fluoride as a protective coating seems to be reasonable but can introduce new challenges. Regarding the interactions of the nanostructure's shell with the water molecules, the weaker interplay for fluorinated shells might destabilise the nanostructure in a watery environment and, by association, favours the assembly of a macroscopic structure from them. On the other hand, the stronger interaction with a hydrated shell more likely stabilises the nanostructure in water, so the dissolution of a macroscopic structure might be easier.

---

Since the adsorption of water molecules on the variously fluorinated different surface cuts of  $\alpha$ -aluminium oxide, corundum, yielded many and quite different structure motifs, like the previously mentioned fivefold coordinated water molecule, the fourth part of this work focused on the possibility to grow a specific ice phase using a certain surface cut with a certain fluorination degree. All the 18 different ice phases had to be studied extensively. Due to only slight differences between certain ice phases, namely the ordered or unordered position of hydrogen atoms, only eleven different ice phases remained for the detailed study. They were examined according to their larger structure motifs, such as smaller substructures, helices, chains of ring, and slices as well as according to their smaller structure motifs like rings. While larger motifs were found by a careful survey of their structure by optical inspection, smaller ones were detected using a computational approach (see subsection 2.2.5 [Analysis of Ice Structures](#)). During this comparison a substantial amount of surfaces seemed to favour the formation of honeycomb-like shaped structure, either provided by slices of adsorbed water or by slice-like structures incorporating terminal surface ligands. Those honeycomb-like shaped structures can result in the growing of five different ice phases: ice-**I<sub>h</sub>**, ice-**I<sub>c</sub>**, ice-**II**, ice-**IV**, and ice-**VII**, depending on how additionally adsorbing water molecules influence the first “water-slice”. Unfortunately, the computational approach for the adsorption of water favours the formation of such slices due to the comparably small UCs and the resulting frequent repetition of them. Thus, other structure motifs, for example, found in ice-**III**, ice-**V**, or ice-**VI** are systematically more unlikely to be found. Nonetheless, this investigation might enable growing ice on those surfaces and confirms the natural abundance of ice-**I<sub>h</sub>** and ice-**I<sub>c</sub>**.

By studying the influence of fluoride ions as dopants in aluminium hydroxides and oxohydroxides and their effect on the systems’ interaction with water, this doctoral thesis investigated the complex process of assembly and dissolution of macroscopic structures by and in nanostructures, respectively. Thus, its results will help to build suitable nanostructure starting structures by improving the educated guess to further

elaborate those complex processes. In addition, the calculation of OH stretch frequencies and NMR shifts of  $^{27}\text{Al}$  and  $^{19}\text{F}$  facilitate experimentalists and other theorists to mutually improve and verify their results regarding these and related compounds.

To progress further in the investigation of formation and dissolution of macroscopic structures like corundum via nanostructures, especially the interaction of water with those materials needs to be studied more and with additional methods. Although three water molecules per UC seems quite dense for quantum chemical calculations, it is way too little water to simulate natural behaviours and processes. Thus, MD is needed to model not only convincing amounts of water which are more close to reality but also its kinetics on the surfaces. Those studies might also reveal if fluoride ions really can operate as protective coatings against dissolution in water, which was not absolutely clarified yet. Since water is very often used in MD calculations, there should be no need to use *ab-initio* MD since there are already sophisticated force fields available. This in turn enables to use of a high amount of water molecules and an investigation over longer time-periods within the MD calculations. Using single “pictures” from these simulations for NMR and frequency calculations, as done in this work, can further improve the cooperation between theory and experiment to understand the processes during formation and dissolution of crystalline systems. Furthermore, using a variety of “pictures” and the corresponding energies might also improve the weightings used in the bulk section of this work, which can then lead to an even more improved educational guess for nanostructures.



## Bibliography

- (1) Wedepohl, K. H. *Geochim. Cosmochim. Ac.* **1995**, *59*, 1217–1232, DOI: [10.1016/0016-7037\(95\)00038-2](https://doi.org/10.1016/0016-7037(95)00038-2) (cit. on p. 1).
- (2) Wefers, K.; Misra, C., *Oxides and hydroxides of aluminum*; Alcoa Laboratories Pittsburgh, PA: **1987** (cit. on p. 1).
- (3) Fomenko, A. N.; Korovin, M. S., **2017**, DOI: [10.1063/1.5001598](https://doi.org/10.1063/1.5001598) (cit. on p. 1).
- (4) Tsukanov, A. A.; Psakhie, S. G., **2017**, DOI: [10.1063/1.5001655](https://doi.org/10.1063/1.5001655) (cit. on p. 1).
- (5) Korovin, M. S.; Fomenko, A. N., **2017**, DOI: [10.1063/1.5001615](https://doi.org/10.1063/1.5001615) (cit. on p. 1).
- (6) Fomenko, A. N.; Korovin, M. S.; Kazantsev, S. O., **2017**, DOI: [10.1063/1.5013734](https://doi.org/10.1063/1.5013734) (cit. on p. 1).
- (7) Schatz, U.; Dotsch, L.; Batton, A.; Decker, J.; Rave, O.; Schuller, H. Procedure for manufacturing of fireproof ceramic molded parts., US Patent 5,124,099, 1992 (cit. on p. 1).
- (8) Baranova, T. *Refract. Ind. Ceram.* **2004**, *45*, 402–407, DOI: [10.1007/s11148-005-0021-6](https://doi.org/10.1007/s11148-005-0021-6) (cit. on p. 1).
- (9) Taut, C. Thermal shield stone for covering the wall of a combustion chamber, combustion chamber and a gas turbine., US Patent 7,540,155, 2009 (cit. on p. 1).

- (10) Liu, Y.; He, J.; Yang, R. *Ind. Eng. Chem. Res.* **2015**, *54*, 5876–5884, DOI: [10.1021/acs.iecr.5b01019](https://doi.org/10.1021/acs.iecr.5b01019) (cit. on p. 1).
- (11) Xie, H.; Yang, W.; Yuen, A. C. Y.; Xie, C.; Xie, J.; Lu, H.; Yeoh, G. H. *Chem. Eng. J.* **2017**, *311*, 310–317, DOI: [10.1016/j.cej.2016.11.110](https://doi.org/10.1016/j.cej.2016.11.110) (cit. on p. 1).
- (12) Craig, L.; Stillings, L. L.; Decker, D. L. *Appl. Geochem.* **2017**, *76*, 112–123, DOI: [10.1016/j.apgeochem.2016.11.011](https://doi.org/10.1016/j.apgeochem.2016.11.011) (cit. on p. 1).
- (13) Dubok, V. A. *Powder Metall. Met. Ceram.* **2000**, *39*, 381–394, DOI: [10.1023/A:1026617607548](https://doi.org/10.1023/A:1026617607548) (cit. on p. 1).
- (14) Krell, A.; Blank, P.; Ma, H.; Hutzler, T.; Bruggen, M. P.; Apetz, R. *J. Am. Ceram. Soc.* **2003**, *86*, 12–18, DOI: [10.1111/j.1151-2916.2003.tb03270.x](https://doi.org/10.1111/j.1151-2916.2003.tb03270.x) (cit. on p. 1).
- (15) Sadik, C.; El Amrani, I.-E.; Albizane, A. *J. Asian Ceram. Soc.* **2014**, *2*, 83–96, DOI: [10.1016/j.jascer.2014.03.001](https://doi.org/10.1016/j.jascer.2014.03.001) (cit. on p. 1).
- (16) Kwon, M. S.; Kim, N.; Park, C. M.; Lee, S. S.; Kang, K. Y.; Park, J. *ChemInform* **2005**, *36*, DOI: [10.1002/chin.200531047](https://doi.org/10.1002/chin.200531047) (cit. on p. 1).
- (17) Lü, Z.; Zhang, F.; Lei, X.; Yang, L.; Xu, S.; Duan, X. *Chem. Eng. Sci.* **2008**, *63*, 4055–4062, DOI: [10.1016/j.ces.2008.05.007](https://doi.org/10.1016/j.ces.2008.05.007) (cit. on p. 1).
- (18) Newell, A.; Thampi, K. R. *Int. J. Hydrogen Energ.* **2017**, *42*, 23446–23454, DOI: [10.1016/j.ijhydene.2017.04.279](https://doi.org/10.1016/j.ijhydene.2017.04.279) (cit. on p. 1).
- (19) Sattler, A. *ACS Catal.* **2018**, 2296–2312, DOI: [10.1021/acscatal.7b04201](https://doi.org/10.1021/acscatal.7b04201) (cit. on p. 1).
- (20) Sihombing, R.; Krisnandi, Y. K.; Widya, R.; Luthfiyah, S. Z.; Yunarti, R. T. *Makara J. Sci.* **2015**, *19*, 131–136, DOI: [10.7454/mss.v19i14.5166](https://doi.org/10.7454/mss.v19i14.5166) (cit. on p. 1).

- 
- (21) Xu, R.; Zhang, M.; Mortimer, R. J. G.; Pan, G. *Environ. Sci. Technol.* **2017**, *51*, 3418–3425, DOI: [10.1021/acs.est.6b05623](https://doi.org/10.1021/acs.est.6b05623) (cit. on p. 1).
- (22) Britto, S.; Kamath, P. V. *J. Solid State Chem.* **2014**, *215*, 206–210, DOI: [10.1016/j.jssc.2014.02.031](https://doi.org/10.1016/j.jssc.2014.02.031) (cit. on p. 1).
- (23) Gai, W.-Z.; Deng, Z.-Y.; Shi, Y. *RSC Adv.* **2015**, *5*, 84223–84231, DOI: [10.1039/c5ra14706a](https://doi.org/10.1039/c5ra14706a) (cit. on pp. 1, 61).
- (24) Gong, W.-X.; Qu, J.-H.; Liu, R.-P.; Lan, H.-C. *Colloid. Surface. A* **2012**, *395*, 88–93, DOI: [10.1016/j.colsurfa.2011.12.010](https://doi.org/10.1016/j.colsurfa.2011.12.010) (cit. on pp. 1, 61).
- (25) Wu, S.; Zhang, K.; He, J.; Cai, X.; Chen, K.; Li, Y.; Sun, B.; Kong, L.; Liu, J. *J. Colloid Interf. Sci.* **2016**, *464*, 238–245, DOI: [10.1016/j.jcis.2015.10.045](https://doi.org/10.1016/j.jcis.2015.10.045) (cit. on pp. 1, 61).
- (26) Zhang, J.; Brutus, T. E.; Cheng, J.; Meng, X. *J. Environ. Sci.* **2017**, DOI: [10.1016/j.jes.2017.03.015](https://doi.org/10.1016/j.jes.2017.03.015) (cit. on pp. 1, 61).
- (27) Jiménez-Becerril, J.; Solache-Ríos, M.; García-Sosa, I. *Water Air Soil Poll.* **2011**, *223*, 1073–1078, DOI: [10.1007/s11270-011-0925-3](https://doi.org/10.1007/s11270-011-0925-3) (cit. on pp. 2, 61).
- (28) Fawell, J.; Bailey, K.; Chilton, J.; Dahi, E.; Fewtrell, L.; Magara, Y., *Fluoride in Drinking-water*; WHO titles with IWA Publishing: **2006** (cit. on p. 2).
- (29) *Fluoride in Drinking Water*; National Academies Press: **2006**, DOI: [10.17226/11571](https://doi.org/10.17226/11571) (cit. on p. 2).
- (30) Gupta, A; Ayoob, S, *Fluoride in Drinking Water*; CRC Press: **2016**, DOI: [10.1201/b21385](https://doi.org/10.1201/b21385) (cit. on p. 2).
- (31) Bashash, M. et al. *Environ. Health Persp.* **2017**, *125*, DOI: [10.1289/ehp655](https://doi.org/10.1289/ehp655) (cit. on p. 2).

- (32) Darchen, A.; Sivasankar, V.; Prabhakaran, M.; Bharathi, C. B. In *Surface Modified Carbons as Scavengers for Fluoride from Water*; Springer International Publishing: 2016, pp 33–62, DOI: [10.1007/978-3-319-40686-2\\_3](https://doi.org/10.1007/978-3-319-40686-2_3) (cit. on p. 2).
- (33) Choi, A. L.; Zhang, Y.; Sun, G.; Bellinger, D. C.; Wang, K.; Yang, X. J.; Li, J. S.; Zheng, Q.; Fu, Y.; Grandjean, P. *Neurotoxicol. Teratol.* **2015**, *47*, 96–101, DOI: [10.1016/j.ntt.2014.11.001](https://doi.org/10.1016/j.ntt.2014.11.001) (cit. on p. 2).
- (34) Peckham, S.; Awofeso, N. *Sci. World J.* **2014**, *2014*, 1–10, DOI: [10.1155/2014/293019](https://doi.org/10.1155/2014/293019) (cit. on p. 2).
- (35) Choi, A. L.; Sun, G.; Zhang, Y.; Grandjean, P. *Environ. Health Persp.* **2012**, *120*, 1362–1368, DOI: [10.1289/ehp.1104912](https://doi.org/10.1289/ehp.1104912) (cit. on p. 2).
- (36) Cheng, K. K.; Chalmers, I.; Sheldon, T. A. *BMJ* **2007**, *335*, 699–702, DOI: [10.1136/bmj.39318.562951.be](https://doi.org/10.1136/bmj.39318.562951.be) (cit. on p. 2).
- (37) Harrison, P. T. *J. Fluorine Chem.* **2005**, *126*, 1448–1456, DOI: [10.1016/j.jfluchem.2005.09.009](https://doi.org/10.1016/j.jfluchem.2005.09.009) (cit. on p. 2).
- (38) Fejerskov, O.; Larsen, M.; Richards, A.; Baelum, V. *Adv. Dent. Res.* **1994**, *8*, 15–31, DOI: [10.1177/08959374940080010601](https://doi.org/10.1177/08959374940080010601) (cit. on p. 2).
- (39) Kleerekoper, M. *Adv. Dent. Res.* **1994**, *8*, 32–38, DOI: [10.1177/08959374940080010801](https://doi.org/10.1177/08959374940080010801) (cit. on p. 2).
- (40) Célérier, S.; Richard, F. *Catal. Commun.* **2015**, *67*, 26–30, DOI: [10.1016/j.catcom.2015.04.003](https://doi.org/10.1016/j.catcom.2015.04.003) (cit. on p. 2).
- (41) Zieliński, M.; Tomska-Foralewska, I.; Pietrowski, M.; Przystajko, W.; Wojciechowska, M. *Catal. Today* **2012**, *191*, 75–78, DOI: [10.1016/j.cattod.2011.12.032](https://doi.org/10.1016/j.cattod.2011.12.032) (cit. on p. 2).

- 
- (42) Demourgues, A.; Penin, N.; Dambournet, D.; Clarenc, R.; Tressaud, A.; Durand, E. *J. Fluorine Chem.* **2012**, *134*, 35–43, DOI: [10.1016/j.jfluchem.2011.02.006](https://doi.org/10.1016/j.jfluchem.2011.02.006) (cit. on p. 2).
- (43) Pietrowski, M.; Wojciechowska, M. *J. Fluorine Chem.* **2007**, *128*, 219–223, DOI: [10.1016/j.jfluchem.2006.12.009](https://doi.org/10.1016/j.jfluchem.2006.12.009) (cit. on p. 2).
- (44) Fujihara, S.; Tokumo, K. *J. Fluorine Chem.* **2009**, *130*, 1106–1110, DOI: [10.1016/j.jfluchem.2009.07.019](https://doi.org/10.1016/j.jfluchem.2009.07.019) (cit. on p. 2).
- (45) Delattre, J. L.; Chupas, P. J.; Grey, C. P.; Stacy, A. M. *J. Am. Chem. Soc.* **2001**, *123*, 5364–5365, DOI: [10.1021/ja015645t](https://doi.org/10.1021/ja015645t) (cit. on p. 2).
- (46) Skapin, T.; Mazej, Z.; Makarowicz, A.; Jesih, A.; Nickkho-Amiry, M.; Schroeder, S. L.; Weiher, N.; Žemva, B.; Winfield, J. M. *J. Fluorine Chem.* **2011**, *132*, 703–712, DOI: [10.1016/j.jfluchem.2011.04.013](https://doi.org/10.1016/j.jfluchem.2011.04.013) (cit. on p. 2).
- (47) Kemnitz, E.; Groß, U.; Rüdiger, S.; Shekar, C. S. *Angew. Chem. Int. Edit.* **2003**, *42*, 4251–4254, DOI: [10.1002/anie.200351278](https://doi.org/10.1002/anie.200351278) (cit. on p. 2).
- (48) Rüdiger, S. K.; Groß, U.; Feist, M.; Prescott, H. A.; Shekar, S. C.; Troyanov, S. I.; Kemnitz, E. *J. Mater. Chem.* **2005**, *15*, 588–597, DOI: [10.1039/b411457d](https://doi.org/10.1039/b411457d) (cit. on p. 2).
- (49) Kemnitz, E.; Wuttke, S.; Coman, S. M. *Eur. J. Inorg. Chem.* **2011**, *2011*, 4773–4794, DOI: [10.1002/ejic.201100539](https://doi.org/10.1002/ejic.201100539) (cit. on p. 2).
- (50) Teinz, K.; Wuttke, S.; Börno, F.; Eicher, J.; Kemnitz, E. *J. Catal.* **2011**, *282*, 175–182, DOI: [10.1016/j.jcat.2011.06.013](https://doi.org/10.1016/j.jcat.2011.06.013) (cit. on p. 2).
- (51) Rüdiger, S.; Kemnitz, E. *Dalton Trans.* **2008**, 1117, DOI: [10.1039/b716483a](https://doi.org/10.1039/b716483a) (cit. on p. 2).
- (52) Wojciechowska, M.; Wajnert, A.; Tomska-Foralewska, I.; Zieliński, M.; Czajka, B. *Catal. Lett.* **2008**, *128*, 77–82, DOI: [10.1007/s10562-008-9731-y](https://doi.org/10.1007/s10562-008-9731-y) (cit. on p. 2).

- (53) Stosiek, C.; Scholz, G.; Schroeder, S. L.; Kemnitz, E. *Chem. Mater.* **2010**, *22*, 2347–2356, DOI: [10.1021/cm903573a](https://doi.org/10.1021/cm903573a) (cit. on pp. 2, 69, 217).
- (54) König, R.; Scholz, G.; Pawlik, A.; Jäger, C.; van Rossum, B.; Oschkinat, H.; Kemnitz, E. *J. Phys. Chem. C* **2008**, *112*, 15708–15720, DOI: [10.1021/jp804662f](https://doi.org/10.1021/jp804662f) (cit. on pp. 2, 69, 70, 81, 217).
- (55) Hemmann, F.; Jäger, C.; Kemnitz, E. *RSC Adv.* **2014**, *4*, 56900–56909, DOI: [10.1039/c4ra09477h](https://doi.org/10.1039/c4ra09477h) (cit. on p. 2).
- (56) Hemmann, F.; Scholz, G.; Scheurell, K.; Kemnitz, E.; Jäger, C. *J. Phys. Chem. C* **2012**, *116*, 10580–10585, DOI: [10.1021/jp212045w](https://doi.org/10.1021/jp212045w) (cit. on p. 2).
- (57) Scalise, V.; Scholz, G.; Kemnitz, E. *J. Solid State Chem.* **2016**, *243*, 154–161, DOI: [10.1016/j.jssc.2016.08.020](https://doi.org/10.1016/j.jssc.2016.08.020) (cit. on p. 2).
- (58) Ahrem, L.; Scholz, G.; Bertram, R.; Kemnitz, E. *J. Phys. Chem. C* **2016**, *120*, 9236–9244, DOI: [10.1021/acs.jpcc.6b01191](https://doi.org/10.1021/acs.jpcc.6b01191) (cit. on p. 2).
- (59) Ahrem, L.; Scholz, G.; Gutmann, T.; Calvo, B.; Buntkowsky, G.; Kemnitz, E. *J. Phys. Chem. C* **2017**, *121*, 12206–12213, DOI: [10.1021/acs.jpcc.7b02535](https://doi.org/10.1021/acs.jpcc.7b02535) (cit. on p. 2).
- (60) Scholz, G.; Brehme, S.; Balski, M.; König, R.; Kemnitz, E. *Solid State Sci.* **2010**, *12*, 1500–1506, DOI: [10.1016/j.solidstatesciences.2010.06.017](https://doi.org/10.1016/j.solidstatesciences.2010.06.017) (cit. on p. 2).
- (61) Scalise, V.; Scholz, G.; Kemnitz, E. *J. Mater. Sci.* **2018**, DOI: [10.1007/s10853-018-2347-8](https://doi.org/10.1007/s10853-018-2347-8) (cit. on p. 2).
- (62) DIN; EN *Anforderungen und Konformitätskriterien von Normalzement* **2004**, 197–1 (cit. on p. 2).
- (63) Yuasa, A.; Inaba, H.; Tadanaga, K.; Tatsumisago, M.; Minami, T. *Proc. Int. Congr. Glass, 17th*, **1995**, *4*, 445–49 (cit. on p. 2).

- 
- (64) Tadanaga, K.; Katata, N.; Minami, T. *J. Am. Ceram. Soc.* **2005**, *80*, 1040–1042, DOI: [10.1111/j.1151-2916.1997.tb02943.x](https://doi.org/10.1111/j.1151-2916.1997.tb02943.x) (cit. on p. 2).
- (65) Wang, D.; Bierwagen, G. P. *Prog. Org. Coat.* **2009**, *64*, 327–338, DOI: [10.1016/j.porgcoat.2008.08.010](https://doi.org/10.1016/j.porgcoat.2008.08.010) (cit. on p. 2).
- (66) Plunkett, R. Tetrafluoroethylene polymers., US Patent 2,230,654, 1941 (cit. on p. 3).
- (67) Edward, H.; Ford, T. Polyvinylidene fluoride and process for obtaining the same., US Patent 2,435,537, 1948 (cit. on p. 3).
- (68) Dong Kang, G.; ming Cao, Y. *J. Membrane Sci.* **2014**, *463*, 145–165, DOI: [10.1016/j.memsci.2014.03.055](https://doi.org/10.1016/j.memsci.2014.03.055) (cit. on p. 3).
- (69) Liu, F.; Hashim, N. A.; Liu, Y.; Abed, M. M.; Li, K. *J. Membrane Sci.* **2011**, *375*, 1–27, DOI: [10.1016/j.memsci.2011.03.014](https://doi.org/10.1016/j.memsci.2011.03.014) (cit. on p. 3).
- (70) Lutterotti, L.; Scardi, P. *J. Appl. Crystallogr.* **1990**, *23*, 246–252, DOI: [10.1107/s0021889890002382](https://doi.org/10.1107/s0021889890002382) (cit. on p. 3).
- (71) Hartree, D. R. *Math. Proc. Cambridge*, **1928**, *24*, 89–110, DOI: [10.1017/s0305004100011919](https://doi.org/10.1017/s0305004100011919) (cit. on pp. 3, 9).
- (72) Hartree, D. R. *Math. Proc. Cambridge*, **1928**, *24*, 111–132, DOI: [10.1017/s0305004100011920](https://doi.org/10.1017/s0305004100011920) (cit. on pp. 3, 9).
- (73) Fock, V. A. *Z. Phys.* **1930**, *61*, 126–148, DOI: [10.1007/bf01340294](https://doi.org/10.1007/bf01340294) (cit. on pp. 3, 9).
- (74) Hohenberg, P.; Kohn, W. *Phys. Rev. B* **1964**, *136*, 864, DOI: [10.1103/physrev.136.b864](https://doi.org/10.1103/physrev.136.b864) (cit. on pp. 3, 12, 41).
- (75) Kohn, W.; Sham, L. J. *Phys. Rev. A* **1965**, *140*, 1133, DOI: [10.1103/physrev.140.a1133](https://doi.org/10.1103/physrev.140.a1133) (cit. on pp. 3, 12, 41).
- (76) Grimme, S. *J. Comput. Chem.* **2004**, *25*, 1463–1473, DOI: [10.1002/jcc.20078](https://doi.org/10.1002/jcc.20078) (cit. on pp. 3, 14, 41).

- (77) Grimme, S. *J. Comput. Chem.* **2006**, *27*, 1787–1799, DOI: [10.1002/jcc.20495](https://doi.org/10.1002/jcc.20495) (cit. on pp. 3, 14, 41).
- (78) Grimme, S.; Antony, J.; Ehrlich, S.; Krieg, H. *J. Chem. Phys.* **2010**, *132*, 154104, DOI: [10.1063/1.3382344](https://doi.org/10.1063/1.3382344) (cit. on pp. 3, 14, 15, 41).
- (79) Grimme, S.; Ehrlich, S.; Goerigk, L. *J. Comput. Chem.* **2011**, *32*, 1456–1465, DOI: [10.1002/jcc.21759](https://doi.org/10.1002/jcc.21759) (cit. on pp. 3, 14, 16, 41).
- (80) Saalfeld, H; Wedde, M *Z. Kristallogr.* **1974**, *139*, 129–135, DOI: [10.1524/zkri.1974.139.16.129](https://doi.org/10.1524/zkri.1974.139.16.129) (cit. on pp. 3, 55, 57).
- (81) Rodgers, K. *Z. Kristallogr.* **1998**, *213*, 96–100, DOI: [10.1524/zkri.1998.213.2.96](https://doi.org/10.1524/zkri.1998.213.2.96) (cit. on pp. 3, 55, 57).
- (82) Balan, E.; Blanchard, M.; Hochepped, J.-F.; Lazzeri, M. *Phys. Chem. Miner.* **2008**, *35*, 279–285, DOI: [10.1007/s00269-008-0221-y](https://doi.org/10.1007/s00269-008-0221-y) (cit. on pp. 3, 55, 57).
- (83) Busing, W.; Levy, H. A. *Acta Crystallogr.* **1958**, *11*, 798–803, DOI: [10.1107/s0365110x58002243](https://doi.org/10.1107/s0365110x58002243) (cit. on pp. 3, 55, 57).
- (84) Bokhimi, X; Toledo-Antonio, J.; Guzman-Castillo, M.; Hernandez-Beltran, F *J. Solid State Chem.* **2001**, *159*, 32–40, DOI: [10.1006/jssc.2001.9124](https://doi.org/10.1006/jssc.2001.9124) (cit. on pp. 3, 55, 57).
- (85) Hockey, B. J.; Handwerker, C. A.; Blendell, J. E.; Carter, W. C.; Roosen, A. R.; Choi, J.-H.; Kim, D.-Y. *J. Am. Ceram. Soc.* **1997**, *80*, 62–68, DOI: [10.1111/j.1151-2916.1997.tb02791.x](https://doi.org/10.1111/j.1151-2916.1997.tb02791.x) (cit. on pp. 4, 83, 85).
- (86) De Leeuw, N. H.; Parker, S. C. *J. Am. Ceram. Soc.* **1999**, *82*, 3209–3216, DOI: [10.1111/j.1151-2916.1999.tb02225.x](https://doi.org/10.1111/j.1151-2916.1999.tb02225.x) (cit. on pp. 4, 83, 85).
- (87) Marmier, A.; Parker, S. C. *Phys. Rev. B* **2004**, *69*, 115409, DOI: [10.1103/physrevb.69.115409](https://doi.org/10.1103/physrevb.69.115409) (cit. on pp. 4, 83, 85, 87, 89, 90).



- 
- (88) Kurita, T.; Uchida, K.; Oshiyama, A. *Phys. Rev. B* **2010**, *82*, 155319, DOI: [10.1103/physrevb.82.155319](https://doi.org/10.1103/physrevb.82.155319) (cit. on pp. 4, 35, 83, 86).
- (89) Manassidis, I; De Vita, A; Gillan, M. *Surf. Sci. Lett.* **1993**, *285*, L517–L521, DOI: [10.1016/0039-6028\(93\)90423-h](https://doi.org/10.1016/0039-6028(93)90423-h) (cit. on p. 4).
- (90) Toofan, J; Watson, P. *Surf. Sci.* **1998**, *401*, 162–172, DOI: [10.1016/s0039-6028\(97\)01031-5](https://doi.org/10.1016/s0039-6028(97)01031-5) (cit. on pp. 4, 87).
- (91) Eng, P. J.; Trainor, T. P.; Brown Jr, G. E.; G. A.; Newville, M.; Sutton, S. R.; Rivers, M. L. *Science* **2000**, *288*, 1029–1033, DOI: [10.1126/science.288.5468.1029](https://doi.org/10.1126/science.288.5468.1029) (cit. on pp. 4, 87).
- (92) Fu, Q.; Wagner, T.; Rühle, M. *Surf. Sci.* **2006**, *600*, 4870–4877, DOI: [10.1016/j.susc.2006.08.008](https://doi.org/10.1016/j.susc.2006.08.008) (cit. on pp. 4, 87).
- (93) Soares, E.; Van Hove, M.; Walters, C.; McCarty, K. *Phys. Rev. B* **2002**, *65*, 195405, DOI: [10.1103/physrevb.65.195405](https://doi.org/10.1103/physrevb.65.195405) (cit. on pp. 4, 87).
- (94) Petrik, N. G.; Huestis, P. L.; LaVerne, J. A.; Aleksandrov, A. B.; Orlando, T. M.; Kimmel, G. A. *J. Phys. Chem. C* **2018**, DOI: [10.1021/acs.jpcc.8b01969](https://doi.org/10.1021/acs.jpcc.8b01969) (cit. on p. 4).
- (95) Hass, K.; Schneider, W.; Curioni, A; Andreoni, W. *J. Phys. Chem. B* **2000**, *104*, 5527–5540, DOI: [10.1021/jp000040p](https://doi.org/10.1021/jp000040p) (cit. on pp. 4, 87).
- (96) Ranea, V. A.; Carmichael, I.; Schneider, W. F. *J. Phys. Chem. C* **2009**, *113*, 2149–2158, DOI: [10.1021/jp8069892](https://doi.org/10.1021/jp8069892) (cit. on pp. 4, 87).
- (97) Wirth, J.; Saalfrank, P. *J. Phys. Chem. C* **2012**, *116*, 26829–26840, DOI: [10.1021/jp310234h](https://doi.org/10.1021/jp310234h) (cit. on pp. 4, 87).
- (98) Wirth, J.; Schacht, J.; Saalfrank, P.; Paulus, B. *J. Phys. Chem. C* **2016**, *120*, 9713–9718, DOI: [10.1021/acs.jpcc.5b10975](https://doi.org/10.1021/acs.jpcc.5b10975) (cit. on pp. 4, 87, 108).

- (99) Kirsch, H.; Wirth, J.; Tong, Y.; Wolf, M.; Saalfrank, P.; Campen, R. K. *J. Phys. Chem. C* **2014**, *118*, 13623–13630, DOI: [10.1021/jp502106t](https://doi.org/10.1021/jp502106t) (cit. on pp. 4, 87).
- (100) Wang, X.-G.; Chaka, A.; Scheffler, M. *Phys. Rev. Lett.* **2000**, *84*, 3650, DOI: [10.1103/physrevlett.84.3650](https://doi.org/10.1103/physrevlett.84.3650) (cit. on pp. 4, 87).
- (101) Trainor, T. P.; Eng, P. J.; Brown, G. E.; Robinson, I. K.; De Santis, M. *Surf. Sci.* **2002**, *496*, 238–250, DOI: [10.1016/s0039-6028\(01\)01617-x](https://doi.org/10.1016/s0039-6028(01)01617-x) (cit. on pp. 4, 87).
- (102) Catalano, J. G.; Park, C.; Zhang, Z.; Fenter, P. *Langmuir* **2006**, *22*, 4668–4673, DOI: [10.1021/la060177s](https://doi.org/10.1021/la060177s) (cit. on pp. 4, 87).
- (103) Tougeri, A.; Methivier, C.; Cristol, S.; Tielens, F.; Che, M.; Carrier, X. *Phys. Chem. Chem. Phys.* **2011**, *13*, 6531–6543, DOI: [10.1039/c0cp01295e](https://doi.org/10.1039/c0cp01295e) (cit. on pp. 4, 87).
- (104) Mason, S. E.; Iceman, C. R.; Trainor, T. P.; Chaka, A. M. *Phys. Rev. B* **2010**, *81*, 125423, DOI: [10.1103/physrevb.81.125423](https://doi.org/10.1103/physrevb.81.125423) (cit. on pp. 4, 87, 88, 218).
- (105) Wirth, J.; Kirsch, H.; Wloszczyk, S.; Tong, Y.; Saalfrank, P.; Campen, R. K. *Phys. Chem. Chem. Phys.* **2016**, *18*, 14822–14832, DOI: [10.1039/c6cp01397j](https://doi.org/10.1039/c6cp01397j) (cit. on pp. 4, 87).
- (106) Kuhs, W. F.; Lehmann, M. S. *J. Phys. Chem.* **1983**, *87*, 4312–4313, DOI: [10.1021/j100244a063](https://doi.org/10.1021/j100244a063) (cit. on pp. 5, 180).
- (107) Kuhs, W. F.; Lehmann, M. S. In *Water Science Reviews 2*, Franks, F., Ed.; Cambridge University Press, pp 1–66, DOI: [10.1017/cbo9780511897504.001](https://doi.org/10.1017/cbo9780511897504.001) (cit. on pp. 5, 180).
- (108) Lisgarten, N. D.; Blackman, M. *Nature* **1956**, *178*, 39–40, DOI: [10.1038/178039a0](https://doi.org/10.1038/178039a0) (cit. on pp. 5, 180).

- 
- (109) Dowell, L. G.; Rinfret, A. P. *Nature* **1960**, *188*, 1144–1148, DOI: [10.1038/1881144a0](https://doi.org/10.1038/1881144a0) (cit. on pp. 5, 180).
- (110) Kamb, B. *Acta Crystallogr.* **1964**, *17*, 1437–1449, DOI: [10.1107/s0365110x64003553](https://doi.org/10.1107/s0365110x64003553) (cit. on pp. 5, 180).
- (111) Kamb, B.; Prakash, A. *Acta Crystallogr. B* **1968**, *24*, 1317–1327, DOI: [10.1107/s0567740868004231](https://doi.org/10.1107/s0567740868004231) (cit. on pp. 5, 180).
- (112) Londono, J. D.; Kuhs, W. F.; Finney, J. L. *J. Chem. Phys.* **1993**, *98*, 4878–4888, DOI: [10.1063/1.464942](https://doi.org/10.1063/1.464942) (cit. on pp. 5, 180).
- (113) Engelhardt, H.; Kamb, B. *J. Chem. Phys.* **1981**, *75*, 5887–5899, DOI: [10.1063/1.442040](https://doi.org/10.1063/1.442040) (cit. on pp. 5, 180).
- (114) Kamb, B.; Prakash, A.; Knobler, C. *Acta Crystallogr.* **1967**, *22*, 706–715, DOI: [10.1107/s0365110x67001409](https://doi.org/10.1107/s0365110x67001409) (cit. on pp. 5, 180).
- (115) Kamb, B. *Science* **1965**, *150*, 205–209, DOI: [10.1126/science.150.3693.205](https://doi.org/10.1126/science.150.3693.205) (cit. on pp. 5, 180).
- (116) Kuhs, W. F.; Finney, J. L.; Vettier, C.; Bliss, D. V. *J. Chem. Phys.* **1984**, *81*, 3612–3623, DOI: [10.1063/1.448109](https://doi.org/10.1063/1.448109) (cit. on pp. 5, 180).
- (117) Kamb, B.; Davis, B. L. *P. Natl. Acad. Sci. USA* **1964**, *52*, 1433–1439, DOI: [10.1073/pnas.52.6.1433](https://doi.org/10.1073/pnas.52.6.1433) (cit. on pp. 5, 180).
- (118) Besson, J. M.; Pruzan, P.; Klotz, S.; Hamel, G.; Silvi, B.; Nelmes, R. J.; Loveday, J. S.; Wilson, R. M.; Hull, S. *Phys. Rev. B* **1994**, *49*, 12540–12550, DOI: [10.1103/physrevb.49.12540](https://doi.org/10.1103/physrevb.49.12540) (cit. on pp. 5, 180).
- (119) Placa, S. J. L.; Hamilton, W. C.; Kamb, B.; Prakash, A. *J. Chem. Phys.* **1973**, *58*, 567–580, DOI: [10.1063/1.1679238](https://doi.org/10.1063/1.1679238) (cit. on pp. 5, 180).
- (120) Hirsch, K.; Holzapfel, W. *Phys. Lett. A* **1984**, *101*, 142–144, DOI: [10.1016/0375-9601\(84\)90510-3](https://doi.org/10.1016/0375-9601(84)90510-3) (cit. on pp. 5, 180).

- (121) Hemley, R. J.; Jephcoat, A. P.; Mao, H. K.; Zha, C. S.; Finger, L. W.; Cox, D. E. *Nature* **1987**, *330*, 737–740, DOI: [10.1038/330737a0](https://doi.org/10.1038/330737a0) (cit. on pp. 5, 180).
- (122) Leadbetter, A. J.; Ward, R. C.; Clark, J. W.; Tucker, P. A.; Matsuo, T.; Suga, H. *J. Chem. Phys.* **1985**, *82*, 424–428, DOI: [10.1063/1.448763](https://doi.org/10.1063/1.448763) (cit. on pp. 5, 180).
- (123) Fukazawa, H.; Mae, S.; Ikeda, S.; Watanabe, O. *Chem. Phys. Lett.* **1998**, *294*, 554–558, DOI: [10.1016/s0009-2614\(98\)00908-7](https://doi.org/10.1016/s0009-2614(98)00908-7) (cit. on pp. 5, 180).
- (124) Koza, M.; Schober, H.; Tölle, A.; Fujara, F.; Hansen, T. *Nature* **1999**, *397*, 660–661, DOI: [10.1038/17717](https://doi.org/10.1038/17717) (cit. on pp. 5, 180).
- (125) Salzmann, C. G.; Radaelli, P. G.; Hallbrucker, A.; Mayer, E.; Finney, J. L. *Science* **2006**, *311*, 1758–1761, DOI: [10.1126/science.1123896](https://doi.org/10.1126/science.1123896) (cit. on pp. 5, 180).
- (126) Salzmann, C. G.; Radaelli, P. G.; Mayer, E.; Finney, J. L. *Phys. Rev. Lett.* **2009**, *103*, DOI: [10.1103/physrevlett.103.105701](https://doi.org/10.1103/physrevlett.103.105701) (cit. on pp. 5, 180).
- (127) Falenty, A.; Hansen, T. C.; Kuhs, W. F. *Nature* **2014**, *516*, 231–233, DOI: [10.1038/nature14014](https://doi.org/10.1038/nature14014) (cit. on pp. 5, 180).
- (128) Strobel, T. A.; Somayazulu, M.; Sinogeikin, S. V.; Dera, P.; Hemley, R. J. *J. Am. Chem. Soc.* **2016**, *138*, 13786–13789, DOI: [10.1021/jacs.6b06986](https://doi.org/10.1021/jacs.6b06986) (cit. on pp. 5, 180).
- (129) Del Rosso, L.; Celli, M.; Ulivi, L. *Nat. Commun.* **2016**, *7*, 13394, DOI: [10.1038/ncomms13394](https://doi.org/10.1038/ncomms13394) (cit. on pp. 5, 180).
- (130) Del Rosso, L.; Grazzi, F.; Celli, M.; Colognesi, D.; Garcia-Sakai, V.; Ulivi, L. *J. Phys. Chem. C* **2016**, *120*, 26955–26959, DOI: [10.1021/acs.jpcc.6b10569](https://doi.org/10.1021/acs.jpcc.6b10569) (cit. on pp. 5, 180).

- 
- (131) Schrödinger, E. *Ann. Phys.* **1926**, *384*, 361–376, DOI: [10.1002/andp.19263840404](https://doi.org/10.1002/andp.19263840404) (cit. on p. 7).
- (132) Schrödinger, E. *Ann. Phys.* **1926**, *384*, 489–527, DOI: [10.1002/andp.19263840602](https://doi.org/10.1002/andp.19263840602) (cit. on p. 7).
- (133) Schrödinger, E. *Ann. Phys.* **1926**, *384*, 734–756, DOI: [10.1002/andp.19263840804](https://doi.org/10.1002/andp.19263840804) (cit. on p. 7).
- (134) Born, M.; Oppenheimer, R. J. *Ann. Phys.* **1927**, *389*, 457–484, DOI: [10.1002/andp.19273892002](https://doi.org/10.1002/andp.19273892002) (cit. on p. 8).
- (135) Slater, J. C. *Phys. Rev.* **1951**, *81*, 385, DOI: [10.1103/physrev.81.385](https://doi.org/10.1103/physrev.81.385) (cit. on pp. 9, 13, 14).
- (136) Slater, J. C. *Phys. Rev.* **1930**, *36*, 57, DOI: [10.1103/physrev.36.57](https://doi.org/10.1103/physrev.36.57) (cit. on p. 11).
- (137) Roothaan, C. C. J. *Rev. Mod. Phys.* **1951**, *23*, 69, DOI: [10.1103/revmodphys.23.69](https://doi.org/10.1103/revmodphys.23.69) (cit. on p. 11).
- (138) Hall, G. G. *P. Roy. Soc. Lond. A Mat.* **1951**, *205*, 541–552, DOI: [10.1098/rspa.1951.0048](https://doi.org/10.1098/rspa.1951.0048) (cit. on p. 11).
- (139) Dirac, P. A. M. *Math. Proc. Cambridge* **1930**, *26*, 376, DOI: [10.1017/s0305004100016108](https://doi.org/10.1017/s0305004100016108) (cit. on p. 13).
- (140) Perdew, J. P.; Wang, Y. *Phys. Rev. B* **1992**, *45*, 13244, DOI: [10.1103/physrevb.45.13244](https://doi.org/10.1103/physrevb.45.13244) (cit. on pp. 13, 14).
- (141) Chachiyo, T. *J. Chem. Phys.* **2016**, *145*, 021101, DOI: [10.1063/1.4958669](https://doi.org/10.1063/1.4958669) (cit. on p. 13).
- (142) Ceperley, D. M.; Alder, B. J. *Phys. Rev. Lett.* **1980**, *45*, 566–569, DOI: [10.1103/physrevlett.45.566](https://doi.org/10.1103/physrevlett.45.566) (cit. on p. 13).
- (143) Perdew, J. P.; Burke, K.; Ernzerhof, M. *Phys. Rev. Lett.* **1996**, *77*, 3865, DOI: [10.1103/physrevlett.77.3865](https://doi.org/10.1103/physrevlett.77.3865) (cit. on pp. 14, 41).

- (144) Perdew, J. P.; Burke, K.; Ernzerhof, M. *Phys. Rev. Lett.* **1997**, *78*, 1396, DOI: [10.1103/physrevlett.78.1396](https://doi.org/10.1103/physrevlett.78.1396) (cit. on pp. 14, 41).
- (145) Perdew, J. P.; Ernzerhof, M.; Burke, K. *J. Chem. Phys.* **1996**, *105*, 9982–9985, DOI: [10.1063/1.472933](https://doi.org/10.1063/1.472933) (cit. on pp. 14, 41).
- (146) Tao, J.; Perdew, J. P.; Staroverov, V. N.; Scuseria, G. E. *Phys. Rev. Lett.* **2003**, *91*, 146401, DOI: [10.1103/physrevlett.91.146401](https://doi.org/10.1103/physrevlett.91.146401) (cit. on p. 14).
- (147) Dirac, P. A. *P. Roy. Soc. Lond. A Mat.* **1929**, *123*, 714–733, DOI: [10.1098/rspa.1929.0094](https://doi.org/10.1098/rspa.1929.0094) (cit. on p. 14).
- (148) Becke, A. D. *Phys. Rev. A* **1988**, *38*, 3098, DOI: [10.1103/physreva.38.3098](https://doi.org/10.1103/physreva.38.3098) (cit. on p. 14).
- (149) Becke, A. D. *J. Chem. Phys.* **1993**, *98*, 5648–5652, DOI: [10.1063/1.464913](https://doi.org/10.1063/1.464913) (cit. on p. 14).
- (150) Lee, C.; Yang, W.; Parr, R. G. *Phys. Rev. B* **1988**, *37*, 785, DOI: [10.1103/physrevb.37.785](https://doi.org/10.1103/physrevb.37.785) (cit. on p. 14).
- (151) Grimme, S. *J. Comput. Chem.* **2006**, *27*, 1787–1799, DOI: [10.1002/jcc.20495](https://doi.org/10.1002/jcc.20495) (cit. on p. 14).
- (152) Tkatchenko, A.; Scheffler, M. *Phys. Rev. Lett.* **2009**, *102*, DOI: [10.1103/physrevlett.102.073005](https://doi.org/10.1103/physrevlett.102.073005) (cit. on p. 14).
- (153) Casimir, H. B. G.; Polder, D. *Phys. Rev.* **1948**, *73*, 360–372, DOI: [10.1103/physrev.73.360](https://doi.org/10.1103/physrev.73.360) (cit. on p. 15).
- (154) Chai, J.-D.; Head-Gordon, M. *Phys. Chem. Chem. Phys.* **2008**, *10*, 6615, DOI: [10.1039/b810189b](https://doi.org/10.1039/b810189b) (cit. on p. 16).
- (155) Becke, A. D.; Johnson, E. R. *J. Chem. Phys.* **2005**, *123*, 154101, DOI: [10.1063/1.2065267](https://doi.org/10.1063/1.2065267) (cit. on p. 16).
- (156) Kittel, C., *Introduction to Solid State Physics*; Wiley & Sons, Inc: **2005**, ISBN: 978-0-471-41526-8 (cit. on pp. 17, 27).

- 
- (157) Bloch, F. *Z. Phys.* **1929**, *52*, 555–600, DOI: [10.1007/bf01339455](https://doi.org/10.1007/bf01339455) (cit. on p. 19).
- (158) Monkhorst, H. J.; Pack, J. D. *Phys. Rev. B* **1976**, *13*, 5188, DOI: [10.1103/physrevb.13.5188](https://doi.org/10.1103/physrevb.13.5188) (cit. on pp. 20, 41).
- (159) Hellmann, H. *J. Chem. Phys.* **1935**, *3*, 61–61, DOI: [10.1063/1.1749559](https://doi.org/10.1063/1.1749559) (cit. on p. 21).
- (160) Hellmann, H.; Kassatotschkin, W. *J. Chem. Phys.* **1936**, *4*, 324–325, DOI: [10.1063/1.1749851](https://doi.org/10.1063/1.1749851) (cit. on p. 21).
- (161) Schwerdtfeger, P. *ChemPhysChem* **2011**, *12*, 3143–3155, DOI: [10.1002/cphc.201100387](https://doi.org/10.1002/cphc.201100387) (cit. on p. 21).
- (162) Kresse, G; Hafner, J *J. Phys. Condens. Mat.* **1994**, *6*, 8245–8257, DOI: [10.1088/0953-8984/6/40/015](https://doi.org/10.1088/0953-8984/6/40/015) (cit. on p. 21).
- (163) Blöchl, P. E. *Phys. Rev. B* **1994**, *50*, 17953, DOI: [10.1103/physrevb.50.17953](https://doi.org/10.1103/physrevb.50.17953) (cit. on pp. 21, 41).
- (164) Slater, J. C. *Phys. Rev.* **1937**, *51*, 846–851, DOI: [10.1103/physrev.51.846](https://doi.org/10.1103/physrev.51.846) (cit. on p. 21).
- (165) Marcus, P. M. *Int. J. Quantum Chem.* **2009**, *1*, 567–588, DOI: [10.1002/qua.560010659](https://doi.org/10.1002/qua.560010659) (cit. on p. 21).
- (166) Andersen, O. K. *Phys. Rev. B* **1975**, *12*, 3060–3083, DOI: [10.1103/physrevb.12.3060](https://doi.org/10.1103/physrevb.12.3060) (cit. on p. 21).
- (167) McQuarrie, D.; Simon, J., *Molecular Thermodynamics*; University Science Books: **1999**, ISBN: 9781891389054 (cit. on p. 24).
- (168) Pickard, C. J.; Mauri, F. *Phys. Rev. B* **2001**, *63*, 245101, DOI: [10.1103/physrevb.63.245101](https://doi.org/10.1103/physrevb.63.245101) (cit. on pp. 29, 32, 41).
- (169) Yates, J. R.; Pickard, C. J.; Mauri, F. *Phys. Rev. B* **2007**, *76*, 024401, DOI: [10.1103/physrevb.76.024401](https://doi.org/10.1103/physrevb.76.024401) (cit. on pp. 29, 41).

- (170) Kokalj, A. *J. Mol. Graph. Model.* **1999**, *17*, 176–179, DOI: [10.1016/s1093-3263\(99\)00028-5](https://doi.org/10.1016/s1093-3263(99)00028-5) (cit. on p. 34).
- (171) Kokalj, A. *Comp. Mater. Sci.* **2003**, *28*, 155–168, DOI: [10.1016/s0927-0256\(03\)00104-6](https://doi.org/10.1016/s0927-0256(03)00104-6) (cit. on p. 34).
- (172) Gibbs, J. W., *The collected works of J. Willard Gibbs*; New York, Longmans, Green: **1928** (cit. on p. 37).
- (173) Wulff, G. *Z. Krist. - Cryst. Mater.* **1901**, *34*, DOI: [10.1524/zkri.1901.34.1.449](https://doi.org/10.1524/zkri.1901.34.1.449) (cit. on p. 37).
- (174) V. Laue, M. *Z. Krist. - Cryst. Mater.* **1943**, *105*, DOI: [10.1524/zkri.1943.105.1.124](https://doi.org/10.1524/zkri.1943.105.1.124) (cit. on p. 37).
- (175) Herrero, C. P.; Ramírez, R. *Phys. Chem. Chem. Phys.* **2013**, *15*, 16676, DOI: [10.1039/c3cp52167b](https://doi.org/10.1039/c3cp52167b) (cit. on p. 39).
- (176) Kresse, G.; Joubert, D. *Phys. Rev. B* **1999**, *59*, 1758, DOI: [10.1103/physrevb.59.1758](https://doi.org/10.1103/physrevb.59.1758) (cit. on p. 41).
- (177) Kresse, G.; Hafner, J. *Phys. Rev. B* **1993**, *47*, 558, DOI: [10.1103/physrevb.47.558](https://doi.org/10.1103/physrevb.47.558) (cit. on p. 41).
- (178) Kresse, G.; Hafner, J. *Phys. Rev. B* **1993**, *48*, 13115, DOI: [10.1103/physrevb.48.13115](https://doi.org/10.1103/physrevb.48.13115) (cit. on p. 41).
- (179) Kresse, G.; Hafner, J. *Phys. Rev. B* **1994**, *49*, 14251, DOI: [10.1103/physrevb.49.14251](https://doi.org/10.1103/physrevb.49.14251) (cit. on p. 41).
- (180) Kresse, G.; Furthmüller, J. *Comp. Mater. Sci.* **1996**, *6*, 15–50, DOI: [10.1016/0927-0256\(96\)00008-0](https://doi.org/10.1016/0927-0256(96)00008-0) (cit. on p. 41).
- (181) Kresse, G.; Furthmüller, J. *Phys. Rev. B* **1996**, *54*, 11169, DOI: [10.1103/physrevb.54.11169](https://doi.org/10.1103/physrevb.54.11169) (cit. on p. 41).
- (182) Wood, D.; Zunger, A. *J. Phys. A - Math. Gen.* **1985**, *18*, 1343, DOI: [10.1088/0305-4470/18/9/018](https://doi.org/10.1088/0305-4470/18/9/018) (cit. on p. 41).



- 
- (183) Pulay, P. *Chem. Phys. Lett.* **1980**, *73*, 393–398, DOI: [10.1016/0009-2614\(80\)80396-4](https://doi.org/10.1016/0009-2614(80)80396-4) (cit. on p. 41).
- (184) Blöchl, P. E.; Jepsen, O.; Andersen, O. K. *Phys. Rev. B* **1994**, *49*, 16223, DOI: [10.1103/physrevb.49.16223](https://doi.org/10.1103/physrevb.49.16223) (cit. on p. 41).
- (185) Methfessel, M.; Paxton, A. *Phys. Rev. B* **1989**, *40*, 3616, DOI: [10.1103/physrevb.40.3616](https://doi.org/10.1103/physrevb.40.3616) (cit. on p. 41).
- (186) Mason, J. *Solid State Nucl. Mag.* **1993**, *2*, 285–288, DOI: [10.1016/0926-2040\(93\)90010-k](https://doi.org/10.1016/0926-2040(93)90010-k) (cit. on p. 41).
- (187) Gregor, T.; Mauri, F.; Car, R. *J. Chem. Phys.* **1999**, *111*, 1815–1822, DOI: [10.1063/1.479451](https://doi.org/10.1063/1.479451) (cit. on p. 41).
- (188) Momma, K.; Izumi, F. *J. Appl. Crystallogr.* **2011**, *44*, 1272–1276, DOI: [10.1107/s0021889811038970](https://doi.org/10.1107/s0021889811038970) (cit. on p. 42).
- (189) Budau, J. H.; Paulus, B.; Steenbergen, K. G. *Chem. Phys.* **2017**, *491*, 112–117, DOI: [10.1016/j.chemphys.2017.05.004](https://doi.org/10.1016/j.chemphys.2017.05.004) (cit. on pp. 43, 45–47, 64, 65).
- (190) Kaawar, Z.; Müller, C.; Paulus, B. *Surf. Sci.* **2017**, *656*, 48–53, DOI: [10.1016/j.susc.2016.06.021](https://doi.org/10.1016/j.susc.2016.06.021) (cit. on p. 56).
- (191) Kanaki, E.; Sansone, G.; Maschio, L.; Paulus, B. *Phys. Chem. Chem. Phys.* **2015**, *17*, 18722–18728, DOI: [10.1039/c5cp02017d](https://doi.org/10.1039/c5cp02017d) (cit. on p. 56).
- (192) Hammerschmidt, L.; Müller, C.; Paulus, B. *J. Chem. Phys.* **2012**, *136*, 124117, DOI: [10.1063/1.3697867](https://doi.org/10.1063/1.3697867) (cit. on p. 56).
- (193) Hemingway, B. S.; Sposito, G., *The environmental chemistry of aluminum*; CRC Lewis, Boca Raton: **1996**, 81–116, ISBN: 9781566700306 (cit. on pp. 57, 58).
- (194) Demichelis, R.; Noël, Y.; Ugliengo, P.; Zicovich-Wilson, C. M.; Dovesi, R. *J. Phys. Chem. C* **2011**, *115*, 13107–13134, DOI: [10.1021/jp200523x](https://doi.org/10.1021/jp200523x) (cit. on p. 57).

- (195) Digne, M.; Sautet, P.; Raybaud, P.; Toulhoat, H.; Artacho, E. *J. Phys. Chem. B* **2002**, *106*, 5155–5162, DOI: [10.1021/jp014182a](https://doi.org/10.1021/jp014182a) (cit. on p. 57).
- (196) Isobe, T.; Watanabe, T.; de la Caillerie, J. d.; Legrand, A.; Massiot, D. *J. Colloid Interf. Sci.* **2003**, *261*, 320–324, DOI: [10.1016/s0021-9797\(03\)00144-9](https://doi.org/10.1016/s0021-9797(03)00144-9) (cit. on pp. 58, 59).
- (197) Damodaran, K.; Rajamohanan, P. R.; Chakrabarty, D.; Racherla, U. S.; Manohar, V.; Fernandez, C.; Amoureux, J.-P.; Ganapathy, S. *J. Am. Chem. Soc.* **2002**, *124*, 3200–3201, DOI: [10.1021/ja011532y](https://doi.org/10.1021/ja011532y) (cit. on pp. 58, 59).
- (198) Slade, R. C. T.; Southern, J. C.; Thompson, I. M. *J. Mater. Chem.* **1991**, *1*, 563–568, DOI: [10.1039/jm9910100563](https://doi.org/10.1039/jm9910100563) (cit. on p. 58).
- (199) Robert, C. et al. *J. Mater. Chem.* **1991**, *1*, 875–879, DOI: [10.1039/jm9910100875](https://doi.org/10.1039/jm9910100875) (cit. on p. 58).
- (200) Meinhold, R. H.; Slade, R. C. T.; Newman, R. H. *Appl. Magn. Reson.* **1993**, *4*, 121–140 (cit. on p. 58).
- (201) Tsuchida, T. *Bull. Fac. Eng. Hokkaido Univ.* **1992**, *160*, 1–9 (cit. on p. 58).
- (202) Ferreira, A. R.; Küçükbenli, E.; Leitão, A. A.; de Gironcoli, S. *Phys. Rev. B* **2011**, *84*, 235119, DOI: [10.1103/physrevb.84.235119](https://doi.org/10.1103/physrevb.84.235119) (cit. on pp. 58, 59).
- (203) Vyalikh, A.; Zesewitz, K.; Scheler, U. *Magn. Reson. Chem.* **2010**, *48*, 877–881, DOI: [10.1002/mrc.2682](https://doi.org/10.1002/mrc.2682) (cit. on pp. 58, 59).
- (204) Tsuchida, T. *Solid State Ionics* **1993**, *63*, 464–470, DOI: [10.1016/0167-2738\(93\)90145-s](https://doi.org/10.1016/0167-2738(93)90145-s) (cit. on p. 58).
- (205) MacKenzie, K. J. D.; Temuujin, J.; Smith, M. E.; Angerer, P.; Kameshima, Y. *Thermochim. Acta* **2000**, *359*, 87–94, DOI: [10.1016/s0040-6031\(00\)00513-x](https://doi.org/10.1016/s0040-6031(00)00513-x) (cit. on p. 58).
- (206) Grabowski, S. J. *J. Phys. Org. Chem.* **2004**, *17*, 18–31, DOI: [10.1002/poc.685](https://doi.org/10.1002/poc.685) (cit. on p. 67).

- 
- (207) Krahl, T.; Vimont, A.; Eltanany, G.; Daturi, M.; Kemnitz, E. *J. Phys. Chem. C* **2007**, *111*, 18317–18325, DOI: [10.1021/jp075450t](https://doi.org/10.1021/jp075450t) (cit. on p. 67).
- (208) Wuttke, S.; Vimont, A.; Lavalley, J.-C.; Daturi, M.; Kemnitz, E. *J. Phys. Chem. C* **2010**, *114*, 5113–5120, DOI: [10.1021/jp911584h](https://doi.org/10.1021/jp911584h) (cit. on p. 67).
- (209) Wuttke, S.; Coman, S. M.; Scholz, G.; Kirmse, H.; Vimont, A.; Daturi, M.; Schroeder, S. L.; Kemnitz, E. *Chem. Eur. J.* **2008**, *14*, 11488–11499, DOI: [10.1002/chem.200801702](https://doi.org/10.1002/chem.200801702) (cit. on p. 67).
- (210) Stosiek, C.; Scholz, G.; Eltanany, G.; Bertram, R.; Kemnitz, E. *Chem. Mater.* **2008**, *20*, 5687–5697, DOI: [10.1021/cm801236v](https://doi.org/10.1021/cm801236v) (cit. on pp. 69, 217).
- (211) König, R.; Scholz, G.; Bertram, R.; Kemnitz, E. *J. Fluorine Chem.* **2008**, *129*, 598–606, DOI: [10.1016/j.jfluchem.2008.04.015](https://doi.org/10.1016/j.jfluchem.2008.04.015) (cit. on pp. 69, 72, 217).
- (212) Fischer, L.; Harlé, V.; Kasztelan, S.; d’Espinoise de la Caillerie, J.-B. *Solid State Nucl. Mag.* **2000**, *16*, 85–91, DOI: [10.1016/s0926-2040\(00\)00058-8](https://doi.org/10.1016/s0926-2040(00)00058-8) (cit. on p. 69).
- (213) Lam, E.; Comas-Vives, A.; Copéret, C. *J. Phys. Chem. C* **2017**, DOI: [10.1021/acs.jpcc.7b07872](https://doi.org/10.1021/acs.jpcc.7b07872) (cit. on pp. 69, 70, 103, 217).
- (214) Born, M.; Huang, K., *Dynamical theory of crystal lattices*; Clarendon press: **1954**, ISBN: 9780198503699 (cit. on p. 83).
- (215) König, R.; Scholz, G.; Veiczi, M.; Jäger, C.; Troyanov, S.; Kemnitz, E. *Dalton Trans.* **2011**, *40*, 8701–8710, DOI: [10.1039/c1dt10514k](https://doi.org/10.1039/c1dt10514k) (cit. on pp. 113, 155, 215, 219).
- (216) Schacht, J.; Budau, J. H.; Gaston, N.; Paulus, B. *J. Comput. Chem.* **2018**, *39*, 1208–1214, DOI: [10.1002/jcc.25183](https://doi.org/10.1002/jcc.25183) (cit. on pp. 113, 177, 215).
- (217) Feyereisen, M. W.; Feller, D.; Dixon, D. A. *J. Phys. Chem.* **1996**, *100*, 2993–2997, DOI: [10.1021/jp9528601](https://doi.org/10.1021/jp9528601) (cit. on p. 177).

- (218) Chaplin, M. *Water Structure and Science*, en. [http://www1.lsbu.ac.uk/water/water\\_structure\\_science.html](http://www1.lsbu.ac.uk/water/water_structure_science.html) (accessed 01/05/2018), Dec. 23, 2017.
- (219) Theodore Gray Element Collection, I. *Abundance in Earth's Crust of the elements*, en. <http://periodictable.com/Properties/A/CrustAbundance.v.html> (accessed 05/09/2018), Oct. 28, 2017 (cit. on p. 215).

# Appendix

## A.1 Molecules

**Table A.1:** Listing of the used k-point grids (see [equation \(2.44\)](#)) for different molecules within a cubic UC of 30 Å - staying with odd integers.

Surface	$Q_1$	$Q_2$	$Q_3$
$[\text{Al}(\text{OH}_2)_6]^{3+}$	1	1	1
$\text{CCl}_3\text{F}$	1	1	1
$\text{H}_2\text{O}$	1	1	1
$\text{HF}$	1	1	1
$\text{H}_3\text{O}^+$	1	1	1

## A.2 Bulk

**Table A.2:** Listing of the used k-point grids (see [equation \(2.44\)](#)) for different crystalline systems and their **UC** and **SC** representations - staying with even integers.

Structure	SC Size	$Q_1$	$Q_2$	$Q_3$
Gibbsite	$1 \times 1 \times 1$	2	4	2
	$2 \times 1 \times 1$	2	4	2
	$2 \times 2 \times 1$	2	2	2
Doyleite	$1 \times 1 \times 1$	2	2	4
	$2 \times 1 \times 1$	2	2	4
	$2 \times 1 \times 2$	2	2	2
Bayerite	$1 \times 1 \times 1$	4	2	2
	$2 \times 1 \times 1$	2	2	2
	$2 \times 2 \times 1$	2	2	2
Diaspore	$1 \times 1 \times 1$	2	4	2
	$2 \times 1 \times 1$	2	4	2
	$2 \times 1 \times 2$	2	2	2
Boehmite	$1 \times 1 \times 1$	8	2	6
	$2 \times 1 \times 1$	4	2	6
	$2 \times 1 \times 2$	4	2	4

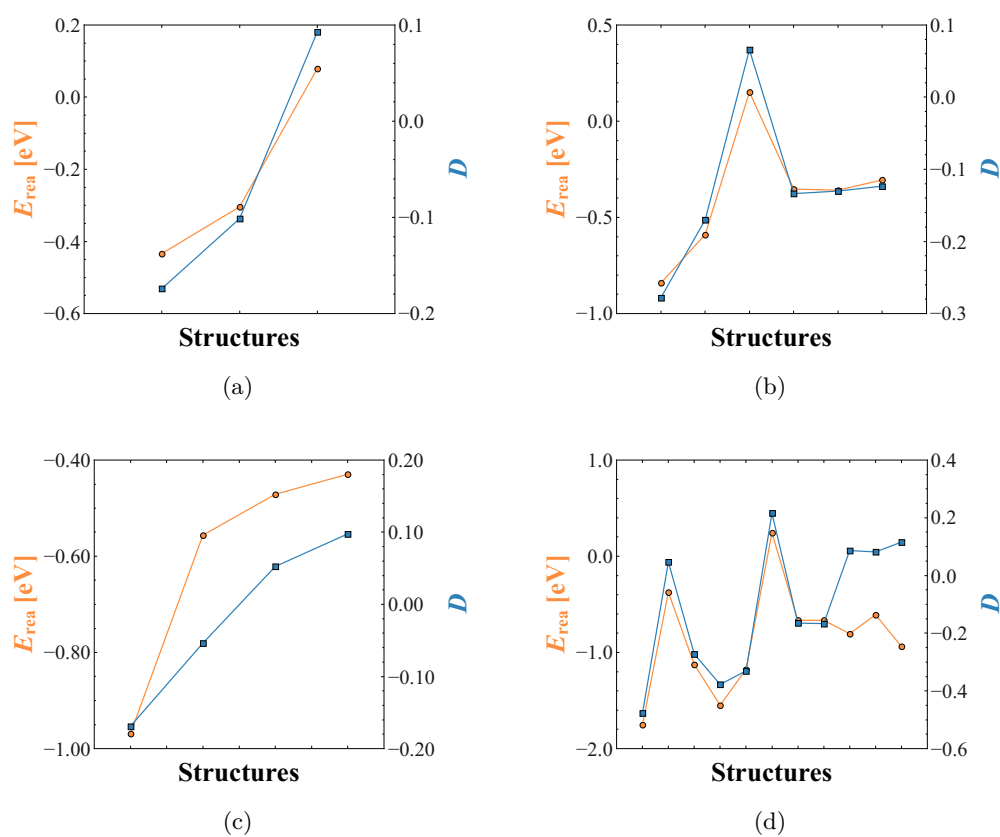


**Figure A.1:** Graphical representation of the reaction energy  $E_{\text{rea}}$  and the structure parameter  $D(i)$  for gibbsite in dependency on the structures per fluorination degree of  $\text{Al}(\text{OH})_{3-x}\text{F}_x$  - (a)  $x = 0.03125$ , (b)  $x = 0.06250$ , (c)  $x = 0.09375$ , and (d)  $x = 0.12500$  (VASP-DFT, PBE/PAW, 600.0 eV energy cut-off, D3-BJ).

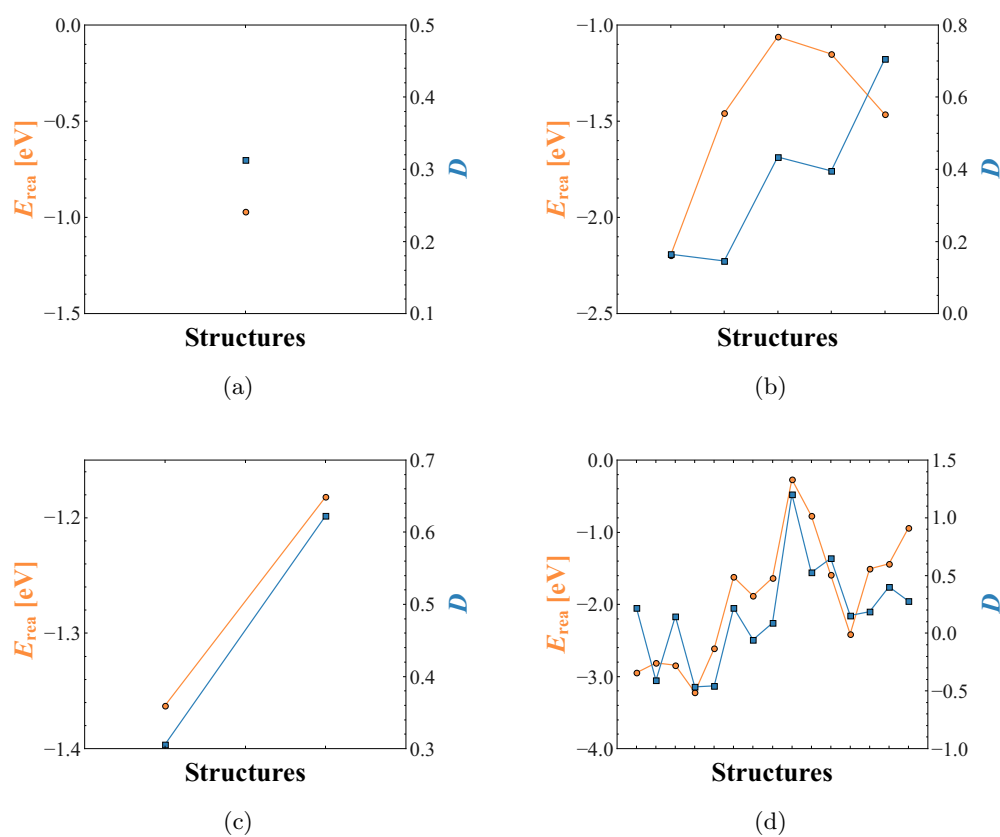


**Figure A.2:** Graphical representation of the reaction energy  $E_{\text{rea}}$  and the structure parameter  $D(i)$  for gibbsite in dependency on the structures per fluorination degree of  $\text{Al}(\text{OH})_{3-x}\text{F}_x$  - (a)  $x = 0.15625$ , (b)  $x = 0.18750$ , (c)  $x = 0.21875$ , and (d)  $x = 0.25000$  (VASP-DFT, PBE/PAW, 600.0 eV energy cut-off, D3-BJ).



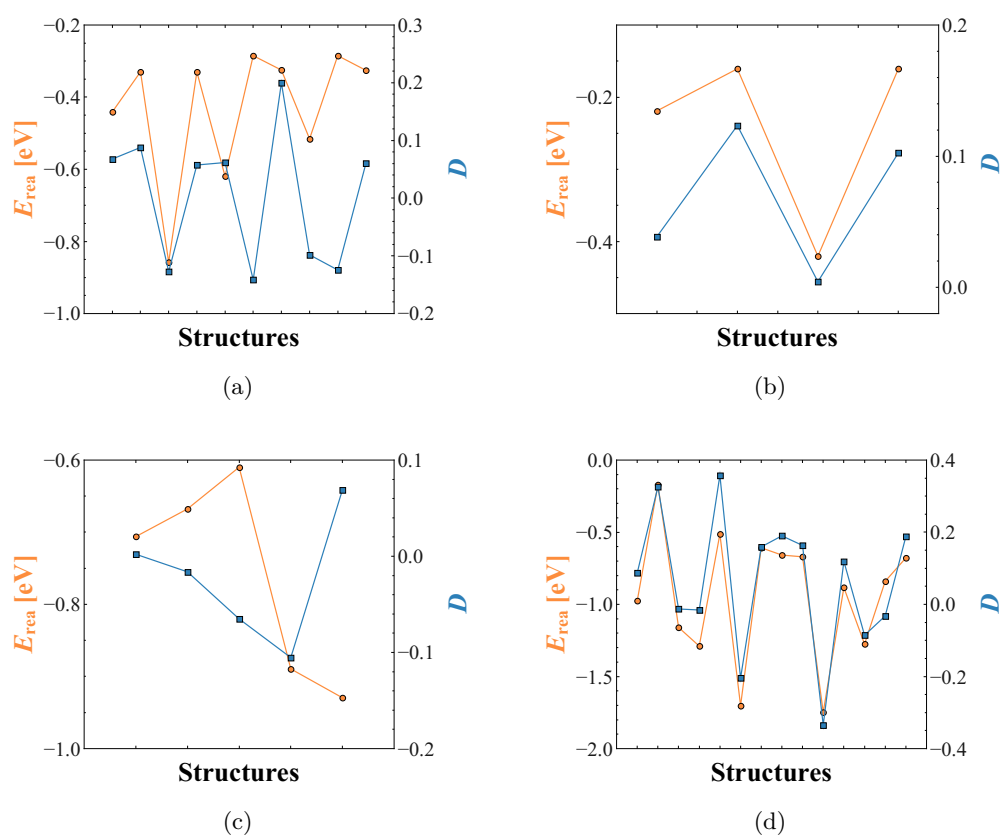


**Figure A.3:** Graphical representation of the reaction energy  $E_{\text{rea}}$  and the structure parameter  $D(i)$  for bayerite in dependency on the structures per fluorination degree of  $\text{Al}(\text{OH})_{3-x}\text{F}_x$  - (a)  $x = 0.03125$ , (b)  $x = 0.06250$ , (c)  $x = 0.09375$ , and (d)  $x = 0.12500$  (VASP-DFT, PBE/PAW, 600.0 eV energy cut-off, D3-BJ).

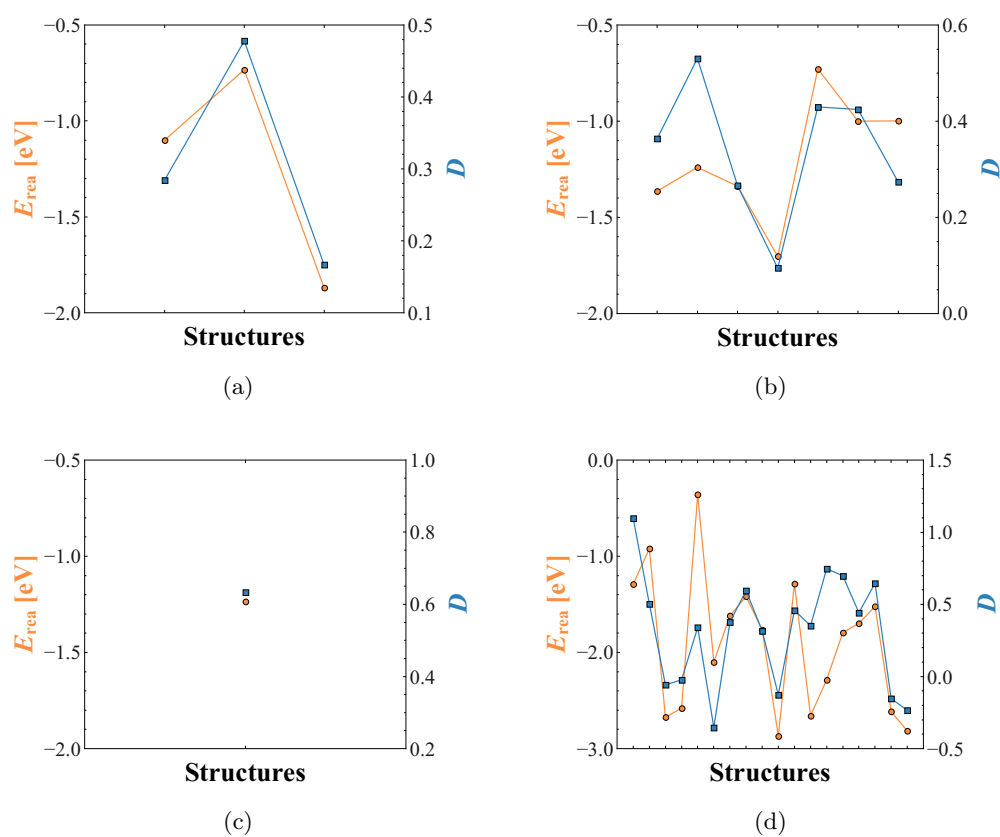


**Figure A.4:** Graphical representation of the reaction energy  $E_{\text{rea}}$  and the structure parameter  $D(i)$  for bayerite in dependency on the structures per fluorination degree of  $\text{Al}(\text{OH})_{3-x}\text{F}_x$  - (a)  $x = 0.15625$ , (b)  $x = 0.18750$ , (c)  $x = 0.21875$ , and (d)  $x = 0.25000$  (VASP-DFT, PBE/PAW, 600.0 eV energy cut-off, D3-BJ).

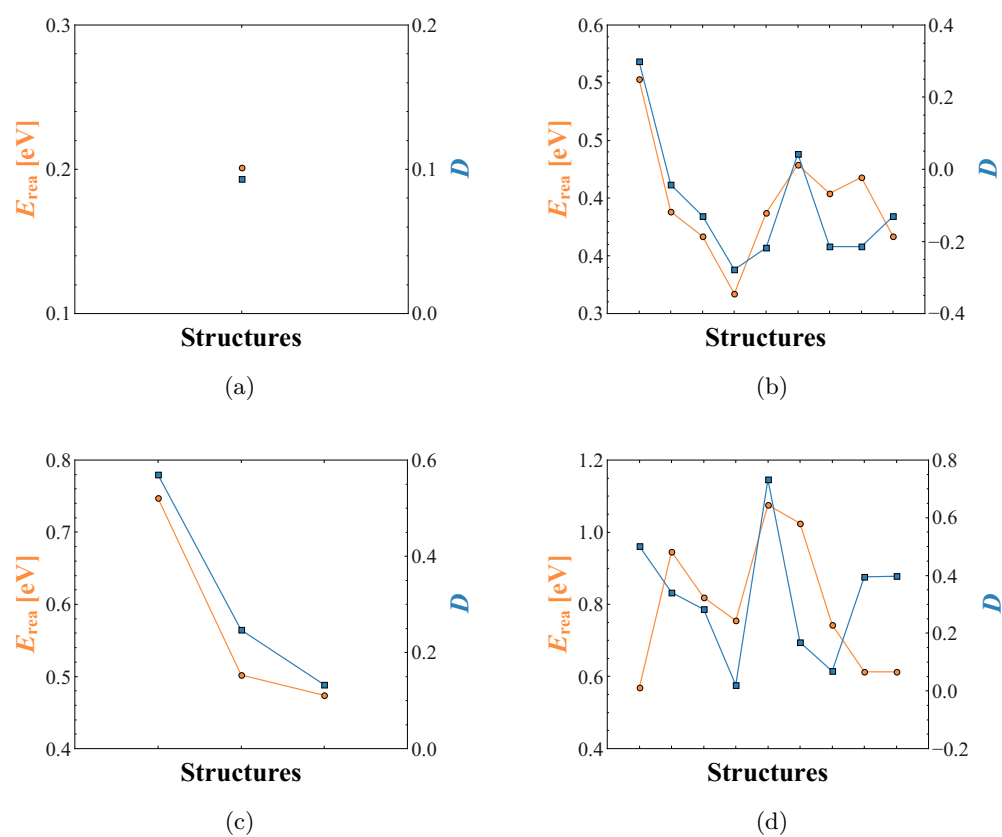


**Figure A.5:** Graphical representation of the reaction energy  $E_{\text{rea}}$  and the structure parameter  $D(i)$  for diasporite in dependency on the structures per fluorination degree of  $\text{AlO}(\text{OH})_{1-y}\text{F}_y$  - (a)  $y = 0.0625$ , (b)  $y = 0.1250$ , (c)  $y = 0.1875$ , and (d)  $y = 0.2500$  (VASP-DFT, PBE/PAW, 600.0 eV energy cut-off, D3-BJ).

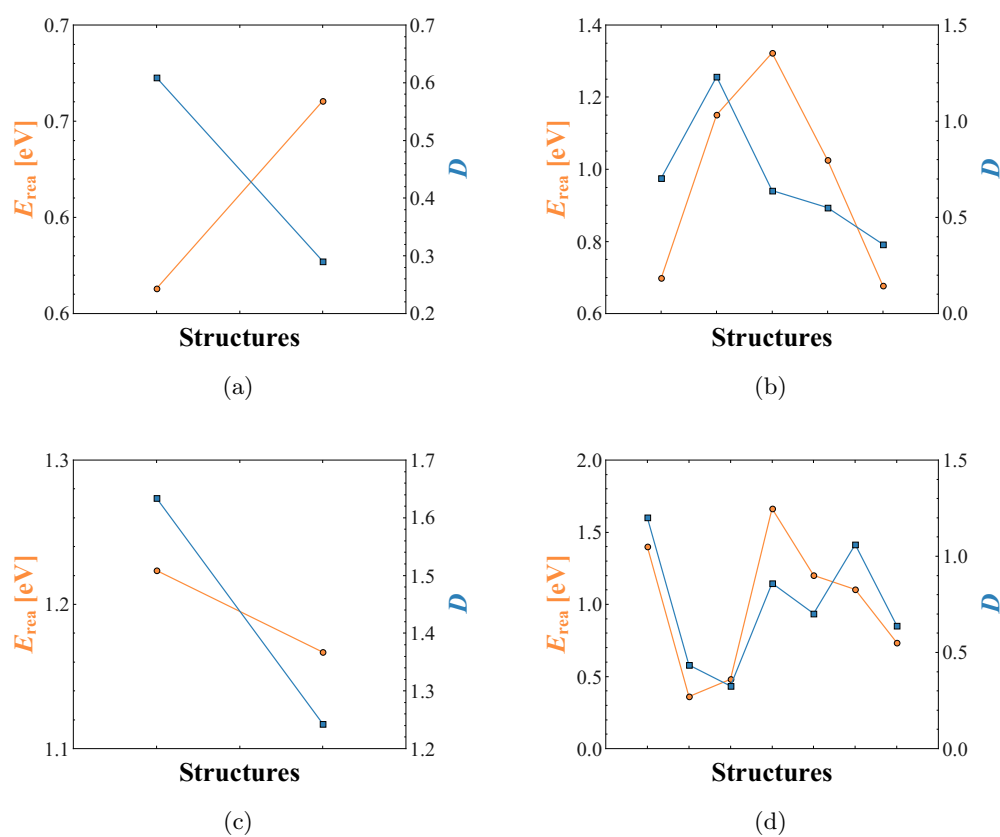


**Figure A.6:** Graphical representation of the reaction energy  $E_{\text{rea}}$  and the structure parameter  $D(i)$  for diasporite in dependency on the structures per fluorination degree of  $\text{AlO}(\text{OH})_{1-y}\text{F}_y$  - (a)  $y = 0.3125$ , (b)  $y = 0.3750$ , (c)  $y = 0.4375$ , and (d)  $y = 0.5010$  (VASP-DFT, PBE/PAW, 600.0 eV energy cut-off, D3-BJ).

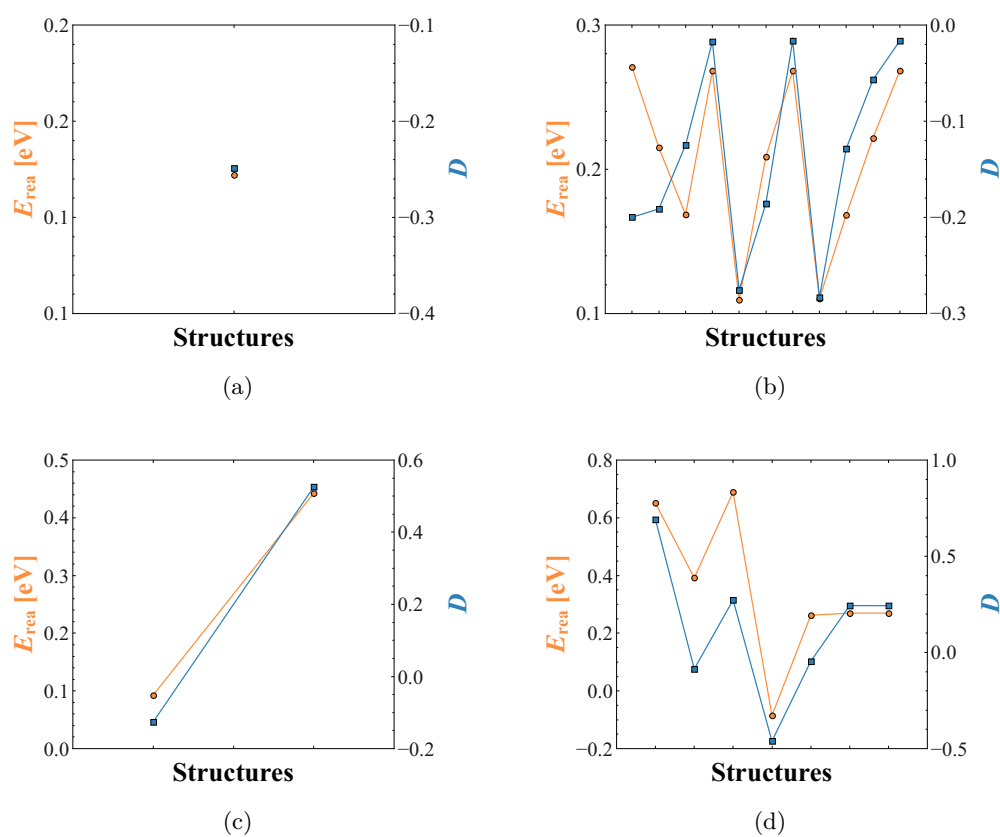


**Figure A.7:** Graphical representation of the reaction energy  $E_{\text{rea}}$  and the structure parameter  $D(i)$  for boehmite in dependency on the structures per fluorination degree of  $\text{AlO}(\text{OH})_{1-y}\text{F}_y$  - (a)  $y = 0.0625$ , (b)  $y = 0.1250$ , (c)  $y = 0.1875$ , and (d)  $y = 0.2500$  (VASP-DFT, PBE/PAW, 600.0 eV energy cut-off, D3-BJ).

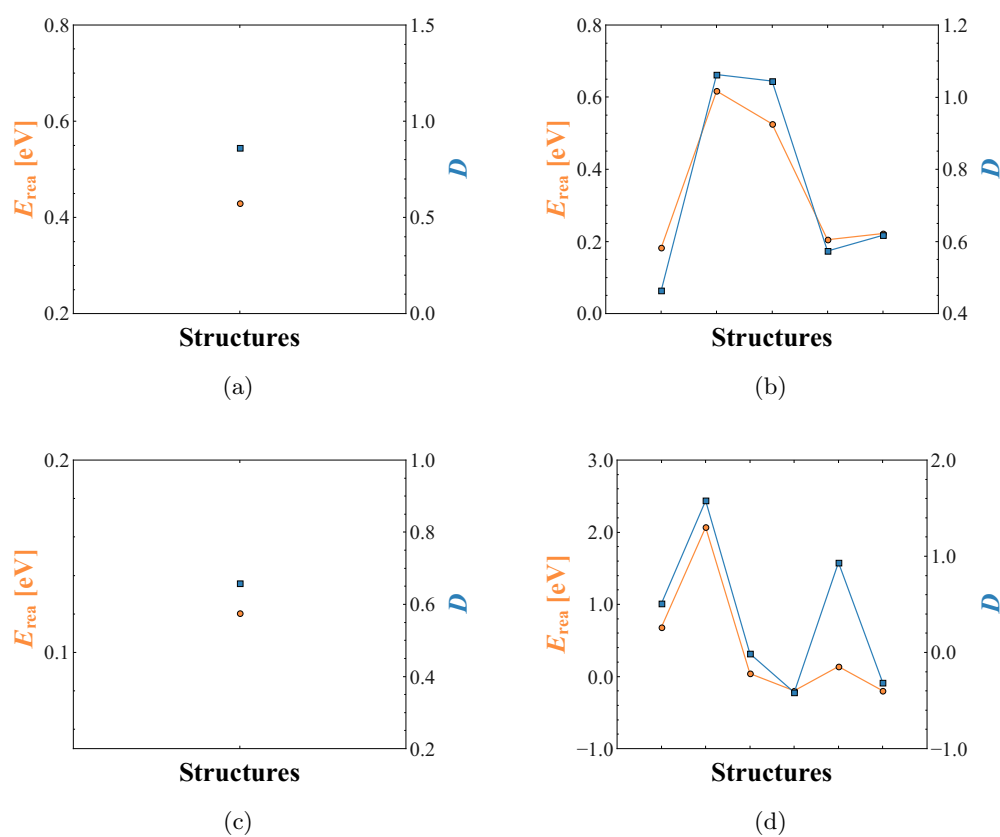


**Figure A.8:** Graphical representation of the reaction energy  $E_{\text{rea}}$  and the structure parameter  $D(i)$  for diaspore in dependency on the structures per fluorination degree of  $\text{AlO}(\text{OH})_{1-y}\text{F}_y$  - (a)  $y = 0.3125$ , (b)  $y = 0.3750$ , (c)  $y = 0.4375$ , and (d)  $y = 0.5010$  (VASP-DFT, PBE/PAW, 600.0 eV energy cut-off, D3-BJ).

**Table A.3:** Reaction energy, parameters and the sum of them for all considered structures of gibbsite (VASP-DFT, PBE/PAW, 600.0 eV energy cut-off, D3-BJ).

Struc.	Energy	Distortion	Charge	FH-Bonds		OH-Bonds		Sym.	F-Distribution			Layer Distance		Layer Stoichio.		$\kappa$
	[eV]		[Å]	$[\frac{1}{\text{Å}}]$	$[\frac{1}{\text{Å}}]$	$[\frac{1}{\text{Å}}]$	$[\frac{1}{\text{Å}}]$		$[\frac{1}{\text{Å}}]$	$[\frac{1}{\text{Å}}]$	$[\frac{1}{\text{Å}}]$	[Å]	[Å]	[Å]		
1-0	-1332.61	0.0420	0.0701	0.5764	0.3590	35.2976	5.4400	1	0.1789	0.0357	0.0116	4.7554	0.0000	0.0208	0.0208	-0.17403
1-1	-1332.48	0.0423	0.0704	0.5584	0.3631	34.2052	5.9417	1	0.1789	0.0357	0.0126	4.7579	0.0000	0.0208	0.0208	-0.10139
1-2	-1332.10	0.0428	0.0734	0.5029	0.3700	34.7478	5.4052	1	0.1789	0.0375	0.0121	4.7740	0.0000	0.0208	0.0208	0.09269
2-0	-1326.69	0.0425	0.0879	1.1580	0.7157	34.7676	5.3422	2	0.1557	0.0131	0.0005	4.7512	0.0000	0.0417	0.0417	-0.27797
2-1	-1326.43	0.0425	0.0866	1.1155	0.7234	31.5692	5.7756	2	0.1557	0.0129	0.0010	4.7570	0.0000	0.0417	0.0417	-0.17026
2-2	-1325.69	0.0429	0.0926	0.0000	0.7709	33.5755	5.2261	2	0.1557	0.0130	0.0010	4.7998	0.0000	0.0417	0.0417	0.06581
2-3	-1326.20	0.0425	0.0723	0.5780	0.7476	34.1788	5.4614	1	0.1557	0.0042	0.0004	4.7737	0.0000	0.0000	0.0417	-0.13371
2-4	-1326.20	0.0425	0.0724	0.5779	0.7477	34.1760	5.4819	1	0.1557	0.0042	0.0004	4.7736	0.0000	0.0000	0.0417	-0.13019
2-5	-1326.15	0.0428	0.0864	1.0520	0.7442	33.1244	5.4873	1	0.0365	0.0195	0.0013	4.7716	0.0000	0.0417	0.0417	-0.12331
3-0	-1320.48	0.0427	0.1020	1.6904	1.0884	33.0779	5.5845	1	0.0360	0.0023	0.0042	4.7605	0.0000	0.0625	0.0625	-0.16895
3-1	-1320.06	0.0432	0.0885	1.1335	1.1095	33.0300	5.4859	1	0.0556	0.0021	0.0002	4.7724	0.0000	0.0208	0.0625	-0.05380
3-2	-1319.98	0.0435	0.0887	1.1135	1.1258	33.5882	5.3940	1	0.0680	0.0024	0.0003	4.7763	0.0000	0.0208	0.0625	0.05252
3-3	-1319.94	0.0434	0.1037	1.0914	1.1426	33.0854	5.4994	1	0.0422	0.0037	0.0045	4.7744	0.0000	0.0625	0.0625	0.09771
4-0	-1314.93	0.0427	0.1192	2.3041	1.4336	33.4820	5.4435	4	0.1094	0.0099	0.0231	4.7572	0.0000	0.0833	0.0833	-0.47664
4-1	-1313.55	0.0445	0.1303	2.1940	1.4307	33.5418	5.3038	4	0.1094	0.0091	0.0221	4.7675	0.0000	0.0833	0.0833	0.04674
4-2	-1314.30	0.0425	0.1206	2.2366	1.4459	27.4056	5.5213	4	0.1094	0.0095	0.0221	4.7568	0.0000	0.0833	0.0833	-0.27220
4-3	-1314.72	0.0425	0.1110	2.2459	1.4440	29.3638	5.2906	4	0.1094	0.0086	0.0210	4.7547	0.0000	0.0833	0.0833	-0.37755
4-4	-1314.35	0.0425	0.1201	2.2283	1.4358	31.4568	4.7163	4	0.1094	0.0099	0.0236	4.7774	0.0000	0.0833	0.0833	-0.33042
4-5	-1312.93	0.0434	0.1309	0.0000	1.5413	31.0956	5.0106	4	0.1094	0.0103	0.0221	4.8609	0.0000	0.0833	0.0833	0.21585
4-6	-1313.84	0.0430	0.0908	1.1667	1.4880	31.3845	5.0376	2	0.0295	0.0081	0.0221	4.8009	0.0000	0.0000	0.0833	-0.16505
4-7	-1313.84	0.0429	0.0908	1.1664	1.4880	31.3858	5.0376	2	0.0295	0.0081	0.0221	4.8012	0.0000	0.0000	0.0833	-0.16686
4-8	-1313.98	0.0430	0.1213	1.0975	1.4872	31.3219	5.6069	2	0.0446	0.0092	0.0219	4.7943	0.0000	0.0833	0.0833	0.08647
4-9	-1313.78	0.0437	0.1158	1.6684	1.4701	32.4714	5.3119	1	0.0233	0.0013	0.0113	4.7758	0.0000	0.0000	0.0833	0.08152
4-10	-1314.11	0.0432	0.1030	1.6891	1.4713	31.8792	5.5960	1	0.0629	0.0047	0.0053	4.7736	0.0000	0.0417	0.0833	0.11580
5-0	-1307.81	0.0438	0.1413	2.2222	1.8095	31.3627	5.1536	1	0.0342	0.0011	0.0136	4.7734	0.0000	0.0208	0.1042	0.31314
6-0	-1302.70	0.0429	0.1454	3.3632	2.1850	30.3029	5.7261	2	0.0660	0.0061	0.0008	4.7626	0.0000	0.1250	0.1250	0.16448
6-1	-1301.96	0.0429	0.1205	2.2732	2.2061	29.0924	4.8809	2	0.0377	0.0061	0.0449	4.8011	0.0000	0.0417	0.1250	0.14588
6-2	-1301.56	0.0441	0.1247	2.2338	2.2370	30.6778	5.4105	1	0.0350	0.0009	0.0001	4.7738	0.0000	0.0417	0.1250	0.43406
6-3	-1301.65	0.0438	0.1699	2.7881	2.1610	30.2112	5.1999	1	0.0367	0.0008	0.0155	4.7678	0.0000	0.0000	0.1250	0.39556
6-4	-1301.97	0.0441	0.1517	2.7685	2.2226	30.2491	5.5450	1	0.0321	0.0138	0.0006	4.7768	0.0000	0.1250	0.1250	0.70589
7-0	-1295.53	0.0440	0.1677	3.3162	2.5467	28.0552	5.4904	1	0.0218	0.0084	0.0084	4.7755	0.0000	0.0208	0.0208	0.30572
7-1	-1295.35	0.0444	0.1621	2.7433	2.6397	28.0564	5.2744	1	0.0298	0.0247	0.0167	4.7934	0.0000	0.0625	0.0208	0.62270

**Table A.3:** Reaction energy, parameters and the sum of them for all considered structures of gibbsite (VASP-DFT, PBE/PAW, 600.0 eV energy cut-off, D3-BJ).

Struc.	Energy	Distortion	Charge	FH-Bonds	OH-Bonds	Sym.	F-Distribution			Layer Distance		Layer Stoichio.		$\kappa$		
	[eV]		[Å]	$[\frac{1}{\text{Å}}]$	$[\frac{1}{\text{Å}}]$		$[\frac{1}{\text{Å}}]$	$[\frac{1}{\text{Å}}]$	$[\frac{1}{\text{Å}}]$	$[\frac{1}{\text{Å}}]$	[Å]					
8-0	-1290.78	0.0428	0.1822	4.4893	2.8900	25.0586	4.2804	4	0.0548	0.0028	0.0003	4.7629	0.0000	0.1667	0.1667	0.21736
8-1	-1290.64	0.0427	0.1165	4.5034	2.8721	23.0007	5.2926	4	0.0168	0.0017	0.0001	4.7590	0.0000	0.0000	0.1667	-0.40954
8-2	-1290.67	0.0435	0.1742	4.4790	2.8896	31.1709	5.6338	4	0.0626	0.0033	0.0692	4.7867	0.0000	0.1667	0.1667	0.14611
8-3	-1291.05	0.0432	0.1851	4.5193	2.8769	31.0920	5.6401	4	0.0084	0.0012	0.0001	4.7721	0.0000	0.0000	0.1667	-0.46492
8-4	-1290.44	0.0421	0.1980	0.0000	2.9013	33.5846	5.2466	4	0.0473	0.0033	0.0000	4.7814	0.0000	0.1667	0.0000	-0.45629
8-5	-1289.45	0.0445	0.1913	4.4210	2.9066	23.1348	4.8017	4	0.0111	0.0022	0.0003	4.7441	0.0000	0.0000	0.1667	0.21968
8-6	-1289.71	0.0447	0.1146	4.4590	2.8409	27.0094	5.3405	4	0.0168	0.0015	0.0001	4.7729	0.0000	0.0000	0.1667	-0.05642
8-7	-1289.46	0.0457	0.1937	4.5380	2.8736	26.9829	4.5773	4	0.0168	0.0019	0.0001	4.7690	0.0000	0.0000	0.0000	0.08834
8-8	-1288.10	0.0458	0.1908	2.0545	3.0767	29.0029	4.5733	4	0.0443	0.0035	0.0690	4.8631	0.0000	0.1667	0.1667	1.20355
8-9	-1288.60	0.0452	0.2108	0.0000	2.9726	31.2427	5.3155	4	0.0424	0.0035	0.0000	4.8197	0.0000	0.1667	0.0000	0.52536
8-10	-1289.42	0.0441	0.1798	3.3190	2.9956	26.9915	4.3508	2	0.0334	0.0039	0.0171	4.8099	0.0000	0.0000	0.1667	0.64836
8-11	-1290.24	0.0428	0.1596	3.3458	2.9211	27.0092	4.9996	2	0.0247	0.0034	0.0340	4.7915	0.0000	0.0000	0.1667	0.15369
8-12	-1289.34	0.0440	0.1908	4.3236	2.9146	28.8447	5.2059	1	0.0168	0.0004	0.0001	4.7856	0.0000	0.0000	0.0000	0.18642
8-13	-1289.27	0.0441	0.1793	3.3199	2.9537	26.3848	5.0299	1	0.0220	0.0186	0.0347	4.7748	0.0000	0.0000	0.0000	0.40222
8-14	-1288.77	0.0442	0.1517	3.3001	2.9629	27.8452	5.1400	1	0.0199	0.0007	0.0516	4.7882	0.0000	0.0000	0.0000	0.27837



**Table A.4:** Reaction energy, parameters and the sum of them for all considered structures of doyleite (VASP-DFT, PBE/PAW, 600.0 eV energy cut-off, D3-BJ).

Struc.	Energy	Distortion	Charge	FH-Bonds		OH-Bonds		Sym.	F-Distribution			Layer Distance		Layer Stoichio.		$\kappa$
	[eV]		[Å]	$[\frac{1}{\text{Å}}]$	$[\frac{1}{\text{Å}}]$	$[\frac{1}{\text{Å}}]$	$[\frac{1}{\text{Å}}]$		$[\frac{1}{\text{Å}}]$	$[\frac{1}{\text{Å}}]$	$[\frac{1}{\text{Å}}]$	[Å]	[Å]	[Å]	[Å]	
16-0	-1,240.14	0.0485	0.3371	9.2200	6.0665	18.1012	3.5601	8	0.1684	0.0011	0.0000	4.5225	0.0000	0.0000	0.0833	1.22266
16-1	-1,239.37	0.0457	0.3397	6.8119	5.8325	17.9130	4.8417	4	0.1684	0.0014	0.0001	4.7119	0.0000	0.2000	0.0833	1.72744
16-2	-1,240.22	0.0445	0.3652	9.0454	5.7292	18.1964	3.0885	8	0.1684	0.0025	0.0001	4.6712	0.0000	0.4000	0.0833	1.55739
16-3	-1,242.92	0.0420	0.3000	9.1887	6.0751	18.6457	4.4671	16	0.1684	0.0012	0.0000	4.4934	0.0000	0.0182	0.0556	-0.43584
16-4	-1,241.49	0.0495	0.3288	9.2118	5.7917	20.4364	6.5296	2	0.1705	0.0015	0.0001	4.5462	0.0000	0.2222	0.0490	1.33412
16-5	-1,242.11	0.0476	0.3268	9.2462	5.7734	21.3486	5.7085	2	0.1705	0.0013	0.0001	4.4455	0.0000	0.1103	0.0556	0.76553

**Table A.5:** Reaction energy, parameters and the sum of them for all considered structures of bayerite (VASP-DFT, PBE/PAW, 600.0 eV energy cut-off, D3-BJ).

Struc.	Energy	Distortion	Charge	FH-Bonds		OH-Bonds		Sym.	F-Distribution		Layer Distance		Layer Stoichio.		$\kappa$	
	[eV]		[Å]	[ $\frac{1}{\text{Å}}$ ]	[ $\frac{1}{\text{Å}}$ ]	[ $\frac{1}{\text{Å}}$ ]	[ $\frac{1}{\text{Å}}$ ]		[ $\frac{1}{\text{Å}}$ ]	[Å]						
1-0	-1,330.89	0.0412	0.0610	0.0000	0.3836	31.6790	3.9709	1	0.1478	0.0294613	0.0121	4.6354	0.0000	0.0208	0.0208	0.03859
1-1	-1,330.83	0.0414	0.0595	0.5102	0.3687	30.1407	3.8011	1	0.1478	0.0356535	0.0111	4.6338	0.0000	0.0208	0.0208	0.12338
1-2	-1,331.09	0.0412	0.0587	0.5064	0.3644	31.2061	3.9024	1	0.1478	0.0294613	0.0106	4.6245	0.0000	0.0208	0.0208	0.00430
1-3	-1,330.83	0.0414	0.0595	0.5100	0.3682	30.1431	3.8012	1	0.1478	0.0356535	0.0111	4.6219	0.0000	0.0208	0.0208	0.10253
2-0	-1,324.78	0.0414	0.0808	0.0000	0.7674	29.6243	3.8288	2	0.1246	0.0140292	0.0015	4.6524	0.0000	0.0417	0.0417	0.06779
2-1	-1,324.66	0.0417	0.0786	1.0161	0.7369	29.5796	3.8681	2	0.1246	0.0220459	0.0009	4.6380	0.0000	0.0417	0.0417	0.08781
2-2	-1,325.19	0.0412	0.0765	1.0069	0.7295	30.7110	3.9175	2	0.1246	0.0140292	0.0000	4.6250	0.0000	0.0417	0.0417	-0.12739
2-3	-1,324.66	0.0417	0.0785	1.0153	0.7362	29.5706	3.8871	2	0.1246	0.0220459	0.0009	4.6271	0.0000	0.0417	0.0417	0.05745
2-4	-1,324.95	0.0415	0.0603	0.5083	0.7471	29.6265	3.7869	1	0.1246	0.0010738	0.0007	4.6425	0.0000	0.0000	0.0417	0.06172
2-5	-1,324.62	0.0415	0.0817	0.0000	0.7517	30.6225	3.8876	1	0.0345	0.0164651	0.0012	4.6254	0.0000	0.0000	0.0417	-0.14153
2-6	-1,324.66	0.0418	0.0616	0.5200	0.7419	28.0607	3.6437	1	0.1246	0.0013726	0.0002	4.6357	0.0000	0.0000	0.0417	0.19988
2-7	-1,324.85	0.0416	0.0790	1.0305	0.7308	29.7136	3.7278	1	0.0434	0.0156137	0.0002	4.6225	0.0000	0.0000	0.0417	-0.09821
2-8	-1,324.62	0.0415	0.0817	0.0000	0.7512	30.6232	3.8874	1	0.0345	0.0164651	0.0010	4.6324	0.0000	0.0000	0.0417	-0.12446
2-9	-1,324.66	0.0417	0.0773	1.0262	0.7387	27.5597	3.6402	2	0.1246	0.0012731	0.0005	4.6093	0.0000	0.0000	0.0417	0.06020
3-0	-1,318.70	0.0418	0.1012	0.5211	1.1222	30.1758	3.8040	1	0.0258	0.0025317	0.0117	4.6352	0.0000	0.0625	0.0625	0.00209
3-1	-1,318.67	0.0418	0.0890	1.0282	1.1094	29.1369	3.7127	1	0.0297	0.0015662	0.0114	4.6398	0.0000	0.0208	0.0625	-0.01620
3-2	-1,318.61	0.0415	0.1023	0.5018	1.1054	30.1008	3.8490	1	0.0337	0.0029718	0.0119	4.6273	0.0000	0.0208	0.0625	-0.06514
3-3	-1,318.89	0.0415	0.0956	1.5579	1.0939	28.5693	3.7213	1	0.0244	0.0019943	0.0122	4.6184	0.0000	0.0625	0.0625	-0.10534
3-4	-1,318.93	0.0415	0.0957	1.0143	1.1044	28.6247	3.7295	1	0.1015	0.0025317	0.0001	4.6441	0.0000	0.0208	0.0208	0.06905
4-0	-1,312.64	0.0416	0.1208	0.0000	1.5086	27.6284	3.8078	4	0.0783	0.0077075	0.0205	4.6711	0.0000	0.0833	0.0833	0.08727
4-1	-1,311.83	0.0423	0.1233	0.0000	1.4828	27.2776	3.6730	4	0.0783	0.0097365	0.0236	4.7003	0.0000	0.0833	0.0833	0.32577
4-2	-1,312.82	0.0418	0.1214	0.0000	1.5336	29.7481	3.9173	4	0.0783	0.0082772	0.0236	4.6411	0.0000	0.0833	0.0833	-0.01287
4-3	-1,312.95	0.0411	0.1048	0.2071	1.4893	23.3751	3.2934	4	0.0783	0.0085667	0.0221	4.6597	0.0000	0.0833	0.0833	-0.01561
4-4	-1,312.18	0.0430	0.1161	2.0811	1.5151	25.6337	3.2094	4	0.0783	0.0091960	0.0236	4.6266	0.0000	0.0833	0.0833	0.35787
4-5	-1,313.36	0.0415	0.1130	2.0144	1.4567	29.7306	3.7179	4	0.0783	0.0078686	0.0236	4.6293	0.0000	0.0833	0.0833	-0.20444
4-6	-1,312.27	0.0424	0.1149	2.0401	1.4625	27.3669	3.8328	4	0.0783	0.0098108	0.0236	4.6566	0.0000	0.0833	0.0833	0.15926
4-7	-1,312.32	0.0418	0.0826	1.0351	1.4978	25.4544	3.5524	2	0.0783	0.0007288	0.0000	4.6475	0.0000	0.0000	0.0833	0.18995
4-8	-1,312.33	0.0420	0.1145	2.0287	1.4776	21.4357	3.0308	4	0.0783	0.0006888	0.0000	4.6017	0.0000	0.0000	0.0833	0.16333
4-9	-1,313.41	0.0413	0.1137	2.0225	1.4585	29.6713	3.9345	4	0.0783	0.0002638	0.0000	4.6252	0.0000	0.0000	0.0833	-0.33461
4-10	-1,312.55	0.0420	0.1134	0.5271	1.5249	29.2047	3.8381	1	0.0227	0.0075001	0.0230	4.6330	0.0000	0.0000	0.0833	0.11921
4-11	-1,312.94	0.0411	0.1161	0.0000	1.5030	24.5423	3.3160	2	0.0452	0.0091978	0.0000	4.6355	0.0000	0.0000	0.0000	-0.08565
4-12	-1,312.50	0.0417	0.0847	1.0308	1.4802	29.1120	3.7323	1	0.0224	0.0012223	0.0229	4.6327	0.0000	0.0000	0.0833	-0.03215
4-13	-1,312.34	0.0420	0.1229	1.0307	1.4864	28.5742	3.6805	1	0.0337	0.0077099	0.0229	4.6241	0.0000	0.0000	0.0833	0.18800
5-0	-1,306.43	0.0423	0.1317	1.0546	1.8690	28.6729	3.7479	1	0.0208	0.0060434	0.0342	4.6288	0.0000	0.0208	0.1042	0.28406
5-1	-1,306.06	0.0423	0.1465	1.0378	1.8906	26.9611	3.5353	1	0.0345	0.0073601	0.0348	4.6452	0.0000	0.0208	0.1042	0.47788
5-2	-1,307.20	0.0418	0.1307	2.0192	1.8481	27.6685	3.6891	1	0.0552	0.0105330	0.0001	4.6337	0.0000	0.0625	0.0625	0.16668
6-0	-1,300.35	0.0424	0.1363	2.0540	2.2193	26.5729	3.5080	2	0.0230	0.0144557	0.0157	4.6514	0.0000	0.0417	0.1250	0.36394
6-1	-1,300.23	0.0421	0.1622	0.0000	2.2418	26.4419	3.6407	2	0.0282	0.0451675	0.0465	4.6366	0.0000	0.0417	0.1250	0.53049
6-2	-1,300.33	0.0422	0.1466	1.0598	2.2347	27.6254	3.5967	2	0.0229	0.0001225	0.0309	4.6264	0.0000	0.0000	0.1250	0.26611
6-3	-1,300.69	0.0412	0.1546	0.0000	2.2361	25.4864	3.5168	2	0.0283	0.0196062	0.0153	4.6537	0.0000	0.0000	0.0417	0.09455
6-4	-1,299.72	0.0424	0.0990	1.0371	2.2392	26.8154	3.5736	1	0.0381	0.0001057	0.0464	4.6504	0.0000	0.0000	0.1250	0.42965
6-5	-1,299.99	0.0417	0.1619	1.0612	2.2420	25.3329	3.7318	1	0.0367	0.0022385	0.0001	4.6618	0.0000	0.0000	0.1250	0.42449
6-6	-1,299.99	0.0418	0.1391	0.5058	2.2641	27.3962	4.0657	1	0.0223	0.0019846	0.0158	4.6590	0.0000	0.0000	0.1250	0.27366

**Table A.5:** Reaction energy, parameters and the sum of them for all considered structures of bayerite (VASP-DFT, PBE/PAW, 600.0 eV energy cut-off, D3-BJ).

Struc.	Energy	Distortion	Charge	FH-Bonds	OH-Bonds	Sym.	F-Distribution		Layer Distance		Layer Stoichio.		$\kappa$			
	[eV]		[Å]	$[\frac{1}{\text{Å}}]$	$[\frac{1}{\text{Å}}]$		$[\frac{1}{\text{Å}}]$	$[\frac{1}{\text{Å}}]$	[Å]							
7-0	-1,293.89	0.0435	0.1711	1.0328	2.6259	26.0475	3.4654	1	0.0184	0.0172976	0.0083	4.6432	0.0000	0.0208	0.0208	0.63405
8-0	-1,287.61	0.0427	0.1997	0.0000	3.0232	19.2707	3.0791	4	0.0424	0.0016589	0.0001	4.7603	0.0000	0.1667	0.1667	1.09619
8-1	-1,287.24	0.0428	0.1277	0.0000	2.9724	23.1331	3.6003	4	0.0142	0.0016875	0.0001	4.6912	0.0000	0.0000	0.1667	0.50392
8-2	-1,288.99	0.0422	0.1919	2.0686	2.9663	25.6008	3.8004	4	0.0142	0.0006202	0.0000	4.6810	0.0000	0.0000	0.0000	-0.05817
8-3	-1,288.90	0.0413	0.1181	0.0000	3.0780	25.6685	3.7887	4	0.0142	0.0014189	0.0001	4.6645	0.0000	0.0000	0.1667	-0.02294
8-4	-1,286.67	0.0428	0.2024	0.0000	2.9301	21.1354	3.2656	8	0.0142	0.0019105	0.0001	4.6569	0.0000	0.0000	0.1667	0.33964
8-5	-1,288.42	0.0418	0.1963	4.1476	2.9190	21.0941	3.0972	8	0.0142	0.0007920	0.0001	4.6851	0.0000	0.1667	0.0000	-0.35357
8-6	-1,287.94	0.0422	0.2060	0.0000	2.9803	25.4971	3.8123	4	0.0142	0.0047659	0.0701	4.5883	0.0000	0.1667	0.1667	0.37782
8-7	-1,287.74	0.0446	0.1874	4.2429	2.9765	21.3367	3.1634	4	0.0142	0.0026925	0.0003	4.6650	0.0000	0.0000	0.0000	0.59470
8-8	-1,288.09	0.0423	0.1171	0.0000	3.0269	25.3403	3.5405	4	0.0146	0.0040478	0.0009	4.6953	0.0000	0.0000	0.1667	0.31632
8-9	-1,289.19	0.0408	0.1757	4.1032	3.0032	17.1305	2.5835	8	0.0235	0.0036996	0.0690	4.6669	0.0000	0.0000	0.1667	-0.12649
8-10	-1,287.60	0.0437	0.1925	4.1130	2.9033	21.3851	3.0018	4	0.0142	0.0009193	0.0001	4.6586	0.0000	0.1667	0.0000	0.45922
8-11	-1,288.98	0.0421	0.1895	2.0997	2.9848	25.4410	3.6988	4	0.0263	0.0019467	0.0003	4.6641	0.0000	0.1667	0.1667	0.35142
8-12	-1,288.60	0.0431	0.1819	0.0000	3.1220	25.4343	3.2063	4	0.0218	0.0018809	0.0689	4.6591	0.0000	0.1667	0.1667	0.74769
8-13	-1,288.11	0.0429	0.1847	1.0401	3.0457	26.6962	3.6698	2	0.0181	0.0195968	0.0349	4.6406	0.0000	0.0000	0.1667	0.69733
8-14	-1,288.02	0.0426	0.1275	2.0523	2.9559	25.4525	3.6077	2	0.0174	0.0011988	0.0346	4.6442	0.0000	0.0000	0.1667	0.44234
8-15	-1,287.84	0.0436	0.1909	1.5348	2.9860	26.0480	3.5177	1	0.0144	0.0003300	0.0088	4.6385	0.0000	0.0417	0.0417	0.64591
8-16	-1,288.93	0.0409	0.1911	0.0000	2.9794	23.4487	3.4458	4	0.0350	0.0019437	0.0014	4.6537	0.0000	0.0000	0.0000	-0.15353
8-17	-1,289.13	0.0407	0.1893	0.0000	2.9993	23.5088	3.4561	4	0.0346	0.0054350	0.0010	4.6382	0.0000	0.0000	0.0000	-0.23441

**Table A.6:** Reaction energy, parameters and the sum of them for all considered structures of diaspore (VASP-DFT, PBE/PAW, 600.0 eV energy cut-off, D3-BJ).

Struc.	Energy	Distortion	Charge	FH-Bonds		OH-Bonds		Sym.	F-Distribution			Layer Distance		Layer Stoichio.		$\kappa$
	[eV]		[Å]	$[\frac{1}{\text{Å}}]$	$[\frac{1}{\text{Å}}]$	$[\frac{1}{\text{Å}}]$	$[\frac{1}{\text{Å}}]$		$[\frac{1}{\text{Å}}]$	$[\frac{1}{\text{Å}}]$	$[\frac{1}{\text{Å}}]$	[Å]	[Å]			
1-0	-424.80	0.0583	0.1998	0.0000	0.3874	9.3220	3.2509	1	0.1015	0.0063	0.0033	2.7326	2.0208	0.1250	0.0625	0.09325
2-0	-418.16	0.0609	0.2214	0.0000	0.7741	8.5207	2.2780	2	0.0827	0.0477	0.0368	2.7826	2.0115	0.2500	0.1250	0.29940
2-1	-418.27	0.0604	0.2243	0.0000	0.7738	8.5874	3.4370	1	0.0076	0.0001	0.0002	2.7720	1.9800	0.2500	0.0000	-0.04279
2-2	-418.29	0.0607	0.2186	0.0000	0.7794	8.5764	3.2473	1	0.0321	0.0002	0.0002	2.7224	2.0167	0.0000	0.1250	-0.12957
2-3	-418.34	0.0604	0.2117	0.0000	0.7769	8.5746	3.4415	2	0.0321	0.0033	0.0006	2.7237	1.9813	0.0000	0.0000	-0.27824
2-4	-418.27	0.0606	0.2211	0.0000	0.7796	8.5520	3.4364	2	0.0321	0.0526	0.0016	2.7232	1.9807	0.0000	0.0000	-0.21786
2-5	-418.23	0.0606	0.2386	0.0000	0.7788	8.5566	3.4405	1	0.0170	0.0003	0.0009	2.7942	1.9768	0.2500	0.0000	0.04259
2-6	-418.26	0.0606	0.2226	0.0000	0.7759	8.5528	3.4441	2	0.0321	0.0526	0.0002	2.7236	1.9808	0.0000	0.0000	-0.21441
2-7	-418.24	0.0606	0.2252	0.0000	0.7756	8.5514	3.4426	2	0.0321	0.0526	0.0002	2.7239	1.9809	0.0000	0.0000	-0.21438
2-8	-418.29	0.0607	0.2186	0.0000	0.7796	8.5753	3.2471	1	0.0321	0.0002	0.0002	2.7213	2.0170	0.0000	0.1250	-0.13029
3-0	-411.58	0.0635	0.2824	0.0000	1.1685	7.7218	2.4668	1	0.0500	0.0010	0.0045	2.8628	1.9637	0.3750	0.0625	0.56948
3-1	-411.82	0.0627	0.2608	0.0000	1.1399	7.8417	3.6344	1	0.0110	0.0005	0.0003	2.7873	1.9831	0.3750	0.0625	0.24673
3-2	-411.85	0.0625	0.2341	0.0000	1.1346	7.8566	3.4321	1	0.0158	0.0003	0.0001	2.8628	1.9784	0.1250	0.0625	0.13277
4-0	-405.42	0.0663	0.2442	0.0000	1.5711	7.0434	1.5011	4	0.0517	0.0034	0.1042	2.8166	1.9939	0.5000	0.2500	0.50151
4-1	-405.04	0.0645	0.2748	0.0000	0.0000	7.1467	1.5225	4	0.0286	0.0011	0.0008	2.8436	1.9364	0.5000	0.0000	0.34130
4-2	-405.17	0.0666	0.2534	0.0000	1.5606	6.9926	1.8804	2	0.0517	0.0006	0.0000	2.7609	1.9931	0.0000	0.2500	0.28272
4-3	-405.24	0.0661	0.2432	0.0000	1.5592	6.9576	1.5030	4	0.0519	0.0062	0.0004	2.7670	1.9237	0.0000	0.0000	0.02030
4-4	-404.91	0.0665	0.3491	0.0000	1.5685	6.8818	1.4961	4	0.0580	0.0021	0.1080	2.9479	1.9109	0.5000	0.0000	0.73256
4-5	-404.97	0.0660	0.2744	0.0000	1.5483	6.9293	1.5141	4	0.0518	0.1403	0.0005	2.7644	1.9267	0.0000	0.0000	0.16854
4-6	-405.25	0.0653	0.2812	0.0000	1.5630	7.0494	3.4332	1	0.0039	0.0005	0.0002	2.7616	1.9344	0.0000	0.0000	0.06827
4-7	-405.38	0.0646	0.2986	0.0000	1.4449	7.1527	3.8215	2	0.0132	0.0003	0.0009	2.8167	1.9475	0.5000	0.0000	0.39538
4-8	-405.38	0.0646	0.2986	0.0000	1.4449	7.1536	3.8254	2	0.0132	0.0003	0.0009	2.8177	1.9488	0.5000	0.0000	0.39734
5-0	-399.09	0.0674	0.2834	0.0000	1.9261	6.3852	3.2353	1	0.0724	0.0003	0.0001	2.7886	1.9628	0.1250	0.1875	0.60903
5-1	-398.99	0.0670	0.2978	0.0000	1.9015	6.3723	3.4273	1	0.0021	0.0003	0.0001	2.7817	1.9300	0.1250	0.0625	0.29067
6-0	-392.62	0.0724	0.2656	0.0000	2.3876	5.5136	1.4810	2	0.0210	0.0009	0.0003	2.8031	1.9672	0.2500	0.3750	0.70420
6-1	-392.17	0.0694	0.3859	0.0000	0.7878	5.6670	0.7485	2	0.0382	0.0020	0.0605	2.8716	1.9399	0.7500	0.1250	1.23135
6-2	-392.00	0.0694	0.3147	0.0000	0.7850	5.6355	1.1359	2	0.0220	0.0016	0.0003	2.8132	1.9215	0.2500	0.1250	0.63951
6-3	-392.29	0.0713	0.3546	0.0000	2.3812	5.3540	1.1005	2	0.0271	0.0007	0.0002	2.8100	1.8635	0.0000	0.0000	0.55071
6-4	-392.64	0.0691	0.3158	0.0000	2.3386	5.6911	3.2258	1	0.0049	0.0003	0.0001	2.7861	1.9227	0.0000	0.1250	0.36007
7-0	-385.76	0.0706	0.4457	0.0000	0.7926	5.0811	0.9304	1	0.0351	0.0015	0.0021	3.0117	1.8786	0.8750	0.0625	1.63416
7-1	-385.82	0.0751	0.4167	0.0000	2.8359	1.5300	0.5396	1	0.0315	0.0007	0.0002	2.8746	1.8236	0.1250	0.0625	1.24301
8-0	-379.25	0.0725	0.5045	0.0000	0.0000	4.4086	0.0000	8	0.0387	0.0013	0.2469	2.9306	1.8440	1.0000	0.0000	1.20077
8-1	-380.29	0.0782	0.2650	0.0000	3.2677	0.0000	0.0000	8	0.0093	0.0011	0.0004	2.8151	1.9152	0.0000	0.5000	0.43476
8-2	-380.17	0.0792	0.2884	0.0000	3.4339	0.0000	0.0000	8	0.0093	0.0004	0.0004	2.8369	1.6734	0.0000	0.0000	0.32528
8-3	-378.98	0.0746	0.4291	0.0000	1.6092	2.0609	0.0000	4	0.0238	0.0013	0.0004	2.9156	1.8155	0.0000	0.0000	0.85998
8-4	-379.45	0.0753	0.3860	0.0000	1.6143	4.1358	0.7227	4	0.0248	0.0007	0.0002	2.9099	1.8123	0.0000	0.0000	0.70213
8-5	-379.54	0.0803	0.4743	0.0000	3.3584	0.0000	0.0000	4	0.0335	0.0010	0.0003	2.8295	1.6569	0.0000	0.0000	1.06112
8-6	-379.91	0.0732	0.3775	0.0000	2.9685	4.2490	3.0035	1	0.0025	0.0002	0.0001	2.8235	1.8347	0.0000	0.0000	0.63951

**Table A.7:** Reaction energy, parameters and the sum of them for all considered structures of boehmite (VASP-DFT, PBE/PAW, 600.0 eV energy cut-off, D3-BJ).

Struc.	Energy	Distortion	Charge	FH-Bonds		OH-Bonds		Sym.	F-Distribution			Layer Distance		Layer Stoichio.		$\kappa$
	[eV]		[Å]	[ $\frac{1}{\text{Å}}$ ]	[ $\frac{1}{\text{Å}}$ ]	[ $\frac{1}{\text{Å}}$ ]	[ $\frac{1}{\text{Å}}$ ]		[ $\frac{1}{\text{Å}}$ ]	[ $\frac{1}{\text{Å}}$ ]	[ $\frac{1}{\text{Å}}$ ]	[Å]				
1-0	-424.31	0.0540	0.1882	0.5808	0.3670	8.6820	4.5770	1	0.1528	0.0040	0.0032	4.4048	1.6664	0.1250	0.0625	-0.24874
2-1	-417.83	0.0543	0.2331	1.1312	0.6988	7.4644	4.2333	2	0.0833	0.0068	0.0019	4.4809	1.6663	0.2500	0.1250	-0.19977
2-2	-417.88	0.0549	0.2345	1.1695	0.7348	7.2734	3.4921	2	0.0833	0.0503	0.0006	4.3775	1.6678	0.0000	0.0000	-0.19130
2-3	-417.93	0.0548	0.2339	1.1310	0.7294	7.3285	3.1683	1	0.0833	0.0006	0.0002	4.5383	1.6691	0.2500	0.0000	-0.12462
2-4	-417.83	0.0549	0.2338	1.1476	0.7359	7.2767	3.4924	1	0.0833	0.0001	0.0001	4.3777	1.6717	0.0000	0.1250	-0.01732
2-5	-417.99	0.0544	0.2339	0.5813	0.3648	8.0272	4.2408	1	0.0258	0.0503	0.0004	4.4472	1.6696	0.2500	0.0000	-0.27547
2-6	-417.89	0.0549	0.2346	1.1733	0.7343	7.2668	3.4950	2	0.0833	0.0503	0.0003	4.3791	1.6683	0.0000	0.0000	-0.18555
2-7	-417.83	0.0549	0.2338	1.1477	0.7359	7.2762	3.4927	1	0.0833	0.0001	0.0001	4.3770	1.6719	0.0000	0.1250	-0.01638
2-8	-417.99	0.0544	0.2340	0.5817	0.3651	8.0382	4.2406	1	0.0258	0.0503	0.0004	4.4409	1.6688	0.2500	0.0000	-0.28322
2-9	-417.93	0.0548	0.2339	1.1311	0.7294	7.3282	3.1683	1	0.0833	0.0006	0.0002	4.5363	1.6687	0.2500	0.0000	-0.12847
2-10	-417.87	0.0548	0.2334	1.1244	0.7328	7.3429	3.5050	2	0.0833	0.0032	0.0004	4.5320	1.6697	0.2500	0.1250	-0.05680
2-11	-417.83	0.0549	0.2338	1.1476	0.7359	7.2815	3.4944	1	0.0833	0.0001	0.0001	4.3769	1.6717	0.0000	0.1250	-0.01654
3-0	-411.67	0.0546	0.2787	0.5682	0.3591	7.4545	4.2412	1	0.0258	0.0337	0.0006	4.4623	1.6669	0.3750	0.0625	-0.12603
3-1	-411.32	0.0557	0.2762	1.6032	1.0501	6.1502	2.8365	1	0.0713	0.0035	0.0020	4.6800	1.6800	0.3750	0.1875	0.52562
4-0	-404.77	0.0564	0.3195	2.0337	0.0000	5.0735	2.1176	4	0.0848	0.0062	0.1019	4.9086	1.6689	0.5000	0.2500	0.69190
4-1	-405.03	0.0562	0.3262	2.2885	1.4116	4.8091	2.8126	4	0.0556	0.0108	0.0004	4.4400	1.6692	0.2500	0.0000	-0.08562
4-2	-404.74	0.0561	0.3221	2.2147	1.3800	4.8251	2.8056	4	0.0556	0.0005	0.0005	4.4388	1.6768	0.2500	0.2500	0.27282
4-3	-405.51	0.0546	0.3241	0.0000	0.0000	7.4615	4.2435	4	0.0330	0.0115	0.0010	4.4256	1.6692	0.2500	0.0000	-0.46092
4-4	-405.16	0.0554	0.3231	2.1210	1.3745	5.0370	2.8350	4	0.0556	0.0023	0.0005	4.7802	1.6704	0.7500	0.0000	-0.04586
4-5	-405.15	0.0561	0.3256	1.7038	1.0989	5.3052	1.7434	1	0.0347	0.0007	0.0002	4.5056	1.6754	0.0000	0.0000	0.24345
4-6	-405.15	0.0561	0.3257	1.7039	1.0990	5.3052	1.7432	1	0.0347	0.0007	0.0002	4.5050	1.6754	0.0000	0.0000	0.24304
5-0	-398.66	0.0563	0.3632	1.5545	0.6815	5.0576	2.4785	1	0.0421	0.0028	0.0001	4.8500	1.6853	0.6250	0.1875	0.86084
6-0	-392.57	0.0558	0.4137	1.1270	0.6984	4.8690	2.8196	2	0.0791	0.0108	0.0006	4.4604	1.6720	0.0000	0.1250	0.46376
6-1	-392.14	0.0580	0.4121	3.3098	2.0461	2.4175	1.0523	2	0.1011	0.0109	0.0001	4.7831	1.6631	0.0000	0.1250	1.06264
6-2	-392.23	0.0566	0.4131	3.2471	2.0741	2.4051	1.4060	2	0.1944	0.0013	0.0003	4.7228	1.6744	0.5000	0.1250	1.04463
6-3	-392.55	0.0560	0.4071	1.0332	0.6773	5.0461	2.8388	2	0.0322	0.0021	0.0003	4.8501	1.6695	0.5000	0.1250	0.57340
6-4	-392.53	0.0561	0.4071	1.0412	0.6887	5.0559	2.8397	2	0.0202	0.0022	0.0001	4.8360	1.6811	0.7500	0.1250	0.61705
7-0	-386.30	0.0562	0.4486	0.5212	0.3530	5.0540	2.8415	1	0.0197	0.0019	0.0002	4.8393	1.6708	0.8750	0.0625	0.65786
8-0	-379.40	0.0597	0.4940	4.4047	2.7024	0.0000	0.0000	8	0.0242	0.0013	0.0014	4.7332	1.6537	0.0000	0.0000	0.50717
8-1	-378.01	0.0586	0.4952	0.0000	3.7955	0.0000	0.0000	8	0.0243	0.0018	0.0002	4.8356	1.7022	0.0000	0.5000	1.57800
8-2	-380.04	0.0564	0.4887	0.0000	0.0000	5.0393	2.8400	8	0.0201	0.0027	0.0006	4.7848	1.6750	1.0000	0.0000	-0.01284
8-3	-380.28	0.0556	0.5029	0.0000	0.0000	4.9176	2.8271	8	0.0096	0.0031	0.0005	4.3762	1.6699	0.0000	0.0000	-0.41539
8-4	-379.94	0.0573	0.5018	1.6747	1.0947	2.8248	0.0000	1	0.0528	0.0011	0.0003	4.5290	1.6836	0.2500	0.0000	0.93476
8-5	-380.28	0.0560	0.5048	0.0000	0.0000	4.8991	2.8262	8	0.0095	0.0031	0.0004	4.3873	1.6739	0.0000	0.0000	-0.31494

### A.3 Surfaces

**Table A.8:** Listing of the used k-point grids (see [equation \(2.44\)](#)) for different surface cuts and their UC representations - staying with odd integers.

Surface	$Q_1$	$Q_2$	$Q_3$
(0001)	5	5	1
( $1\bar{1}02$ )	5	5	1
( $11\bar{2}3$ )	5	3	1

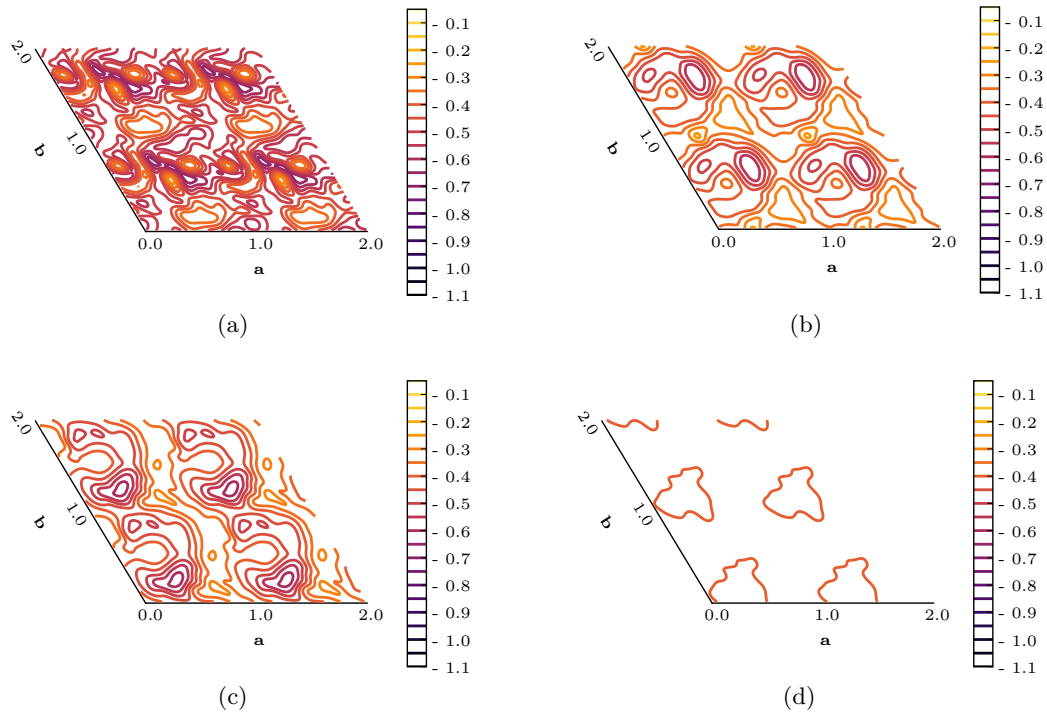


**Figure A.9:** Adsorption energy surface [eV] of the first water molecule on the UC of the hydrated and fluorinated (0001) surfaces; (a) hydrated, (b) singly, (c) doubly, and (d) triply fluorinated (VASP-DFT, PBE/PAW, 600.0 eV energy cut-off, D3-BJ).

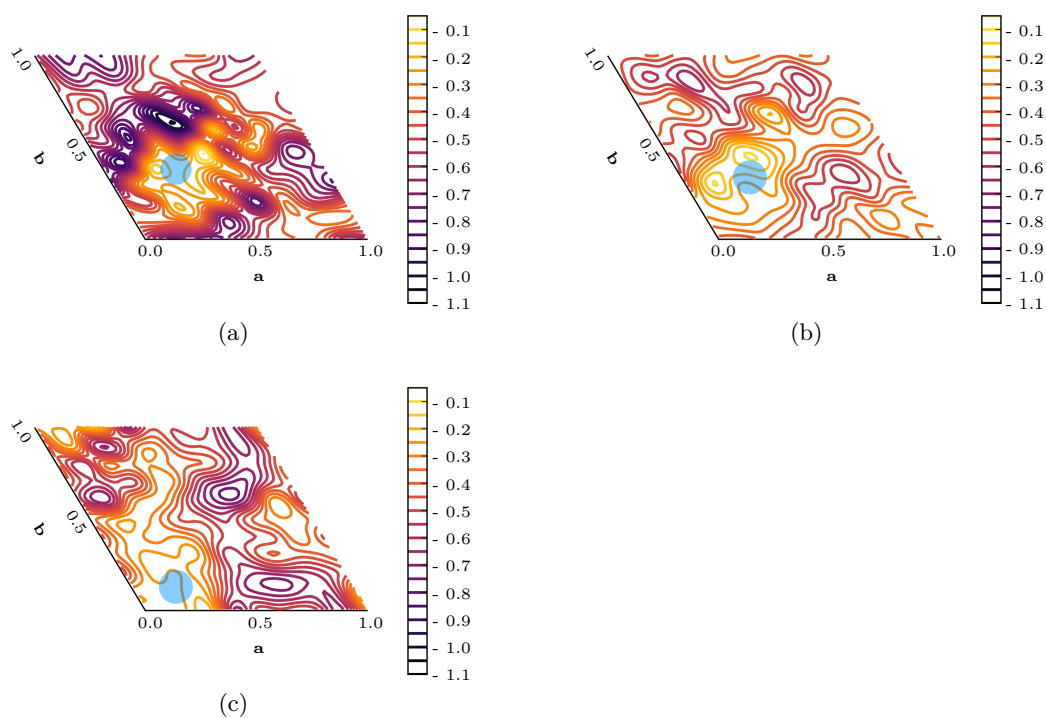


**Figure A.10:** Adsorption energy surface [eV] of the second water molecule on a  $2 \times 2 \times 1$  SC of the hydrated and fluorinated (0001) surfaces; (a) hydrated, (b) singly, (c) doubly, and (d) triply fluorinated - light blue circles represent the first water molecule (VASP-DFT, PBE/PAW, 600.0 eV energy cut-off, D3-BJ).

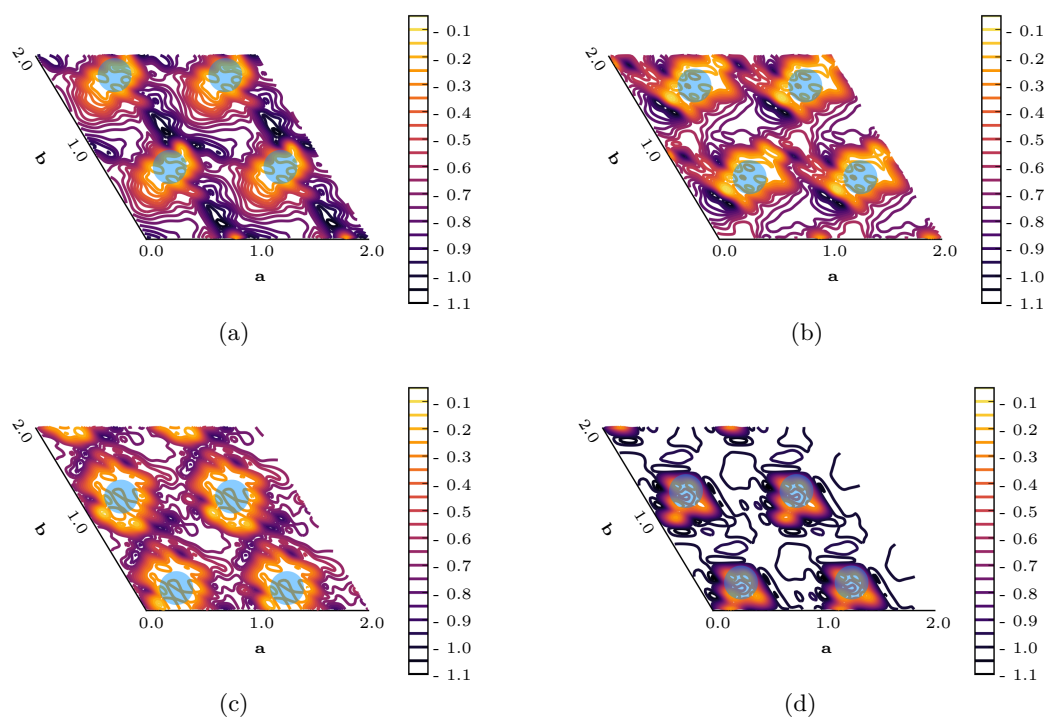


**Figure A.11:** Adsorption energy surface [eV] of the second water molecule on the UC of the hydrated and fluorinated (0001) surfaces; (a) hydrated, (b) singly, (c) doubly, and (d) triply fluorinated - light blue circles represent the first water molecule (VASP-DFT, PBE/PAW, 600.0 eV energy cut-off, D3-BJ).



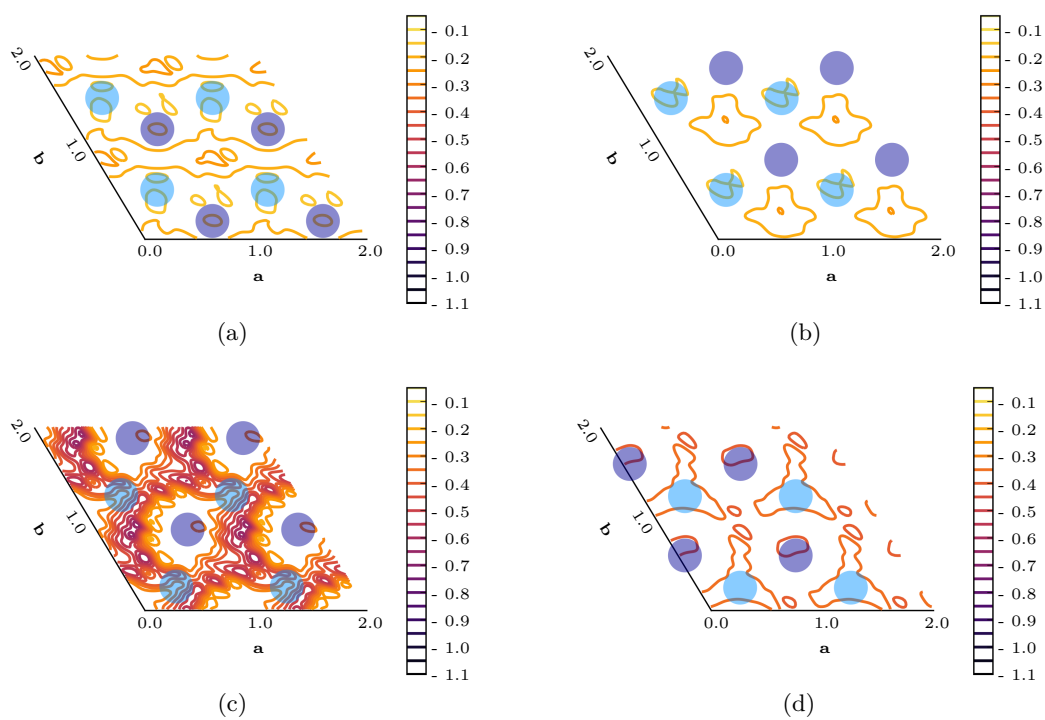


**Figure A.12:** Adsorption energy surface [eV] of the third water molecule on the UC of the hydrated and fluorinated (0001) surfaces; (a) hydrated, (b) singly, (c) doubly, and (d) triply fluorinated - blue circles represent the first (light blue) and the second (blue) water molecule (VASP-DFT, PBE/PAW, 600.0 eV energy cut-off, D3-BJ).

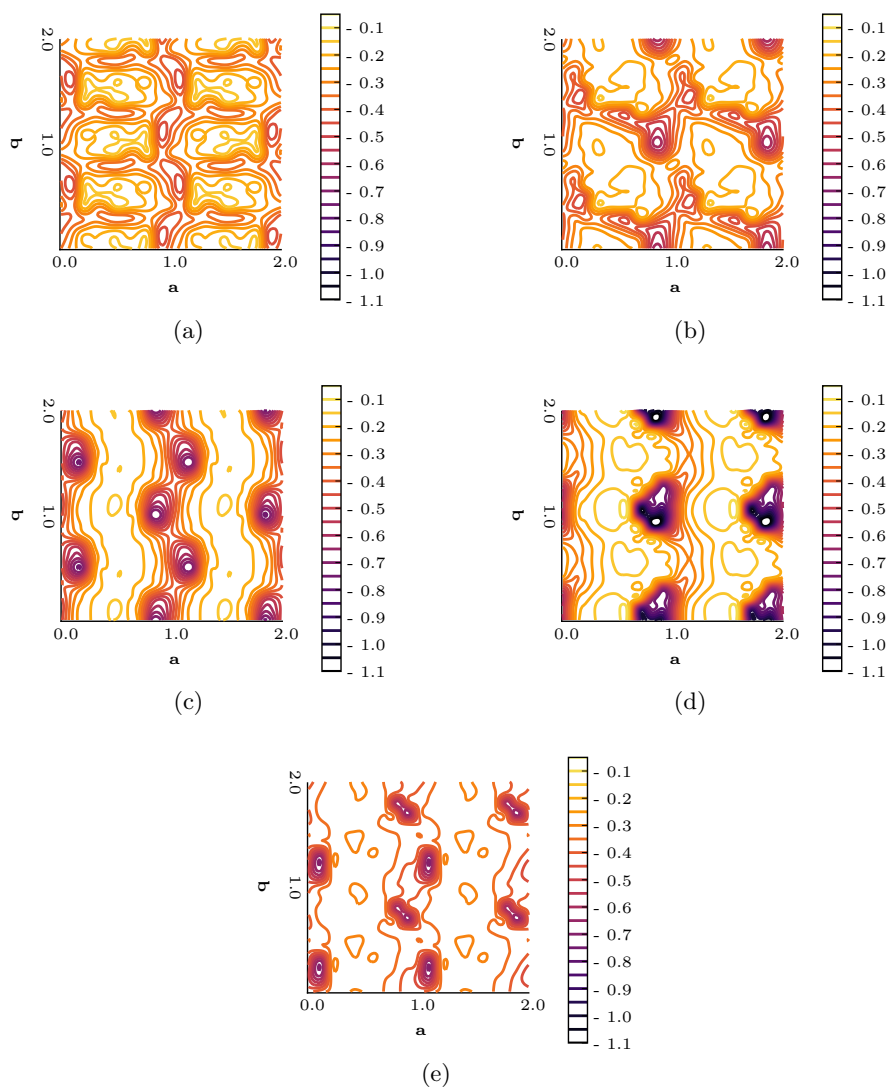


**Figure A.13:** Adsorption energy surface [eV] of the first water molecule on the UC of the hydrated and fluorinated (1102) surfaces; (a) hydrated, (b) singly, (c) doubly, (d) triply, and (e) fourfold fluorinated (VASP-DFT, PBE/PAW, 600.0 eV energy cut-off, D3-BJ).

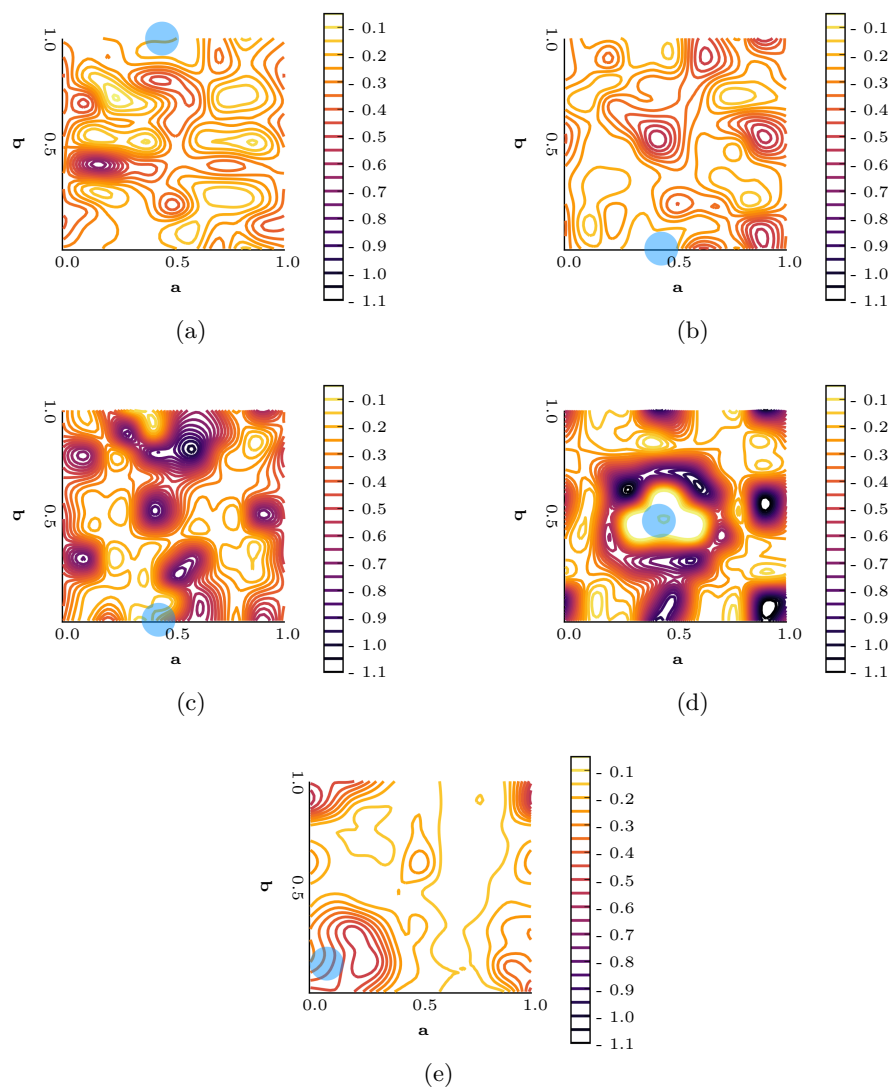


**Figure A.14:** Adsorption energy surface [eV] of the second water molecule on a  $2 \times 2 \times 1$  SC of the hydrated and fluorinated (1102) surfaces; (a) hydrated, (b) singly, (c) doubly, (d) triply, and (e) fourfold fluorinated - light blue circles represent the first water molecule (VASP-DFT, PBE/PAW, 600.0 eV energy cut-off, D3-BJ).

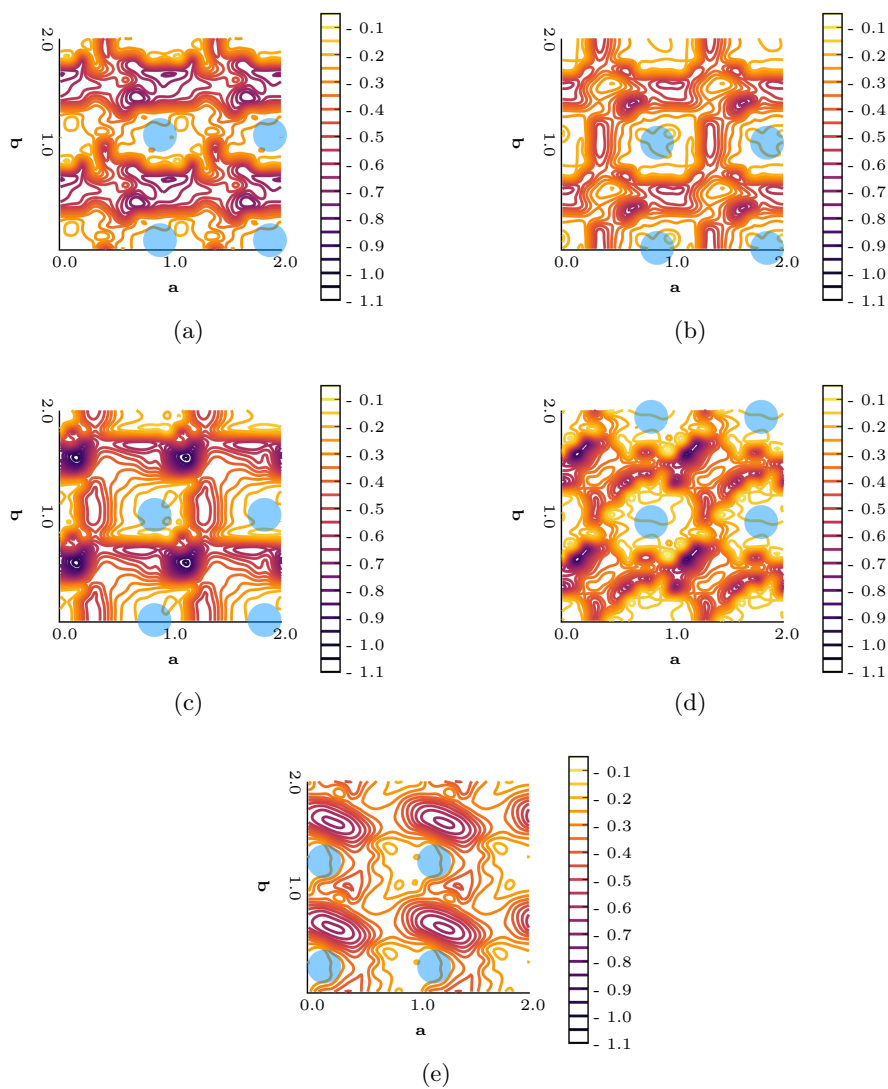


**Figure A.15:** Adsorption energy surface [eV] of the second water molecule on the UC of the hydrated and fluorinated (1102) surfaces; (a) hydrated, (b) singly, (c) doubly, (d) triply, and (e) fourfold fluorinated - light blue circles represent the first water molecule (VASP-DFT, PBE/PAW, 600.0 eV energy cut-off, D3-BJ).

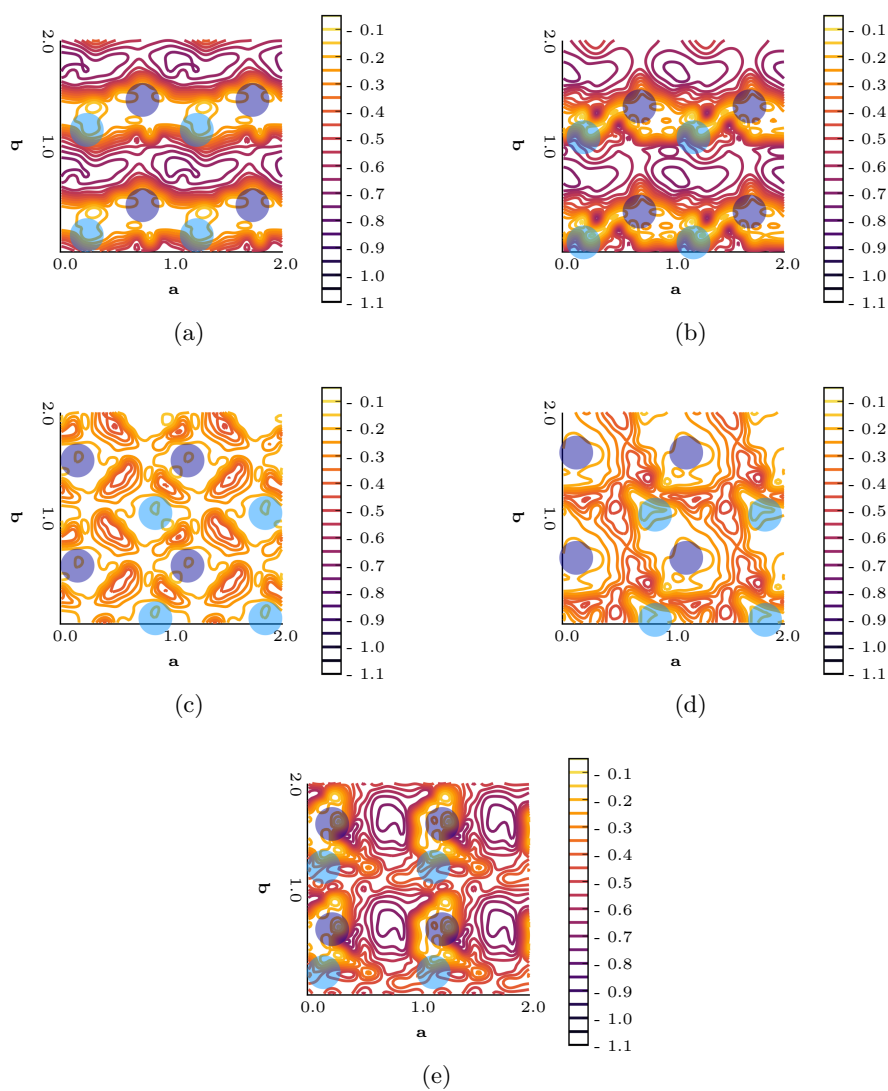


**Figure A.16:** Adsorption energy surface [eV] of the third water molecule on the UC of the hydrated and fluorinated ( $1\bar{1}02$ ) surfaces; (a) hydrated, (b) singly, (c) doubly, (d) triply, and (e) fourfold fluorinated - blue circles represent the first (light blue) and the second (blue) water molecule (VASP-DFT, PBE/PAW, 600.0 eV energy cut-off, D3-BJ).

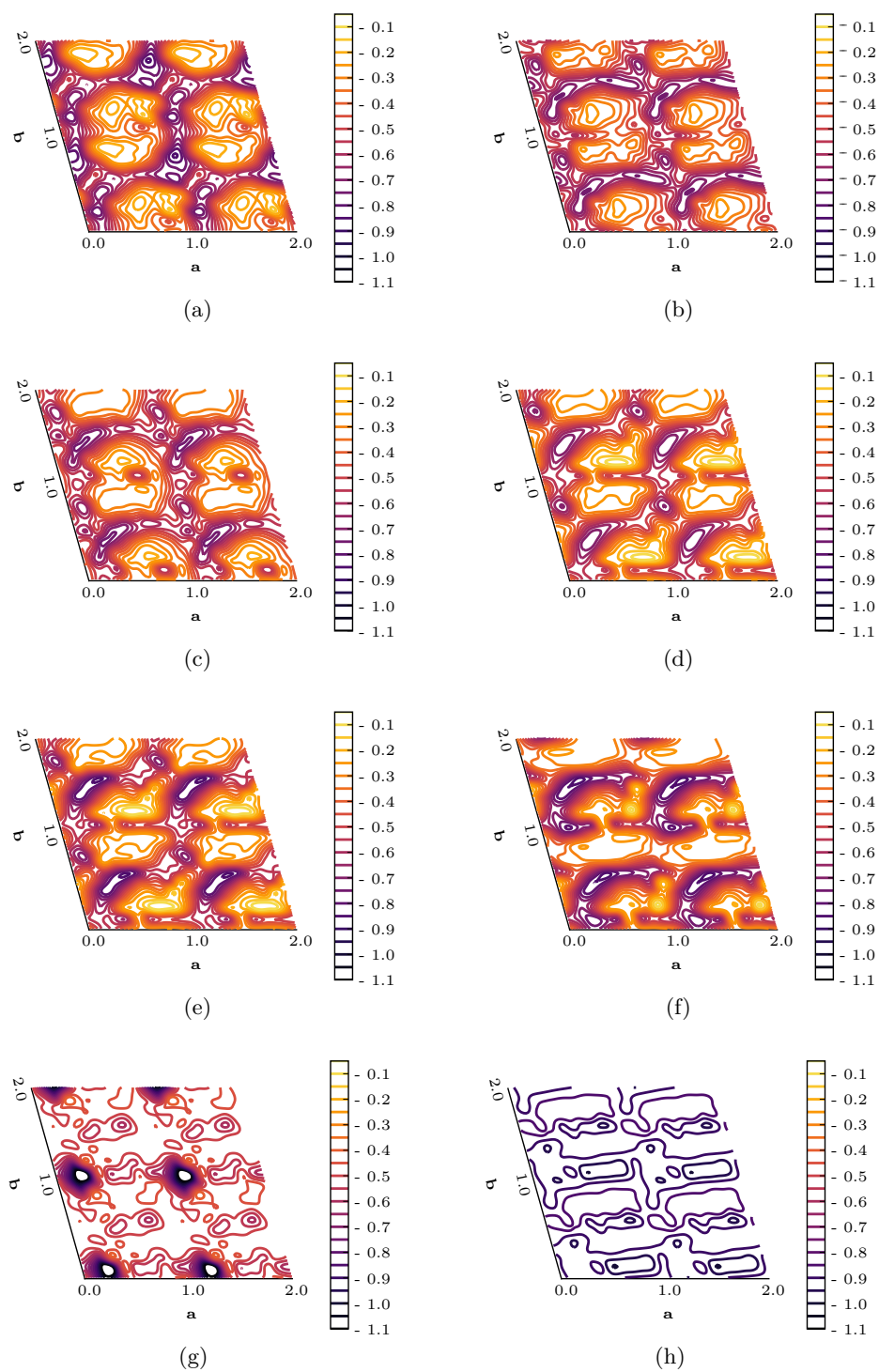


**Figure A.17:** Adsorption energy surface [eV] of the first water molecule on the UC of the hydrated and fluorinated (1123) surfaces; (a) hydrated, (b) singly, (c) doubly, (d) triply, (e) fourfold, (f) fivefold, (g) sixfold, and (h) sevenfold fluorinated (VASP-DFT, PBE/PAW, 600.0 eV energy cut-off, D3-BJ).

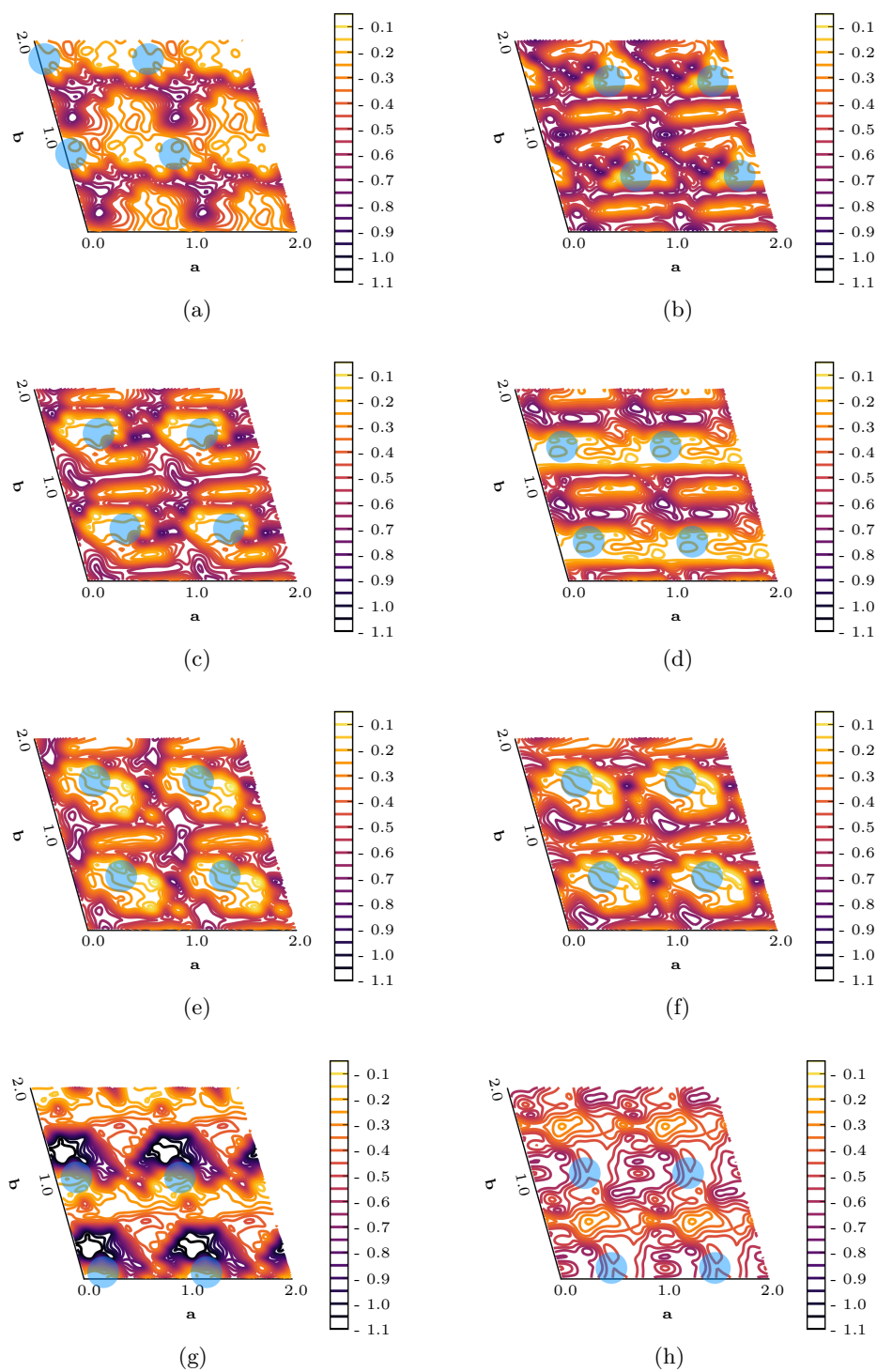


**Figure A.18:** Adsorption energy surface [eV] of the second water molecule on the UC of the hydrated and fluorinated  $(11\bar{2}3)$  surfaces; (a) hydrated, (b) singly, (c) doubly, (d) triply, (e) fourfold, (f) fivefold, (g) sixfold, and (h) sevenfold fluorinated - light blue circles represent the first water molecule (VASP-DFT, PBE/PAW, 600.0 eV energy cut-off, D3-BJ).

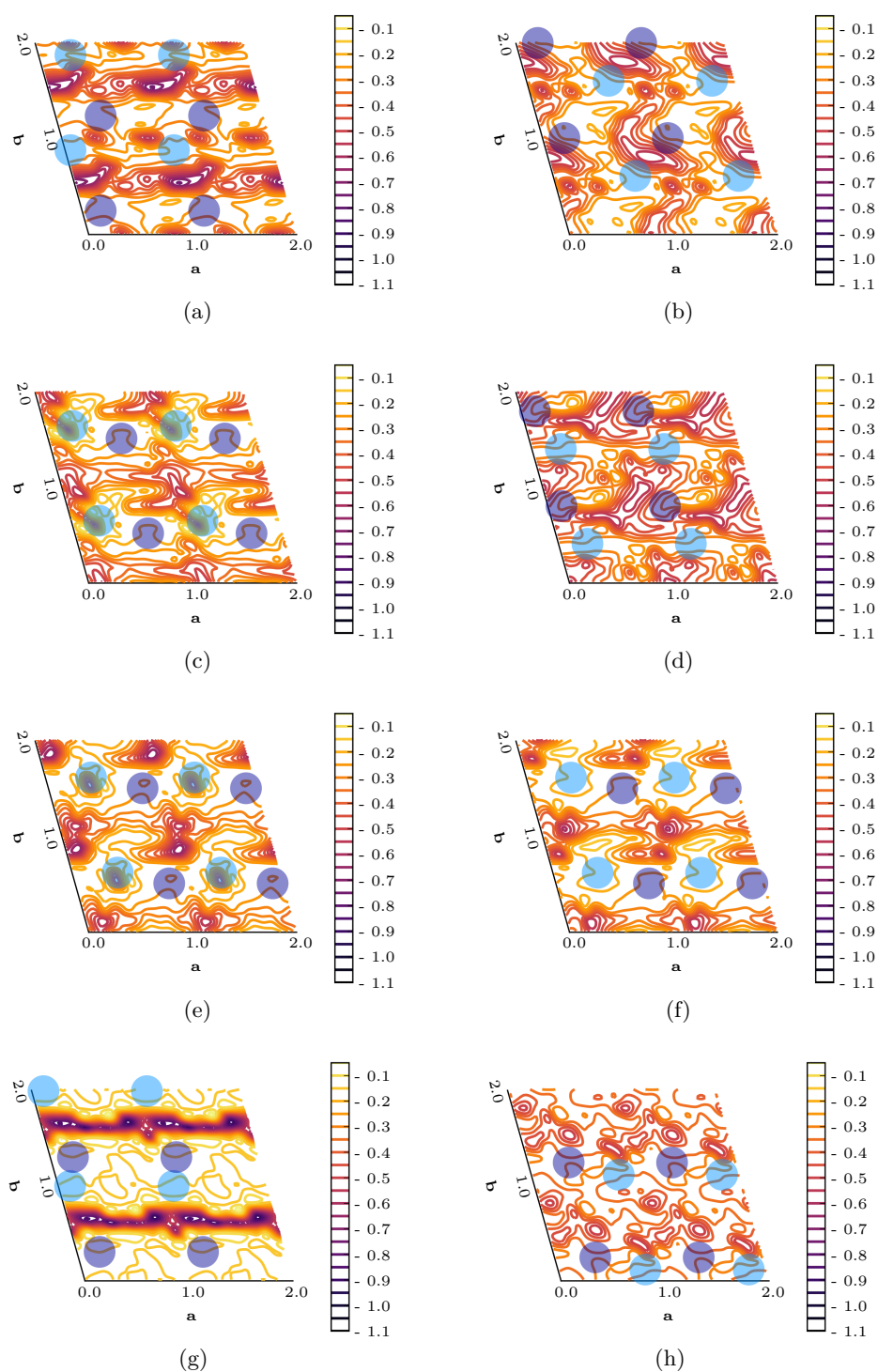


**Figure A.19:** Adsorption energy surface [eV] of the third water molecule on the UC of the hydrated and fluorinated  $(11\bar{2}3)$  surfaces; (a) hydrated, (b) singly, (c) doubly, (d) triply, (e) fourfold, (f) fivefold, (g) sixfold, and (h) sevenfold fluorinated - blue circles represent the first (light blue) and the second (blue) water molecule (VASP-DFT, PBE/PAW, 600.0 eV energy cut-off, D3-BJ).



## A.4 Ice



**Figure A.20:**  $O_8$ -rings found in ice-II - hydrogen atoms are left out, red = oxygen, and green = hydrogen bond.

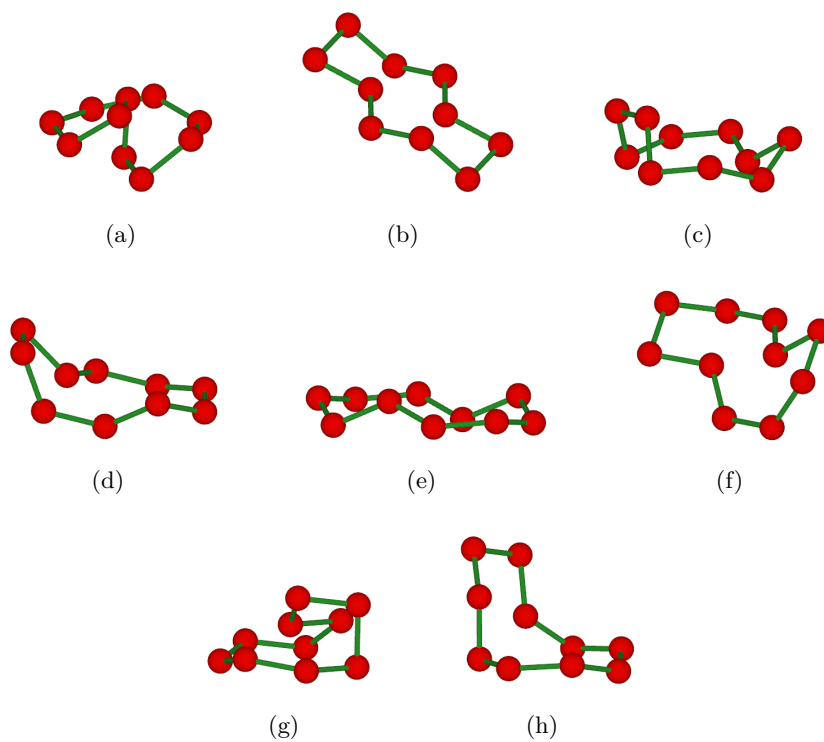


**Figure A.21:**  $O_{10}$ -rings found in ice-II - hydrogen atoms are left out, red = oxygen, and green = hydrogen bond.

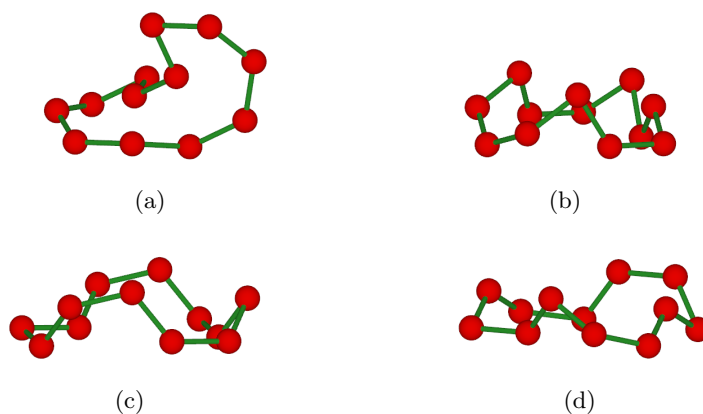


**Figure A.22:**  $O_{12}$ -rings found in ice-II - hydrogen atoms are left out, red = oxygen, and green = hydrogen bond.

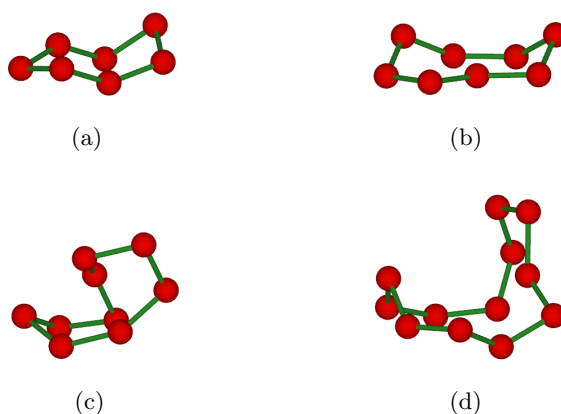


**Figure A.23:** Water structure motifs found in ice-III; (a)  $O_7$ -ring, (b)  $O_8$ -ring, (c)  $O_9$ -ring, and (d)  $O_{12}$ -ring - hydrogen atoms are left out, red = oxygen, and green = hydrogen bond.

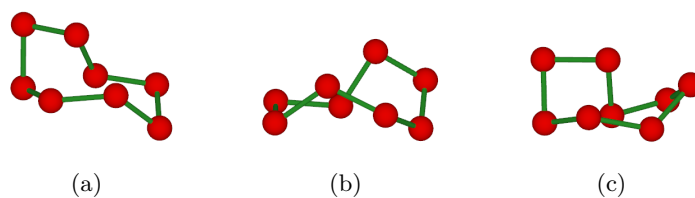


**Figure A.24:**  $O_8$ -rings found in ice-IV - hydrogen atoms are left out, red = oxygen, and green = hydrogen bond.

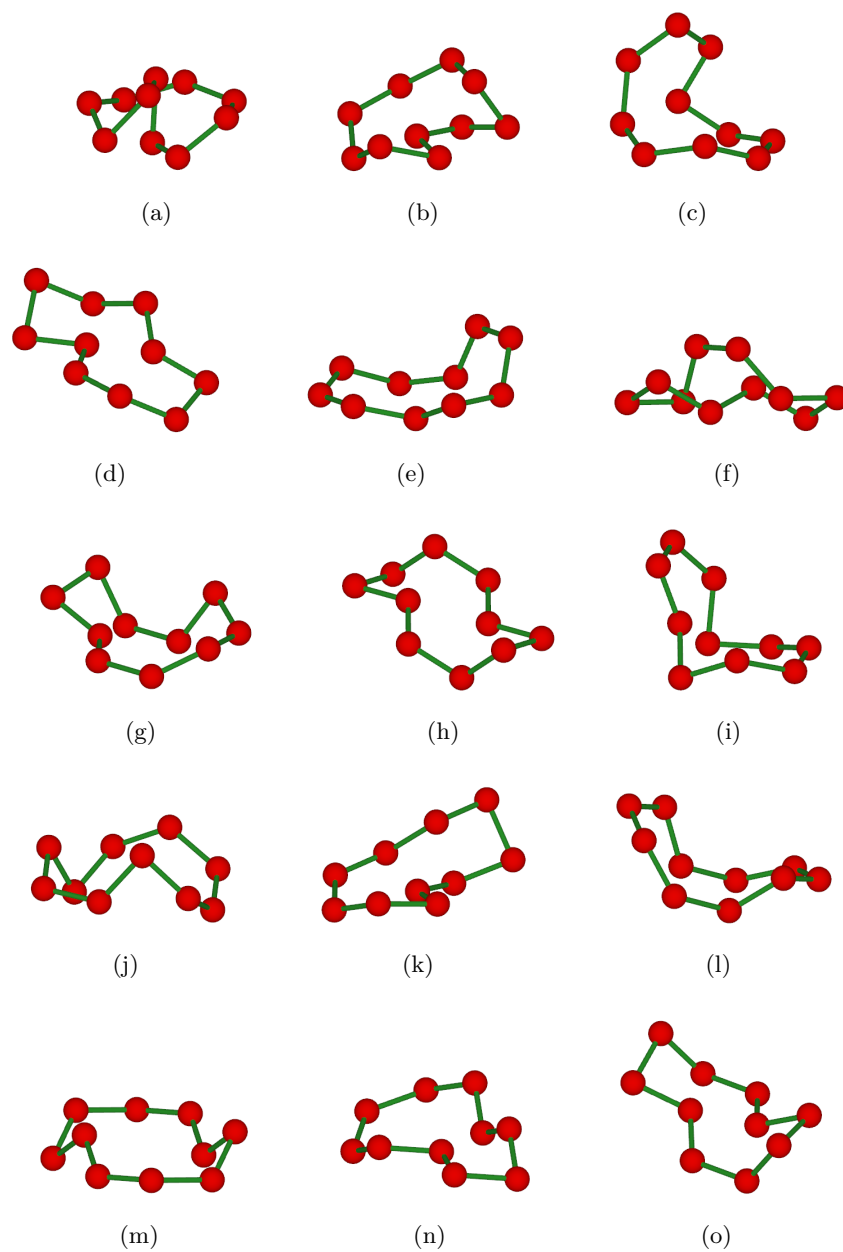


**Figure A.25:**  $O_{10}$ -rings found in ice-IV - hydrogen atoms are left out, red = oxygen, and green = hydrogen bond.

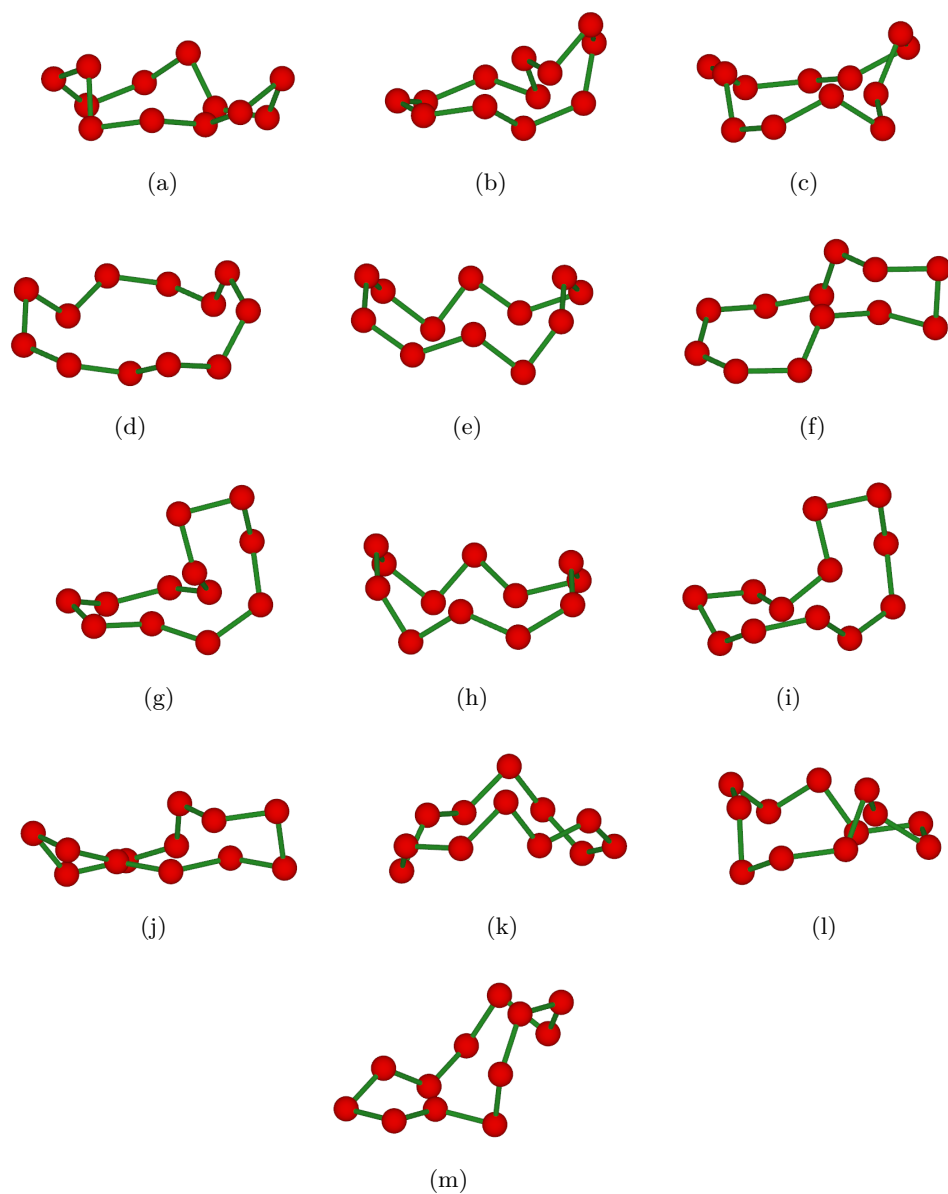


**Figure A.26:**  $O_{12}$ -rings found in ice-IV - hydrogen atoms are left out, red = oxygen, and green = hydrogen bond.

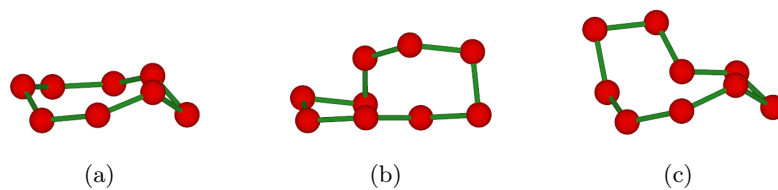


**Figure A.27:** Water structure motifs found in ice-V; (a) O<sub>8</sub>-ring, (b) first O<sub>9</sub>-ring, and (c) second O<sub>9</sub>-ring - hydrogen atoms are left out, red = oxygen, and green = hydrogen bond.

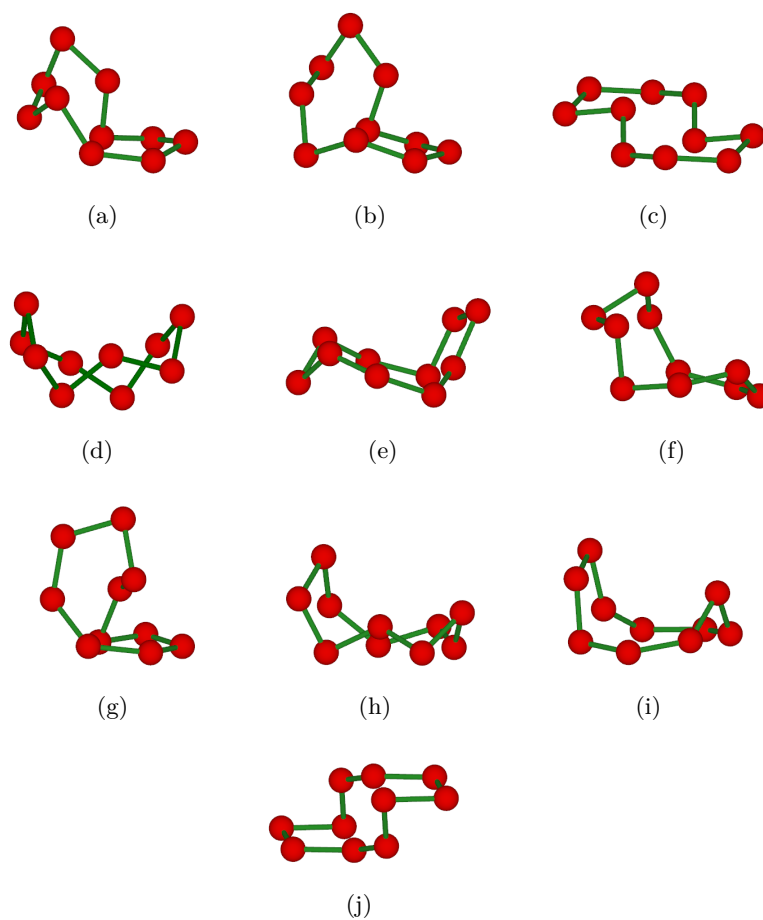


**Figure A.28:** O<sub>10</sub>-rings found in ice-V - hydrogen atoms are left out, red = oxygen, and green = hydrogen bond.

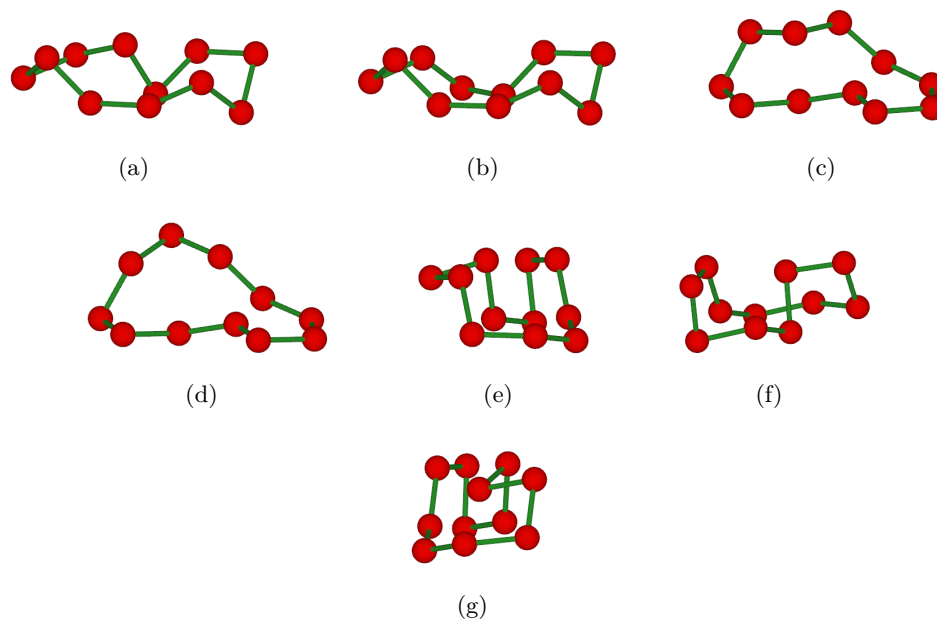


**Figure A.29:**  $O_{11}$ -rings found in ice-V - hydrogen atoms are left out, red = oxygen, and green = hydrogen bond.

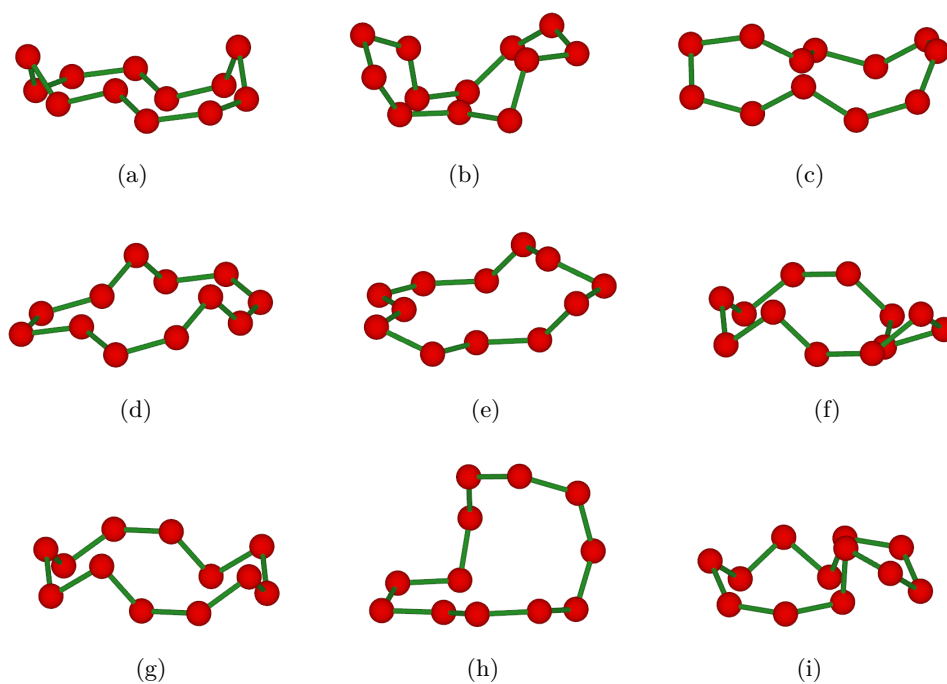


**Figure A.30:**  $O_{12}$ -rings found in ice-V - hydrogen atoms are left out, red = oxygen, and green = hydrogen bond.

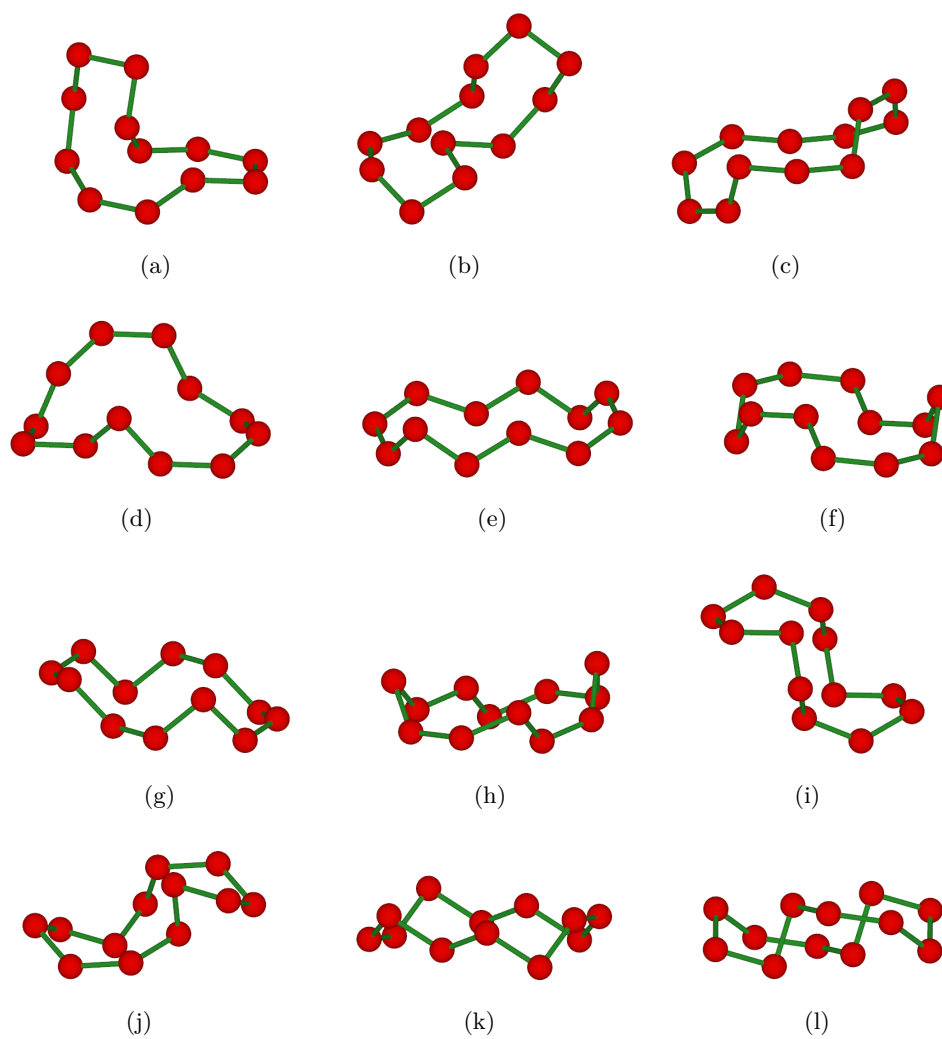


**Figure A.31:**  $O_{12}$ -rings found in ice-V - hydrogen atoms are left out, red = oxygen, and green = hydrogen bond.

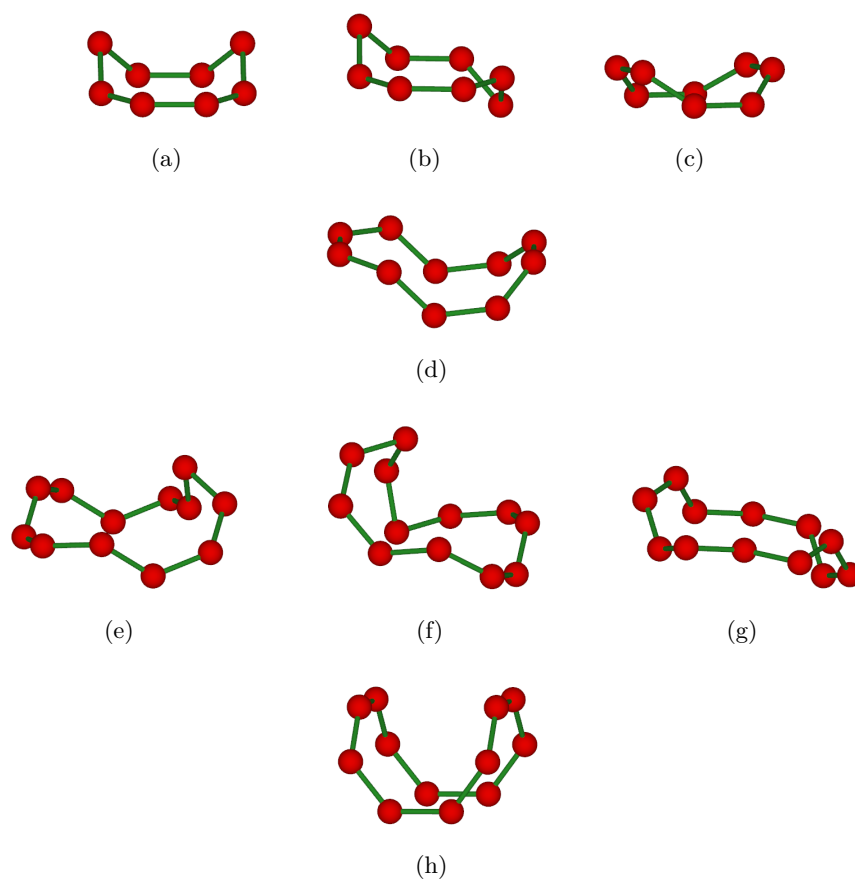


**Figure A.32:** Water structure motifs found in ice-VI; (a) first O<sub>8</sub>-ring, (b) second O<sub>8</sub>-ring, (c) third O<sub>8</sub>-ring, (d) O<sub>10</sub>-ring, (e) first O<sub>12</sub>-ring, (f) second O<sub>12</sub>-ring, (g) third O<sub>12</sub>-ring, and (h) fourth O<sub>12</sub>-ring - hydrogen atoms are left out, red = oxygen, and green = hydrogen bond.



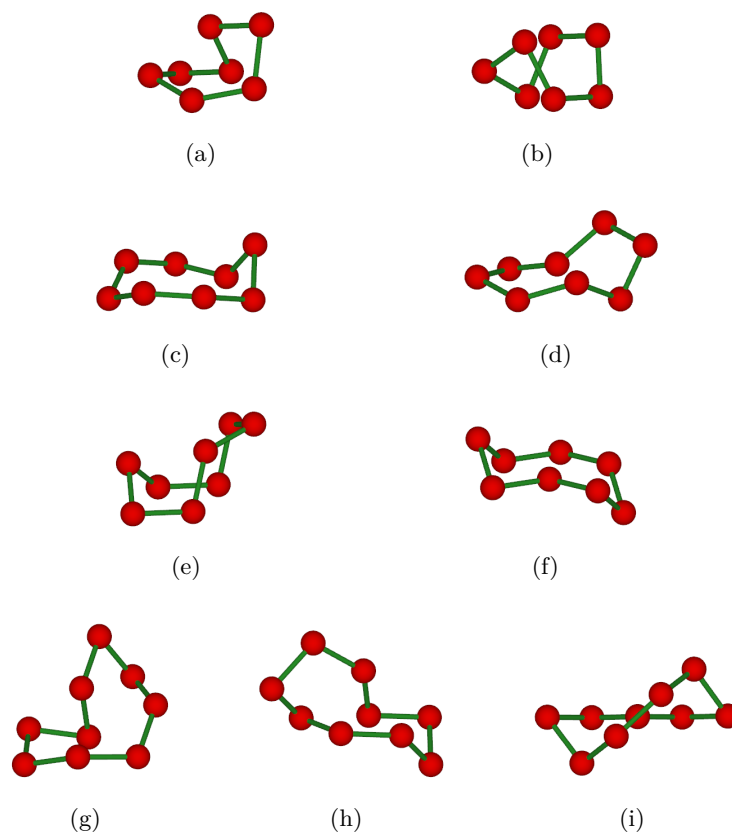


**Figure A.33:** Water structure motifs found in ice-**XII**; (a) first  $O_7$ -ring, (b) second  $O_7$ -ring, (c) first  $O_8$ -ring, (d) second  $O_8$ -ring, (e) third  $O_8$ -ring, (f) fourth  $O_8$ -ring, (g) first  $O_9$ -ring, (h) second  $O_9$ -ring, and (i) third  $O_9$ -ring - hydrogen atoms are left out, red = oxygen, and green = hydrogen bond.

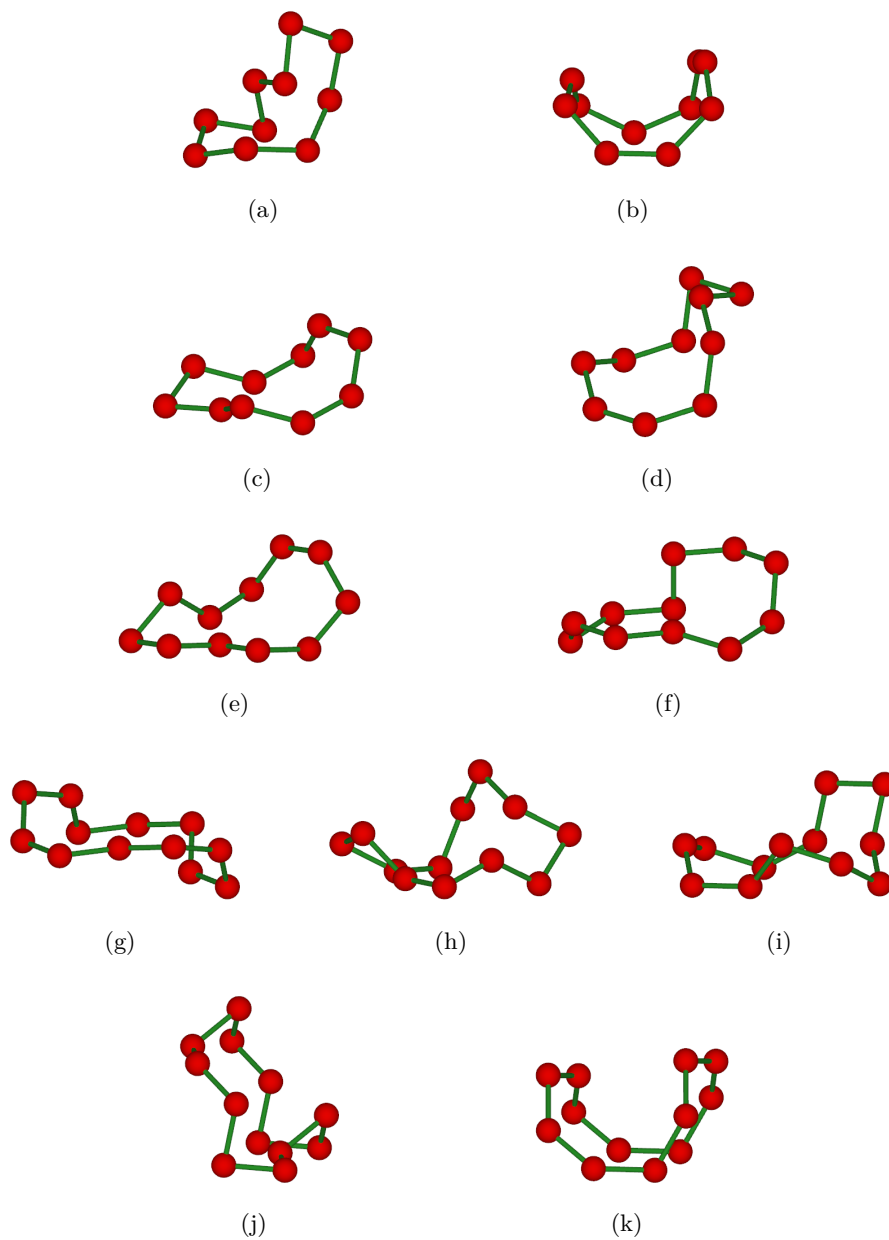


**Figure A.34:** Water structure motifs found in ice-**XII**; (a) first  $O_{10}$ -ring, (b) second  $O_{10}$ -ring, (c) third  $O_{10}$ -ring, (d) fourth  $O_{10}$ -ring, (e) first  $O_{11}$ -ring, (f) second  $O_{11}$ -ring, (g) first  $O_{12}$ -ring, (h) second  $O_{12}$ -ring, (i) third  $O_{12}$ -ring, and (j) fourth  $O_{12}$ -ring - hydrogen atoms are left out, red = oxygen, and green = hydrogen bond.

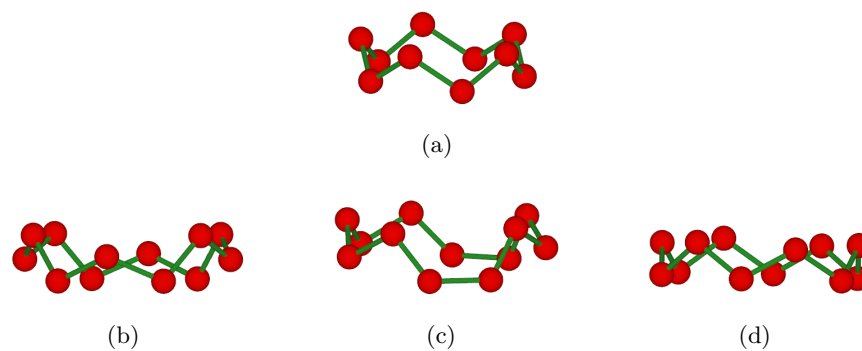


**Figure A.35:** Water structure motifs found in ice-**XVI**; (a) O<sub>10</sub>-ring, (b) first O<sub>12</sub>-ring, (c) second O<sub>12</sub>-ring, and (d) third O<sub>12</sub>-ring - hydrogen atoms are left out, red = oxygen, and green = hydrogen bond.

## A.5 Adsorbed Water

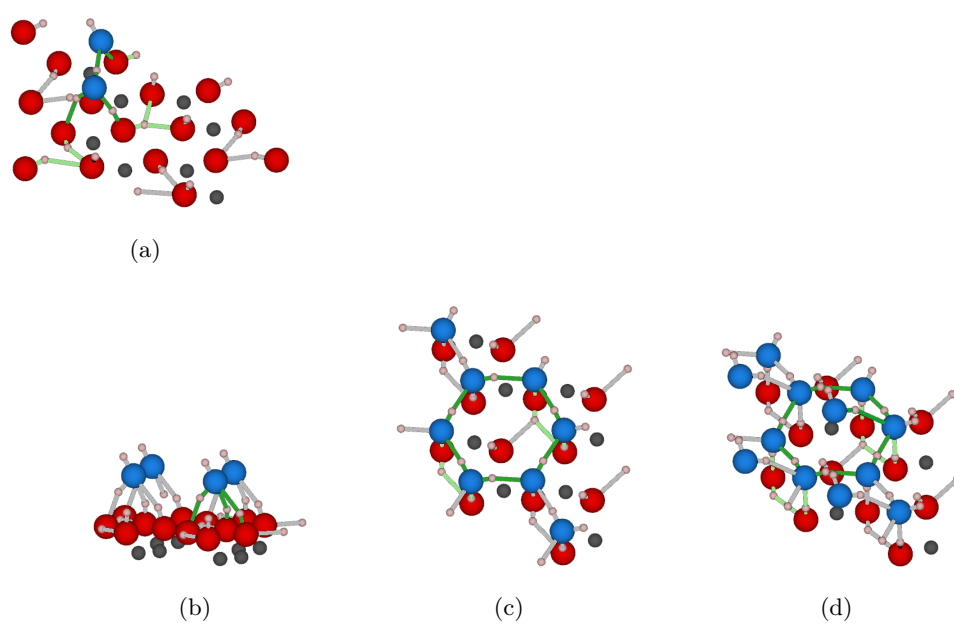


**Figure A.36:** Water structure motifs found on the hydrated (0001) surface; (a) two water molecules on a  $2 \times 2 \times 1$  SC, (b) one water molecule per UC, (c) two water molecules per UC, and (d) three water molecules per UC - gray = aluminium, red = oxygen, white = hydrogen, light blue = water oxygen, green = structure motif, light green = 2nd structure motif/supporting structure motif, and light gray = de-emphasised hydrogen bonds (VASP-DFT, PBE/PAW, 600.0 eV energy cut-off, D3-BJ).

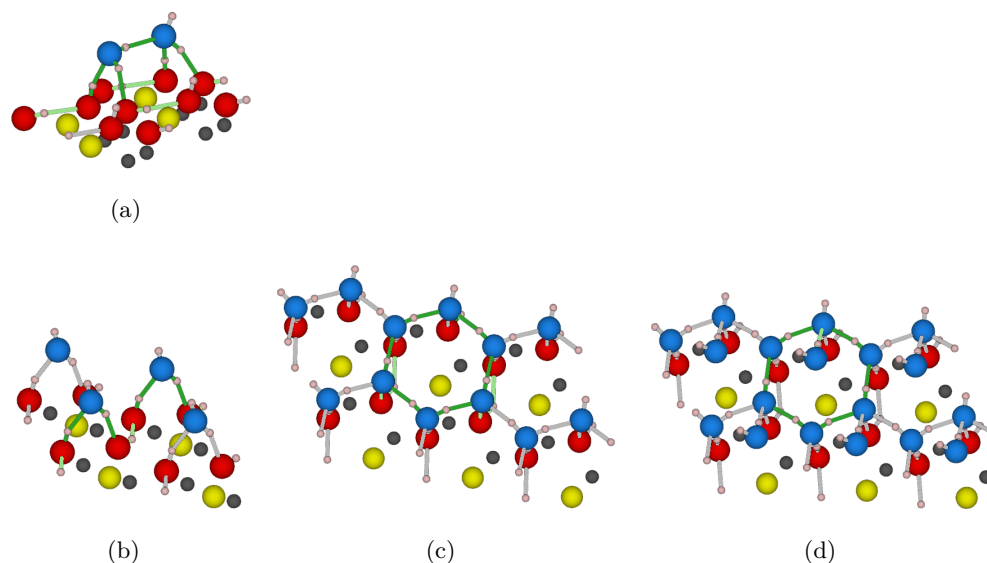


**Figure A.37:** Water structure motifs found on the singly fluorinated (0001) surface; (a) two water molecules on a  $2 \times 2 \times 1$  SC, (b) one water molecule per UC, (c) two water molecules per UC, and (d) three water molecules per UC - gray = aluminium, red = oxygen, yellow = fluoride, white = hydrogen, light blue = water oxygen and , green = structure motif, light green = 2nd structure motif/supporting structure motif, and light gray = de-emphasised hydrogen bonds (VASP-DFT, PBE/PAW, 600.0 eV energy cut-off, D3-BJ).

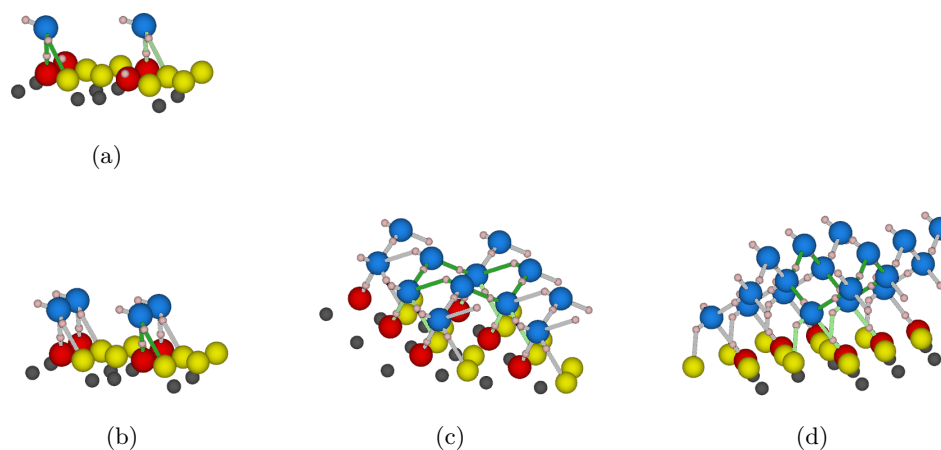


**Figure A.38:** Water structure motifs found on the doubly fluorinated (0001) surface; (a) two water molecules on a  $2 \times 2 \times 1$  SC, (b) one water molecule per UC, (c) two water molecules per UC, and (d) three water molecules per UC - gray = aluminium, red = oxygen, yellow = fluoride, white = hydrogen, light blue = water oxygen, green = structure motif, light green = 2nd structure motif/supporting structure motif, and light gray = de-emphasised hydrogen bonds (VASP-DFT, PBE/PAW, 600.0 eV energy cut-off, D3-BJ).

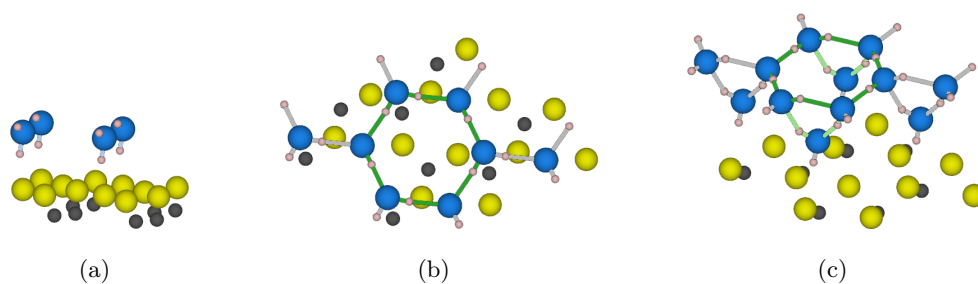


**Figure A.39:** Water structure motifs found on the triply fluorinated (0001) surface; (a) one water molecule per UC, (b) two water molecules per UC, and (c) three water molecules per UC - gray = aluminium, red = oxygen, yellow = fluoride, white = hydrogen, light blue = water oxygen, green = structure motif, light green = 2nd structure motif/supporting structure motif, and light gray = de-emphasised hydrogen bonds (VASP-DFT, PBE/PAW, 600.0 eV energy cut-off, D3-BJ).

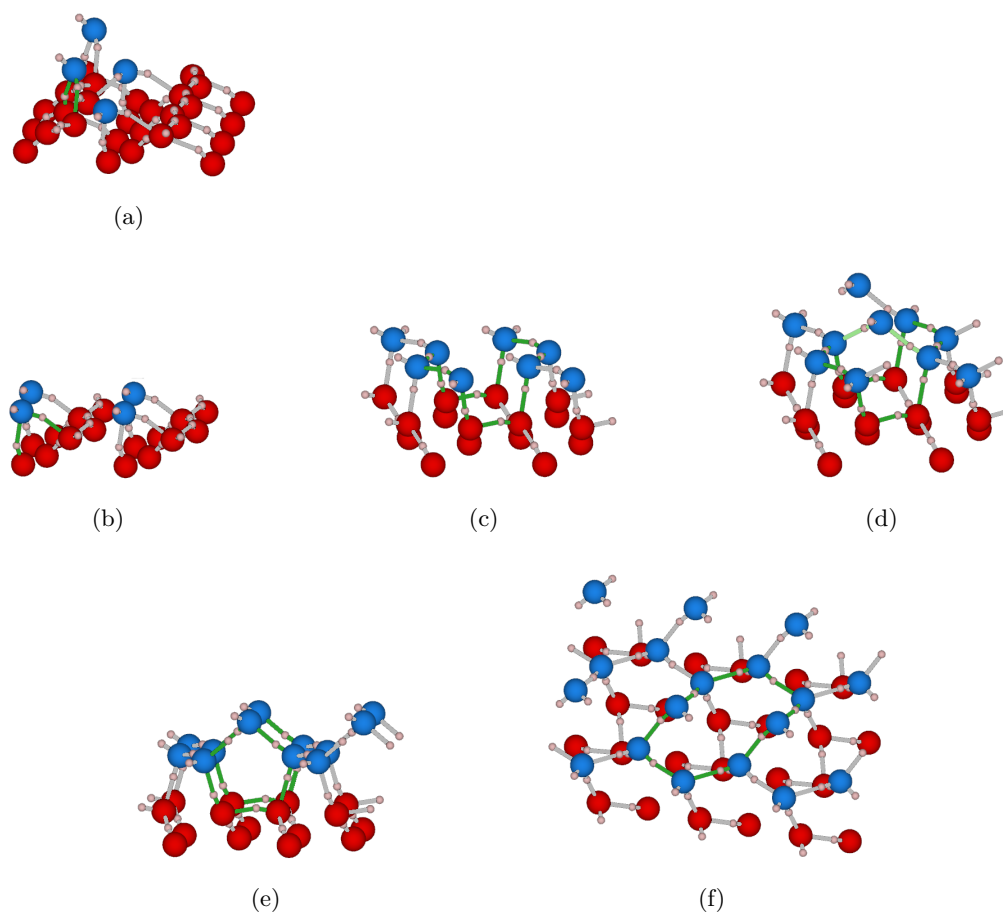


**Figure A.40:** Water structure motifs found on the hydrated  $(1\bar{1}02)$  surface; (a) two water molecules on a  $2\times 2\times 1$  SC, (b) one water molecule per UC, (c) two water molecules per UC, and (d), (e), and (f) three water molecules per UC - gray = aluminium, red = oxygen, white = hydrogen, light blue = water oxygen, green = structure motif, light green = 2nd structure motif/supporting structure motif, and light gray = de-emphasised hydrogen bonds (VASP-DFT, PBE/PAW, 600.0 eV energy cut-off, D3-BJ).

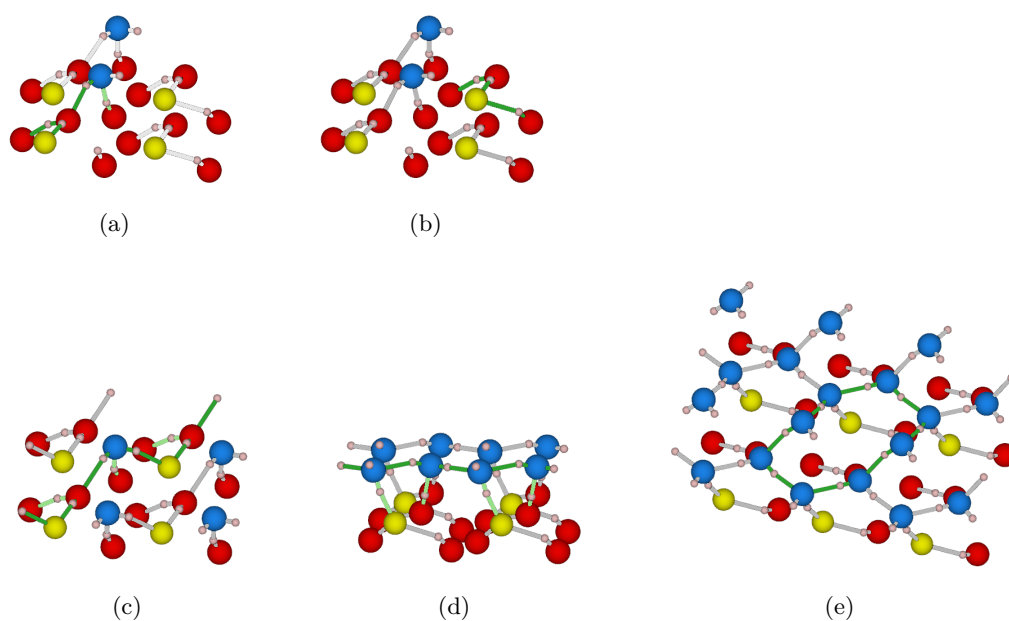


**Figure A.41:** Water structure motifs found on the singly fluorinated ( $1\bar{1}02$ ) surface; (a) and (b) two water molecules on a  $2\times 2\times 1$  SC, (c) one water molecule per UC, (d) two water molecules per UC, and (e) three water molecules per UC - gray = aluminium, red = oxygen, yellow = fluoride, white = hydrogen, light blue = water oxygen, green = structure motif, light green = 2nd structure motif/supporting structure motif, and light gray = de-emphasised hydrogen bonds (VASP-DFT, PBE/PAW, 600.0 eV energy cut-off, D3-BJ).



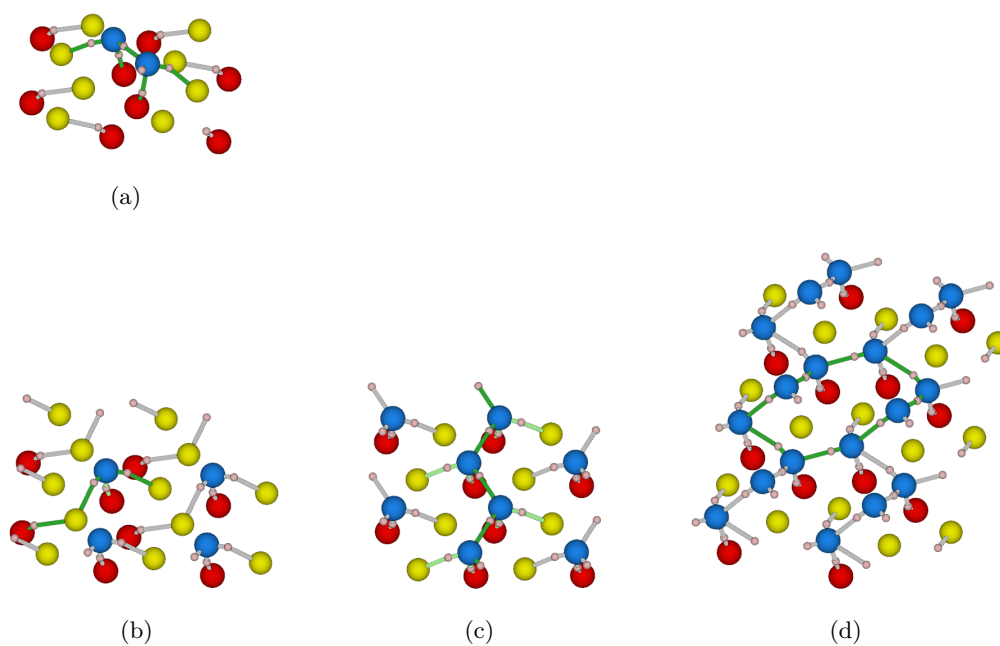


**Figure A.42:** Water structure motifs found on the doubly fluorinated  $(1\bar{1}02)$  surface; (a) two water molecules on a  $2\times 2\times 1$  SC, (b) one water molecule per UC, (c) two water molecules per UC, and (d) three water molecules per UC - gray = aluminium, red = oxygen, yellow = fluoride, white = hydrogen, light blue = water oxygen, green = structure motif, light green = 2nd structure motif/supporting structure motif, and light gray = de-emphasised hydrogen bonds (VASP-DFT, PBE/PAW, 600.0 eV energy cut-off, D3-BJ).

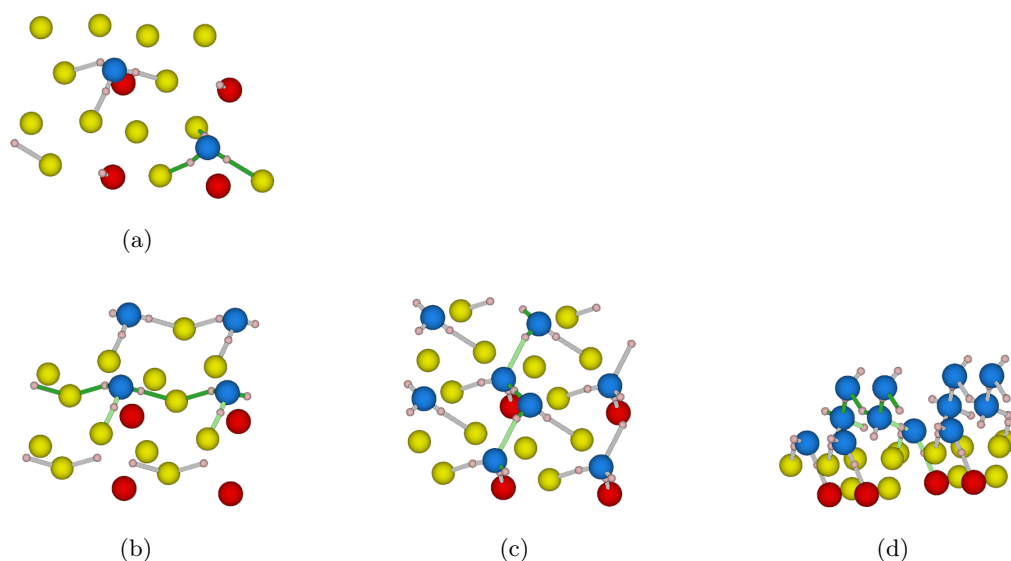


**Figure A.43:** Water structure motifs found on the triply fluorinated  $(1\bar{1}02)$  surface; (a) two water molecules on a  $2\times 2\times 1$  SC, (b) one water molecule per UC, (c) two water molecules per UC, and (d) three water molecules per UC - gray = aluminium, red = oxygen, yellow = fluoride, white = hydrogen, light blue = water oxygen, green = structure motif, light green = 2nd structure motif/supporting structure motif, and light gray = de-emphasised hydrogen bonds (VASP-DFT, PBE/PAW, 600.0 eV energy cut-off, D3-BJ).

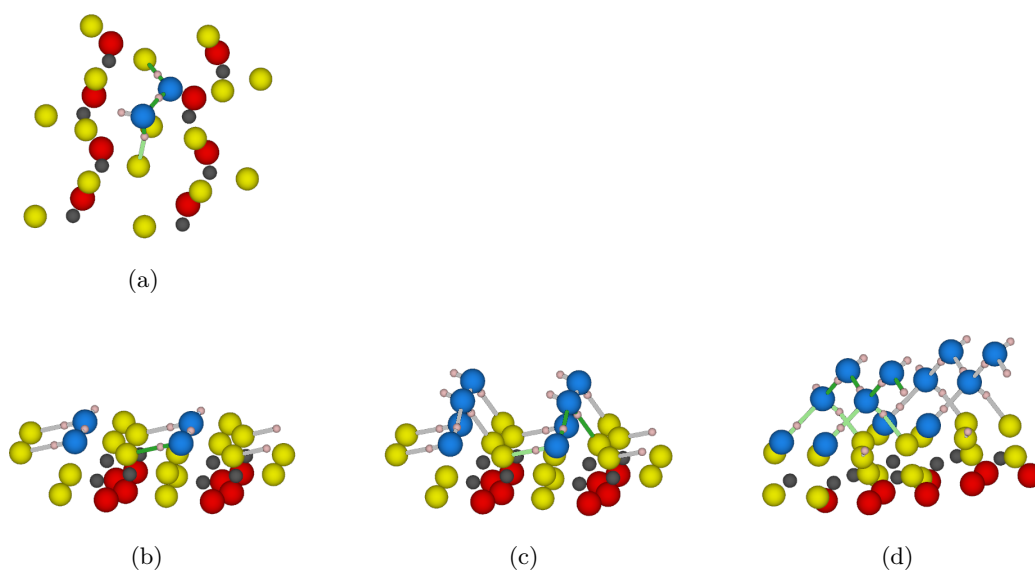


**Figure A.44:** Water structure motifs found on the fourfold fluorinated  $(1\bar{1}02)$  surface; (a) two water molecules on a  $2\times 2\times 1$  SC, (b) one water molecule per UC, (c) two water molecules per UC, and (d) three water molecules per UC - gray = aluminium, red = oxygen, yellow = fluoride, white = hydrogen, light blue = water oxygen, green = structure motif, light green = 2nd structure motif/supporting structure motif, and light gray = de-emphasised hydrogen bonds (VASP-DFT, PBE/PAW, 600.0 eV energy cut-off, D3-BJ).

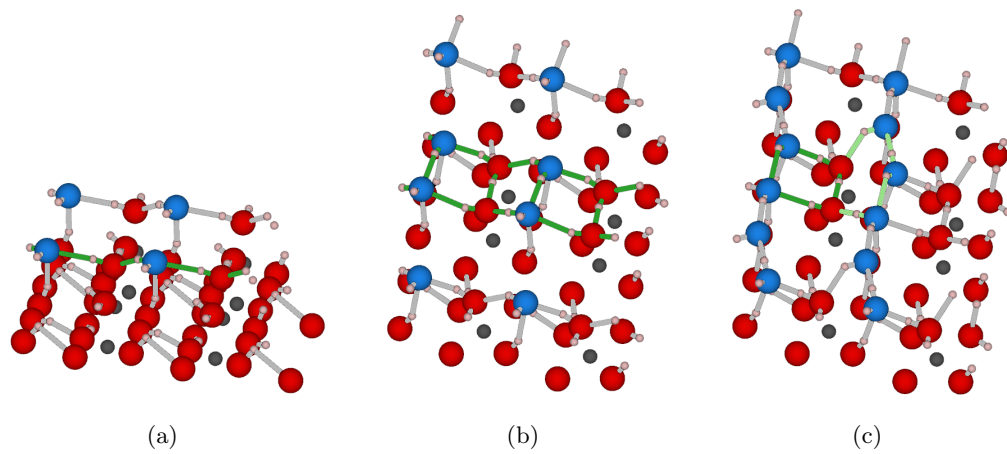


**Figure A.45:** Water structure motifs found on the hydrated  $(11\bar{2}3)$  surface; (a) one water molecule per UC, (b) two water molecules per UC, and (c) three water molecules per UC - gray = aluminium, red = oxygen, white = hydrogen, light blue = water oxygen, green = structure motif, light green = 2nd structure motif/supporting structure motif, and light gray = de-emphasised hydrogen bonds (VASP-DFT, PBE/PAW, 600.0 eV energy cut-off, D3-BJ).

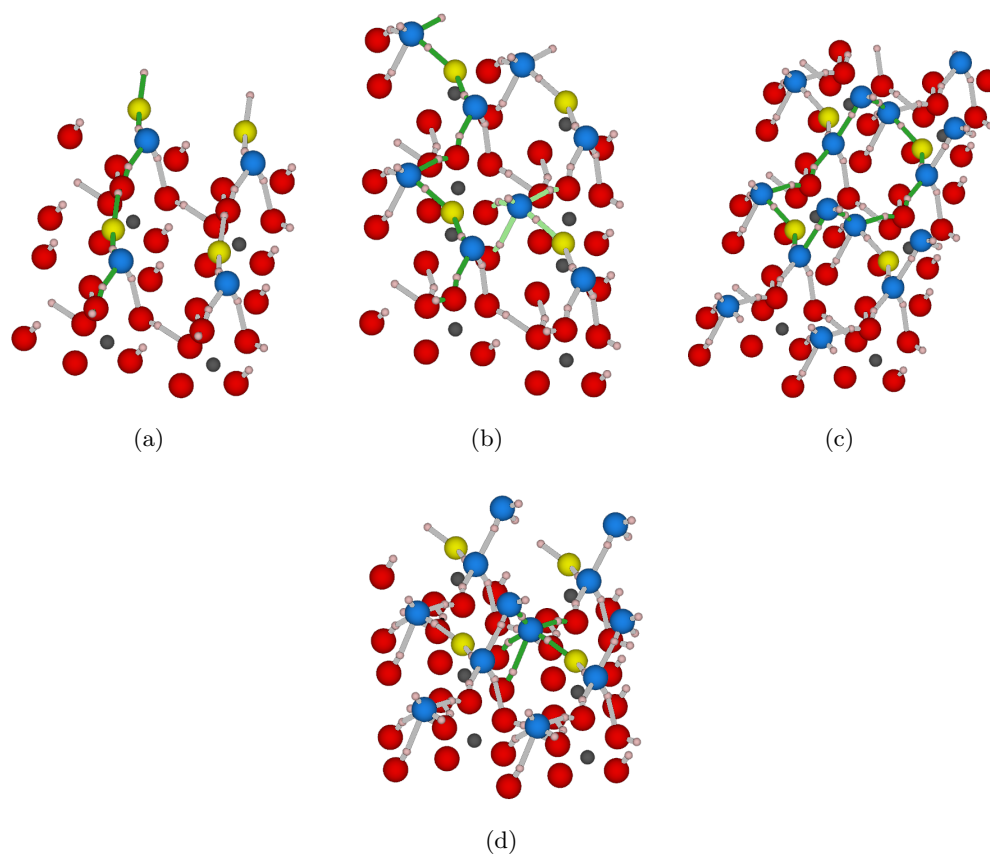


**Figure A.46:** Water structure motifs found on the singly fluorinated  $(11\bar{2}3)$  surface; (a) one water molecule per UC, (b) two water molecules per UC, and (c) and (d) three water molecules per UC - gray = aluminium, red = oxygen, yellow = fluoride, white = hydrogen, light blue = water oxygen, green = structure motif, light green = 2nd structure motif/supporting structure motif, and light gray = de-emphasised hydrogen bonds (VASP-DFT, PBE/PAW, 600.0 eV energy cut-off, D3-BJ).

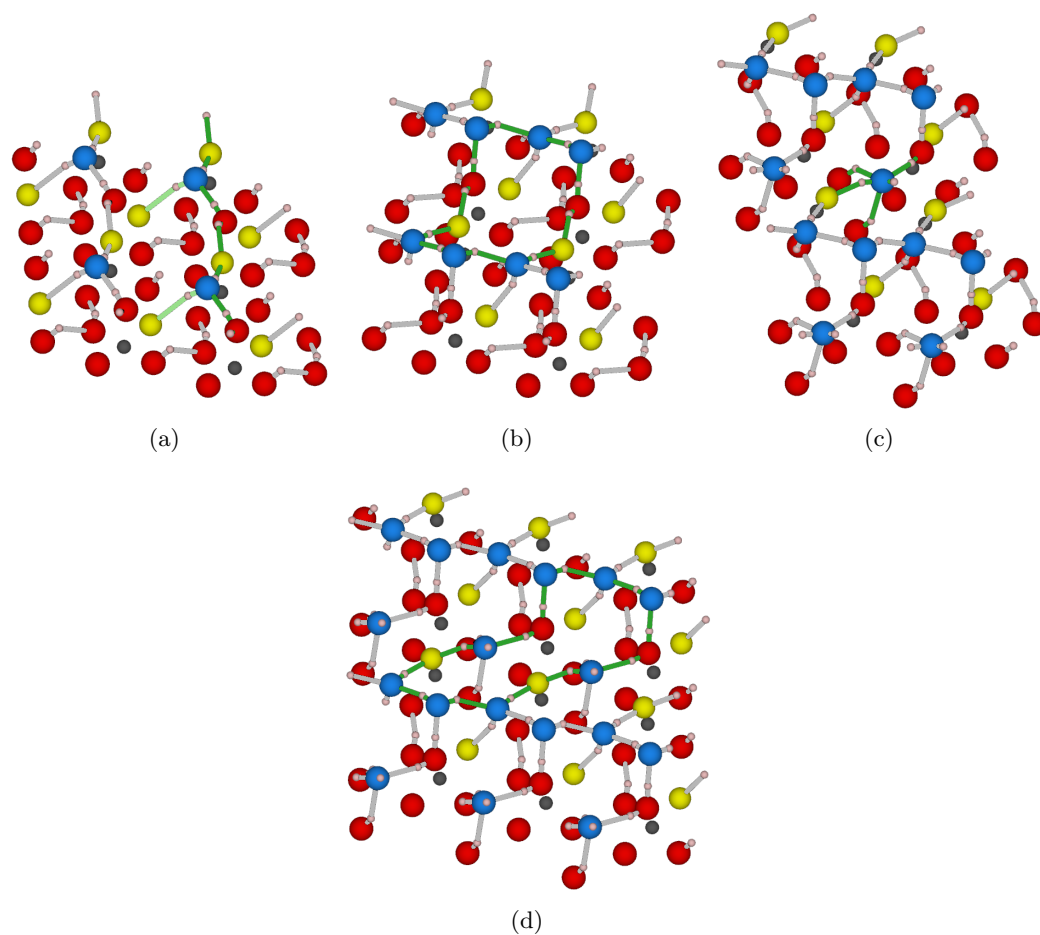


**Figure A.47:** Water structure motifs found on the doubly fluorinated  $(11\bar{2}3)$  surface; (a) one water molecule per UC, (b) two water molecules per UC, and (c) and (d) three water molecules per UC - gray = aluminium, red = oxygen, yellow = fluoride, white = hydrogen, light blue = water oxygen, green = structure motif, light green = 2nd structure motif/supporting structure motif, and light gray = de-emphasised hydrogen bonds (VASP-DFT, PBE/PAW, 600.0 eV energy cut-off, D3-BJ).

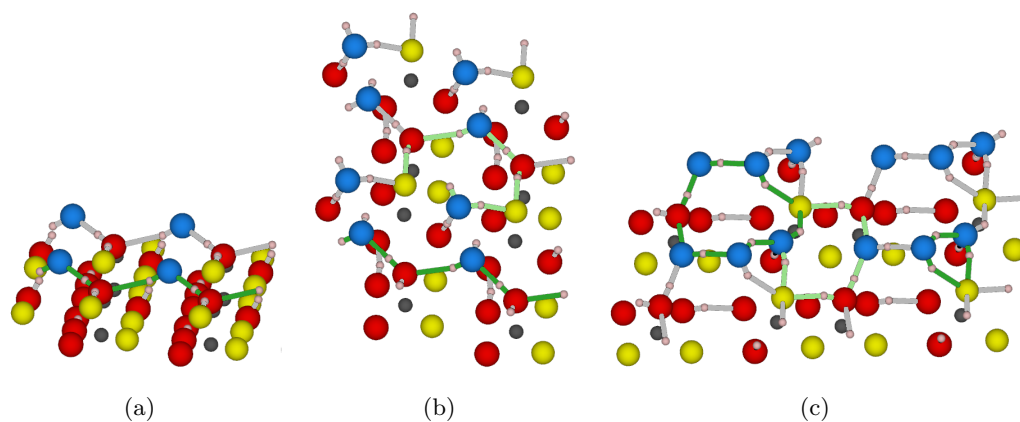


**Figure A.48:** Water structure motifs found on the triply fluorinated  $(11\bar{2}3)$  surface; (a) one water molecule per UC, (b) two water molecules per UC and, (c) three water molecules per UC - gray = aluminium, red = oxygen, yellow = fluoride, white = hydrogen, light blue = water oxygen, green = structure motif, light green = 2nd structure motif/supporting structure motif, and light gray = de-emphasised hydrogen bonds (VASP-DFT, PBE/PAW, 600.0 eV energy cut-off, D3-BJ).

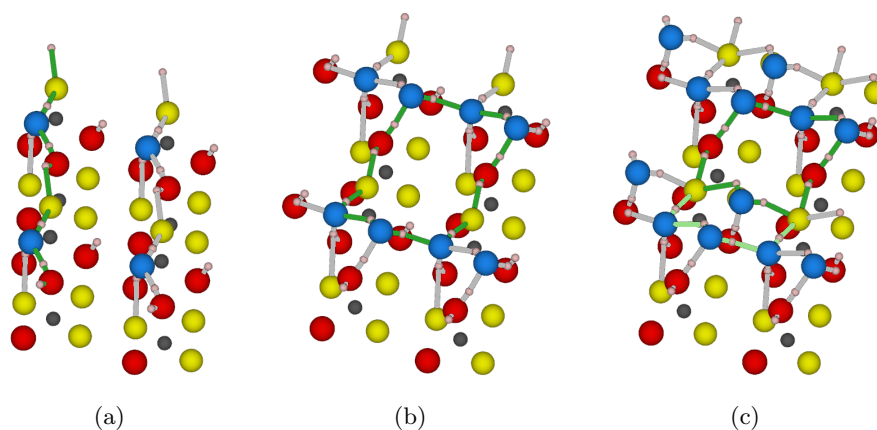


**Figure A.49:** Water structure motifs found on the fourfold fluorinated  $(11\bar{2}3)$  surface; (a) one water molecule per UC, (b) two water molecules per UC, and (c) three water molecules per UC - gray = aluminium, red = oxygen, yellow = fluoride, white = hydrogen, light blue = water oxygen, green = structure motif, light green = 2nd structure motif/supporting structure motif, and light gray = de-emphasised hydrogen bonds (VASP-DFT, PBE/PAW, 600.0 eV energy cut-off, D3-BJ).

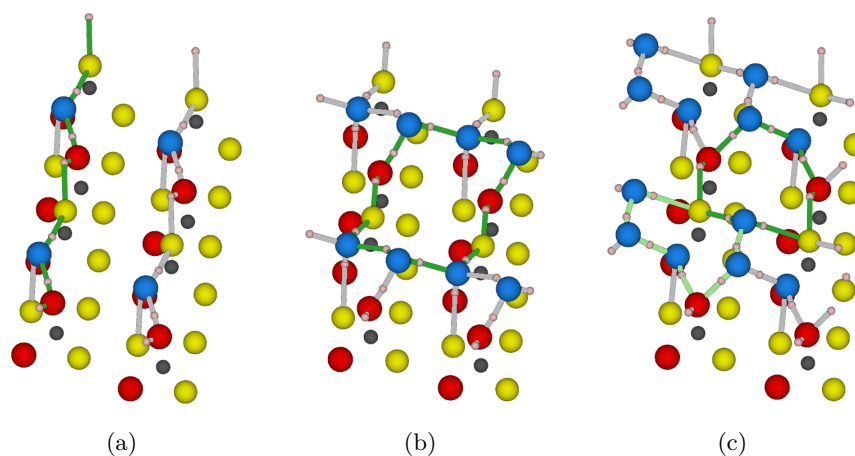


**Figure A.50:** Water structure motifs found on the fivefold fluorinated  $(11\bar{2}3)$  surface; (a) one water molecule per UC, (b) two water molecules per UC, and (c) three water molecules per UC - gray = aluminium, red = oxygen, yellow = fluoride, white = hydrogen, light blue = water oxygen, green = structure motif, light green = 2nd structure motif/supporting structure motif, and light gray = de-emphasised hydrogen bonds (VASP-DFT, PBE/PAW, 600.0 eV energy cut-off, D3-BJ).

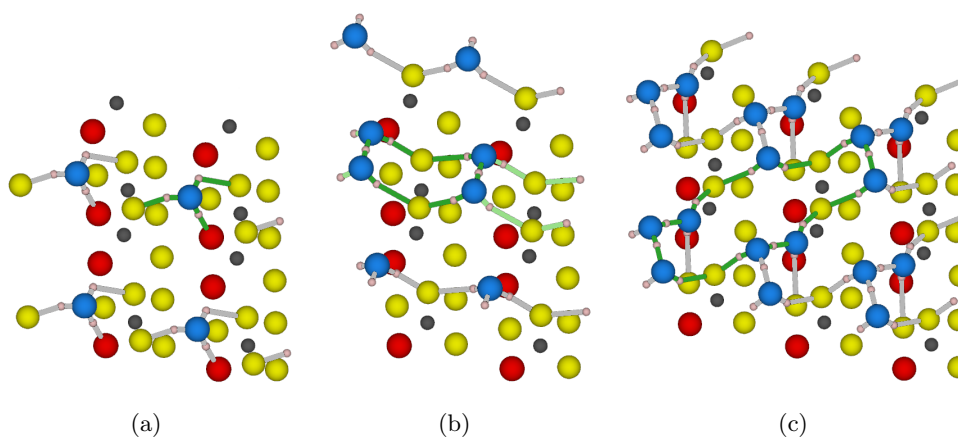


**Figure A.51:** Water structure motifs found on the sixfold fluorinated  $(11\bar{2}3)$  surface; (a) one water molecule per UC, (b) two water molecules per UC, and (c) three water molecules per UC - gray = aluminium, red = oxygen, yellow = fluoride, white = hydrogen, light blue = water oxygen, green = structure motif, light green = 2nd structure motif/supporting structure motif, and light gray = de-emphasised hydrogen bonds (VASP-DFT, PBE/PAW, 600.0 eV energy cut-off, D3-BJ).

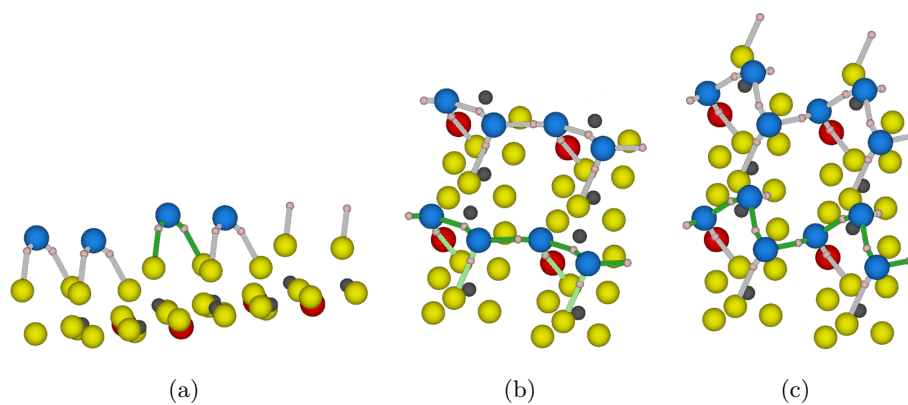


**Figure A.52:** Water structure motifs found on the sevenfold fluorinated  $(11\bar{2}3)$  surface; (a) one water molecule per UC, (b) two water molecules per UC, and (c) three water molecules per UC - gray = aluminium, red = oxygen, yellow = fluoride, white = hydrogen, light blue = water oxygen, green = structure motif, light green = 2nd structure motif/supporting structure motif, and light gray = de-emphasised hydrogen bonds (VASP-DFT, PBE/PAW, 600.0 eV energy cut-off, D3-BJ).